Single Particle Tracking as a Tool to Investigate the Dynamics of Integrated Membrane Complexes *in vivo*



Alex Robson

Brasenose College & Department of Physics

University of Oxford

A thesis submitted for the degree of

Doctor of Philosophy

Date: Michaelmas 2012

Acknowledgements

First and foremost my supervisors, Dr Mark Leake and Prof. Kevin Burrage. Both have been pretty patient throughout especially during writing up. Next up, are the other members of Mark's group that I've worked with; Ollie and Isabel. Ollie who would let me raid his lab in physics for parts, sometimes with permission, and Isabel who wrote the excellent and overused tracking software. Other members I worked with are Dr Ian Dobbie, for helpful tips in optics and Nic Delalez for raiding his lab in biochem for reagents. Outside of the group, Sarah Matthews who was instrumental for my experiments. I've lost count on how many reagents you prepared for me. Also a nod to the former post-doc Quan Xue who wrote the original tracking code. Outside of the group my thanks go to Irwin for the diffusion discussions and for having the same late night working hours as me. Outside of departments I need to say thanks to a few other Oxford based friends. Tom A, Tom H and especially Lee. Source of continual g-chat interruptions and other inane distractions, made up for being the part of the 2B crowd and Five pound 'aspiring' thursdays. Others are David P in London and Andy I, whichever country you're in. Also to my Churchill buddies, Emma F, JV, Newy, Nick W, Rich W, Jacquie & Lawrence, Jason C, Chris T, Pav, and finally Ku for the good memories. Finally, I want to acknowledge my entire family; especially my dad and sis for being supportive throughout.

Statement of Originality

This thesis submitted to the University of Oxford in fulfillment of the requirements of the degree of Doctor of Philosophy. This thesis contains no material previously submitted for a degree or diploma at this University of any other institution. There are three sets of experimental data used, one of which I had no role in collection (Tat) and were obtained by Dr Mark Leake and Dr. Ben Berks at the department of Biochemistry, University of Oxford. The OXPHOS data was partially collected by me initially, but the data used here were gathered predominately by Oliver Harriman (Leake group, Oxford Physcs), Heiko Erhardt (Institut für Organische Chemie und Biochemie, Freiburg, Germany) and Dr Tchern Lenn (formerly Queens Mary University, London). All helix data presented were obtained and analysed by me solely. BODIPY data were obtained with Dr Tchern Lenn. Imaging and tracking algorithms were written by Isabel Llorente (Leake group, Oxford Physics), although applied and modified by me, except for in Chapter 5. All data presented in Chapter 1 are from research papers or collaborators data and any other review elements are indicated. Otherwise all results presented are my own original work towards this research degree.

Alex Robson

Department of Physics

University of Oxford

Michaelmas 2012

Publications and Presentations arising from this D.Phil work

Published papers

[1] A. Robson, K. Burrage and M. C. Leake, 'Inferring diffusion in single live cells at the single-molecule level.', *Philosophical transactions of the Royal Society of London. Series B, Biological sciences*, vol. 368, no. 1611, p. 20 120 029, Jan. 2013

[2] I. M. Dobbie, A. Robson, N. Delalez and M. C. Leake, 'Visualizing single molecular complexes in vivo using advanced fluorescence microscopy.', *Journal of visualized experiments : JoVE*, no. 31, p. 1508, Jan. 2009

Papers in preparation

[1] A. Nenninger, G. Mastroianni, A. J. Robson, Y. T. Lenn, Q. Xue, M. C. Leake and C. W. Mullineaux, 'Independent mobility of proteins and lipids in the plasma membrane of Escherichia coli', *In preparation*, 2012

[2] I. Llorente-Garcia, T. Lenn, H. Erhardt, O. L. Harriman, L. Liu, A. Al-Mahmood, A. Robson, S.-W. Chiu, S. Matthews, C. Bray, T. Friedrich, C. W. Mullineax and M. C. Leake, 'Molecular architecture and dynamics of functional oxidative phosphorylation machinery observed by in vivo single-molecule imaging', *In preparation*, 2013

[3] A. Robson, A. Nenninger, C. W. Mullineax and M. Leake, 'Passive partitioning of a non-native transmembrane helix protein into transition-temperature sensitive membrane domains of Escherichia-coli', *In preparation*, 2013

Conference papers, posters, talks and other presentations

[1] A. Robson, M. Tyndall, P. Maini and M. C. Leake, 'Developing Statistical Diagnostic Tools For Discriminating Between Different Diffusive Modes Of Fluorescently

Tagged Protein Complexes In Living Cells For Short Duration Trajectories', *Biophysical Journal*, vol. 96, no. 3, 33a, Feb. 2009

Single Particle Tracking as a Tool to Investigate the Dynamics of Integrated Membrane Complexes *in vivo*

Alex Robson

Brasenose College & Department of Physics

University of Oxford

A thesis submitted for the degree of

Doctor of Philosophy

Date: Michaelmas 2012

The last decade has seen substantial advances in single-molecule tracking methods with nano-metre level precision. A powerful tool in single-molecule tracking is fluorescence imaging. One particular application, total internal reflection microscopy, can capture biological processes at high contrast video rate imaging at the single-particle level. This thesis presents methodologically novel methods in analysing single particle tracking data. Presented here is an application of a Bayesian statistical approach that can discriminate between the different diffusive modes that appear with the presence of membrane architecture. This algorithm is denoted BARD; a Bayesian Analysis to Ranking Diffusion. These algorithms are applied to a total internal fluorescence microscopy based experimental data of a novel membrane probe in *Escherichia coli*. This probe is a plasmid expressed, non-native membrane integrating trans-membrane helix and thus acts as an ideal protein based probe under no specific native control. Two experiments were performed using a combination of varying helix probe size and growth temperature experiments effectively altering the transition temperature of the membrane. These data are suggestive of a passive partitioning of the helix protein into mobile and immobile domains that emerge from the underlying phase behaviour of the membrane.

Contents

Contents vii

Nomenclature xi

List of Figures xiii

List of Tables xxxi

1 Bacterial Membrane Heterogeneity 3

1.1 Introduction 4

1.2 Experimental Methods in Membrane Biophysics 8

1.3 Origins of Biological Membrane Heterogeneity 12

1.3.1 The Lipid Raft-domain Hypothesis 12

1.3.2 Investigations with Model Membranes - Phase Separation and Critical Fluctuations in Model Membranes 15

1.3.3 Domain Dynamics in Biological Membranes 15

1.3.4 Kinetics of Domain Growth 17

1.4 Dynamics of Integrated Membrane Complexes 19

1.4.1 Crowding 19

1.4.2 The Effect of the Actin-cytoskeletal Network 20

1.4.3 Curvature Mediation 20

1.5 Candidate Biological Models in Single-Molecule Fluorescence 22
1.5.1 Prokaryotic *E. Coli* as a Model Organism 22
1.5.2 Use of a Helix Protein as a Novel Non-native Probe of Membrane Biophysics 23
1.5.3 BODIPY as a Fluorescent Lipid Analogue 24
1.5.4 Twin Arginine Translocase 24
1.5.5 Bioenergetics 24
1.6 Discussion 26
1.7 Chapter Summary 27

2 Single-Molecule Fluorescence Microscopy: Principles, Protocols and Calibration 29

2.1 Introduction 30
2.2 The Principles and Theory of Single Molecule Fluorescence Microscopy 31
2.2.1 Stokes Shift 31
2.2.2 Blinking and Bleaching 31
2.2.3 Refraction and Evanescent Field Illumination 36
2.3 Protocols in Experimental Fluorescence Microscopy 37
2.3.1 Excitation Modes 37
2.3.2 A Custom-built Inverted TIRF microscope 39
2.3.3 Widefield/Fluorescence Imaging 42
2.4 Image Acquisition and Analysis 46
2.5 Calibrating single-molecule fluorescence microscopy 47
2.5.1 TIR Calibration 47
2.5.2 Stoichiometric Calibration 48
2.6 Sources of Experimental Error 58
2.6.1 Errors in Tracking 58
2.6.2 Systematic Error in Experimental Set-up; Alignment 60

2.6.3 Experimental Calibration Error Propagation . . . 62
2.7 Chapter Summary . . . 67

3 Bayesian Inference for Single Particle Tracking 69
3.1 Introduction . . . 70
3.1.1 Statistical approaches to discriminate competing models . . . 80
3.2 Theory . . . 83
3.2.1 Biological Models of Diffusion . . . 83
3.2.2 The Principles of Bayesian Statistical Inference . . . 88
3.3 A novel application of a Bayesian scheme to SPT in live cells. . . . 93
3.3.1 Likelihood Functions . . . 94
3.3.2 Prior Formulation . . . 97
3.3.3 Inference scheme . . . 101
3.3.4 Accurate model selection and parameter inference . . . 103
3.3.5 Numerical Methods . . . 104
3.4 Results . . . 107
3.4.1 Model Ranking: Classification . . . 107
3.4.2 Sensitivity Analysis . . . 112
3.4.3 Multistate kinetics: Identifying dynamics . . . 115
3.4.4 Multistate kinetics: Identifying sub-populations . . . 116
3.5 Discussion . . . 121
3.6 Conclusion . . . 122
3.7 Future Work . . . 124
3.8 Chapter Summary . . . 127

4 Characterising *Escherichia Coli* Biological Membrane Heterogeneity through a non-native transmembrane helix and fluorescent lipid probes 129
4.1 Introduction . . . 130

4.2 Materials and Methods . . . 134
4.2.1 Analysis . . . 138
4.3 Results . . . 139
4.3.1 Lipid and protein mobility in the plasma membrane of *E. coli* . . . 139
4.3.2 Spot stoichiometry has no relation to other mobility parameters . . . 142
4.3.3 Overview of size and growth temperature dependence . . . 142
4.3.4 Domain mobility is heterogeneous . . . 146
4.4 Discussion . . . 151
4.5 Conclusion . . . 154
4.6 Future Work . . . 155
4.7 Chapter Summary . . . 157

5 Characterising *Escherichia Coli* Biological Membrane Heterogeneity through native protein-FP fusion hybrids. 159

5.1 Abstract . . . 159
5.2 Introduction . . . 160
5.3 Materials and Methods . . . 161
5.3.1 Bacterial cell strain and preparation . . . 161
5.4 Results . . . 162
5.4.1 Application to experimental Tat data. . . . 162
5.4.2 Application to experimental OXPHOS data . . . 165
5.5 Conclusion . . . 165
5.6 Summary . . . 166

6 Conclusions 169

6.1 Future Work and Outlook . . . 171
6.1.1 Outlook . . . 172

Appendix A **173**

A.1 Numerical Integration routine pseudocode 173

A.2 Estimating Stoichiometry 173

Appendix B **175**

A.3 Mathematical Appendix 175

A.3.1 Functions and Operators used in Diffusion Theory 175

A.3.2 Laplace's Method 175

List of Figures

1.1 Figure taken from [12]) Shells, complexes and nanoclusters range from 1-10nm, whereas nanodomains and caveolae can be up to 100nm. Larger domains on a microscopic scale may organise on a long-distance scale. 6

1.2 Length scales of domains in biomembranes 9

1.3 The lipid raft concept. Cholesterol and sphingolipid associated into a dense ordered domain. Raft proteins have a preferential association with such domains 13

1.4 Anomalous mobility spike at growth temperatures 18

1.5 Diffusion coefficient of BODIPY in the working paper [3] at two different growth temperatures, over a temperature range. BODIPY is a fluorescent lipid analogue discussed in §1.5.3. There is a peak, within error, at both growth temperatures of the diffusion rate of BODIPY. 18

1.6 Proteins investigated in this thesis. The helix has no native function and acts as a membrane probe. Schematic of (a) membrane bound ring-architecture [91] of a Twin-Arginine Translocase TatA nanopore allowing translocation of a full folded protein substrate across the cytoplasmic membrane, and of (b) the TatA-YFP, TatB, TatC and Helix1021-GFP proteins (coloured circles indicating individually amino acid residues in the native proteins). The helix protein has no known homologue and acts as an ideal probe. Images adapted from [1, 47] 25

LIST OF FIGURES

2.1 Schematic for fluorescence imaging. A molecule of interest is tagged (MOI) with a fluorophore (F). For GFP, excitation is with a 473 nm laser. The stokes shift is represented by the red shifting of the emitted photons. 30

2.2 Jablonski diagram displaying the energy states of a molecule. Molecules not absorbing energy are mainly confined to the lowest vibrational states of the ground state S_0. (b) The spectral characteristics related to absorption and emission of energy by a molecule can be related to the size of the energy steps needed to bring a molecule from one energy level to another. The absorption and emission spectra of the common fluorophore Fluorescein isothiocyanate (FITC) are shown in the Jablonski diagram. Each vertical grey line aligns the spectra with the energy of the absorbed (arrows pointing up) or emitted (arrows pointing down) photons. The arrows are coloured to represent the wavelength of the photons. For example, the purple arrow to the left represents the energy of an ultraviolet photon that can cause the molecule to undergo a transition from the ground state to the second singlet excited state. The orange arrow on the right represents the lowest energy photon that can be emitted by this molecule as it drops back from the lowest energy state of S1 to a high vibrational state of S0. Note in the region of overlap of the absorption and emission spectra, some photons (for example, the green, up-pointing arrow) are absorbed when the vibrational level is not at its lowest level. Also note the symmetry between the absorption and emission curves owing to the similarity of transitions to vibrational states in S0 and S1. (c) The typical times that the various steps in fluorescence excitation and emission and phosphorescence take. [94] 34

2.3 The illumination mode beyond the interface is governed by three variables. These are the refractive indices n_1 and n_2, and the incident illumination angle θ_1. The critical angle θ_c is governed by a function of the two refractive indices. At incident illumination angles below the critical angle, incident radiation propagates through the interface. At incident illumination angles beyond the critical illumination angle, the bulk of the radiative energy is totally internally reflected. However, a thin evanescent field of illumination propagates through the interface. 36

2.4 Excitation fields used. A) Epi-fluorescence. Radiation is perpendicular to the interface and is effectively uniform over the region of interest in the medium. B) Shallow-angle epi-fluorescence. Radiation enters away from the normal. This reduces some illumination of the sample and media reducing back scatter. C) TIRF radiation totally internally reflects. 37

2.5 The home-built TIRF inverted bespoke microscope 40

2.6 Overview of optical set up. Incident radiation enters the objective lens after the dichroic mirror and illuminates the sample. Excitation and emission beams then exit the objective, with the excitation path reflecting back of the dichroic mirror. The emission path then passes through the tube lens, intermediate lens and the final camera lens respectively. 41

2.7 Imaging protocol. To focus at 100nm, the focus is adjusted to maximise the contrast of the 200nm latex beads on the coverslip - specifying a focus of around 100nm, as indicated in the dashed red circle. Then, the stage is moved to a nearby cell (within the range of the piezo controller on the order of a few microns) and another bright-field image is taken. Top right: epi-fluorescence imaging at 100nm focus. Bottom left: mid cell focus. Bottom right: epi-fluorescence imaging at the midcell. 44

2.8 Schematics of slides used in this thesis. A top-down diagram of a flow-cell. The outer boundary represents the glass slide, the middle square represents the coverslip, the two rectangular sections represent the vacuum grease or double sided sticky tape and finally the blurred blue section in the middle represents the solution in the flow-cell. This is depicted with excess solution to indicate fluid on the exit points of the flow-cell to prevent dehydration. 45

2.9 Tracks are found from a spot-finding algorithm (A). In each case, the Point Spread Function (PSF) of the spot is fitted by a two-dimensional Gaussian at point C_{xy} ($I_{fit} \times \mathcal{N}(C_{xy}, \sigma)$), and the local background intensity I_{bg}, the height and the standard deviation of the PSF are found. (C) The process is repeated for all spots in the frame. D) Spots are linked into trajectories by using heuristic measures such as the centroid separation and the change in intensity between the two spots. 46

2.10 a) TIRF Calibration geometry. The θ represents the respective the angles with respect to the normals incident to the surface of the respective interfaces. θ_a represents the exit angle, θ_c represents the angle normal to the cube-air interface, θ_g represents the normal to the glass-cube interface and θ_g represents the exit angle from the objective lens and the incident angle from the oil-glass interface. b) Measured laser angles as a function of mirror displacement from epi-fluorescence. Red: O_o, exit angle from objective. Blue: exit angle from glass into glass-air interface (without a cube). The solid black lines indicate the maximum predicted angle for a 1.45 and a 1.50 NA objective respectively. The dash blue lines indicate the glass-air horizon and the oil-sample horizon (the onset of TIR). The dashed-black line represents a polynomial fit of order 2 to the the angle-data at the objective output. 49

2.11 Left: Depth of penetration versus incident laser angle. Error bars are standard deviation error by quadrature error propagation. Right: Excitation field as a function of distance from the sample-coverslip for varying depths of penetration. 50

2.12 Fourier step-detection for a 100 W /cm^{2}epi-fluorescence illumination. A) Photoblinking steps in a single GPF molecule. The two lines indicate the raw data and the filtered data respectively. The signal is background corrected with the noise. B) Histogram of all pair-wise intensity differences. C) Fourier transform of pair-wise intensity differences. Peaks in the data trace are identified. The peak identified in this case is 1.99×10^3, in agreement with the data presented in Figure 2.14. 53

2.13 Left: Point spread functions from a GFP field imaged from the protocol in Section 2.5.2. The heterogeneity in the peak sizes implies that GFP aggregation has occurred, and that these are not single GFP molecules. This is further seen with photobleaching curves. The black sides where there is a drop off in intensity is due to the shutters. Right: Single GFP molecule excitation step as a function of epi-fluorescence illumination intensity in a 20 µm beam (blue circles) and TIR illumination (evaluated 5 nm from the coverslip, red circles). The x-axis is the radiation flux, the y-axis is the noise-corrected count integrated over the GFP spot (see §2.5.2.1) with SD error bars. The levelling off from around 7 mW (1000 W /cm)^2 is due to putative photosaturation of the GFP, comparable to other values [102], imaged under comparable conditions (phosphate buffered saline (PBS), pH 7.5) The linear regime agrees with other results under similar experimental conditions (approximately 1000 counts for 0.77 mW) due to the cage like structure of GFP [103]. This is supported by the independent measure of the mean photoactive time, which stabilises at these illumination intensities as the on/off time-scale ratios equilibrate. Fitting values are $C_s = 8.6883 \times 10^3$ counts and $\xi = 210.9$ W /cm^2 54

2.14 Identifying single molecule switching in GFP imaged at 7 mW under epi-fluorescence excitation. In the upper panel, a time series of frame-averages (10 frames, non-overlapping) is shown. The off-on-off activity of the GFP is seen clearly, but also the flickering between frames 540-550. In the lower panel, the intergrated intensity trace is shown. In the trace, photoactive GFP are marked where the intensity is above $3\sigma_{bg}$. The 3σ threshold is as discussed in Section 2.5.2 is the high probability threshold, and the flickering between frames 540 and 600 does appear to be captured by this threshold, which can be seen by eye in the upper panel. 55

2.15 Estimating *in vivo* stoichiometry. The data are taken from a TIR acquisition of the helix-x1 protein (see Chapter 4) under approximately 500 W /cm^{2}illumination. Absolute time refers to the time from the onset of illumination. The beginning of the data trace commences when the tracking software identifies a diffusing spot. The dashed black line represents the fitting (Equation A.2, and the grey background represents one standard deviation in uncertainty about the fit - as estimated from §2.6.3. From this fitting, an estimate of I_0, the estimated intensity at the commencement of illumination of the sample. From this, the stoichiometry is estimated by the ratio of this intensity value divided by the estimated single fluorophore intensity value under excitation conditions. This particular fitting has values of $I_0 \approx 4 \times 10^5$ counts, $\tau = 0.3$ sand $\nu = 0.2 \times 10^5$ counts. Under these illumination conditions, stoichiometry is estimated at 138 units. Accounting for fitting uncertainty, and angle calibration errors, this is between the range of 110-168 to one standard deviation. The estimated number of photons emitted before photobleaching is approximately 2×10^5 for around 140 units, which is $\approx 1.4 \times 10^3$ photons/GFP. Reference [104] reports that single molecules GFP emit $\leq 4 \times 10^5$ before photodestruction. This difference is accounted in part by the photon detection efficiency of around 10%. The remaining fraction, I attribute to non-uniform illumination, lack of tracking when the Signal-to-Noise ratio has fallen sufficiently and different experimental conditions that may impact the number of GFP photons emitted. 57

2.16 Centroid localisation. In a) the centroid localisation accuracy is given for typical values with $s = 75$ nmand $a = 50$ nm. The SNR is defined as the ratio of the mean of the signal over the standard deviation of the background (bg) $\mu_{\text{signal}}/\sigma_{\text{bg}}$. b) An example track, taken from fluorescence imaging of a protein-GFP (see Chapter 4). In the case here, the y-intercept is at approximately 0.002 µm^{2}corresponding to an initial uncertainty of around 50 nm. 60

2.17 Upper: bright-field illumination of an empty region. Lower: Typical variation of noise across the image profile at 7 mW illumination with a 20 μmradius 473 nm illumination field. Each section is a piecewise intensity time-series profile along the horizontal x-axis uniformly divided along the y-axis. Although the coverslip is empty, the dark regions on the bright-field is dust/dirt on one of the mirrors, which is the (probable) origin of the dip in the fluorescence profile seen in the last two intensity profiles in the lower panel. 61

2.18 TIR objective. Salt deposits formed crystals about the edge of the objective, where TIR appears. The likely source of these is deposited media that then evaporates, leaving salt deposits which crystallise. As these were found around the edge of the objective, where high-angle TIR beams originate from, this was found to create diffraction patterns and scattering when imaging under TIR. 62

2.19 Geometry in angle calibration. 63

3.1 The complexity of molecular diffusion in living cells. (a), Schematic of diffusion (orange track) of a single molecule or complex (pink circle) in a live cell with (b) simulated data for the typical spatial localizations of tracked molecules in the specimen xy plane of a typical optical microscope illustrating four common modes of diffusion. (c) Idealized forms of mean-squared displacement (MSD) relations for anomalous (green), Brownian (blue), confined (red) and directed (cyan) diffusion. (d) Experimental traces of a real data-set with different stoichiometries of the Tat dataset analysed in chapter 5. Tracks are sampled at 40ms video rate imaging, with typically 5-15 data points. (e) the mean average of many simulated MSD relations (blue line), blue shading indicating the stochastic spread at one standard deviation, illustrating the marked heterogeneity due just to stochastic dispersion [122]. 73

3.2 Three scenarios depicting origins of subdiffusion. Left: The tracer particle is 'raft' bound. As the particle diffuses, the preferential association with a lipid patch, which also diffuses, may introduce correlations such as in FBM. Middle: A random walk in a dynamic environment. The tracer particle experiences transient traps with a lifetime diverging with density. This may be modelled as a CTRW with power-law distributed waiting times. Right: A Random walk with static obstacles such as the cytoskeleton, or protein anchors. This may be modelled by a random walk on a percolation cluster. 75

3.3 Interpolation. The *stochastic* dispersion for a given model. The expected dispersion in the time-averaged MSD for a given track length N at sample point n is given by σ_v. 82

3.4 Time-averaging of tracks in normal diffusion or the non-ergodic CTRW in the time-averaged mean-squared displacement of Equation 3.7. Left: A simulated particle with diffusion coefficient of $D = 0.01\mu m^2/s$ under a sampling time of 0.04s. Right: A CTRW model with anomalous coefficient $\alpha = 0.8$, using the simulation method in Reference [127]. In both cases, the ensemble is over a hundred identically simulated tracks using the un-averaged MSD. 83

3.5 Numerical simulations. Leftmost (a); a slice of the solution to the anomalous diffusion equation. Middle (b) ; Brownian. Rightmost (c): Simulated confined. The PDFs to these were detailed in §3.2.1 with a look up table given in Table 3.1. The numerical solution of a) is given by a rejection sampling algorithm of Equation 3.19. b) is calculated using standard libraries in `MATLAB`. c) The displacements in xy are of a highly sampled confined track with colouring added to indicate procession with time proceeding from red at the origin to light green. The inset shows the observed track with just $N = 10$ data points at video-rate sampling. Confinement radius $l = 0.1\mu m$. 87

3.6 Schematic representation of Bayesian Inference. A posterior distribution $P(\mathbf{w}|\mathcal{D})$ is defined as the product of the likelihood $P(\mathcal{D}|\mathbf{w})$ with the prior distribution $P(\mathbf{w})$, divided by the evidence $P(\mathcal{D})$. Bayesian inference updates a prior with data $\mathcal{D}$. . . 90

3.7 Model Comparison 92

3.8 Bayesian Occam Razor. The Occam factor $\sigma_{w|D}/\sigma_w$ has magnitude less than one. This acts as a penalty term to the model M_i. 93

3.9 Upper row. To avoid overfitting to short tracks that just by stochastic dispersion appear confined, a prior on $P(C)_0$ - the probability of confinement - is used (Equation 3.47). This follows given the informative prior on the confinement size (bottom row). For short duration tracks, the potential region explored by a tracer is small. For long duration tracks, and given assumptions about the domain sizes, I expect confinement models to be able to be resolved. Thus, there is an interpolation of $P(C)_0$ ranging from zero to one. Similar arguments on time-scale can be applied to other models. Lower row: Prior about the confinement radius is informed from previous experiments. The plot is of Equation 3.46 using the value in Table 3.2. . . 100

3.10 The BARD algorithm. Each number corresponds to the enumerated list in §3.3.3 . 103

3.11 Implementing BARD. **A:** Simulated Brownian tracks (grey) all with diffusion coefficient $D = 0.01$ μm^2/s, with one of these tracks highlighted (black) for BARD analysis. **B:** Distribution of measured microscopic diffusion coefficient Dm values from tracks in (A) with Gamma fit indicated (dashed line), that forms the prior in the top panel in (C) **C:** Constructing probability distributions used in BARD for the highlighted track of (a) tested against a Brownian diffusion model showing the unnormalised prior (upper panel), likelihood (middle panel) and posterior (lower panel). Testing against the three other diffusion model generates two-dimensional unnormalised posterior distributions for **D:** anomalous, **E:** confined and **F:** directed diffusion models. For the highlighted track shown in (a) the highest ranking probability was measured at 65% for the Brownian mode, thus correctly identified with a probability which was more than twice as much as the next ranked mode of anomalous diffusion. 109

3.12 Characterizing the error in the BARD analysis using classification matrices for (a) the MSD method, and (b) the PDF method. Each 'pixel' in the matrix represents a combination of a type of simulated track against an inferred highest ranked diffusion model from the BARD analysis, with gray scale indicating the individual inference ranking percentage. Each diffusion mode here was simulated with three different tracks, and therefore each matrix is composed of individual 3x3 sub-matrices, with the percentage in red indicating the mean average inference ranking *relative* percentage within that sub-matrix. Thus, the diagonal of (a) and (b) constitutes the true-positive classification values. There are a range of values presented in each 9 element square. For A, the three rows for anomalous sources represent D=0.005, 0.01, 0.5 $\mu m^2/s$ (rows 1, 2, 3). This is repeated down the rows, with rows 4, 5, 6 and 7, 8, 9 corresponding to $D = 0.005, 0.01, 0.5$ $\mu m^2/s$, respectively. The columns of A represent different degrees of anomalous subdiffusion (0.7, 0.8, 0.9), respectively. Likewise, the columns of 'Confined' represent different domain sizes, (50,100,200 nm). The percentage overlay gives the average of each 3x3 block. Rows sum to one hundred to complete the set of tested models, with the remaining percentages being the percentage classified as 'Directed' modes (12, 6 and 0% for simulated anomalous, Brownian and confined modes respectively). Similar tests were not included for directed modes. 110

3.13 Applying BARD to simulated data of increasing complexity. In the upper row, freely diffusing Brownian unconfined tracks are simulated. The middle row has purely confined tracks ($L = 0.1\mu m$. The latter row has both sets. The blue MSD traces indicate track averages of mobile (i.e. Brownian) tracks. The red traces indicate track averages of confined tracks. From top to bottom, the mobile/immobile rankings were 41/9,30/20 and 35/65 (of which 25 were correctly classified as confined and the remaining 10 miscategorised). The second column are the kernel density estimates of the inferred confinement size. 111

3.14 Variation of ranking probability with number of track data points. A single track was simulated using a confinement radius $l = 0.1\mu m$ and microscopic diffusion coefficient of $D = 0.01\mu m^2 s^{-1}$. Model ranking inference was then applied against two possible diffusion models of confined (blue) and Brownian (green) diffusion, with the vertical axis here indicating the inference ranking probability for confined diffusion. 114

3.15 Directed diffusion validation. Tracks were simulated over a variety of non-dimensional parameters ξ. ξv is a measure of degree of directed to random drift and is given by $\xi_v = (vt)^2/((vt)^2 + 4Dt))$. Y-intercept and control simulations (where there is no directed motion) gives an estimate of the systematic error at around 20%. The diffusion coefficients simulated were $D = 1 \times 10^{-5}, 10^{-4}$ and 10^{-3} $\mu m^2 s^{-1}$ with corresponding velocities of v of 1,10 and 20 nm/s (see Table 3.3). In addition, three controls were performed at the listed diffusion coefficients at zero velocity. . A similar test was performed for the confinement with $\xi_L = ND\delta t/L^2$. This is displayed in the right figure. 115

3.16 Schematic of mode switching. Left: A particle goes from one lipid environment to another, modulating the diffusion coefficient. Right: A particle goes from a confining microdomain to freely diffusing. The underlay in both represents the appearance of lipid microdomains. 117

3.17 Inferring a sudden change in diffusion coefficient. (a) MSD relation for a single track simulated assuming Brownian diffusion (black) and the mean average of 20 such tracks (blue) for which the diffusion coefficient D switches from 0.01 to 0.10 $\mu m^2/s$. (b) Associated ranking inference probabilities for a single D Brownian (B) and two D Switching (S) model. (c) MSD relation for a single track (black) and average of several tracks (blue) for which D switches from 0.01 to 0.05 $\mu m^2/s$. (d) Associated ranking inference predictions 118

3.18 a) The MSDs of the mixed Brownian distribution, simulated with a 50/50 mix of D =0.01 and 0.02 μm^2/s respectively, and then shortened to a randomly chosen uniformly distributed length of [5,20] Key: Red: Confined (36 identified confined), Blue: Brownian (58), Green: Anomalous (6), Directed (0). b) The GMM of fit of the 3D parameter space ($D_\mu, D_\sigma, P(B)$) in the (x,y,z) axes respectively. The ellipsoidal boundaries of the Gaussians are drawn at 2σ; representing 87% of the probability mass. The blue points are the data, with a size to portray depth as an inverse function of distance away from the origin. c) The KDE estimate with the two fitted Gaussians (blue: KDE, green: individual Gaussian fit, red: GMM fit). Means of the GMM parameters are summarised in Table 3.6 118

3.19 GMM clustering. The upper row represent the AIC (blue), BIC (red) metrics, varying with the number of Gaussian Mixture components. Using the models described as full and mid detail, both of which account for $P(B)$, the minimum BIC is at with two Gaussians ((A) and (B) respectively). This minimum shifts to four when $P(B)$ isn't accounted for, shown in (C) with four Gaussians (Note that four Gaussians are plotted, one has a high variance and therefore not well identified on the contour map). The bottom row are the Gaussian clusters identified. The fourth pair (D,H) are the control, with only one population of freely diffusion protein ($N = 100$,$D = 0.01\mu m^2/s$). The minimum number of Gaussian clusters identified by BIC here is 1. Note that the Information metrics are not comparable, to different models or to each other. For example, AIC cannot be compared to BIC or the BIC in A compared to the BIC in B). In all cases here AIC is a poor metric for discrimination. 120

4.1 Variation of the transition temperature with the growth temperature in *E. coli*. Data taken from reference [192]. The growth temperatures used in reference [192] are at 17,27 and 38 ^{o}C, similar to the growth temperatures used in this report of 15,25,39 and 37 ^{o}C. The red line is a linear fit with the equation in-picture where x is the growth temperature and y is the transition temperature. 131

4.2 Helix protein. ***A)*** Each multimer of the helix protein has a GFP attached to it on the cytoplasmic side. The helix protein has four different molecular weights by repeated single transmembrane motifs. Helix protein imaging sequences. ***B)*** Epi-fluorescence imaging. The presence of a halo appearing indicates membrane localisastion. ***C)*** TIR images for TIR illumination of the helix-x1 protein. These images also show the higher contrast images possible with TIR. 137

4.3 a) Helix1021-GFP at high promoter concentration (10mM arabinose) b) Helix1021-GFP at low promoter concentration (1mM arabinose). At this level of expression contrast is sufficient to resolve individual spots. c) and d) BODIPY incubation under two different concentration levels. . At low concentrations, putative spots are found that are identified by the tracking algorithm. At high concentrations (d), spots are much less discernible as both cellular fluorescence and background noise increases. Spots are resolvable at low concentrations (c). 139

4.4 TIR data of a single 'x1' TIR dataset. *a*) time-averaged MSD traces. The gray traces represent individual tracks. Coloured traces represent averaged tracks of different diffusion modes plus and minus one standard error. Average tracks are not plotted unless there are at least three tracks at time t. The key is blue (Brownian) and red (confined). *b)* The weighted kernel density estimates of the Brownian diffusion coefficient for all tracks *c)* Inferred stoichiometry vs. confinement radius for confined tracks. 141

4.5 BODIPY analysis. ***a)*** Averaged tracks (Key: Blue: Brownian, Red: Confined). ***b)*** Normalised Intensity. As a stoichiometry assay was not done for BODIPY, the estimated initial intensities are normalised by their mean ($N = 17$) and plotted in as a Kernel Density Estimate with the error distribution given as one S.E.M. c) The WKDE of the confinement radius. The typical average*initial* localisation error is marked (dashed red line), but it should be noted that this error increases as fluorophores photobleach. 141

4.6 Stoichiometry per spot versus measured parameters. Key: Brownian (grey circles), Confined (White squared). ***A)*** Stoichiometry versus the confinement probability. ***B)***Stoichiometry versus the model diffusion coefficient. ***C)*** Stoichiometry versus the confinement radius. In each case, there is no clear association with the stoichiometry. The typical average*initial* localisation error is marked (dashed red line), but it should be noted that this error increases as fluorophores photobleach. 143

4.7 Comparison of the stoichiometry versus the model diffusion coefficient for all TIR data analysed. a)-d) are 15,25,30 and 37^{o}C datasets, and e)-h) are the x1,x2,x4 and x6 datasets. No clear trends or clustering is seen. 144

4.8 Helix mobility measurements for molecular weight (upper) and growth (critical) temperature dependence (lower). Key: Brownian (grey circles), Confined (White squared), Anomalous (black diamond), all tracks (black circles). ***A:*** Mean model probability ranking estimate of BARD with respect to the helix molecular weight. ***B:***. The variation in the model diffusion coefficient (D_C) and (D_B) for confined and Brownian tracks respectively. ***C:*** Confinement radius with respect to helix molecular weight. ***D:*** The stoichiometry propensity comparing Brownian and confined modes (Equation 4.1)

E: Mean model probability ranking estimate of BARD with respect to the temperature difference. Linear trend fit demonstrates an increase in mobile modes (anomalous and Brownian motion) with respect to increased temperature difference, with a respective decrease in mean confinement probability with respect to increasing temperature difference. ***F:***. The variation in the Brownian diffusion coefficient for all tracks. ***G:*** Confinement radius with respect to the temperature dependence. The general trend is an increasing confinement radius with respect to decreasing temperature. ***H:*** The stoichiometry ratio between Brownian and confined modes with respect to the temperature difference. 148

4.9 Helix partitioning model. ***A:*** The FWHM of the PSF for only Brownian and confined modes. In each case, I see that the FWHM for brownian motion is higher than the respective confined spot size FWHM. ***B:*** The variation of the FWHM of the PSF with respect to the inferred confinement radius. ***D:*** The PSF for a single immobilised GFP and a combined PSF. ***D:*** The helix protein partitions into microphase separated lipid domains of around 100 nm. They exist in two forms; mobile and immobile. The size of these domains are related to critical phase transition temperature of the system. 149

4.10 The relation of the extrapolated domain size to the Brownian diffusion spots. The Saffman-Delbrück Equation predicts log-sensitivity between the domain radius and the diffusion coefficient. 150

5.1 The Tat system was suggested to exist in two forms; either a ring system or a disk system. Figure adapted from [47]. 163

5.2 Variation in (a) the probability that the top ranked diffusion mode will be confined, (b) the inferred Brownian diffusion coefficient and (c) the confinement radius R versus estimated molecular stoichiometry for the TatA-YFP complexes, predicted confined (white squares) and mobile (grey circles) tracks indicated. 164

5.3 Spot mobility analysis. A) Kernel Density Distribution of Brownian diffusion coefficients across all cell strains. B) Examples of the mean-squared displacement (Key: Blue (Brownian) Red (Confined)) of one strain (NuoF-GFP). C) KDE of confinement radius across all cell strains. 165

LIST OF FIGURES

List of Tables

3.1 Equations of numerical solutions to Equations 3.10 & 3.11 87

3.2 Parameter prior distributions. Each coefficient is considered to vary over a given range, in which the prior of the parameter is assumed to follow the distribution given. As a uniform prior is given for the anomalous coefficient, there are no parameters for it. For the transport parameters, the parameters for the Gamma distribution are determined by a Gamma fit to the diffusion coefficients. For the drift speed and confinement radius, the parameters given are the characteristic parameters. These are the parameters that govern their regularising exponential decay functions. . . . 99

3.3 Typical mean equation parameters used representing membrane diffusion, with cited sources. 99

3.4 Typical algorithm Parameters. The key parameters of the algorithm were determined by two sets of parameters. These together form the density in which the distributions were sampled in the numerical integration. 107

3.5 The upper table represents tests on a set of confined tracks with varying the parameters of the prior distributions. Numbers indicate percentage identification of the respective mode (A=Anomalous, B = Brownian, C=Confined, D= Directed) For example, for a parameter $(1/\lambda)$ of 0.05, 32% of the tracks are identified as anomalous. Numbers are highlighted in green to indicate the most ideal results (upper table, high C percentages, lower table, high B percentages). Red highlights indicate poor results: (upper table: high B per percentages, lower table, high C percentages). The last row indicates the sensitivity accounting for both datasets. The numbers in brackets indicate the summation over the number of true positive classifications. In other words, 45% represents 22 correct C identifications out of 50 plus 23 correct B identifications out of 50. 113

3.6 Gaussian parameter fits of Figure 3.19. The ensemble is a 50/50 mix ($N = 100$) of two Brownian populations of $D = 0.01$ and $D = 0.02$ $\mu m^2/s$ of track length between 5 and 20. Accuracy is seen to decrease with model resolution. The Full model using all of the parameters D, D_σ and $P(B)$ identifies correctly the 50/50 mix of D =0.01 and 0.02 $\mu m^2/s$ diffusion rates with appropriate clustering. The control is the correct identification of D =0.01 $\mu m^2/s$. These are depicted in Figure 3.19. The N/As are where the information is not used for the model detail. 117

3.7 Multimode parameter clustering. A combined set of confined ($N = 25, D = 0.01\mu m^2/s, L = 0.05\mu m$ and Brownian $D = 0.01\mu m^2/s$) P(M) is the probability of the respective mode. 119

4.1 Helix protein mobility analysis, indicating proportion of tracks in each dataset being identified as either anomalous, Brownian, confined or directed of the analysed TIR datasets. 143

5.1 Helix protein mobility analysis, indicating proportion of tracks in each dataset being identified as either anomalous, Brownian, confined or directed of the analysed TIR datasets. 166

Nomenclature

Roman Symbols

D	Diffusion coefficient
E	Evidence. Also known as the marginal likelihood
i	integer index
j	integer index
K_α	anomalous transport coefficient
k_B	Boltzmann Factor
n	Track index. Runs from $n = 1...N$, where $T = n\delta t$
P	Probability
t	Absolute time
T	Temperature
v	particle velocity
W	Propagator probability
w	Parameter vector
$\mathbf{x}$	Displacement vector
X^2	Mean Squared Deviation

Greek Symbols

α	Anomalous coefficient
χ	Diffusant Mobility
Γ	Gamma distribution

λ	Prior parameter
μ	Mean
$\boldsymbol{\mu}$	Mean vector
$\mathbf{\Pi}$	Mixing Coefficient
$\mathbf{\Sigma}$	Co-variance matrix
σ	Standard deviation
δt	Sampling time
τ	Time-lag

Other Symbols

$\mathcal{D}$	Data
$\mathcal{L}$	Likelihood
$\mathcal{M}$	Model
$\mathcal{N}$	Normal Gaussian Distribution
$\mathcal{R}$	Regulariser

Acronyms

AFM	Atomic Force Microscopy
AIC	Akaike Information Criterion
BARD	Bayesian Analysis for Ranking Diffusion.
BIC	Bayes Information Criterion
CL	Cardiolipin (Bacterial phosophilipid)
CTRW	Continuous Time Random Walk
DOPC	dioleoyphosphatidylcholine
EAMSD	Ensemble-averaged MSD
FBM	Fractional Brownian Motion
FCS	Fluorescence Correlation Spectroscopy
FP	Fluorescent Protein
FRAP	Fluorescence Recovery After Photobleaching

GFP Green Fluorescent Protein

GMM Gaussian Mixture Model

GPI glycosylphosphatidyinositol

KDE Kernel Density Estimate

MSD Mean Squared Deviation

NMR Nuclear Magnetic Resonance

OXPHOS Oxidative Phosphorylation

PDF Probability Density Function

PE Phsphatidylethanolamine (Bacterial phospholipid)

PG Phosphatidyglycerol

SPT Single Particle Tracking

STED Stimulated Emission Depletion

TAMSD Time-averaged MSD

TAT Twin Arginine Translocase

TIRFM Total Internal Reflection Fluorescence Microscopy

WKDE Weighted Kernel Density Estimate

Introduction

Foreword and Chapter Organisation

The aim of this research is to investigate the dynamics of membrane bound complexes as they partition into the heterogeneous biological membrane. The primary contributions of this thesis are the development of analytical tools to quantitatively investigate the diffusive behaviour of single particle tracks acquired through single molecule fluorescence microscopy, that I apply to the accompanying experimental data. These experimental methods are a substantive investigation into the behaviour of integrated membrane proteins through the use of an ideal non-native transmembrane helix probe, and a fluorecent lipid probe. These investigations are compared to two other biological datasets of natively expressed protein complexes. The helix probe is a non-native transmembrane protein that is under no known native control and therefore a natural membrane probe. By varying the growth temperature to change the putative critical transition temperature, and by varying the probe size, I investigate how mobility and partitioning of the membrane probes varies under different conditions. By varying the growth temperature, I effectively perturb the critical transition temperature of the membrane. By varying the helix probe size, with the growth temperature fixed, is I investigate how mobility changes as a function of ideal probe size. For each experiment, I consider how the mobility measurements, and partitioning into putative lipid submicrometre patches, vary. I calculate the differences between the distributions, looking at stoichiometry, domain sizes, and mobility. I consider two data-sets of protein complexes that are native to E. coli, and extract similar mobility measurements. I conclude my findings in the final chapter.

0. INTRODUCTION

The chapter organisation is as follows. I provide a review of the literature (Chapter 1) followed by an experimental calibration chapter (Chapter 2). This is followed by the development of a quantitative toolkit in which I develop methods in statistical inference for application to single particle tracks (Chapter 3). I apply these quantitative tools to a model biological dataset based on a ideal GFP non-native helix probe and lipid probes (Chapter 4). In the subsequent Chapter 5, I again apply these tools to a more complicated biological dataset where there is evidence and reasonable speculation of there being more *in vivo* control. This work expands the toolbox for investigating the *in vivo* dynamics of integrated membrane proteins.

- Chapter 1 - Bacterial Membrane Heterogeneity
- Chapter 2 - Single-Molecule Fluorescence Microscopy: Principles, Protocols and Calibration
- Chapter 3 - Bayesian Inference for Single Particle Tracking
- Chapter 4 - Characterising *Escherichia Coli* Biological Membrane Heterogeneity through a non-native transmembrane helix and fluorescent lipid probes
- Chapter 5 - Characterising *Escherichia Coli* Biological Membrane Heterogeneity through native protein-FP fusion hybrids
- Conclusions

Chapter 1

Bacterial Membrane Heterogeneity

Abstract

In this chapter, the background of relevant research is reviewed in the field of membrane biophysics including the present state of the field in both the experimental and relevant theoretical literature. The first section gives a brief outline of the previous conceptions of the biological membrane, then outline the relevant experimental approaches and compare and contrast these to Single Particle Tracking (SPT) methods. I then outline recent work in the field with their differing experimental approaches; *in vivo* live cells, *in vitro* model membranes and modelling approaches *in silica*. This section ranges from concepts in lipid lateral heterogeneity to transmembrane protein dynamics. Next, the experimental tools used herein are outlined including *Escherichia coli* as a model organism and the helix protein probe used in experimental work. The chapter concludes with an overview of research aims and provide an overview of subsequent chapters. This chapter is a review chapter. All work presented here is by other researchers, but they present the context for my original research.

1.1 Introduction

All cells are delineated by membranes, defining the boundary between the internal cellular space and the extracellular environment. Membranes are formed from lipids, typically consisting of two hydrophobic fatty acid tails connected to a charged or polar head group. The degree of unsaturation of the alkyl chains greatly effects the properties of the lipids, and their associations within the membrane. It is the hydrophobic interactions that drive lipid self-association, and together with the hydrophilic moieties, lipids in an aqueous environment can spontaneously form a lipid bilayer. This property of amphipathicity of lipids is the chemical property that allows cells and organelles to segregate their internal workings from the surroundings, a common property in biology. The biological membrane is also host to a substantial proportion of cellular activity, with about one-third of the genome encoding for membrane-integrated protein in *E. coli*. Membranes by weight are the base for disproportionately more activity than the rest of the cell. Membranes have become an object of research beyond biochemists, with interest from physical chemists, physicists and applied mathematicians. This is largely due, along with broader trends towards interdisciplinary science, to the development of advanced technological methods that are able to probe membrane structure and behaviour with increasing resolution in both temporal and spatial scales.

Biological membranes are typically 6-10 nm thick, though the raw lipid bilayer with no associated protein is around 3 nm. Prokaryotic cells themselves typically vary from 1µm to 10µm. When referring to the membrane, *E. coli* proteins are often referred to as being on the cytosolic or periplasmic side, referring to which side the protein protudes. The cytosolic side is the inside of the cell (the cytosol), and the periplasmic is external; in *E. coli* and other Gram Negative bacteria there is also a second outer membrane beyond the periplasmic region. As each lipid bilayer is comprised of two layers of lipid, they are referred to as the inner and outer leaflet. Membranes are known to have asymmetry in composition between the two leaflets. [7]

In order to discuss the present state of membrane research, the context is first set by recounting the earlier accepted model and the drawbacks of it. The prevalent model in the 1980s was the

Singer and Nicholson model [8]. This was referred to as the fluid-mosaic model and described the plasma membrane described by two chief assumptions; one that protein was at low density in the membrane and second, that the membrane is laterally homogeneous. Effectively, it treated proteins as 'islands in a sea of lipid'. Reference [9] modelled the expected diffusion rate by treating a protein as a rotating cylinder in a viscous media. Consider a system with thermal energy k_BT. Here, T is the temperature and k_B is the Boltzmann constant. For an inclusion with a cylindrical geometry of radius a, with a thickness equal to the radius of the membrane as h, embedded in a two-dimensional fluid of viscosity μ in an aqueous medium of viscosity μ', the rotational and translational diffusion coefficients are given by the Saffman-Delbrück model:

$$D_T = \frac{k_BT}{4\pi\mu h}\left(\log\frac{\mu h}{\mu' a} - \gamma\right) \tag{1.1}$$

$$D_R = \frac{k_BT}{4\pi\mu a^2 h} \tag{1.2}$$

where γ is the Euler constant (≈ 0.5772).

Further, the Einstein-Stokes equation relates the mobility of the particle to the diffusion coefficient:

$$D = \chi k_BT \tag{1.3}$$

where χ is the mobility of the diffusant, equal to the reciprocal of the frictional drag.

Over the last decade, multiple investigations have shown that the membrane can no longer be regarded with the Singer and Nicholson model of cell membranes. Comparatively recent experimental advances have shown that this model needs a 'paradigm shift' [10, 11] to a partitioned fluid in which heterogeneity dominates. Indeed, this heterogeneity is due to a sophisticated organisation of the plasma membrane on all spatial scales, as depicted in Fig. 1.1. It is the origin and implications of this organisation which is one of the prominent questions in membrane biophysics.

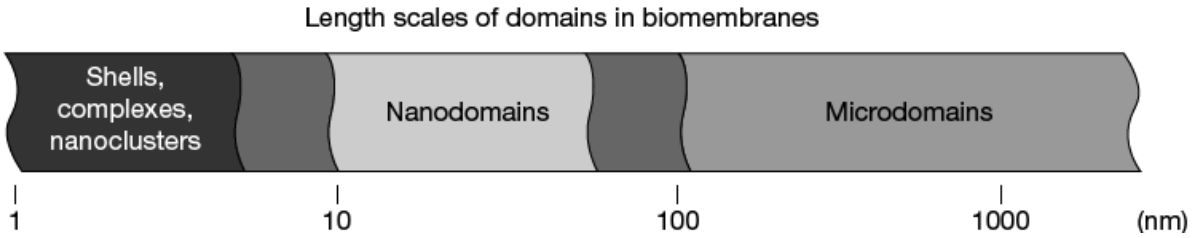


Figure 1.1: *Figure taken from [12]) Shells, complexes and nanoclusters range from 1-10nm, whereas nanodomains and caveolae can be up to 100nm. Larger domains on a microscopic scale may organise on a long-distance scale.*

Kusumi and others [13] identify several weaknesses of the fluid-mosaic model. First, experiments comparing the diffusivity rates of proteins in the plasma membrane are substantially less than those in artificially reconstituted membrane, between 5 and 50 times slower. These are the macroscopic diffusion rates on spatial scales of several hundred nanometres. Second, 'hop' diffusion has been observed in the plasma membrane but not in liposomes due to the lack of a cytoskeletal elements. In their work, they identified signals in the single particle tracking data where a tracer protein was seen to be temporarily corralled, and then 'hopped' into another trap and so on. This can be seen in the SPT data through points in which the tracer molecule is clearly confined with a certain dwell time. This corralling occurs due to the interactions with the membrane cytoskeletal network creating a patchwork network of 'fences'. Third, there are substantial drops in the diffusivity rate or immobilisation upon oligomerisation of membrane proteins, contrasting with the weak logarithmic dependence predicted by Equation 1.1.

One key deviation from the Singer-Nicholson model is the lack of spatial homogeneity creating definite length scales (see Figure 1.1). This is due to the presence of membrane architecture (cytoskeleton) and underlying lipid heterogeneity and the high density of protein present in the membrane. In the Singer-Nicholson model, proteins are treated as relatively sparse in a sea of homogeneous lipid. The reality is of a highly crowded system with mobile and immobile proteins. With the combination of immobile protein and the cytoskeletal network, Kusumi proposed the fence and picket model and suggested a partitioned fluid plasma membrane [10].

In the following section I outline specific examples incommensurate with the Saffman-Delbruck model. While a considerable fraction of this work is applied to eukaryotes, I will review the evidence suggesting similar heterogeneity in prokaryotic bacteria in §1.3.1.1. Most of the evidence comes from; sudden deviations in diffusion rates, a difference in prediction of the size-dependence of the diffusion rate, and observations of subdiffusion in cell membranes.

1.1.0.1 Oligomerisation-Induced Trapping

Protein-protein interactions are further attributed to the retarded diffusion values observed in single particle tracking. The partitioning of the membrane into multiple compartments explains how diffusion is sensitive to the formation of molecule complexes. Such an effect would only have a weak logarithmic dependence on size in the continuum model, as indicated by the Saffman-Delbrück Equation 1.1. However earlier work identified a substantial drop in the diffusivity rate upon oligomerisation, incommensurate with the logarithmic dependence in Equation 1.1. Interestingly, this has been found in signalling molecules; by oligomerisation they create a localised trap. This has biological advantages; corralling signalling molecules reduces the time for receptor and co-factors to interact, correspondingly speeding up signalling.

1.1.0.2 Size-dependent Diffusion of Membrane Inclusion

With the predicted logarithmic dependence of the mobility of a membrane inclusion to its hydrodynamic radii, it was thought for a while that little information on the size of diffusion objects could be extracted from measurements of lateral mobility. Drawbacks of the Saffman-Delbruck model are apparent when considering the extremes of large or small radii. These regimes are apparent from the spurious result of Equation 1.1 having negative diffusion coefficients for $\mu h < \mu' a$. The Saffman-Delbruck model was developed further by *Hughes et al.* [14] into a full analytical treatment that extended to radii of arbitrary size. A more analytically deployable approximation (without calculation of complex coefficients) of this was given by *Schwille et al. 2007* [15], that was validated with experimental data [16].

However, following Kusumi's paradigm shift paper [10], work by the authors of [17, 18, 19] have shown further that there is a far stronger dependence on the membrane inclusion radius than the logarithmic relation inferred from the Saffman-Delbrük scaling beyond a defined length scale. Experiments by *Gambin et al.* [17] over a wider range of membrane proteins and peptides, a $D \propto 1/R$ scaling emerged beyond a radius of around $a_c \approx h\mu/2\mu'$. This ratio is a function of the membrane viscosity (μ) to the bulk viscosity of the surrounding water (μ'). Some hydrodynamic calculations have predicted an even stronger $1/R^2$ scaling [20], later also seen experimentally [21].

1.1.0.3 Observations of Anomalous Subdiffusion

Cellular complexity has been attributed to observations of other non-Brownian diffusion. An additional family of diffusive models is known as anomalous subdiffusion. In single particle tracking experiments where the mean squared displacement is measured, Brownian motion has a linear squared deviation proportional to time. Subdiffusion is where there is a non-linear relationship scaling as t^α. The subject of anomalous diffusion has been a source of debate [22, 23, 24]. The emerging consensus is that subdiffusion arises due to microheterogeneities in the membrane. This creates a dynamic and rugged energy landscape for a protein or other diffusing molecule, either through volume exclusion or microphase separation. The Singer-Nicholson model would not predict non-Brownian motion for bulk diffusion. This is by construction; given the assumptions listed in §1.1.

1.2 Experimental Methods in Membrane Biophysics

In this section, I review the different experimental methods that are used in membrane biophysics, and compare them to approaches used in Single Particle Tracking, the principal method used here. The accessible time and length scales in SPT are shown in Figure 1.2, along side the time and length scales of putative biological phenomena.

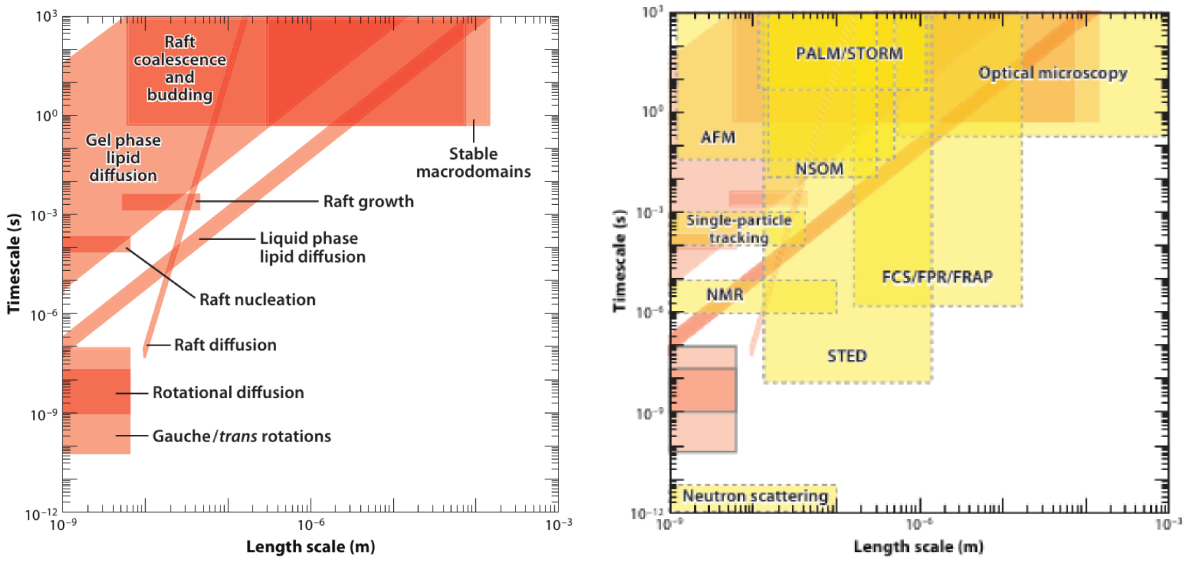


Figure 1.2: *(Figure taken from Reference [25] presents an overview of the time and length scales of membrane dynamics (left) and the time and length scales of present experimental techniques (right). See main text for details §1.2*

Single Particle Tracking (SPT)

Fluorescent Single Particle Tracking involves the tagging of fluorophores to proteins, lipids or other biomolecular components[1]. In a typical setup, a laser of appropriate wavelength illuminates the cell, either within a confocal volume or over an evanescent field, and stimulates photoemission of the fluorophore. This redshifted light is then observed by a detector. Processing algorithms are used to detect single particles in the observed images, and identifying single particle tracks. Tracking can in principle be combined with single molecule manipulation techniques such as optical tweezers, through the use of tethered protein-bead conjugates [26]. Continuous high resolution tracking is a benchmark in describing diffusive phenomena, as it is not an ensemble average method such as Fluorescent Correlation Spectroscopy (§1.2). Sampling times can vary from video rate imaging (40 ms) to 1 ms times, dependent upon the fluorophore used. Single particle methods may be specific or non-specific. Specificity here whether a specific molecule of interet is tagged, i.e. photophysically poor but

[1]The SPT methods used later; namely epi-fluorescence and TIRF, have a separate review in a later experimental chapter.

monomeric genomically expressed fluorophore-protein fusion hybrids. Alternatively, non-specific experiments may use more general fluorescent probes, such as light-scattering non-photobleaching gold particles that are not subject to specific binding.

Förster Resonance Energy Transfer (FRET)

FRET is a mechanism describing non-radiative energy transfer between two fluorophores, such as protein-protein fluorophore hybrids. An example application is in Homo-FRET, where the acceptor and donor are the same species. This was used to measure the fluorescence of glycosylphosphatidylinositol (GPI) anchored proteins; they would only fluoresce if they were clustered and nearest neighbours were within the 10 nm Förster radius. Applications of FRET are typically to investigate how molecular species interact. A recent review for the applications of FRET is given in the reference [27].

Near-field scanning optical microscopy (NSOM)

Near-field Scanning Optical Microscopy images below the conventional optical limit through the use of an optical probe that emits an evanescent wave, exciting only a small region of the sample. The detector is placed very close to the specimen and images evanescent excitations by rastering across the sample. NSOM is an order of magnitude slower than SPT methods, with imaging times between 10 milliseconds and 10 seconds. It also has lower resolution imaging from 10 nanometres to micrometres [28].

Fluorescence Correlation Spectroscopy (FCS)

FCS relies on the analysis of fluctuations in the number of fluorescence particles in a volume defined by a focused laser spot. Parameters of the system, such as the number of particles, or diffusion passage time, are quantitatively related to the measured intensity fluctuations through an autocorrelation function. This method belongs to a 'few molecule regime' but does have single molecule sensitivity, typically determining concentration and diffusion time. As this is a small-

ensemble method, many of the experiments in this area have focused on aggregate behaviour; e.g. looking at the effect of crowding on bulk diffusion. An apt review comparing SPT to FCS is given by [29].

Stimulated Emission Depletion (STED) Microscopy

In STED, a confocal laser scanning microscope focuses a laser beam onto a small section of a sample. This laser excites fluorescence dye molecules in the sample, where the relaxation emission is observed by a detector. The depletion component has strong de-excitation of dye molecules surrounding the targeted stimulated emission spot; switching them off, thereby increasing the signal as the target is illuminated and the surrounding fluorphores are deactivated. A key paper is in reference [30] where the authors see transient trapping over 10-20 ns of GPI-anchored proteins in cholesterol mediated molecular complexes of the order of 20 nm diameter area.

Atomic Force Microscopy (AFM)

AFM is a type of scanning probe microscopy, with a very high sub-nanometre resolution of around 1000 times that of the optical diffraction limit. It works via a cantilever with a sharp tip of the order of nanometres that, when brought to proximity with the cell surface, is elastically deflected, a function of the forces between the contact surface and the cantilever. AFM can work on live cells and is well suited to characterise nano-domains but not their dynamics, as AFM sampling time is longer than the time-scales of interest such as lipid domain growth or diffusion 1.1. AFM is therefore typically used to probe the geometry of a surface, but not probe the dynamics, although improvements in high-speed AFM are allowing for investigating some dynamic behaviour. Examples in the literature of AFM applications are given by in references [31, 32, 33]

1.3 Origins of Biological Membrane Heterogeneity

In the following sections, the details of present themes of membrane research are outlined. The lipid 'raft' concept is first discussed, following research from 1995-2005, but then the more subtle interpretation is discussed, invoking the heterogeneity originating from phase behaviour of biological membranes.

1.3.1 The Lipid Raft-domain Hypothesis

The lipid raft hypothesis was one of the first proposals in describing the heterogeneous distribution of protein and lipid in biological membrane. It proposes [34] that the lipid bilayer is not a structurally passive solvent but a preferential association between sphingolipids, sterols and specific proteins laterally segmenting the plasma membrane. The origin of the lipid raft hypothesis was as an explanation of the self-associative properties unique to sphingolipid and cholesterol *in vitro* facilitating selective lateral segregation in the membrane plane and serve as a basic for lipid sorting *in vivo*. They are regarded as being more ordered and tightly packed than the surrounding bilayer, but freely diffusing domains, hence the term 'raft'. Cholesterol is referred to as the 'glue' that creates rafts by preferential association with sphingolipids. The L_o phase in artificial membrane are the hypothesised phase separated regions that may form lipid rafts *in vivo* [1].

Lipid raft like domains may act as specialised membrane microdomains. They are hypothesised to serve as sorting centres for proteins, especially signalling molecules [35, 36]. Near-field microscopy has confirmed a nanoscale bias in the distribution of raft-associating proteins in fixed cells [37]. Less perturbing measurements have provided corroborating data [34]. Although it has been suggested that clustering of membrane proteins is energetically favoured, it is not clear how these are maintained in the face of lateral diffusion and transiency of corrals to confer advantages in biological time-scales. One suggested model was that trafficking keeps the membrane out of equilibrium and maintains lateral heterogeneity [38]. Raft associated protein may stabilise raft domains in the face of lateral

[1] these are strictly defined by an order parameter that is not accessible *in vivo*, so lipid raft-like structures are not referred to as the L_o phase *in vivo*

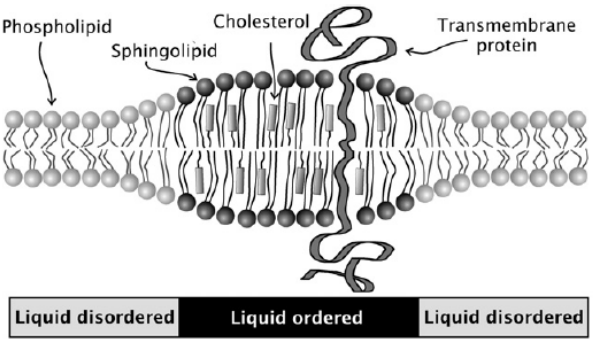


Figure 1.3: *The lipid raft concept. Cholesterol and sphingolipid associated into a dense ordered domain. Raft proteins have a preferential association with such domains*

diffusion. Antibody cross-linking has been implicated in causing raft proteins and lipids to co-patch, excluding non-raft proteins [39]. The non-random coalescence behaviour observed in these artefactual cross-linking studies suggest that raft organisation may be functionalised to larger, more physiologically relevant temporal and spatial scales. A key contention of the lipid raft hypothesis is that dynamic nano-scale heterogeneity can be stabilised to coalesce into larger raft domains by specific lipid-lipid protein-lipid and protein-protein interactions.

However, much of the evidence for lipid rafts is indirect or potentially suffering as an artefact of the experiment. As an example, the resistance to cold detergent extraction was one of the early suggestions of raft domains. However, this method has been called into question due to the extraction method [40]. The observed membrane properties are a strong function of the isolation conditions [40] - i.e. in the chemicals used to induce membrane blebbing in plasma membrane vesicles. The authors in [40] identify domains with over a large continuum of varying stabilities, orders and compositions induced by only small differences in isolation conditions. The authors in [40] conclude that domains of various properties can be produced in membrane environments with complexity commensurate with biological membranes. Further, raft size measurements for example have varied with measurement technique from the micrometre range from confocal imaging of fluorescence-labelled live cells down to under 40 nm from optical trapping experiments [41].

Despite this, there is an emerging consensus for some properties of these specialised membrane

nanodomains and their importance for various biological functions. These properties are that they are asserted to fall within the 10-200 nm range, small rafts can be stabilised to form larger platforms though protein-protein and protein-lipid interactions, and finally that rafts exist in the L_o phase.

1.3.1.1 Bacterial Micro-domains

Much of the work on the raft concept came from eukaryote cells. Prokaryotes are less studied in this context. Prokaryotic membrane have a similar multitude of lipids, with three principal lipids dominating. There are three principal types; phospholipid, glycolipid and cholesterol in eukaryotes. Cholesterol is a eukaryotic compound, and is absent from prokaryotes. Sterols in general are not found in bacterial membrane. However cardiolipin is thought to be a cholesterol analogue in prokaryotic organisms in that it creates functionally distinct lipid domains in bacteria [42]. Each bilayer membrane in bacteria is typically composed of three major phospholipids; phosphatidylethanolamine (PE) phosphatidylglycerol (PG) and cardiolipin (CL). *E. coli* for example, is 75-80, 15-20 and 2-6 mol % (molar weight) respectively [43].

Despite these differences in lipid composition, heterogeneity observed in bacterial cells has suggested that similar dynamics are at play. Phospholipid domains were observed by using a staining technique [44, 45] identified raft-like structures in *Bactillus subtilis* and cardiolipin domains have been observed to localise preferentially to the poles of *Escherichia coli* cells [46]. As with much of lipid raft research in eukaryotes, much of their evidence is indirect. However, there is a growing body of research pointing to a similar lateral segregation in bacterial membrane. For example, in work on the Twin Arginine Translocase (Tat) system [47], and bioenergetic complexes in *E. coli* [48], putative confinement zones of around 100 nm were found. Other work has indicated that cardiolipin has a tendency to form domains [44], particularly near poles of the cell. However, this may be a curvature mediated effect, as discussed in [49] (§1.4.3)

1.3.2 Investigations with Model Membranes - Phase Separation and Critical Fluctuations in Model Membranes

That lipids are able to self-assemble into two-dimensional liquid crystalline bio-membranes is a key property. It has become apparent that lipid self-association can confer organisation beyond non-specific measures of fluidity. An important advance in model membrane systems was the discovery of phase separation in reconstituted lipid bilayers over physiological temperatures [25]. This created a physical segregation of the plasma membrane into two phases; a liquid ordered L_0 phase co-existing with a liquid disordered phase [50]. This immiscible liquid phase coexistence *in vitro* has been suggested as the physical principle underlying rafts *in vivo* [51].

Veatch *et al.* [50] investigated this phase behaviour. They found that artificially constituted GPMVs (Giant Plasma Membrane Vesicles) resembling real plasma membrane, have compositions such that they reside close to a miscibility critical point. They explain the heterogeneity on the order of <50 nm effective diameter as compositional fluctuations present in GPMV membranes at physiological temperatures. Residing close to such miscibility critical points in phase transition would reduce the energy cost in maintaining lateral heterogeneity of the membrane. They indicate that these fluctuations may be related to functional lipid domains such as rafts in live cells. However, in this simplest membrane representation, there is no cytoskeletal network or mediating proteins. Later modelling work by the same group however indicated how coupling to the actin cytoskeleton [52] may reproduce experimental observations. In general, thermodynamics of model membrane systems have been studied extensively allowing for detailed statistical-mechanical models in both single, binary and ternary systems [53]. Trinary systems best represent the lipid composition of the plasma membrane with three principal lipids are present.

1.3.3 Domain Dynamics in Biological Membranes

Real biological systems are more complicated than model member systems. Phase separation in simple systems at thermodynamic equilibrium *in vitro* cannot be translated fully into *in vivo*

systems. Model membrane observations merely suggest the underlying physics [54, 55]. In real systems, protein at high concentration will have a substantial effect of the phase profile of membrane, complicating the model concept [56, 57]. Moreover, terms like liquid-ordered and liquid-disordered should only be applied to *in vitro* experiments where the order parameters specifying them can be accurately measured. These may be e.g. the deuterium orientation parameter from X-ray scattering, density in *in silica* simulations. The disordered phases do not fully capture the equivalent phases *in vivo*. One example can be seen in protein partitioning. One of the characteristics of 'raft' domains is the preferential uptake or depletion of certain protein in model membranes. Although raft markers - defined by their insolubility in extraction - co-patch at the cell surface with raft transmembrane proteins, raft transmembrane proteins are depleted from the L_o phase when reconstituted in model systems [34, 58]. Thus, the L_o phase in model membranes is likely different to that in the plasma membrane where putative raft-based domains selectively *includes* raft transmembrane proteins [39].

Although phase coexistence is manifested in the plasma membrane at physiological temperatures [50], model membranes are limited in how well they represent the plasma membrane, as these model systems only allow probing of membrane properties divorced from cellular complexity. Cyto-skeletal elements, non-equilibrium membrane trafficking or high surface density of protein are all features of real membrane that may impact the phase behaviour.

1.3.3.1 Active membrane environments

These features of real membrane make the plasma membrane in biological cells an active environment. It has long been known that organisms such as *E. coli* have homeoviscous adaption; a modulation in the composition of membrane lipids, to regulate the viscosity of the membrane. [59] One experiment varied the growth temperature and identified a small change in the lipid constituents - particularly the acyl chain composition - of *E. coli* membrane to a 'window' between the lamella gel phase and non-lamella phases [43]. Further, previous work have suggested that growth temperatures may be close to the critical point. There is some evidence of this in *E. coli* by the work of Jin and co-workers [60]. They observed a peak in the diffusion rate of a fluorescence probe near to the growth

temperature of membrane extract. Overall, there is a roughly linear dependence with respect to temperature, as expected by Equation 1.1. This has been partially reproduced in living cells as seen in Figures 1.5. As indicated earlier proximity to transition points has also been suggested in model membrane experiments [50].

1.3.4 Kinetics of Domain Growth

In this section I detail some of the theories that describe the pathways to domain formation. Pathways are varied given there is still a degree of experimental uncertainty. Lipid nanodomains have varying lifetimes under differing conditions. Long lifetime lipid nanodomains that are stable at equilibrium may form from kinetic pathways originating from tiny lipid cluster nanodomains. The smallest length scale is a model in which proteins, enclosed in lipid shells of around 15-30 molecules, cluster to form lipid domains. One model of raft formation [61] suggests that small mobile L_o domains spontaneous appear and disappear with short lifetimes (0.1 ms) rather than supposing stable pre-existing L_o nano domains. These domains may be stabilised to form the larger nanoscopic (50-100 nm) domains observed, by lipid anchored or trans-membrane proteins. Reference [61] describes the kinetic stages of domain formation corresponding to an initial non-equilibrium homogeneous state. This is followed by a nucleation growth phase in which clusters above a critical size enlarge by absorbing surrounding lipids. Mobile domains merge and small or individual lipids diffuse adsorbing into larger domains. At equilibrium, budding from larger domains balances growth by merger. Much of this system is parametrised by the line tension, the boundary energy per unit metre. Consequently, a spate of subsequent research has considered the line tension in synthetic membranes [50]. However, artificial membrane experiments have questioned this process. In experiments such as those by Veatch [50], they show that these domains are not stable, but are instead transient entities that arise due to stochastic thermal fluctuations and need not necessarily form from coalescence with other domains [40]. However, how these domains are stabilised is unclear and remains an open question.

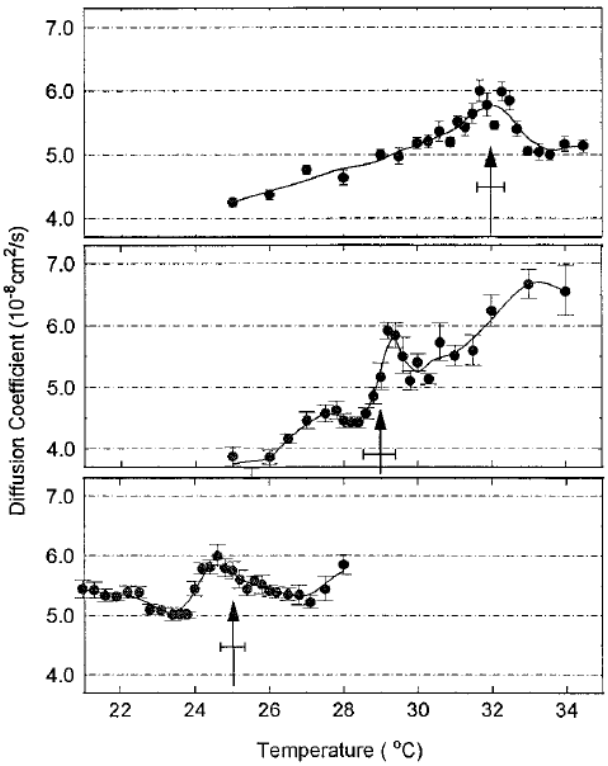


Figure 1.4: *From reference [60], an anomalous spike at the growth temperature is reported based on extractions of the membrane lipids with a fluorescent probe. The arrows indicate the growth temperatures. Errorbars are one standard deviation.*

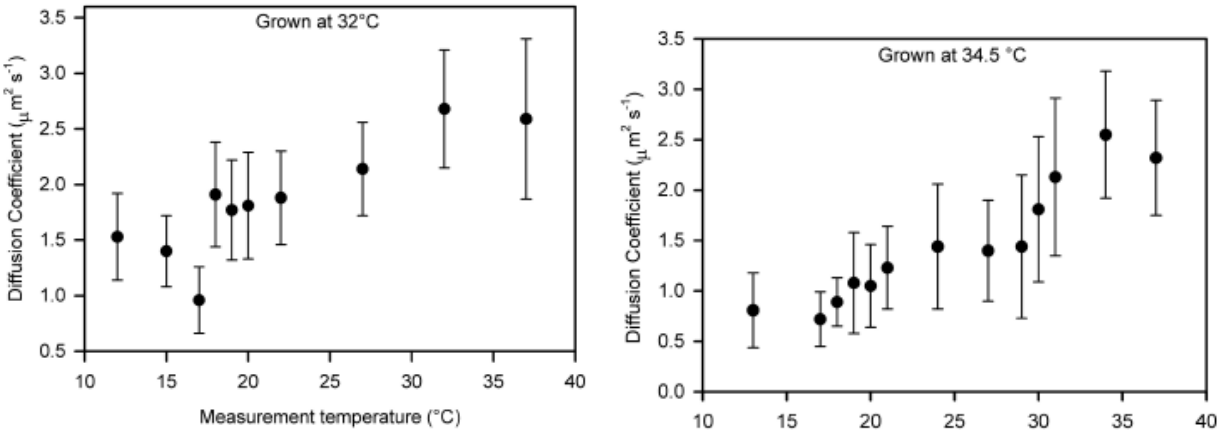


Figure 1.5: *Diffusion coefficient of BODIPY in the working paper [3] at two different growth temperatures, over a temperature range. BODIPY is a fluorescent lipid analogue discussed in §1.5.3. There is a peak, within error, at both growth temperatures of the diffusion rate of BODIPY.*

1.4 Dynamics of Integrated Membrane Complexes

Moving away from domains, in this section, I give an overview of the present themes in research of the behaviour of proteins in the membrane. This includes how proteins partition into the membrane, their diffusive behaviours, and their kinetic interactions that ultimately drive membrane-bound chemistry. These factors may be separated into physical factors and biological factors. The physical factors are the behaviours that can be reproduced in model membrane. These are for example the geometric constraints incurred onto single molecules by the curved, visco-elastic nature of the membrane, and the crowding and space depletion effects of other protein. The biological factors are the components of membrane architecture that make the membrane active. These include the effect of the cytoskeleton and the broad and rugged energy landscape that defines the network of interactions of membrane proteins [62].

1.4.1 Crowding

In the biological membrane there are a variety of geometric obstacles that can impede solute diffusion in media. In cell membranes, there are examples of both Brownian and anomalous motion, with the latter associated with a host of biological phenomena that will be described in greater detail later in the discussion on anomalous diffusion in Chapter 3.

Searching for a target is a key and ubiquitous function in biology. On the cellular level, many reactions are assumed to be driven by diffusion. But how does this occur in the volume excluding crowded milieu? In one surprising result, Guigas and Weiss [20] have suggested that crowding induced anomalous diffusion can *enhance* the probability of interaction between target and tracer (in the context of the cytoplasm). A similar question was approached by Deeds considering how protein-protein interactions were robust in crowded environments; given that interaction pairs may exist at low relative concentrations and thus be presented with many more opportunities for promiscuous interactions compared with specific interaction possibilities [62]. They argue that protein-protein interactions are robust within a window in which the system energy (temperature)

is below a regime in which promiscuous interactions dominate, and greater than an aggregation energy. This is one in which interactions will not become 'sticky'; stable and specific interactions have significant difficulty forming reliably, especially at lower relative concentrations.

Although both are applied in context to the cellular cytoplasm, similar issues arise in the context of the plasma membrane. In the biological membrane, protein are often highly packed occupying 30-50% of the membrane surface area. In colliodal and polymer chemistry [63], theoretical descriptions have a high degree of predictive ability supported by experimental accessibility. The cell, however, offers a much more complicated environment and therefore the transport dynamics at the cellular level are less amenable to inference or prediction. As the previous sections have shown, the exact chemical surroundings of diffusing probes operate are unclear. Several reviews on crowding are provided by [64, 65, 66]

1.4.2 The Effect of the Actin-cytoskeletal Network

The cytoskeleton is one of the key elements that are not reproduced in model membranes. Phase separation in a multi-component membrane may be strongly effected by the cell's cytoskeleton. The cytoskeleton has been implicated in the origins on membrane heterogeneity. Dependent upon the temperature and membrane composition, this may lead to a precipitation of highly dynamic membrane domains (rafts), or prevent large-scale phase separation. Interactions with the membrane skeleton enhances subdiffusion and, over larger time-scales may lead to hop-diffusion of lipids. The actin-cytoskeleton has been implicated in shifting and potentially broadening the membrane phase transition temperature window, when compared to model membranes without an underlying cytoskeleton. References [67, 68] demonstrate further that the cytoskeletal mesh may be an origin of transient anomalous subdiffusion in near-critical membranes.

1.4.3 Curvature Mediation

Many proteins reside at the cell poles in rod-shaped bacteria. This has lead to the hypothesis being formed that there may be a connection between protein localisation and regions of high

Gaussian curvature. In an excellent test of this, Renner and co-workers [46] developed a technique of forming *Escherichia coli* spheroplasts of defined shape thereby modulating the membrane curvature. Coupled with optical microscopy, they observed that cardiolipin (CL) domains localised to areas of high intrinsic negative curvature. They show further that the *E. coli* protein, MinD, localised not through preferential partitioning into cardiolipin domains, but through curvature sensing. This is not biological sensing, but rather driven by energetic considerations [69]. The Min systems works through a reaction diffusion mechanism; waves of one protein member of the Min system diffuse from pole-to-pole and through a short series of interactions, they effectively set up a diffusion gradient that is peaked at the poles and minimal at the mid-cell. This allows the cell to set up a self-referential geometry for cell division and other biological processes. This clustering of high intrinsic curvature lipids at the poles may in turn lead to local microphase separation.

Lipid composition and curvature coupling has also been noted in model and eukaryotic systems, but the principle is similar. Lipids have an intrinsic curvature, that may be modulated further by curvature sensitive protein. Thus, curvature leads to a lipid sorting. The lab of Bassereau demonstrated that differences in lipid composition can build up between a curved and a non-curved membrane, an effect only seen if the membrane is close to a de-mixing point [70].

Other observations suggest that curvature strongly influences curvature-sensitive membrane protein recruitment. In other experiments by Bassereau *et al.*[71], their lab demonstrated that, at low dynamin concentration, polymer nucleation strongly depends on membrane curvature. This suggests that dynamin may be recruited to to regions of high membrane curvature. They further argued that *any* protein that binds or self-assembles onto membranes in a curvature-coupled way should behave in a qualitatively similar manner. They thus conclude that membrane curvature is also a precursor to some protein functions.

The Howard lab have however concluded on experiments on model membrane systems that lipid shape alone is not enough to drive measurable lipid sorting; lipid-lipid interactions or lipid-protein interactions are necessary to amplify the curvature-based sorting, especially for larger domains. [72]

1.5 Candidate Biological Models in Single-Molecule Fluorescence

In this section, I review the biological models presented in this thesis. All the biological models use *E. coli* as the model host organism, primarily due to genetic tractability. These models range from non-native protein and lipid probes, to the *in vivo* membrane-ranging Tat system, up to the bioenergetics system of the oxidative phosphorylation processes. These different models have different levels of complexity. The protein and lipid probes can explore passive processes of partitioning in the membrane. These can be compared to the two native systems. These are the Tat system which can be seen at the single molecule level and is membrane-ranging, and the OXPHOS system, which consists of a more biologically complex set of interactions.

1.5.1 Prokaryotic *E. Coli* as a Model Organism

E. coli is the most widely used model organism in prokaryotes and is widely studied. It is easy to maintain and breed in a laboratory setting with a high growth rate, well established genetics and an established genomic sequence. More is known about *E. coli* than any other organism. As an example, there have been several papers looking at the dynamics of membrane bound complexes in *E. coli*, ranging from single particle tracking studies, FCS, and AFM to computational modelling that will be referenced throughout this review. The approximate lipid composition of *E. coli* is known and has been used as a probe of both curvature sensing experiments and domain structures. Further similarities have been found between prokaryotes and eukaryotes; prokaryotes have also been found to have cytoskeletal analogues. [73, 74].

The basic structure of *E. coli* is a medicine capsule shaped organism with a cytoplasmic bulk, that is enclosed within a cell envelope. Progressing from inside to the outside, the envelope consists of the inner cytoplasmic membrane, the periplasma, and the outer membrane. Within the periplasm, a thin layer of peptidoglycan (murein) forms the cell wall. The outer membrane is principally anchored to the peptidoglycan layer through a lipoprotein called Lpp. Other proteins in the outer membrane, but also some in the inner cytoplasmic membrane, also have binding sequences to this

murein layer. These protein anchors, alongside turgor pressure, may lead to interactions between the inner cytoplasmic membrane and the murein layer [75][76].

1.5.2 Use of a Helix Protein as a Novel Non-native Probe of Membrane Biophysics

The following text is adapted from the working paper [3]. Collaborators from the lab of Conrad Mullineaux, QMUL, constructed a gene coding for a model membrane protein using as a starting point the open reading frame sll1021 in the cyanobacterium *Synechocystis sp.* PCC6803, coding for a membrane protein with no identified homologues in *E. coli.* The protein has unknown function but has been identified in the plasma membrane of *Synechocystis* [77]. The predicted gene product has 673 amino-acids with a single predicted transmembrane alpha-helix close to the N-terminus. The ends of the predicted transmembrane helix lack any of the two-residue motifs that appear important for specific interactions with phospholipid head-groups [78]. A portion of the sll1021 sequence coding for 38 amino-acids including the predicted transmembrane alpha-helix was fused it in-frame to the gene coding for GFPmut3* [79] with a linker of 5 asparagine residues. The construct was expressed in *E. coli* cells from the arabinose-inducible pBAD24 vector [80]. The predicted topology of the model protein (helix1021-GFP) is illustrated in Figure 1.6. The GFP domain is almost certainly on the cytoplasmic side of the membrane, since there are no Sec or Tat [47] leader sequences present to initiate the translocation of GFP into the periplasm [81, 82]. These are particular motifs that promote translocation across the membrane. Cells expressing helix1021-GFP were fractionated and proteins of the periplasmic, cytoplasmic and plasma membrane fractions separated by SDS-PAGE (sodium dodecyl sulfate polyacrylamide gel electrophoresis) and probed with anti-GFP antibody. GFP was detected only in the plasma membrane, where the antibody recognized a protein running at 28-29 kDa, consistent with the predicted gene product. The band ran at a slightly higher molecular weight than free GFP, confirming that the protein integrates into the plasma membrane as expected, and the GFP tag is not cleaved off the transmembrane helix. Images recorded at high z-axis resolution show green fluorescence confined to a halo at the

periphery of the cell, a characteristic of confocal images of GFP-tagged membrane proteins in *E. coli* [83]. These halo images were also found in my data in Chapter 4.

Due to the lack of a homologue in *E. coli*, this property allows the helix to function as an 'ideal' molecular probe and not precipitate any specific protein-protein interactions. Further, multiple oligomerisation states allow for experiments in quantifying how stoichiometry and domain partitioning or recruitment changes as a function of helix size.

1.5.3 BODIPY as a Fluorescent Lipid Analogue

BODIPY - short for boron-dipyrromethene, has been used as a fluorescent analogue in various experiments [83, 84, 85, 86, 87, 88, 89]. It is incorporated by simply incubating *E. coli* with BODIPY, and is trafficked into the plasma membrane. It is a green fluorophore linked to a 12-carbon fatty acyl tail. It is shown to localise into the inner membrane of *E. coli*. This is used in Chapter 4. BODIPY is known to be toxic at levels above around 10μM, which is a ten-fold increase in concentration to that reported here[90].

1.5.4 Twin Arginine Translocase

The twin-arginine translocation (tat) system transports folded proteins across the bacterial cytoplasmic membrane. The essential components of the Tat pathway are the membrane proteins TatA, TatB and TatC. It is TatA that is thought to be the protein translocating element of the Tat system, meditating the diffusion of folder proteins through the membrane. The TatA system has been shown to have a variable stoichiometry; assembling into variably sized ring complexes [47]. The Tat system makes an appropriate probe in single-particle tracking experiments because imaging can read the single particle level.

1.5.5 Bioenergetics

Organisms in general are able to synthesis most ATP (adenosine triphosphate) using OXPHOS (oxidative phosphorylation). The mitochondria in eukaryotes perform OXPHOS in the inner

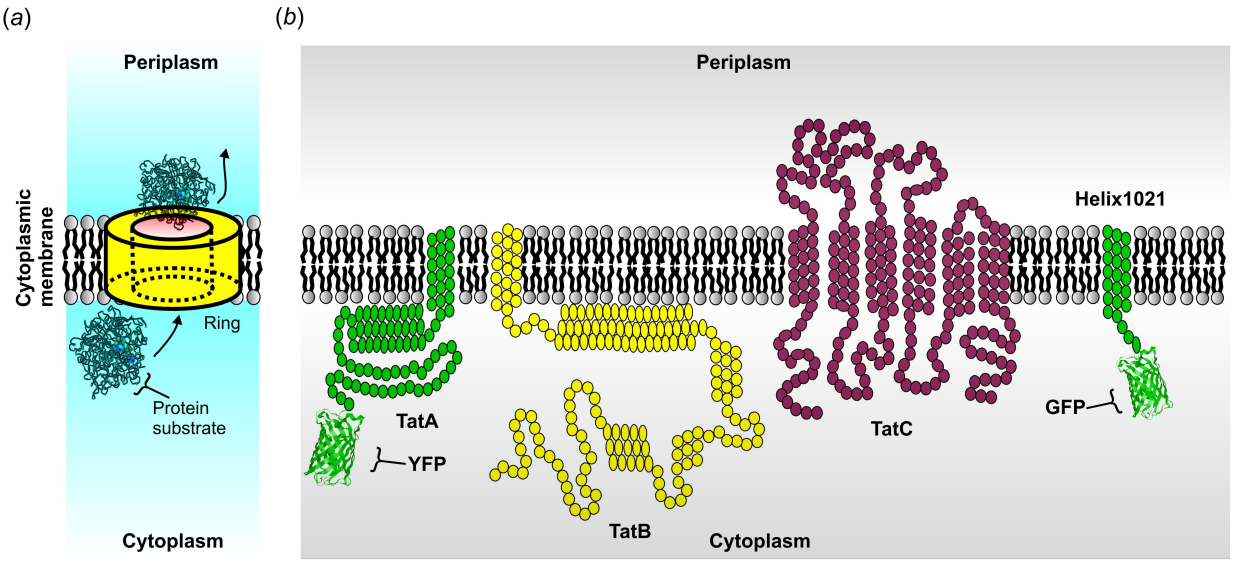


Figure 1.6: *Proteins investigated in this thesis. The helix has no native function and acts as a membrane probe. Schematic of (a) membrane bound ring-architecture [91] of a Twin-Arginine Translocase TatA nanopore allowing translocation of a full folded protein substrate across the cytoplasmic membrane, and of (b) the TatA-YFP, TatB, TatC and Helix1021-GFP proteins (coloured circles indicating individually amino acid residues in the native proteins). The helix protein has no known homologue and acts as an ideal probe. Images adapted from [1, 47]*

mitochondrial membrane. This is in contrast to prokaryotes, where this energy production chain is performed in the plasma membrane. The OXPHOS system is the basis of the electron transport respiratory chain (ETC). Oxidation of electron donors by membrane-bound enzymes is coupled by a series of stepwise redox reactions, resulting in the generation of the p.m.f. (proton-motive force). This powers the F_1F_0-ATPase machine, generating the universal cellular fuel of ATP. It largely consists of five enzyme complexes: Complex I (NADH dehydrogenase), Complex II (succinate dehydrogenatse), Complex III (cytochrome bc_1, Complex IV (cytochrome c oxidase) and Complex V (the F_1F_0-ATPase). In addition, there are mobile electron carriers, uniquinol and cytochrome c, which functionally link complexes I-IV, making up the ETC. This in turn is linked to Complex V by the p.m.f. that is generated through the coupling of proton translocation with the electron transfer reactions in the ETC.

1.6 Discussion

From the past few years of experiments, it would appear that membrane heterogeneity cannot be ascribed to proteins or lipids alone. Rather, it is the complex network of interactions between them. These may be further coupled to the underlying cytoskeletal network. Further, it appears that these processes may be coupled to underlying physical properties. To break further assumptions of the Singer-Nicholson model, these interactions do not occur on a flat rigid sheet; but in a rugged curved elastic landscape. Experiments on GUVs (giant unilamellar vesicles) have been very informative of the potential underlying physical processes that drive and maintain lateral heterogeneity but ultimately it is the cell itself that needs to be studied. Non-perturbing *in vivo* experimental methods offer the most appropriate instruments in probing native conditions.

The key questions of the field are:

- What biophysical processes drive membrane heterogeneity?
  - What is the origin of membrane domains? Do they originate from biological recruitment (i.e. specific interactions between protein and lipid) or are they the product of thermal fluctuations - i.e. stochastically driving the transient formation of domain that are stabilised? In either case, what is the kinetic route to forming stable membrane structures over relevant biological spatial and temporal scales?
- How is lateral organisation maintained with lateral diffusion?
- How are these utilised to optimise membrane-bound chemistry?

1.7 Chapter Summary

- Provided a historic account of membrane biophysics.
- Detailed the variety of experimental methods used in membrane experiments.
- Discussed the putative origins of membrane heterogeneity:
  - including the lipid raft hypothesis
  - the relationship to phase behaviour
- Described the nature of the membrane as seen at the level of the protein including the forces that drive membrane organisation and prevent global mixing.
- Detailed appropriate biological models including
  - *E. coli* as a model prokaryote.
  - two appropriate membrane probes; a helix protein and BODIPY, a fluorescent lipid analogue.
  - two native *E. coli* protein systems.

Chapter 2

Single-Molecule Fluorescence Microscopy: Principles, Protocols and Calibration

Abstract

Chapter 1 provided an overview of the present research in membrane biophysics; reviewing the present state of the field, along with an overview of the various experimental approaches used. Here, I review the specific experimental methods in fluorescence microscopy used in this thesis (Chapters 2, 4 & 5). These include single particle tracking methods through surface-immobilized and *in vivo* epi-fluorescence, shallow-angle and total internal reflection illumination. In this chapter, I review the principles behind these methods of fluorescence excitation, and their use as a tool in experimental biophysics. Following on from this, I then outline the protocols in fluorescence imaging used in later chapters. This includes all stages in fluorescence microscopy; from preparation of live samples to fluorescence imaging protocols. It also includes an outline of the tracking techniques used to analyse experimental data and convert them into single particle tracking data. The chapter outlines the

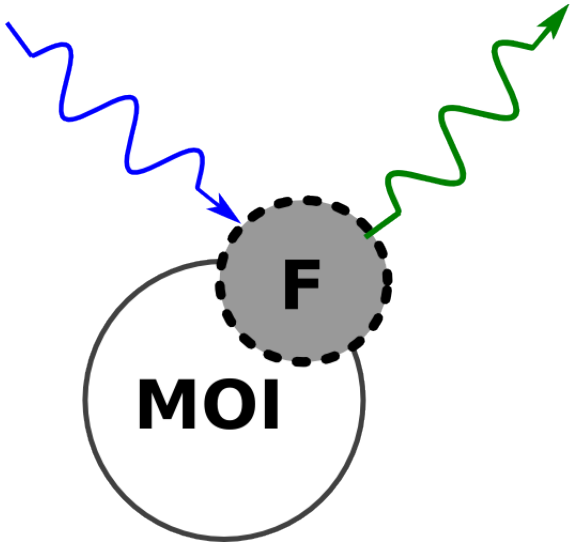


Figure 2.1: *Schematic for fluorescence imaging. A molecule of interest is tagged (MOI) with a fluorophore (F). For GFP, excitation is with a 473* nm *laser. The stokes shift is represented by the red shifting of the emitted photons.*

experimental methodology used in later chapters (chapters 4 & 5), methods used for stoichiometry and excitation field calibrations. It includes a thorough discussion of errors and how I propagate them through to the experimental analysis presented in later chapters.

2.1 Introduction

Fluorescence microscopy is a powerful technique for investigating biological processes in cell membranes. One classification between the different experimental approaches of fluorescent microscopy is the distinction between ensemble and single molecule level experiments. Assays such as fluorescence recovery after photobleaching (FRAP) can obtain population level measurements of protein mobility, whereas single particle tracking (SPT) can obtain individual protein diffusion data. In fluorescence experiments on biological systems, a biological molecule of interest (MOI) is labelled with a fluorophore (F). This labelling is either at the level of the DNA code (a fluorescent protein fusion) or as an analogue (the fluorescent analogue replaces, associates or intercalates with a MOI). A MOI-F fusion hybrid is depicted in Figure 2.1.

2.2 The Principles and Theory of Single Molecule Fluorescence Microscopy

The physical basis of fluorescence is the emission of light by a molecule relaxing from an electronically excited state. Appropriate photonic excitation stimulates an electronic transition from a lower (ground) state to a higher (excited) state. A Jablonski diagram illustrates the various electronic states and the transitions between them (Figure 2.2).

Biological applications typically have emission spectra in the visible range of the electromagnetic spectrum. Fluorescent markers can be used as biological probes when they are conjugated to molecules of interest enabling data collection of relevant biological information; localisation, tracking and/or quantification of biological molecules.

2.2.1 Stokes Shift

The Stokes Shift, represented either in wavelength or in frequency, represents the difference between the maxima of the absorption and emission spectra. In the context of fluorescence microscopy, this is the wavelength shift between the excitation spectra and the emission spectra. It is this shift that allows for optical imaging, as emission filters can block out the excitation flux and pass through only the emission.

2.2.2 Blinking and Bleaching

Fluorophores complicate experimental measurement with *fluorescence intermittency*. This is where the fluorophore switches between an 'on' and 'off' state. This is unobservable in bulk studies, but at low or single concentrations, the blinking intensity time-series profile can be seen. In reference [92], the authors image individual fluorophore and monitor the on/off states. Similar protocols were used in §2.5.2.1, as a measure of the fluorescent intensity of single fluorophores. An example of fluorescent blinking is seen in Figure 2.14.

Irreversible photobleaching occurs when a fluorophore permanently loses the ability to fluoresce

upon photon-induced excitation; a permanent 'off' state. This occurs through photon-induced chemical damage and covalent modification. Upon transition from an excited singlet state to the excited triplet state, fluorophores may interact with another molecule to produce irreversible covalent modifications. The lifetimes of each of these states is different with the triplet state being relatively long-lived. These transitions are usually schematically depicted in a Jablonski diagram (Figure 2.2)

The limiting feature of photobleaching is the finite imaging time-scale in which fluorescent marker proteins can fluoresce. The time-scale in which irreversible photobleaching occurs is a strong function of the structure of the fluorophore and the local environment. GFP-protein fusions are particularly limited, but other assays such as gold-particles have a practically unlimited imaging period. Kusumi's paper [93] is a typical example of this. For protein-fluorophore fusions, however, fluorescence imaging becomes a delicate balance between signal to noise and length of signal. Ideally, fluorescent proteins are long-lived but practically there is a limited number of photons emitted before photobleaching. As the signal to noise ratio is a strong function of incident photon flux onto a cell, microscopy protocols often require adjustment of the radiation flux through neutral density filters or shutter-controlled exposures.

Assays have been built around this limitation. One microscopy assay utilises irreversible photobleaching through the Fluorescence Recovery After Photobleaching (FRAP) assay §2.3.1, by looking at the recovery of fluorescence after bleaching a section of a cell. For fast diffusion, fluorescence is recovered in the bleached section rapidly. For slow diffusion, this process is limited. Consequently, FRAP is a bulk ensemble measure of diffusion rates.

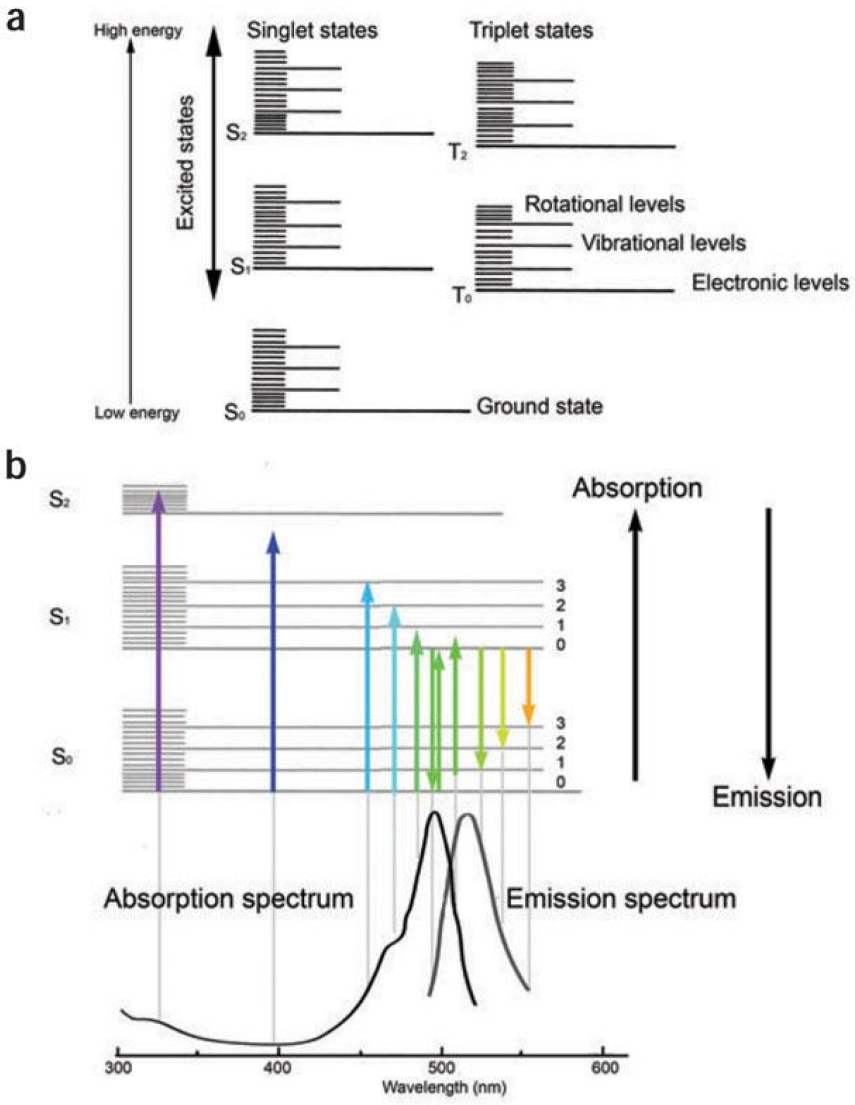

a
High energy
Singlet states
Triplet states
Excited states
S₂
T₂
Rotational levels
Vibrational levels
S₁
T₀
Electronic levels
Low energy
S₀
Ground state
b
S₂
Absorption
S₁
3
2
1
0
S₀
Emission
Absorption spectrum
Emission spectrum
300
400
500
600
Wavelength (nm)
c
S₂
Internal conversion
pico 10⁻¹² s
Vibrational relaxation
S₁
Intersystem crossing
T₁
Excitation
femto
(10⁻¹⁵ s)
Fluorescence
nano (10⁻⁹ s)
Phosphoresence
≥micro (10⁻⁶ s)
S₀

Figure 2.2: *Jablonski diagram displaying the energy states of a molecule. Molecules not absorbing energy are mainly confined to the lowest vibrational states of the ground state S_0. (b) The spectral characteristics related to absorption and emission of energy by a molecule can be related to the size of the energy steps needed to bring a molecule from one energy level to another. The absorption and emission spectra of the common fluorophore Fluorescein isothiocyanate (FITC) are shown in the Jablonski diagram. Each vertical grey line aligns the spectra with the energy of the absorbed (arrows pointing up) or emitted (arrows pointing down) photons. The arrows are coloured to represent the wavelength of the photons. For example, the purple arrow to the left represents the energy of an ultraviolet photon that can cause the molecule to undergo a transition from the ground state to the second singlet excited state. The orange arrow on the right represents the lowest energy photon that can be emitted by this molecule as it drops back from the lowest energy state of S1 to a high vibrational state of S0. Note in the region of overlap of the absorption and emission spectra, some photons (for example, the green, up-pointing arrow) are absorbed when the vibrational level is not at its lowest level. Also note the symmetry between the absorption and emission curves owing to the similarity of transitions to vibrational states in S0 and S1. (c) The typical times that the various steps in fluorescence excitation and emission and phosphorescence take. [94]*

The general consideration in all photonic imaging experiments is the *photon budget*. This, essentially, describes the balance between strong signal-to-noise imaging, and long lifetime imaging. Fluorescent proteins emit a finite number of photons during imaging, going from a fluorescent state to a photobleached non-emitting state. A stronger excitation yields a stronger signal (more photons over the imaging time), but decreases the imaging time (the fluorophore bleaches). This means that both the choice of sampling time, and the sampling frequency, are important.

In general, the typical per fluorophore photobleaching time and signal-to-noise ratio, are comparable to other TIR experiments [47]. This is because the imaging conditions are typically comparable for the same fluorophore; laser illumination power, sampling rate and pH. All else being equal, the differences arise in the stoichiometry in the observed point spread functions. Stronger signals are yielded in high stoichiometry spots relative to low stoichiometry spots meaning that, all else being equal, differing spot stoichiometries may mean that that the photon budget considerations are different.

The second considerations is related to the biological system being investigated. Mobile fluorescence, compared to immobile or low mobility fluorescence, may need a greater SNR as the dynamic error, the blurring of the point spread function for a mobile spot, will be greater. Furthermore, differing

sampling times may be required in order to observer a fluorescent protein behaving on different length scales. One immediate example is the confinement effects seen in single particle tracks for a fluorescent protein confined within a membrane domain. Certain membrane architecture, such as the 'hopping' observed by Kusumi, would only be observed over a certain imaging time-scale. Too short, and the confinement would not be seen. Too long, and the confinement would manifest only globally as a somewhat slower diffusive rate.

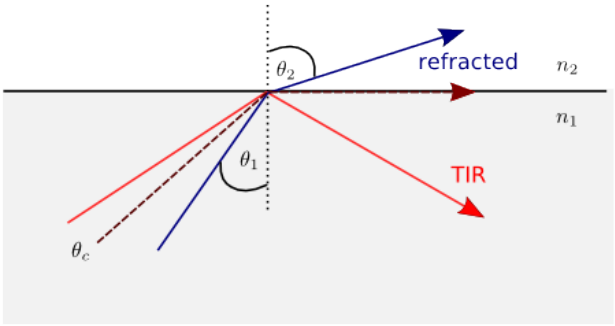


Figure 2.3: *The illumination mode beyond the interface is governed by three variables. These are the refractive indices n_1 and n_2, and the incident illumination angle θ_1. The critical angle θ_c is governed by a function of the two refractive indices. At incident illumination angles below the critical angle, incident radiation propagates through the interface. At incident illumination angles beyond the critical illumination angle, the bulk of the radiative energy is totally internally reflected. However, a thin evanescent field of illumination propagates through the interface.*

2.2.3 Refraction and Evanescent Field Illumination

Refraction is the change in direction of an electromagnetic (EM) wave at the interface between two different media due to a change of the speed of propagation. It is governed by Snell's Law (Equation 2.1), which emerges from Maxwells' equations governing the behaviour of EM radiation at an interface [95, 96].

$$n_1 \sin\theta_1 = n_2 \sin\theta_2 \tag{2.1}$$

As indicated in Figure 2.3, as the incidence angle from the objective θ_o increases, the propagation angle in the glass, θ_g increases, according to Equation 2.1. As the incident illumination angle changes, a special case emerges whereby the light no longer refracts into the lower medium but propagates parallel to it.

The evanescent field intensity decays exponentially with increasing distance from the interface according to the equation:

$$I(z) = I(0)\exp^{-z/d} \tag{2.2}$$

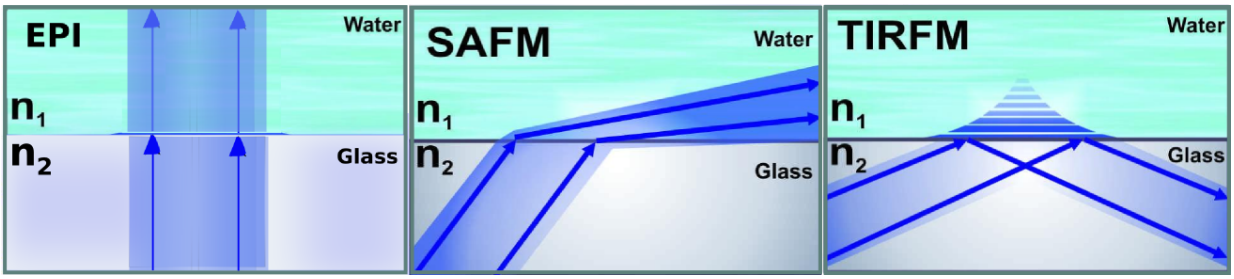


Figure 2.4: *Excitation fields used. A) Epi-fluorescence. Radiation is perpendicular to the interface and is effectively uniform over the region of interest in the medium. B) Shallow-angle epi-fluorescence. Radiation enters away from the normal. This reduces some illumination of the sample and media reducing back scatter. C) TIRF radiation totally internally reflects.*

where $I(z)$ represents the intensity at a perpendicular distance z from the interface and $I(0)$ is the intensity at the interface. The characteristic penetration depth d at wavelength $\lambda(0)$ (in vacuum) of incident radiation is given by: [97]

$$d = \frac{\lambda(0)}{4\pi(n_1^2 \sin^2\theta - n_2^2)^{1/2}} \tag{2.3}$$

2.3 Protocols in Experimental Fluorescence Microscopy

2.3.1 Excitation Modes

As we see in Figure 2.3, there are three regimes of illumination. The first is epi-fluorescence; illumination is directly along the normal between the interfaces, $\theta_1 = \theta_2 = 0$. The second is shallow angle or oblique epi-fluorescence, $\theta_1 < \theta_c$. The third is Total Internal Reflection Evanescent illumination; $\theta_1 > \theta_c$. These are depicted in Figure 2.4. I now discuss each of these in turn. The microscope used in this research supports all of these excitation modes, as depicted in §2.3.2 and Figure 2.5.

Epi-fluorescence

Epi-fluorescence is the excitation mode where the incident laser radiation is perpendicular to the mounting cover slip. This provides an effectively uniform illumination field over the cell. Under these illumination conditions, cells with membrane integrated protein-fluorophore hybrids tend to have 'halos'. This is an effect of the uniform illumination field over the cell; although the membrane at the surface at the bottom of the cell is illuminated and the corresponding fluorophores are excited, there is a much greater collective response for fluorophores in the membrane at the side of the cell. In other words, if we sliced the cell up along the z-axis and added up the fluorescence of each layer, in epi-fluorescence the fluorophores in membrane beyond the bottom membrane layer (> 100 nm) integrate creating a halo effect. Strictly, this is when there is no real cytoplasmic content, and the protein-fluorophore is membrane integrated. If the fluorophore is in the cytoplasm, then the cytoplasm will be excited and the cell will have uniform fluorescence.

Oblique Epi-fluorescence

Oblique epi-fluorescence is an excitation mode where the incident radiation propagates at an angle to the normal, but less than the critical angle required to induce total internal reflection. This is similar to normal epi-fluorescence, with the excitation beam still refracting through the glass-sample interface, but enters the solution phase at a shallow angle. This excitation mode is correspondingly also known as shallow angle epi-fluorescence. This illumination method reduces some out of focus media excitation and back-scatter.

Total Internal Reflection

In TIRF, this angle is such that the energy of the incident beam is reflected, rather than transmitted. This creates an evanescent field within the coverslip with an exponential decay. The key principle of Total Internal Fluorescence Microscopy (TIRFM) is that a thin, exponentially decaying, evanescent field of excitation (≈ 100 nm) is generated at the interface between these two media. The illuminated

volume is smaller than a confocal volume in a confocal setup, which typically has an axial resolution of $2n\lambda/NA^2 > 600$ nm where n is the refractive index of the mounting media, λ is the wavelength of light and NA is the numerical aperture of the objective lens.

Fluorescence Recovery After Photobleaching (FRAP)

A FRAP assay is an approach to quantify two-dimensional diffusion of fluorescently tagged probes, such as *in vivo* cellular imaging. The essential technique is to photobleach a portion of a cell and measure the recovery rate as fluorophores diffuse back into the bleached section. It can be used to measure the rate of diffusion (or immobility) of tagged fluorophores [83, 47].

2.3.2 A Custom-built Inverted TIRF microscope

The multiple illumination-path custom-built inverted fluorescence microscope (Nikon) with a 1.45 high NA (Plan Fluor 1.45/100x, Nikon UK) oil objective used in this thesis was built by Dr Ian Dobbie and designed by Dr M.C. Leake. There are multiple illumination and excitation paths. There were four coaxial illumination sources at wavelengths of 561, 532, 473 and 445 nm and two excitation pathways; one for TIRF/epi-fluorescence and another for FRAP assays. The relative proportion of radiation between the two excitation fields was controlled by an adjustable half-wave plate followed by a polarisation splitter. The excitations were recombined by a second polarisation cube. Excitation was incident on an appropriate dichroic filter set (for 473nm excitation this is Semrock, part Di01-R488-25x36). A schematic is shown in Figure 2.5. The sample was housed onto a slide holder attached to a 3-axis piezoelectric nanostage (Mad City Labs). A white-light lamp was used for low-intensity bright-field illumination which was focused onto the sample using a long working distance condenser. Excitation path shutters on each path were controlled either manually or from a custom-programmed `LabView` (V8.5, National Instruments) GUI. Fluorescence emission passed through a 473nm notch filter (Semrock, part ZET473-NF)

To switch between epi-fluorescence, oblique-epi fluorescence and TIRF imaging, a movable lens was used controlled by `LabView`. In epi-fluorescence, laser illumination was coaxial with the centre of

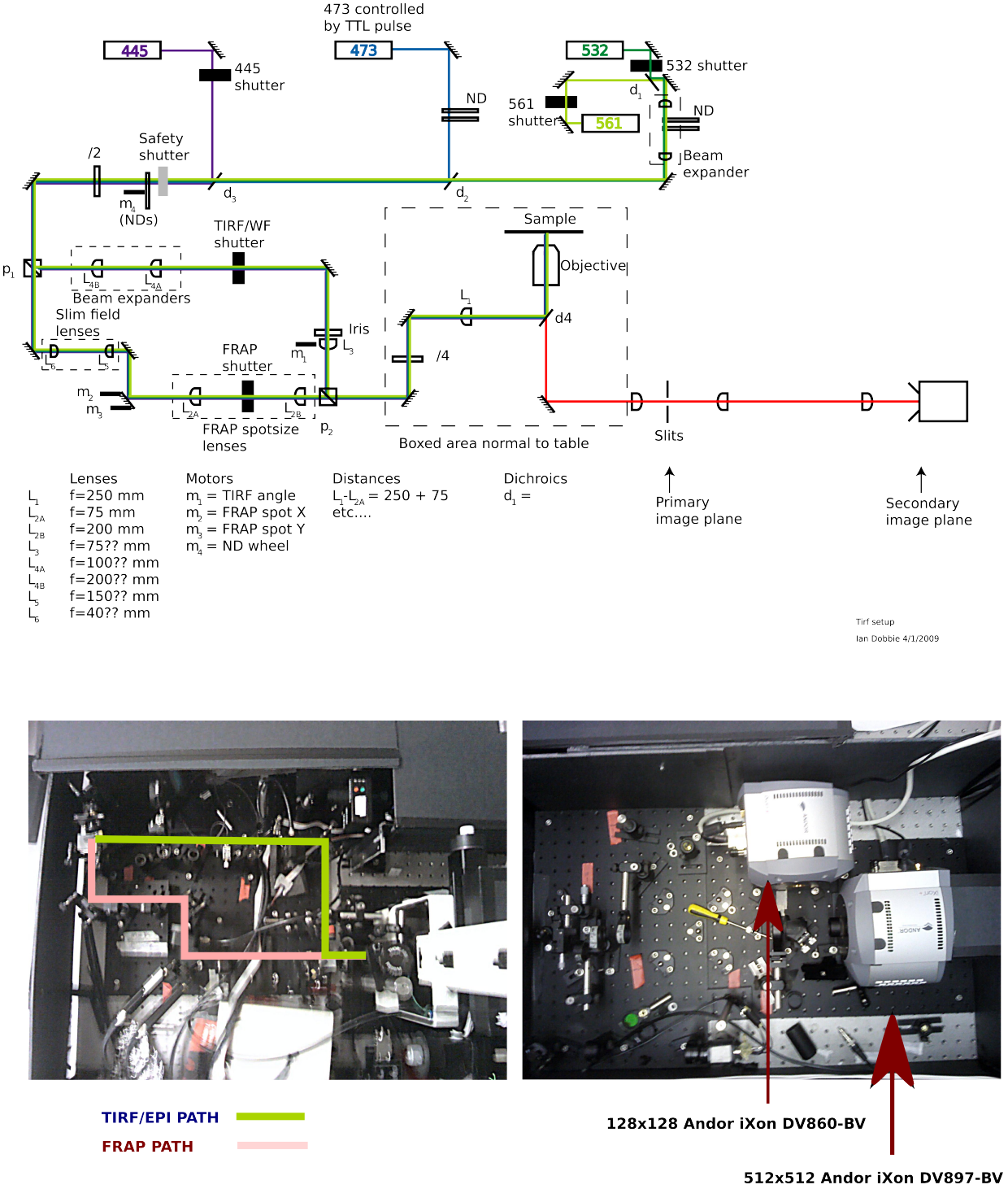


Figure 2.5: *The home-built TIRF inverted bespoke microscope*

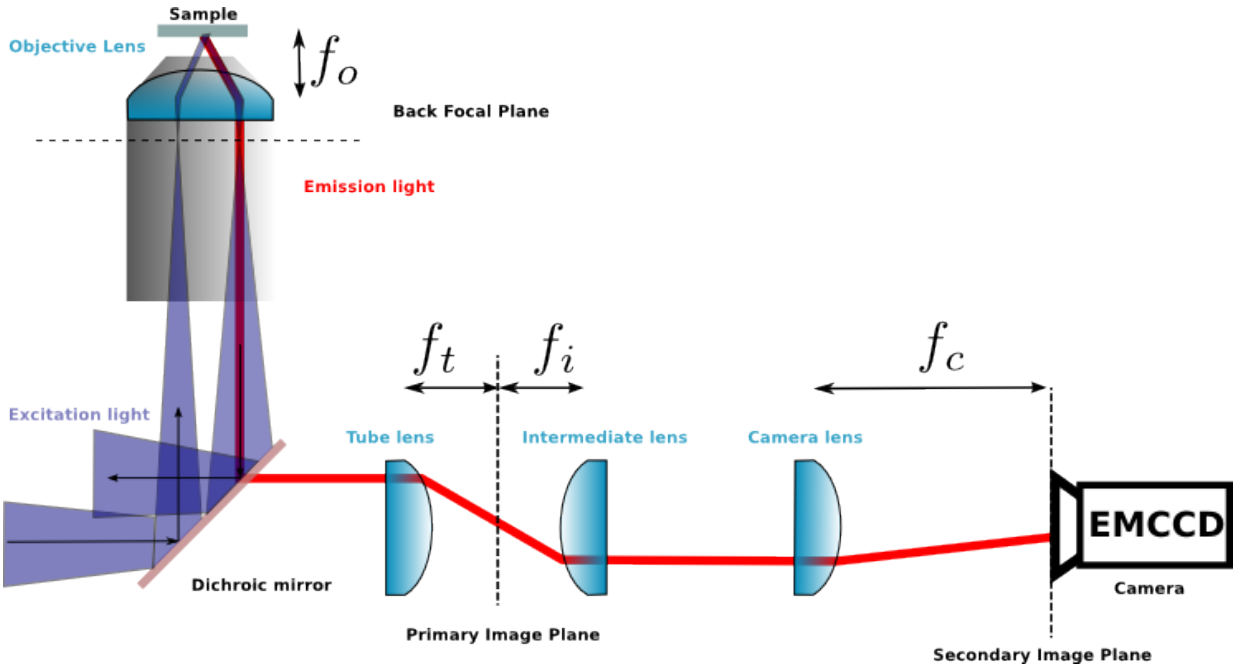


Figure 2.6: *Overview of optical set up. Incident radiation enters the objective lens after the dichroic mirror and illuminates the sample. Excitation and emission beams then exit the objective, with the excitation path reflecting back of the dichroic mirror. The emission path then passes through the tube lens, intermediate lens and the final camera lens respectively.*

the mirror; as the mirror was displaced, the offset changed the angle of entry into the objective at the back focal plane, and thus the illumination mode at the sample. Emission from the sample was recorded onto an EMCCD camera. One a 128x128 pixel (iXon DV860-BV, Andor Technology) fast acquisition camera and another 512x512 pixel camera (iXon DU897-BV, Andor Technology), where a flip-mirror was used to switch between cameras.

The magnification at the level of the sample at the primary image plane is given simply by $M_p = f_t/f_o$, the ratio of focal lengths. The magnification at the level at the sample is the magnification of the two remaining lens pairs and the final magnification is thus $M_c = (f_t/f_o)(f_c/f_i) = 450$ after substituting in values. Thus, the pixel size of the 128x128 camera and 512x512 cameras are equivalent to 52.8 nm and 35.6 nm/pixel respectively. This is as shown in Figure 2.6. These measurements were also confirmed through the use of a slide graticule.

The numerical aperture also determines the depth of field. High numerical aperture microscopes

have high axial resolving power. This is the resolution in the z axis, the vector normal to the optical plane. The expression for the depth of field is given[98], for excitation wavelength λ, lateral resolution (the minimum distance to resolve two objects) r, refractive index of the medium n and magnification of the objective M by Equation 2.4

$$d_{\text{dof}} = \frac{\lambda_0 n_{\text{oil}}}{(NA)^2} + \frac{n_{\text{oil}}}{M(NA)} r \tag{2.4}$$

The lateral resolution is calculated by Rayleigh criterion:

$$r = \frac{0.51\lambda}{NA} \tag{2.5}$$

For the microscope used in this work, this gives an axis resolution/depth of field of ≈350nm.

2.3.3 Widefield/Fluorescence Imaging

The general protocol in imaging regardless of illumination mode was to obtain both bright-field and fluorescence images. With the excitation laser off, the stage is translated until an ideal cell, or group of cells, is/are found. The typical characteristic of these are cells that are immobile, correctly shaped with the characteristic medicine capsule appearance, and have a relatively high contrast in bright-field. This is relative to damaged or broken cells, where the contrast is reduced. The cell is then focused at the mid-cell and a short imaging sequence is taken.

The next stage depends upon the illumination mode, or more specifically the targeted focal depth. Epi-fluorescence is typically imaged at the mid-cell, but some applications may use 100 nm plane imaging. This is always true in TIRFM imaging, as the fluorescence volume is limited to approximately 100 nm from the cover slip. In order to locate the 100 nm focal plane, 200 nm diameter latex beads are used. These are non-fluorescent, and can be used to find the appropriate focal plane in a similar manner to finding the mid-level of a cell; by finding the point of maximum contrast. Even at low concentrations, they can still be used to calculate the offset from the coverslip to the mid-cell by adjusting the piezo stage. Once the appropriate focal depth is found, the stage

is then moved to centre over the target cells and the imaging protocol begins. The process is demonstrated in Figure 2.7.

The fluorescence excitation field is controlled by a movable lens as detailed in §2.3.2. This is zeroed before any image acquisition through a painted 'X' directly above the objective lens. For oblique epi-fluorescence or TIRF the appropriate displacement is set through a calibration as detailed in §2.5.1. Then, the bright-field illumination light is shuttered, and the sample covered by closing the stage box. Imaging conditions are set in the `Andor` camera software, and then image acquisition is triggered. Immediately after image acquisition commences, the laser shutter is opened, allowing for fluorescence illumination.

Preparation of Bacteria

Experimental cultures were grown from frozen (-80 ^{o}C) $\sim$ 50 µl stocks overnight at 37^o. Then, 50 µl of the grown solution was subcultured into either 5 ml minimal media (either M63 or M9). They were then grown for varying times, dependent upon the strain used, to mid-log phase. These were typically grown with 0.2 mM arabinose, to express the Helix probe, and ampicillin, an antibiotic. Frozen stocks were prepared by growing bacterial cultures on a plate, then picking one colony and snap-freezing in the cryo-protectant dimethyl sulphoxide (DMSO). This is a cold-shock protector to prevent the cell from lysing. Cells prepared from frozen are clonal, and have limited genetic variation.

Preparation of Flow cells

Flow cells were prepared as in the protocol in [2]. Image preparation begins with clean coverslips prepared by suspending in a solution of KOH in ethanol for 2 hours in a fume cupboard. Then to prepare the slides, two lines of vacuum grease or double sided sellotape 1 mm apart were put onto a glass slide. Then a clean 22x22x0.1 mm coverslip was pressed down onto the slides to create a $\sim$ 20 µl chamber. Fluid is injected on one side of the coverslip and then wicked on the other. The chamber was washed through with the 100 µl of minimal media the cells were grown up in (M63

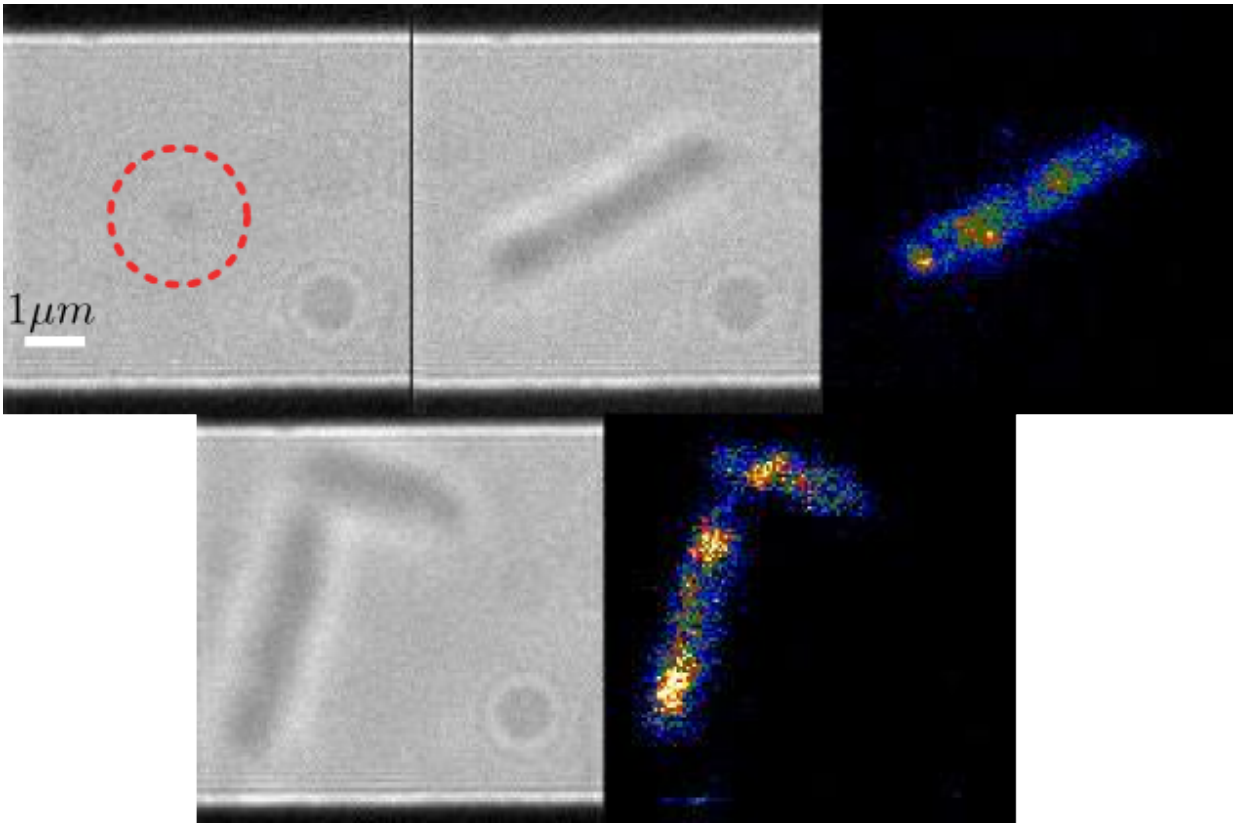


Figure 2.7: *Imaging protocol. To focus at 100nm, the focus is adjusted to maximise the contrast of the 200*nm *latex beads on the coverslip - specifying a focus of around 100*nm*, as indicated in the dashed red circle. Then, the stage is moved to a nearby cell (within the range of the piezo controller on the order of a few microns) and another bright-field image is taken. Top right: epi-fluorescence imaging at 100*nm *focus. Bottom left: mid cell focus. Bottom right: epi-fluorescence imaging at the midcell.*

or M9) by injecting the fluid on one side of the coverslip and then wicking on the other, drawing the fluid through by capillary action Then, 10 μl of poly-L-lysine were added and left to incubate for two minutes. Another minimal media wash was performed to remove unadhered poly-L-lysine, then 10 μl of cell culture was added. The flow cell was placed inside a humidity chamber and left to incubate for 20 minutes. Then, another minimal media wash was performed and finally for TIRF imaging 200 nm diameter latex beads were added followed by a subsequent minimal media wash. Care is taken when injecting fluid to not allow air bubbles to form. This would both interfere with imaging and be damaging to cells. Before imaging, a few microlitres of minimal media is added

to the sides of the flow-cell to prevent drying out during data acquisition, which can often last for several hours per sample. This protocol is as shown in [2]. A schematic of the flow-cell is shown in Figure 2.8

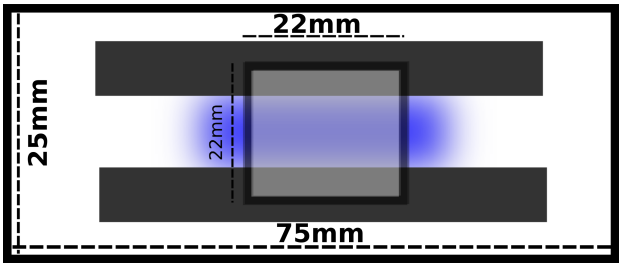


Figure 2.8: *Schematics of slides used in this thesis. A top-down diagram of a flow-cell. The outer boundary represents the glass slide, the middle square represents the coverslip, the two rectangular sections represent the vacuum grease or double sided sticky tape and finally the blurred blue section in the middle represents the solution in the flow-cell. This is depicted with excess solution to indicate fluid on the exit points of the flow-cell to prevent dehydration.*

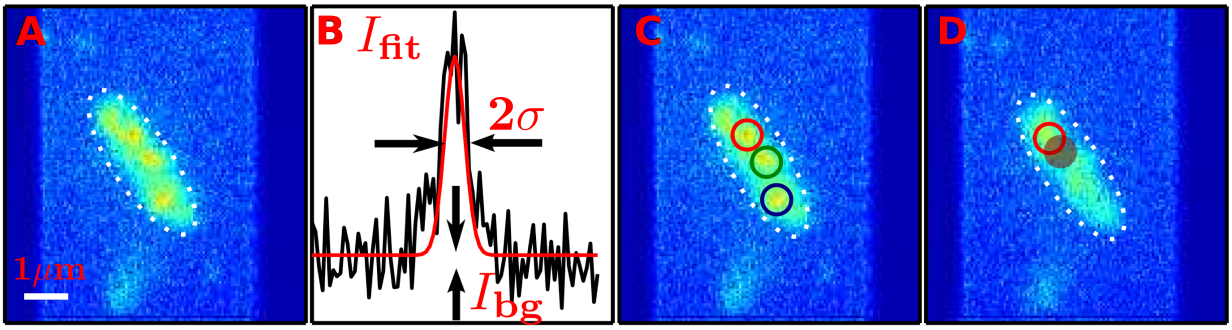


Figure 2.9: *Tracks are found from a spot-finding algorithm (A). In each case, the Point Spread Function (PSF) of the spot is fitted by a two-dimensional Gaussian at point C_{xy} ($I_{fit} \times \mathcal{N}(C_{xy}, \sigma)$), and the local background intensity I_{bg}, the height and the standard deviation of the PSF are found. (C) The process is repeated for all spots in the frame. D) Spots are linked into trajectories by using heuristic measures such as the centroid separation and the change in intensity between the two spots.*

2.4 Image Acquisition and Analysis

Tracking was performed by code written by the post-doc Isabelle Llorente-Garcia. The algorithm follows usual image tracking heuristics, and a description is included here for completeness.

Optical resolution is typically presented as the Rayleigh length of the order $\lambda/2$ where λ is the wavelength. Below this limit, the point spread functions (PSF) cannot be separated. A PSF describes the *response* of an imaging system to a *point source* or point object. A PSF can be thought of as the spatial extent of an image that represents an unresolved object. However, although the details of the spot are not resolvable below the Rayleigh limit, the centre of the spot and hence the location of the fluorophore can be determined to a greater precision. This effectively allows for sub-resolution single particle tracking. I discuss the accuracy of centroid localisation in a later section.

2.5 Calibrating single-molecule fluorescence microscopy

2.5.1 TIR Calibration

To calibrate the TIR exit-angle, a BK7 substrate (Thorlabs) polarising beam-splitter was placed on the glass slide. At 473 nm excitation, BK7, has a refractive index of 1.52, approximately the same as the fluorescent free (Type FF) oil used. To measure the exit angle, the deflected laser spot was measured on the wall around 1.5 m away. A second test was used after the microscope realignment, where a series of coverslips were placed on top of each other with a drop of immersion oil between each. The geometry for the beam-splitter setup is shown in 2.10.

To determine ψ, the incident angle from the objective lens onto the coverslip, I determine θ by measuring the height of the laser spot on the wall and then using Snell's law (Equation 2.1) to determine the objective lens exit angle. Given the set of refractive indices of air, cube, glass slide, coverslip, oil and water are $n_{\text{air}} = 1, n_{\text{cube}} = 1.52, n_{\text{glass}} = 1.52, n_{\text{coverslip}} = 1.52, n_{\text{oil}} = 1.52, n_{\text{water}} = 1.33$ respectively, then I obtain the objective lens exit angle by applications of Equation 2.1.

$$n_{\text{air}} \sin(\theta_{\text{air}}) = n_{\text{cube}} \sin(\theta_{\text{cube}}) \tag{2.6}$$

Then, to determine the angle incident (and hence the excitation field) into the sample (as in Figure 2.4) then:

$$n_{\text{coverslip}} \sin(\theta_{\text{coverslip}}) = n_{\text{oil}} \sin(\theta_{\text{oil}}) \tag{2.7}$$

$$n_{\text{water}} \sin(\theta_{\text{water}}) = n_{\text{coverslip}} \sin(\theta_{\text{coverslip}}) \tag{2.8}$$

Then, returning to Equation 2.3 I obtain the penetration depth.

$$d = \frac{\lambda(0)}{\sqrt{4\pi(n_{\text{glass}}^2 \sin^2(n_{\text{glass}}) - n_{\text{sample}}^2)}}; \tag{2.9}$$

I can also calculate the critical angles at both the glass-sample interface, and the glass-air interface as:

$$\sin^{-1}\left(\frac{n_{\text{coverslip}}}{n_{\text{water}}}\right) = 61.7^o \tag{2.10}$$

$$\sin^{-1}\left(\frac{n_{\text{glass}}}{n_{\text{air}}}\right) = 41.5^o. \tag{2.11}$$

That there are two critical angles is observed in the exit behaviour of the beam. As the incident angle becomes increasingly shallow (θ_o increases), the laser beam goes from exiting the sample, to being bounded to within the glass at beyond the air-glass interface - this creates a light scattering within the microscope slide, lighting it up, as the light is trapped. As the second critical point is reached - the onset of TIR at the level of the sample - this scattering decreases as there is reduced laser energy propagating through to the glass.

Finally, I can calculate and compare the maximum exit angle supported by the high NA objective. This is 71^o and is given by:

$$\theta_{\text{MAX}} = sin^{-1}\left(\frac{NA}{n_{\text{oil}}}\right). \tag{2.12}$$

I depict this in Figure 2.11.

2.5.2 Stoichiometric Calibration

In order to get single molecule intensity levels for GFP under imaging conditions the following protocol is used starting from a dry flow cell:

- Flow through 100 µl of minimal media
- Flow in GFP antibody (α -GFP) 5 µg/µl(1:100)
- 5 minute wait

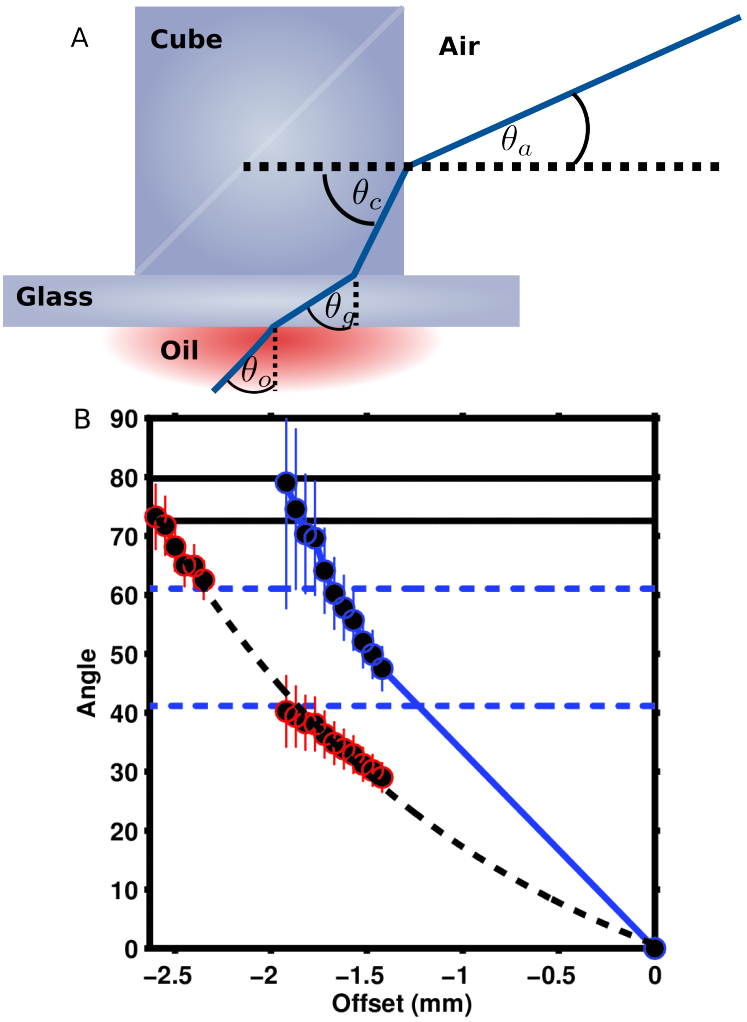


Figure 2.10: *a) TIRF Calibration geometry. The θ represents the respective the angles with respect to the normals incident to the surface of the respective interfaces. θ_a represents the exit angle, θ_c represents the angle normal to the cube-air interface, θ_g represents the normal to the glass-cube interface and θ_g represents the exit angle from the objective lens and the incident angle from the oil-glass interface. b) Measured laser angles as a function of mirror displacement from epi-fluorescence. Red: O_o, exit angle from objective. Blue: exit angle from glass into glass-air interface (without a cube). The solid black lines indicate the maximum predicted angle for a 1.45 and a 1.50 NA objective respectively. The dash blue lines indicate the glass-air horizon and the oil-sample horizon (the onset of TIR). The dashed-black line represents a polynomial fit of order 2 to the the angle-data at the objective output.*

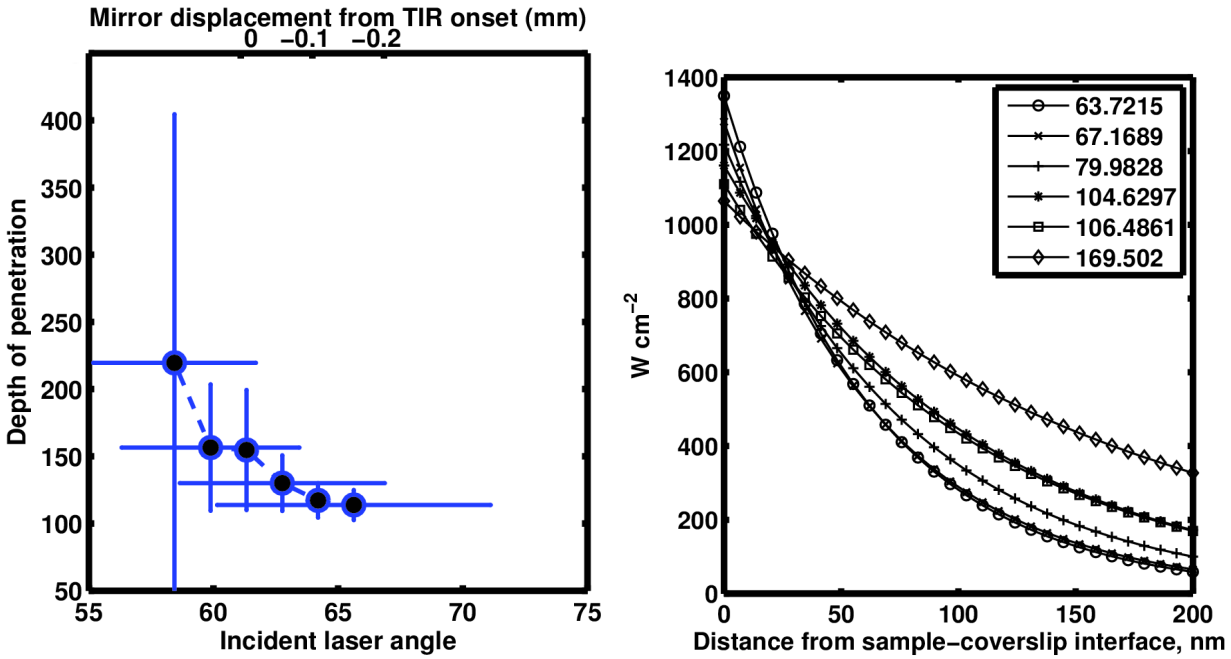


Figure 2.11: *Left: Depth of penetration versus incident laser angle. Error bars are standard deviation error by quadrature error propagation. Right: Excitation field as a function of distance from the sample-coverslip for varying depths of penetration.*

- Flow through 100 µl minimal media
- Flow through 20 µl of GFP (1:500)
- Wait 5 minutes
- Flow through 100 µl minimal media
- Flow in 20 µl (1:500) 200 nm latex beads,
- Wait five minutes
- Flow through 100 µl minimal media.

The GFP antibodies have a Stokes radius of around 5 nm [99, 100]. GFP itself has a hydrodynamic radius of around 2.4 nm. With these figures, I expect little rotation under shear stress of the GFP, confirmed through the static diffraction limited point spread function image of the attached GFP fluorophore. In order to find the focal plane of the GFP, the focal plane is found during excitation; revealing a field of immobilised GFP molecules, under the partially closed field-iris which allowed a small spot of laser light through of approximately 40 µm radius. Originally latex beads were used to find the field place; the beads are used to calibrate the position by changing the focus between the beads and the GFP-antibody focal plane, this was used to calibrate the change in focal depth for or alternatively illuminating the GFP field with a narrow field iris and focussing on the GFP field then translating the piezo stage in x-y to an unbleached region. Small x-y translations of the stage generally do not perturb the z axis. Latex beads were not used in this experiment because GFP were found to strongly adhere to the latex, breaking the assumption of a single molecule population. As it happens, the GFP molecule field was found not to be populated by single GFP molecules but a distribution of stoichiometries. A possible reason for this is aggregation of the GFP molecules in the Eppendorf tube, as it was stored at 5^o, rather than $<0^o$.

In order to obtain single molecule photobleaching step behaviour, the following analysis was performed. Individual spots on the image frames from the experimental protocol above were used to

obtain fluorescence intensity time-series data of 800 frames length at 40 ms sampling time per image frame over a range of excitation intensities and illumination modes. The entire intensity time-series profile was not used for analysis; the last 300 frames were used to investigate the photobleaching intensity step where molecules were seen to be blinking at the single molecule level. Each intensity time-series is background corrected by profiling the noise at a manually selected ROI of the image that is away from the 200-300 nm point spread function of any GFP molecule. This was chosen by viewing the frame average over the sampled pixels. A frame average is computed by taking the mean intensity at each pixel over the range of frames used over the duration of the time-series. As the GFP are immobilized, this averages out any photodynamics of the GFP molecules such as photoblinking where GFP may not be fluorescing. Correction works by subtracting the noise intensity intensity time-series profile from the image data. These were then smoothed using a Chung-Kennedy filter [101]. This is an algorithm that filters noisy time-series data by a bank of weighted forward and backwards predictors that perform windowed averaging. The next stage is to identify single GFP within this intensity trace.

2.5.2.1 Identifying Single GFP

To identify single GFP, the following algorithm was used. The standard deviation of the integrated intensity noise spot, σ_{BG}, was calculated. Then, all points above $I_{\text{spot}} - 3\sigma_{\text{BG}}$ were identified. The trace was then analysed from the first point in which the intensity is below this threshold, and all intensity values subsequently above the threshold were extracted. This procedure is demonstrated in Figure 2.14. This approach was complemented by a Fourier analysis of the intensity time-series for the initial 300 frames [47]. For each individual filtered time-series, the pairwise difference of the intensity signal is computed, to form a histogram of intensity jumps. This is separated into both the entire series of jumps, positive jumps and negative jumps. This is to separate into both photo-activation and photo-deactivation from photoblinking and photobleaching events. Similar steps were performed for the noise intensity time-series with the profile obtained for the background noise. In Figure 2.12 I demonstrate this process using all pair-wise intensity differences. However, I

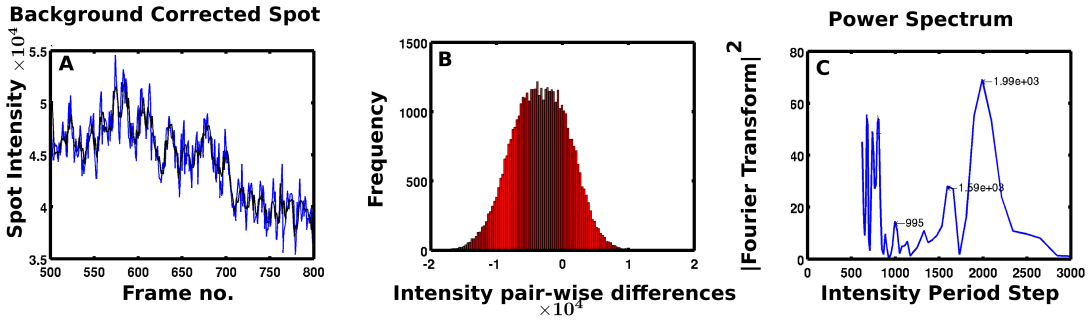


Figure 2.12: *Fourier step-detection for a 100 W /*cm^2 *epi-fluorescence illumination. A) Photoblinking steps in a single GPF molecule. The two lines indicate the raw data and the filtered data respectively. The signal is background corrected with the noise. B) Histogram of all pair-wise intensity differences. C) Fourier transform of pair-wise intensity differences. Peaks in the data trace are identified. The peak identified in this case is* 1.99×10^3*, in agreement with the data presented in Figure 2.14.*

use the photoblinking method for the data present in 2.14.

These steps were completed over a range of experimental imaging protocols. Here, the 473 nm imaging laser power varied from 20 mW down to 5 mW in epi-fluorescence mode. Further imaging was taken 7 and 8 mW laser power over a range of excitation modes ranging from epi-fluorescence, oblique shallow angle epi-fluorescence, and total internal reflection fluorescence, by varying the incident angle. This was to cover the range in excitation modes used during *in vivo* acquisition; as there was a small variance in the laser illumination intensity used to quantify the change in the photobleaching step. Secondly, because a mixture of epi-fluorescence, oblique epi-fluorescence and total internal fluorescence illumination was used, these profiled single molecule imaging over these different illumination modes.

The unitary step size for single GFP data under EPI and TIR illumination modes are summarised in Figure 2.13. This figure contains both the unitary integrated photon count over a single frame image acquisition, and the average 'on' time for a GFP. The fit of the radiation flux Ξ and the photon count is through Equation 2.13, where C_s is the saturation count and ξ is the saturation flux.

$$C = C_s \frac{\Xi/\xi}{1 + \Xi/\xi} \tag{2.13}$$

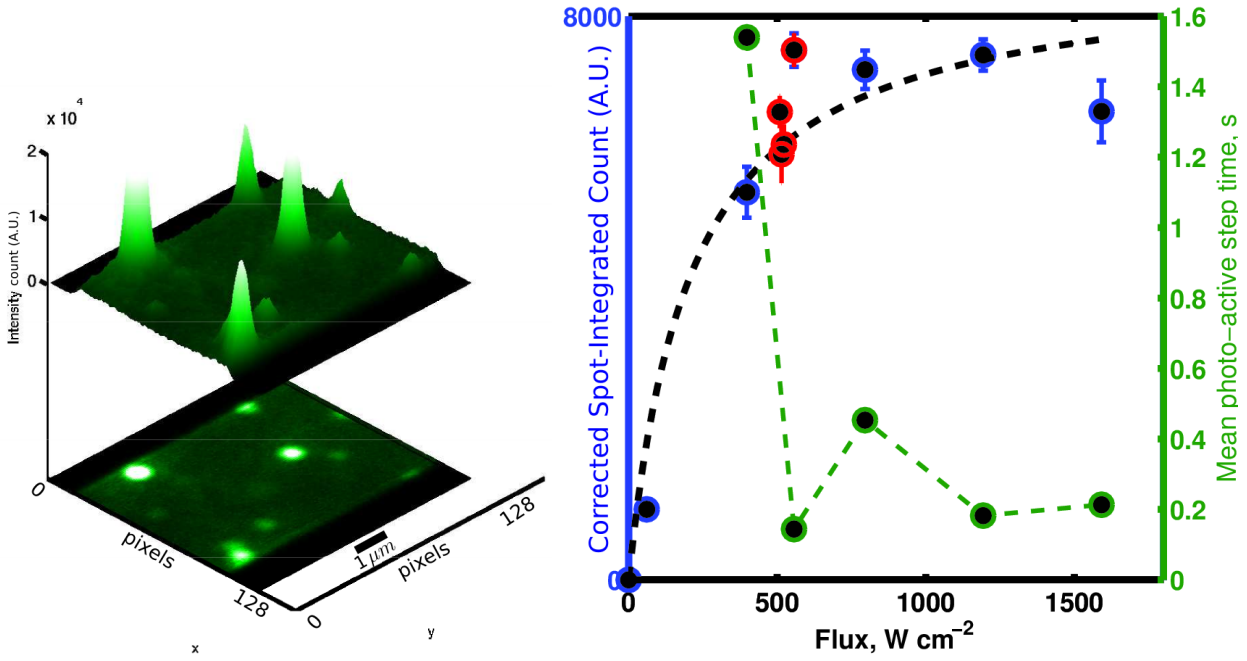


Figure 2.13: *Left: Point spread functions from a GFP field imaged from the protocol in Section 2.5.2. The heterogeneity in the peak sizes implies that GFP aggregation has occurred, and that these are not single GFP molecules. This is further seen with photobleaching curves. The black sides where there is a drop off in intensity is due to the shutters. Right: Single GFP molecule excitation step as a function of epi-fluorescence illumination intensity in a 20* μm *beam (blue circles) and TIR illumination (evaluated 5* nm *from the coverslip, red circles). The x-axis is the radiation flux, the y-axis is the noise-corrected count integrated over the GFP spot (see §2.5.2.1) with SD error bars. The levelling off from around 7* mW *(1000* W /cm$)^2$ *is due to putative photosaturation of the GFP, comparable to other values [102], imaged under comparable conditions (phosphate buffered saline (PBS), pH 7.5) The linear regime agrees with other results under similar experimental conditions (approximately 1000 counts for 0.77* mW*) due to the cage like structure of GFP [103]. This is supported by the independent measure of the mean photoactive time, which stabilises at these illumination intensities as the on/off time-scale ratios equilibrate. Fitting values are* $C_s = 8.6883 \times 10^3$ *counts and* $\xi = 210.9$ W /cm^2

For *in vivo* data, stoichiometry estimates are made by the ratio of the observed integrated photon count to the interpolated single GFP integrated photon count. However, in image acquisition, fluorophore point spread functions are not necessarily tracked from the onset of illumination. The

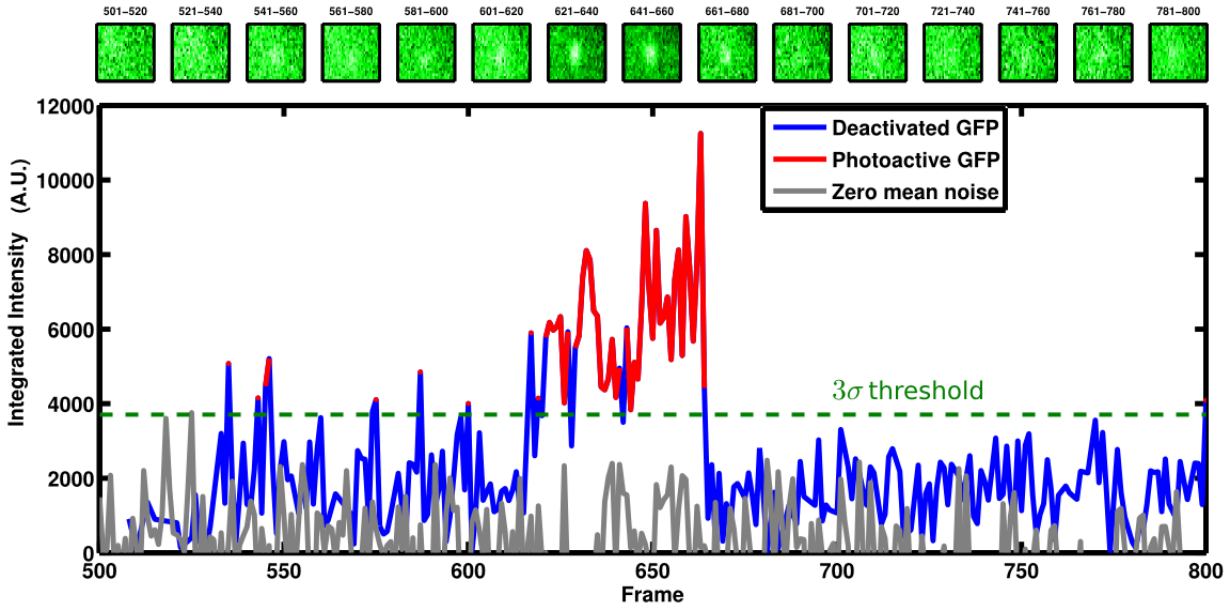


Figure 2.14: *Identifying single molecule switching in GFP imaged at 7* $\mathrm{m}W$ *under epi-fluorescence excitation. In the upper panel, a time series of frame-averages (10 frames, non-overlapping) is shown. The off-on-off activity of the GFP is seen clearly, but also the flickering between frames 540-550. In the lower panel, the intergrated intensity trace is shown. In the trace, photoactive GFP are marked where the intensity is above* $3\sigma_{bg}$*. The* 3σ *threshold is as discussed in Section 2.5.2 is the high probability threshold, and the flickering between frames 540 and 600 does appear to be captured by this threshold, which can be seen by eye in the upper panel.*

tracking algorithm may not identify the spot initially, or fluorophores may be diffusing in and out of the focal plane, preventing detection. To obtain a stoichiometry estimate for *in vivo* data, I therefore interpolate the photobleaching curve to $t = 0$. This uses the variables I_0, the estimated initial intensity at $t = 0$, τ, the photobleaching decay constant, and ν, which measures the background noise asymptote at high t where the photobleaching curve decays to the background intensity. This is depicted in Figure 2.15. I interpolated the intensity of a fluorescent spot from before the tracking algorithm captures it to the onset of illumination by an interpolation function of the form Equation 2.14:

$$I_{\mathbf{est}}(t) = I_0 \exp\left(-\frac{t}{\tau}\right) + \nu. \tag{2.14}$$

When considering multiple tracks, the fitting is done simultaneously for all tracks, with a global ν and τ, and I_0 allowed to vary. The pseudo code for this algorithm is given in the Appendix in §A.2. A photobleaching trace such as this will be relatively accurate through a uniform illumination field as in epi-fluorescence, but this is not true in TIR. In the cell, proteins are diffusing around the cell membrane. So far, this has been described in Cartesian coordinates with a z displacement from the cover-slip, and planar $x - y$ diffusion. However, In TIR, the excitation field strength varies due to the evanescent decay. (Figure 2.11). For typical diffusion rates, acquisition time-scales and cell sizes, I assume that there is only a marginal effect of out-of-field excitation and thus I do not correct for this. Correcting for this would require an estimation of where the spot has diffused.

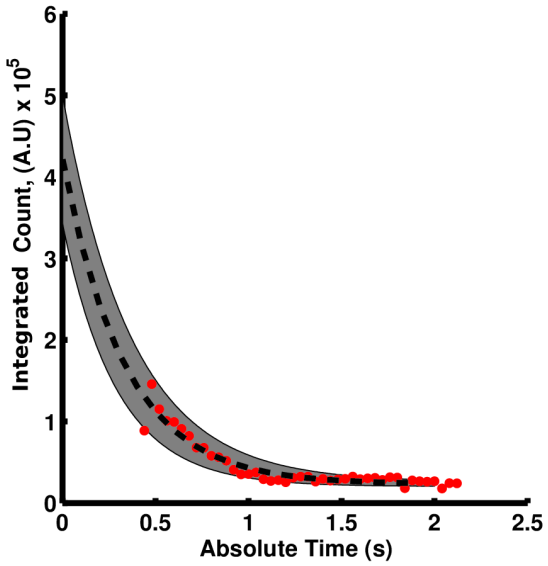


Figure 2.15: *Estimating in vivo stoichiometry. The data are taken from a TIR acquisition of the helix-x1 protein (see Chapter 4) under approximately 500 W* $/\mathrm{cm}^2$ *illumination. Absolute time refers to the time from the onset of illumination. The beginning of the data trace commences when the tracking software identifies a diffusing spot. The dashed black line represents the fitting (Equation A.2, and the grey background represents one standard deviation in uncertainty about the fit - as estimated from §2.6.3. From this fitting, an estimate of* I_0*, the estimated intensity at the commencement of illumination of the sample. From this, the stoichiometry is estimated by the ratio of this intensity value divided by the estimated single fluorophore intensity value under excitation conditions. This particular fitting has values of* $I_0 \approx 4 \times 10^5$ *counts,* $\tau = 0.3$ *s and* $\nu = 0.2 \times 10^5$ *counts. Under these illumination conditions, stoichiometry is estimated at 138 units. Accounting for fitting uncertainty, and angle calibration errors, this is between the range of 110-168 to one standard deviation. The estimated number of photons emitted before photobleaching is approximately* 2×10^5 *for around 140 units, which is* $\approx 1.4 \times 10^3$ *photons/GFP. Reference [104] reports that single molecules GFP emit* $\leq 4 \times 10^5$ *before photodestruction. This difference is accounted in part by the photon detection efficiency of around 10%. The remaining fraction, I attribute to non-uniform illumination, lack of tracking when the Signal-to-Noise ratio has fallen sufficiently and different experimental conditions that may impact the number of GFP photons emitted.*

2.6 Sources of Experimental Error

This section details a variety of sources of experimental errors of which some have been quantified. There are a variety of sources of experimental error due to the experimental framework. There were multiple users of the microscope and more than once the system had to be realigned. On occasion, experimental data was taken despite this, with the disclaimer that it is predominantly stoichiometry data that is affected, as it is due to laser power, illumination fields and alignment. Tracking data is much more robust to these sources because of the heuristics used in experimental tracking, as detailed in §2.4. Example sources are, laser alignment being off-centre, laser or off-axis (not normal to the image plane), edge diffraction along laser path or interference due to dust or other errant particles on optical components.

2.6.1 Errors in Tracking

Savin [105] identifies two principal sources of error in the statistical analysis of single particle tracks; static and dynamic. Static errors arise from the intrinsic noise in the experimental method. These are the identification of the particle position [106] as a result of underlying signal to noise ratio, finite pixel size or time-position offsets. Dynamic errors arise from the finite acquisition time or shutter speed, integrating over an sampling time of δt whilst the particle is moving [107]. However, these uncertainties are separate to the statistical variance that emerges from the stochastic nature of the diffusion process. In this section, I outline the sources of *experimental* error. In Chapter 3, I outline the sources of stochastic error.

2.6.1.1 Static errors

The errors in tracking emerge from the localisation error of the centroid of the point-spread function. Centroids can be located to sub-optical-resolution accuracy. The accuracy of sub-resolution tracking scales as an inverse function of the number of photons. The principle origins of noise are shot noise and background noise for out-of-focus fluorescence. Charge-coupled device readout noise and dark

current are among other factors also influence the localisation precision. Reference [106] derives an expression based on Shot Noise and background noise as Equation 2.15. This is using background noise b (in units of counts), signal photon count N, pixel size a and standard deviation of the point spread function s as:

$$\langle(\Delta x)^2\rangle = \overbrace{\frac{s^2 + a^2/12}{N}}^{\text{Shot noise}} + \overbrace{\frac{\sqrt{\pi} s^3 b^2}{a N^2}}^{\text{Background Noise}} \tag{2.15}$$

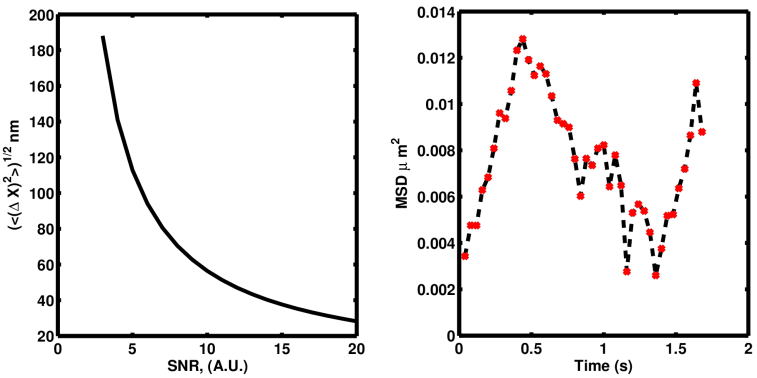
For typical values for this microscope, isolated single GFP have a FWHM of around 150-250 nm corresponding to a standard deviation of around 60-100 nm. For the equivalent 2D expression given in Equation 2.16 and using the signal to noise ratio (SNR) as b/N I plot the centroid localisation error with respect to the signal to noise ratio in Figure 2.16. During an imaging experiment, it should be noted that this uncertainty is will grow as fluorophores in the PSF begin to photobleach, thereby reducing the signal-to-noise.

$$\langle(\Delta x)^2\rangle = \frac{s^2 + a^2/12}{N} + \frac{8\pi s^4 b^2}{a^2 N^2} \tag{2.16}$$

Other errors emerge in the Cartesian assumption of the tracking algorithm. A thorough treatment would require recasting the tracking coordinate system into the local coordinate system of the cell in curvilinear coordinates. For typical cell diameters of 1 µm, diffusion rates and acquisition times and a depth of field for this microscope of 350 nm this approaches a reasonable source of error in epi-fluorescence imaging. In TIR, this effect is reduced as the field is typically over 100 nm.

2.6.1.2 Dynamic errors

Dynamics errors emerge from the finite acquisition time. The expected ratio between the FWHM (Full Width Half Maximum) of the PSF of mobile and immobile particles is related by the integration time δt, diffusion coefficient D and single PSF standard deviation s and is given Equation 2.17:



(a) *(b)*

Figure 2.16: *Centroid localisation. In a) the centroid localisation accuracy is given for typical values with* $s = 75$ nm *and* $a = 50$ nm*. The SNR is defined as the ratio of the mean of the signal over the standard deviation of the background (bg)* μ_{signal}/σ_{bg}*. b) An example track, taken from fluorescence imaging of a protein-GFP (see Chapter 4). In the case here, the y-intercept is at approximately 0.002* μm^2 *corresponding to an initial uncertainty of around 50* nm*.*

$$R = \sqrt{1 + \frac{D\delta t}{s_0^2}} \tag{2.17}$$

2.6.1.3 Photonic budget

2.6.2 Systematic Error in Experimental Set-up; Alignment

In Figure 2.17, a control experiment is displayed. This is a frame average from a video trace in which there are no GFP are present. This is to estimate the degree in which the illumination field is heterogeneous across the field of view. For a centred 20 μm illumination field operating in TEM_{00} mode, this should be minimal. This can be estimated for a well-aligned laser for a 6.9 μm squared field of view at the sample by $I_0^{centre}/I_0^{edge} \approx \exp(-r_{edge}^2/\sigma_{beam}^2) \approx 0.94 \approx 6\%$. As single GFP molecule is being detected with a signal strength of above $3\sigma_{BG}$, the predicted correction term is within 3%.[1] Despite this, the noise variance was greater than expected at around 8% as seen from a

[1] Assuming shot noise then $\sqrt{\sigma_I} \approx I \rightarrow \sigma_{\sigma_I|\delta I} \approx \sqrt{\delta I/I} \approx \sqrt{0.94} \approx 3\%$

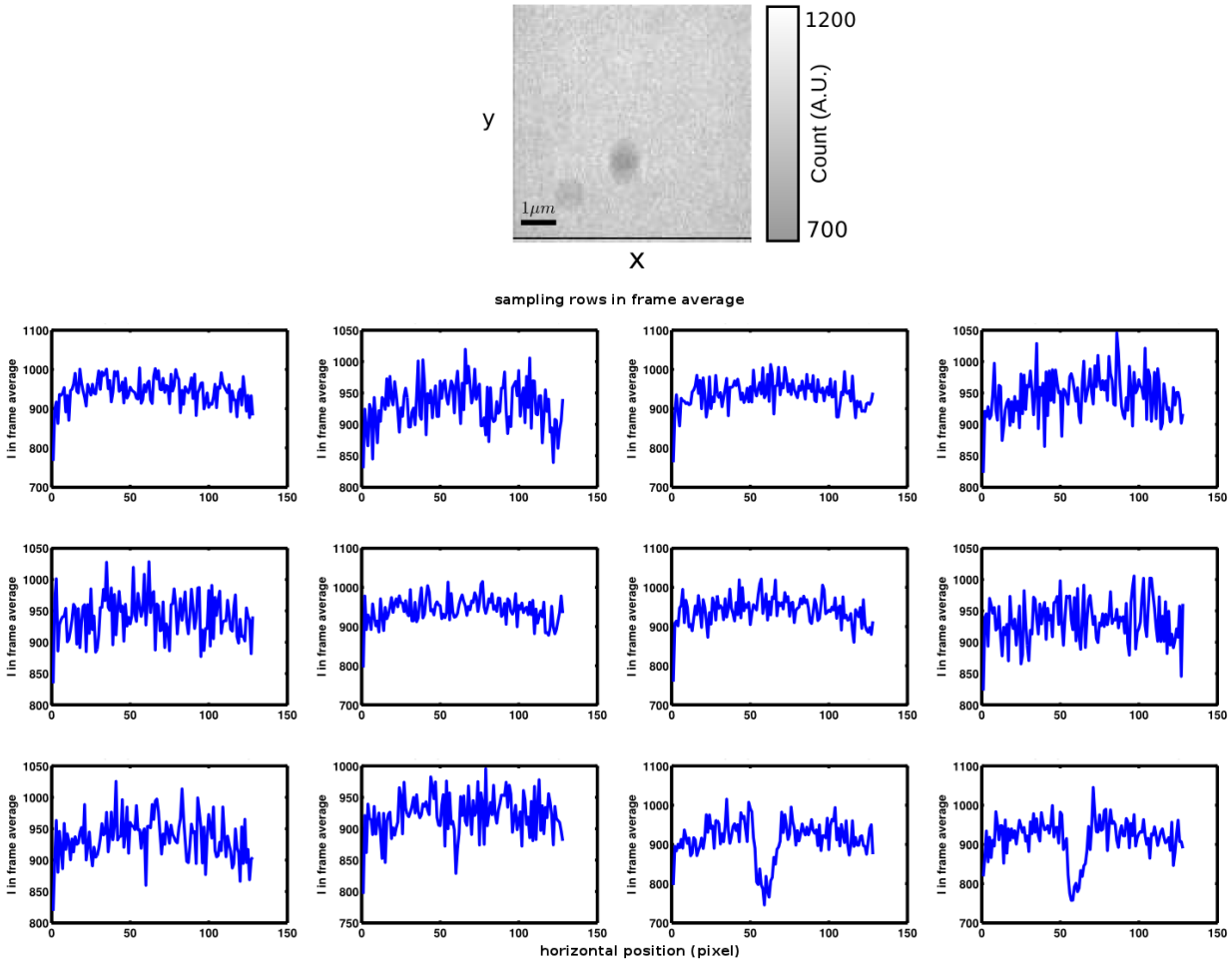


Figure 2.17: *Upper: bright-field illumination of an empty region. Lower: Typical variation of noise across the image profile at 7* m*W illumination with a 20* µm*radius 473* nm *illumination field. Each section is a piecewise intensity time-series profile along the horizontal x-axis uniformly divided along the y-axis. Although the coverslip is empty, the dark regions on the bright-field is dust/dirt on one of the mirrors, which is the (probable) origin of the dip in the fluorescence profile seen in the last two intensity profiles in the lower panel.*

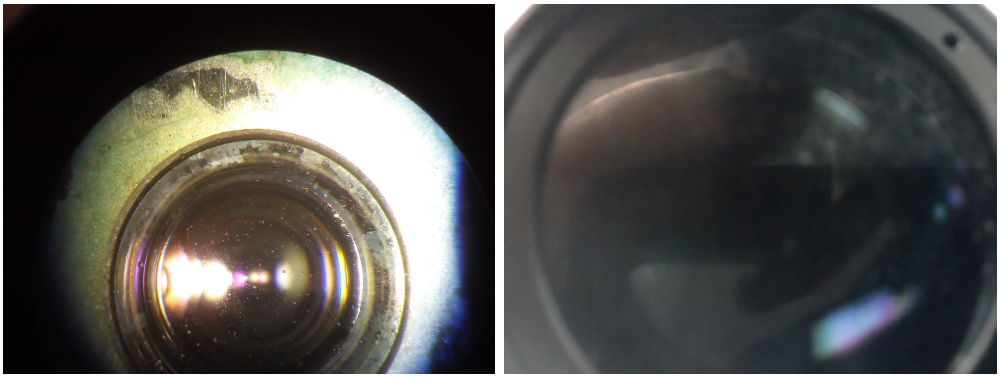


Figure 2.18: *TIR objective. Salt deposits formed crystals about the edge of the objective, where TIR appears. The likely source of these is deposited media that then evaporates, leaving salt deposits which crystallise. As these were found around the edge of the objective, where high-angle TIR beams originate from, this was found to create diffraction patterns and scattering when imaging under TIR.*

frame average with 9 uniformly spaced noise ROIs [1] of the noise across the field of view.

It was seen that there were dim diffraction patterns appearing in the image plane during both epi-fluorescence and evanescent field illumination. The source was never identified, and is seen during low emission-response excitations although probably due to the laser alignment. Various approaches were used to try and identify and remove the source. These included testing for whether it was polarisation related, by comparing with and without the circular waveplate[2] prior to entering the microscope chasis. Other approaches included cleaning the objective lens (see Figure 2.18) and removing back-scattering by applying black tape at beam reflection points or enclosing the stage in a box.

2.6.3 Experimental Calibration Error Propagation

Experimental errors are calculated using standard quadrature error analysis [108]. In general, error propagation for a function $Z = Z(A, B...)$ where A, B, etc. are independent is through Equation 2.18:

[1] As in, for multiple points on an image, record the standard deviation of each, and then compute the standard deviation of these

[2] Circular polarisation is used to average out any effects of polarisation

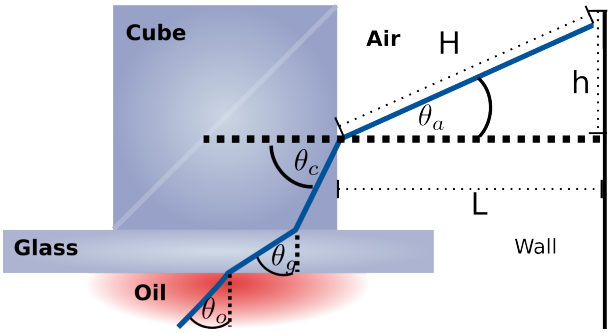


Figure 2.19: *Geometry in angle calibration.*

$$(\sigma_z)^2 = \left(\frac{\partial Z}{\partial A}\sigma_A\right)^2 + \left(\frac{\partial Z}{\partial B}\sigma_B\right)^2 + \dots \tag{2.18}$$

Where possible, I propagate errors forward using the quadrature approach. An example of the error calculation in the TIR calibration is given. Errors begin to propagate in the uncertainty in the calibration experiments. In the first step, I estimate the error on the angle calibration and the depth of field. The next step was to calculate the error on the intensity field. The final result of this error propagation is the error in the uncertainty in the intensity field at distance z from the coverslip. I propagate these uncertainties forward to stoichiometry calibrations by considering the error on the unitary intensity of a single GFP that were measured experimentally.

When considering *in vivo* data, the error propagation becomes more complicated in that I use fits to estimate I_0. When making such fits the uncertainty is measured by considering the standard deviation of the parameter fits - usually through a Jacobian estimate [108]. If the Jacobian cannot be found I revert to an ensemble standard error estimate for use as an error.

Angle Calibration and Depth of Field Error Propagation

In Figure 2.19, the geometry of the angles are depicted. Here, H is the calculated hypotenuse of the spot-angle on the wall, and σ_H is the associated uncertainty. L and h are the distance to the wall and the height respectively. The remaining variables, θ_{air} are variables identified in earlier sections referring to the laser angle in the air, oil etc. The final equation gives the uncertainty in the depth

of penetration d.

Starting from the error in the sine of the angle of the laser in the air:

$$H = \sqrt{L^2 + h^2} \tag{2.19}$$

$$\sigma_H = H\sqrt{\frac{\sigma_L^2}{L^2} + \frac{\sigma_h^2}{h^2}} \tag{2.20}$$

$$\sin(\theta_{\mathbf{air}}) = h/H \tag{2.21}$$

$$\tag{2.22}$$

Converting this to the error on the laser exit from the objective lens:

$$\sigma_{\theta_{\mathbf{air}}} = \sqrt{\frac{1}{1 - \sin(\theta_{\mathbf{air}})^2}}\sigma_{\sin(\theta_{\mathbf{air}})} \tag{2.23}$$

$$\sin(\theta_{\mathbf{oil}}) = \frac{n_{\mathbf{air}}}{n_{\mathbf{oil}}}\sin(\theta_{\mathbf{air}}) \tag{2.24}$$

$$\sigma_{\theta_{\mathbf{oil}}} = \sqrt{\frac{1}{1 - \sin(\theta_{\mathbf{oil}})^2}}\sigma_{\sin(\theta_{\mathbf{oil}})} \tag{2.25}$$

$$\tag{2.26}$$

I then obtain the error about the penetration depth:

$$d = \frac{1}{4\pi}\frac{\lambda}{\sqrt{(n_{\mathbf{oil}}\sin(\theta_{\mathbf{oil}}))^2 - n_{\mathbf{sample}}^2}} \tag{2.27}$$

$$\sigma_d = \frac{1}{4\pi}\frac{\lambda n_{\mathbf{oil}}^2 \sin(\theta_{\mathbf{oil}})}{(n_{\mathbf{oil}}\sin(\theta_{\mathbf{oil}}))^2 - n_{\mathbf{sample}}^2{}^{3/2}}\sigma_{\sin(\theta_{\mathbf{oil}})} \tag{2.28}$$

Intensity Field Error Propagation

The error on the intensity profile is a little more complicated. The intensity at depth z in TIR at illumination angle θ is given by:

$$I(I_0, d, z) = I_0\cos(\theta)\exp\left(\frac{-z}{d}\right) \tag{2.29}$$

The depth of penetration d, however, is a function of θ, and Equation 2.18 is only valid for independent errors. Depth of penetration is a function of θ, meaning the variables $d[\theta]$ and $\cos(\theta)$ have correlated errors. The independent variable is θ so, re-writing I with the dependence on θ we have the error on $I[I_0, \theta]$:

$$\sigma_I^2 = \left(\frac{\partial I}{\partial I_0}\right)^2 \sigma_{I_0}^2 + \left(\frac{\partial I}{\partial(\theta)}\right)^2 \sigma_\theta^2 \tag{2.30}$$

$$\sigma_I^2 = \left(\cos(\theta)\exp\left(\frac{-z}{d}\right)\right)^2 \sigma_{I_0}^2 + I_0^2\left(\sin(\theta)\exp\left(\frac{-z}{d}\right) + \frac{z\cos(\theta)}{d^2}\exp\left(\frac{-z}{d}\right)\frac{\partial d}{\partial\theta}\right)^2 \sigma_\theta^2 \tag{2.31}$$

$$\frac{\sigma_I^2}{I^2} = \left(\frac{\sigma_{I_0}}{I_0}\right)^2 + \frac{1}{\cos^2(\theta)}\left(\sin(\theta) + \frac{z\cos(\theta)}{d^2}\frac{\partial d}{\partial\theta}\right) \tag{2.32}$$

$$\frac{\sigma_I^2}{I^2} = \left(\frac{\sigma_{I_0}}{I_0}\right)^2 + \tan^2(\theta)\left(1 + \frac{4\pi z}{\lambda} n_{\mathbf{oil}}^2 \cos^2(\theta)\right)^2 \sigma_\theta^2 \tag{2.33}$$

This uses that

$$\frac{\partial d}{\partial\theta} = d\frac{n_{\mathbf{oil}}^2 \sin(\theta)\cos(\theta)}{\sqrt{n_{\mathbf{oil}}^2 \sin^2(\theta) - n_{\mathbf{sample}}^2}} \tag{2.34}$$

$$\frac{\partial d}{\partial\theta} = d^2 n_{\mathbf{oil}}^2 \sin(\theta)\cos(\theta)\frac{4\pi}{\lambda} \tag{2.35}$$

Fitting Errors

Fitting errors are estimated by the following approach[108]. With ν degrees of freedom, the standard deviation of the residuals R is found as:

$$\text{SDR} = \sqrt{(R^2/\nu)} \tag{2.36}$$

The residuals are the difference between the fitting function F and the observed data O. These are the fitted intensity profile and the observed intensity profile such as that in Figure 2.15.

$$R = \sum_n F_n - O_n \tag{2.37}$$

The Jacobian $\mathbf{J}$ of the fitting function F is then estimated as a function of the estimated values. Then, the parameter standard errors about these estimates are found by the covariance matrix:

$$\Sigma = \mathrm{SDR}^2(\mathbf{J}^T\mathbf{J})^{-1}. \tag{2.38}$$

through which I identify the standard error estimates σ of the parameters as the diagonal elements of Σ:

$$\sigma = \sqrt{\mathrm{diag}(\Sigma)} \tag{2.39}$$

2.7 Chapter Summary

- Discussed the principles underlying single molecule fluorescence microscopy.
- Outlined the imaging protocols and experimental assays in fluorescence microscopy.
- Outlined the methods to calibrate single molecule microscopy by:
  - the effect of imaging conditions on excitation mode; from EPI to TIR.
  - a stoichiometric calibration of imaging conditions on observed single GFP molecules.
  - detailing the source of experimental artefacts and noise.
- Detailed how errors would propagate forward into later experimental chapters.

Chapter 3

Bayesian Inference for Single Particle Tracking

Abstract

Fluorescence microscopy is a powerful technique for investigating biological processes in cell membranes. Assays such as fluorescence recovery after photo-bleaching can obtain population level measurements of protein mobility, but in averaging over multiple molecules important stochastic dynamics over small time and length scales are hidden. At the single particle level, the behaviour of individual tracks may capture these features. Previous investigations have found several modes that deviate from simple Brownian motion including confinement effects, directed motion and anomalous diffusion. Diffusion analysis is generally performed using the mean-squared displacement of tracked particles. However, these heuristic measures rely on long, well sampled tracks. Due to complicating photo-physics and optics of these experiments in living cells only short tracks are typically obtained, and stochastic effects become dominant. Presented here is a novel application of a Bayesian ranking method that discriminates between different diffusive modes. I find that it is capable of working on short fluorescent tracks both from realistic simulated trajectories and experimental fluorescent protein fusion data from bacteria, and can discriminate probabilistically

between anomalous, Brownian, confined and directed modes, and sub-populations within. The framework established can be generalised and further used to capture transitory or mode switching behaviour.

3.1 Introduction

In this chapter, I introduce the fundamentals of Bayesian Inference and outline the development of a statistical scheme that I have used in subsequent chapters to infer the diffusive behaviour of single particle tracks. This work is detailed in [1]. This chapter is the most theoretical of this thesis but most of the models are taken from appropriate references. As this Chapter is largely on model selection, I first provide an outline of the differing types of diffusion models. This is then followed by the principles of Bayesian statistical inference. Bayesian techniques and specifically model selection approaches are not widely applied in the Biophysics field, except until very recently [109]. The intention of this Chapter is to present an inference scheme that can separate the diffusive modes of individual trajectories without population averaging in a quantitative, probabilistic fashion. This is achieved under conditions imposed by real experimental data. This is done using the core of Bayesian principles, incorporating *a priori* knowledge, where our priors are based on simulation and real *in vivo* experimental work. In the subsequent chapters, I then demonstrate its utility to challenging, noisy live cell data by applying the scheme to *in vivo* data.

Several methods have been tried for characterising diffusion in the membrane in addition to standard Saffman-Delbrück modelling[9]. This has been demonstrated in simple lipid mixtures [110] but *in vivo* many exceptions have been found [17, 111, 112]. The most common metric to measure the spatial extent of random motion is the mean-squared displacement (MSD). The MSD measures the second moment of the underlying probability density function (PDF). The PDF is the underlying distribution describing the probability of a particular displacement over a time t. A common implementation of the MSD in model selection has been to measure the ratio of the measured mean-squared deviation (MSD) with that expected from simple Brownian motion. This defines

the relative deviation parameter [93]. In general, most commonly applied techniques use some form of analysis that is derived from the mean-squared displacement [113, 114]. This is usually smoothed by plotting against the time-interval (or time-lag) τ rather than the absolute time t. This denotes a temporal averaging. It works by averaging over all displacements over a certain time-lag over the duration of the signal. When the relative deviation was first used, Kusumi *et al.* identified three principle diffusive modes. These were directed, confined and Brownian diffusion. Brownian motion represents simple diffusion and is the simplest mode characterized by a linear relation between the MSD $\langle X^2 \rangle$ and t (Figure 3.1) However, a tracked protein trajectory for which the MSD reaches a plateau at high t is indicative of confined diffusion suggesting that the protein is being trapped by its local environment. Such corrals have been hypothesised as being important in forming nanometre length scale reaction chambers, thereby greatly enhancing the chemical efficiency [10][115][93][116][48]. Directed motion has a typically upward parabolic MSD function versus t and is seen, for example, during active diffusive processes such as those which occur when molecular motors migrate along microtubules [117]. Since then, another major category of diffusion has been identified: *anomalous diffusion*. This final class of diffusion has many examples in biology and particularly in the crowded membrane environment, is often observed as being sub-diffusive [118]. This motion is modelled with an MSD being proportional to t^{α} where α is a coefficient between 0 and 1. This mode may represent the percolation of a protein through the disordered media of the membrane, hopping across corrals or interactions with specialized domains [119, 112, 120, 35]. Together, these four principal different diffusive modes are illustrated schematically in Figure 3.1, plotting idealised time-averaged mean-squared displacement (TAMSD) versus time interval τ [93]. However, analysis approaches are weak on several levels when applied to tracks generated from fluorescent protein tagged molecular complexes *in vivo*. Firstly, experiments such as TIRFM are typically data-rich in the number of tracks, but trajectories are determined from a low signal-to-noise ratio environment. Under these conditions, only tracks of short duration are able to be measured due primarily to the poor photophysics of the fluorophore resulting in scant, imprecise MSD information at high values of τ [121]. This creates data traces of typically spanning

only decade, usually around 10-30 data points at 40 ms video rate imaging. Longer tracks are recorded, but these are typically non-representative as they are much more likely to be confined or immobile proteins where the tracking algorithm can follow. Often, interpreting MSD traces for model selection is highly reliant upon an accurate measurement of the diffusion coefficient, which in the noisy, heterogeneous environment of the cell membrane may prove challenging. Secondly, trajectories are stochastic in nature, implying significant deviations from the idealised graphs in Figure 3.1. Third, multiple dynamical processes may be occurring through interactions with the surrounding environment creating a highly heterogeneous environment, imparting a signature onto the MSD traces that is unaccounted for in the four simple principle families of models presented.

An appeal of MSD analysis lies in its relative simplicity to address semi-quantitative questions concerning the membrane environment, for example effects of molecular crowding or confinement [20, 123]. However, as Figure 3.1 illustrates there is a representative statistical spread of the MSD traces for pure Brownian diffusion which could be erroneously interpreted as a different diffusive behaviour judged by any individual MSD curve from a single particle trajectory [122]. Population averaging can smooth out such variation to obtain average behaviour, but at the expense of being able to interpret individual tracks, and thereby view the heterogeneity in the data. Some recent improvement to MSD analysis have involved applications of the propagators directly, used in estimating cumulative probability distributions to substantiate the presence of different non-Brownian diffusive modes [112, 124, 125, 126].

Further complications arise when considering whether there is some redundancy in the models. Different stochastic generators may have similar moments for given parameters, meaning that the MSD traces cannot by themselves separate different families. This is exemplified by the variety of sources for anomalous diffusion. Anomalous diffusion emerges with a 'fractional' treatment of the diffusion equation, and can arise through temporal trapping (time-fractional), or spatial heterogeneity (space fractional), such as due to transient trapping or molecular crowding [120]. Three types of propagators have been considered in recent literature - continuous time random walks

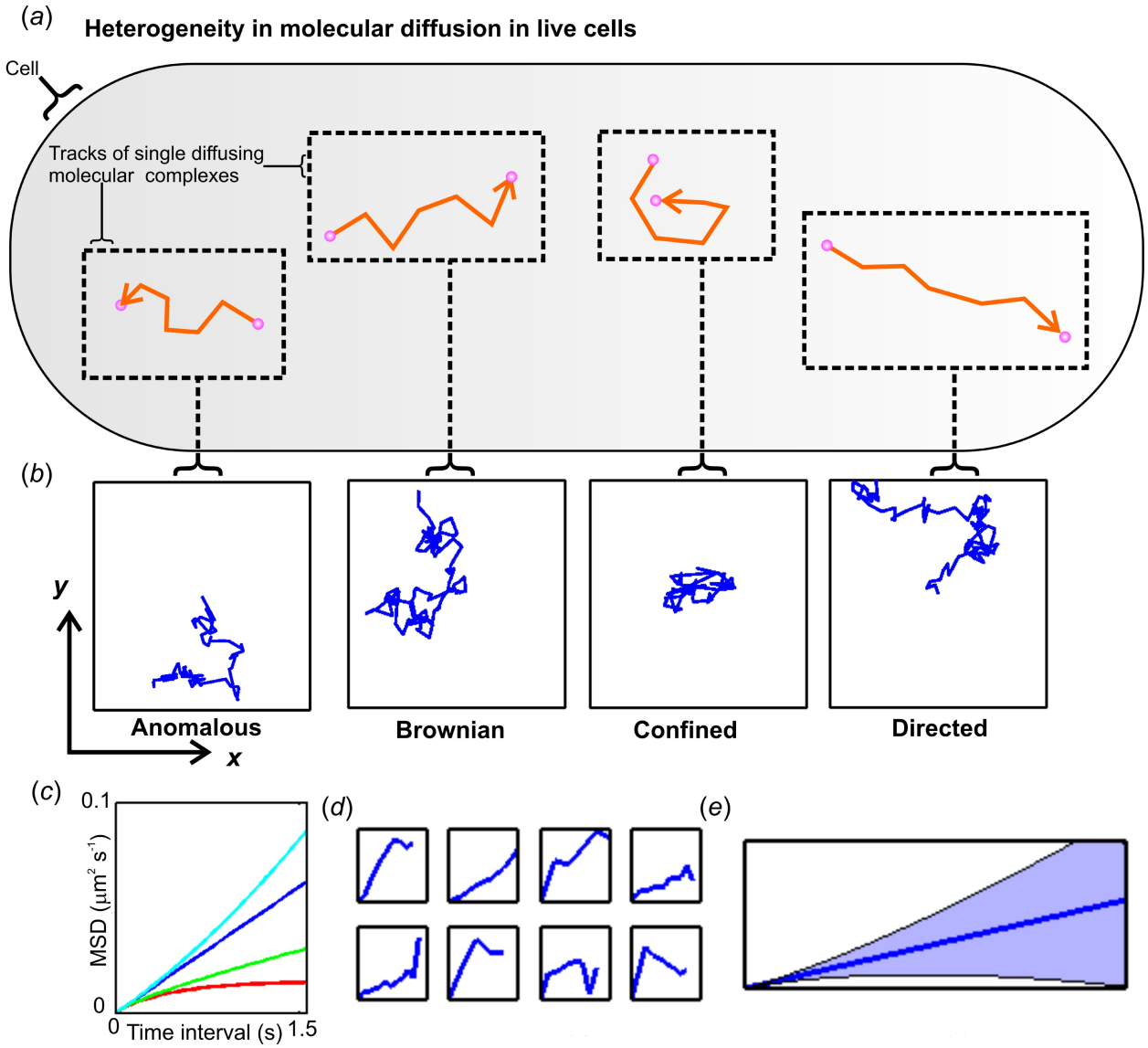


Figure 3.1: *The complexity of molecular diffusion in living cells. (a), Schematic of diffusion (orange track) of a single molecule or complex (pink circle) in a live cell with (b) simulated data for the typical spatial localizations of tracked molecules in the specimen xy plane of a typical optical microscope illustrating four common modes of diffusion. (c) Idealized forms of mean-squared displacement (MSD) relations for anomalous (green), Brownian (blue), confined (red) and directed (cyan) diffusion. (d) Experimental traces of a real data-set with different stoichiometries of the Tat dataset analysed in chapter 5. Tracks are sampled at 40*ms *video rate imaging, with typically 5-15 data points. (e) the mean average of many simulated MSD relations (blue line), blue shading indicating the stochastic spread at one standard deviation, illustrating the marked heterogeneity due just to stochastic dispersion [122].*

(CTRW), fractional Brownian motion (FBM) and percolation propagators [127]. When considering these models, there are statistical caveats that arise through the method in which these are data smoothed or averaged, such as in with the time-averaged MSD (§3.1.1.2). This naturally further complicates interpreting SPT tracks. The difficulty in interpreting heterogeneous data sets can potentially therefore be ascribed to four different sources of variation:

1. Experimental limitations; the unavoidable statistical scatter due to a finite time-series. SPT methods in non-perturbing *in vivo* systems typically suffer from limited long, well-sampled data traces.

2. Biological complexity; the unquantified biological heterogeneity of the protein environment. SPT traces *in vivo* are exposed to a much more complicated, heterogeneous environment, relative to model systems.

3. Statistical methodology; the statistical operations that combine the ensemble or smooth individual SPT traces. The smoothing operations may influence model interpretation.

4. Model redundancy; metrics such as the MSD may have similar profiles under given parameters.

In the following sections, I discuss the modelling approaches that have been used to describe the array of putative environments that have described biological membrane environments. I discuss the different origins of anomalous diffusion, and go through the basic derivations of the origins of the transport equations. Finally, I outline the statistical methods previously applied to biological SPT data.

3.1.0.1 Observations and Models of Anomalous Diffusion in the Biological Membrane

Membrane proteins are embedded in a highly crowded, dynamic environment. This has significant consequences for the transport dynamics. There is also an underlying substructure; a lateral phase separation or other mechanisms that organises lipids into micro-domains. The observation of a substantial reduction of lateral protein diffusivity through multiple experiments has been observed

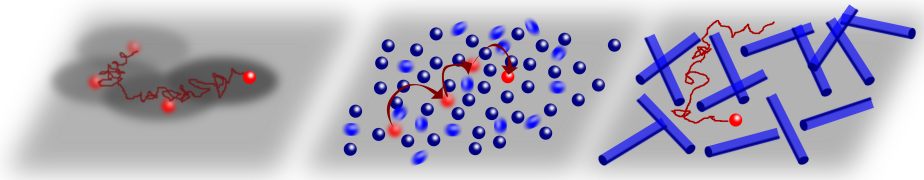


Figure 3.2: *Three scenarios depicting origins of subdiffusion. Left: The tracer particle is 'raft' bound. As the particle diffuses, the preferential association with a lipid patch, which also diffuses, may introduce correlations such as in FBM. Middle: A random walk in a dynamic environment. The tracer particle experiences transient traps with a lifetime diverging with density. This may be modelled as a CTRW with power-law distributed waiting times. Right: A Random walk with static obstacles such as the cytoskeleton, or protein anchors. This may be modelled by a random walk on a percolation cluster.*

in SPT[125], FCS [128] and FRAP[83]. The typical conclusion of these experiments is that many of these proteins are undergoing a form of anomalous transport. There have been several microscopic models for anomalous subdiffusion, each of which have been studied intensively. Obstructed or percolation models, fractional Brownian motion and continuous time random walks are candidate models however there is no consensus on which of these models explains observed subdiffusion.

I review each of these models in turn. The discussion is far from in-depth, and is only done to outline the variety of models describing anomalous membrane diffusion, emphasising the experimental and analytical implications. They are included only to convey the rich array of modelling present in anomalous diffusion and provide the motivation to why researchers are interested in it, and why identifying anomalous diffusion is important.

Putative biological origins of anomalous diffusion are depicted in Figure 3.2. At present, a great many researchers are investigating the different underlying propagators of anomalous or confined diffusion [129, 130, 127, 131, 132, 133, 134, 125, 135, 136]. A common theme in their research is to establish a relation between diffusion profiles and the underlying membrane substrate or the dynamics of protein or lipid complexes [137, 52, 130, 138, 139, 140, 32]. These vary from controlled *in vitro* experiments [127, 141, 142] to noisy *in vivo* experiments [143, 144, 145]. These include both membrane integrated complexes and cytoplasmic constituents, which exhibits a similar crowded environment as the membrane. These different arrays of models have different biological

interpretations. Subdiffusion has been identified as the result of the fraction of mobile/immobile protein [65], the coupling to the cytoskeleton in near-critical phase separation[68], and mobile membrane patches in lipid-raft riding proteins [35] among other phenomena.

The underlying PDF describing the diffusion of proteins *in vivo* has substantial implications for the reaction-kinetics of the system. Many modellers in systems biology experiment with different kinetics mechanisms to investigate the effect upon cellular chemistry [35, 146, 147, 148, 149, 150, 36]. There are many factors involved here when modelling membrane-bound chemistry; ranging from the (fractional) reaction-kinetics to ensuring the robustness of protein-protein interactions in the crowded membrane environment. How, for example, does a protein find its target given the relatively low number of interaction pairs (considering all the other proteins on the cell) [20, 151] . How have proteins evolved to interact in this environment; balancing interacting protein-protein 'stickiness' with the associated penalty of promiscuous interactions? [62].

3.1.0.2 Obstructed Percolating Diffusion

Spatial inhomogeneities have been suggested to induce subdiffusion. Michael Saxton began the first computational investigations into anomalous diffusion due to crowding, looking at the microscopic origins of anomalous diffusion by modelling diffusion of tracer particles with mobile and immobile obstacles [119] [22], exemplified by de Gennes' 'ant in a labyrinth' [152] [1]. This toy model demonstrated how an ant (i.e. a protein) can navigate the labyrinth (the membrane) by randomly walking in any direction. As the density of objects increases, there were fewer routes to and from a target. Saxton uses this lattice based model to simulate obstructed membrane diffusion and uses the MSD to report on the diffusion properties. Supported by earlier theoretical work he identifies two key transition points. The first is a crossover time between normal and anomalous diffusion for obstructed diffusion [22, 23]. As the timescale of observation increases, anomalous diffusion manifests as reduced rate normal diffusion. The second is a percolation threshold. As the static object density approaches the percolation threshold, the crossover time diverges due to long

[1] http://www.larecherche.fr/content/recherche/article?id=14386 (French language article)

range percolation stopping. This prevents global diffusion of tracer particles [36], locally confining particles. Saxton also studied percolation near this threshold. Under these circumstances, the lattice forms a 'fractal'[153]. These have been explored in model membrane [154] in single molecule level experiments.

For the simple square lattice treatment this percolation threshold is predicted to occur at a unitless density of around 70 %. This is with immobile obstacles. By comparison the biological membrane has $\approx$ 25,000 mobile and immobile proteins per μm^2, with a global area occupancy of around 35%[155]. However, there may be regions of the membrane that have substantially higher protein concentration [156].

The percolation propagator deviates from the Gaussian propagator scales as a stretched Gaussian [157, 158]:

$$W(x,t) \sim \frac{x}{t^{\alpha/2}} \exp(-\frac{x}{t^{\alpha/2}}) \tag{3.1}$$

This stretched Gaussian propagator yeilds a subdiffusive ($\alpha < 1$) mean-squared displacement that scales as $< X^2 > \ t^{\alpha}$. On inspection, as the diffusion becomes less subdiffusive ($\alpha \to 1^-$), normal Brownian motion is restored. The effect of this distrbution as the propagator is to draw out the tails of the Gaussian.

3.1.0.3 Continuous Time Random Walks

The second mechanism that may generate biological observed anomalous subdiffusion is through continuous time random walks. This is a dynamic model compared to the static assumptions in a percolation model. A candidate biological model of this is as follows. In the membrane or cytoplasm, there may be binding sites. When binding sites are present, they induce transient anomalous diffusion by transiently immobilising a tracer particle [22]. A particle has a waiting time related to the energy of the trap, with an escape time given by a Boltzmann factor $\exp(-\Delta E/k_B T)$, where ΔE is the binding energy, and $k_B T$ the thermal energy. In the CTRW formulation a particle

undergoes a jump-wait process; the particle takes a diffusion step (the jump) L, from a jump distribution, then has a waiting time before the next jump governed by a waiting time distribution τ. Assuming the jump length and waiting time are independent (and separable) are drawn from the PDF $\psi(x,t) = w(t)\lambda(x)$ then I have the jump length PDF given by [120][159][160]:

$$\lambda(x) = \int_0^x \psi(x,t)dt \tag{3.2}$$

with a waiting time governed by the PDF:

$$w(t) = \int_{-\infty}^{\infty} \psi(x,t)dx \tag{3.3}$$

To relate this to a biological example, these trapping times relate to dissociation times in chemical binding interactions, or transient cages in crowded environments. A power law waiting time may produce subdiffusion, provided the sampling time was sufficient. When the expectation of the waiting time is divergent (i.e. 'infinite'), particles will always exhibit anomalous signatures irrespective of the experimental time-scale. In contrast, the crossover time observed in obstructed diffusion will interpolate between subdiffusion to Brownian motion. If $\langle\tau\rangle$ is finite, then a cross-over time is again expected. This leads to a time-dependency of the observed variables such as α, the measured subdiffusive coefficient in the mean-squared deviation, where they gradually increase to $\alpha = 1$. This aging process means that a CTRW model is *non-ergodic*; the *ensemble* of experimental data does not match the *time-averaged* experimental data. This is an important caveat of analysis and discussed further in §3.1.1.2 as this property has been used to distinguish between different models of subdiffusion.

This relationship of interactions with binding-trap sites, and subdiffusive behaviour, was demonstrated experimentally in reference [161], where they found that ATP depletion reduced the anomalous behaviour of Cajal bodies. Cajal bodies are small organelles between 0.3-1.0 μm in diameter found in the nucleus of proliferative cells. They alternate in between association with chromatin and diffusion in the interchromatin space. Saxtons model of this [22] was that the ATP depletion allowed

the Cajal bodies to equilibrate with the binding sites, thereby reducing the subdiffusive behaviour.

3.1.0.4 Fractional Brownian Motion

Fractional Brownian motion was introduced to take into account the correlations observed in random walks [162]. For negatively correlated FBM, a particle would tend to move in the opposite direction after moving forward. This results in subdiffusive behaviour. More formaly, the tracer particle has a memory effect such that the state of the system at time t is related to the state of the system at time t', where $t' < t$. In FBM this is modelled by changing Gaussian noise $dB(t)$ to fractional Gaussian noise B_H.

To see how displacement changes with time, the autocorrelation function for FBM in 1D is:

$$\langle X^H(t_1)X^H(t_2)\rangle = \frac{K_1}{2}\left(t_1^{2H} + t_2^{2H} - |t_1 - t_2|^{2H}\right). \tag{3.4}$$

The parameter H is the Hurst exponent, and related to the anomalous sub-diffusion exponent α by $\alpha = 2H$. The motion is negatively correlated if $H < 1/2$, and positively correlated if $H > 0.5$. Standard Brownian motion is recovered at $H = 0.5$, where motion is uncorrelated [129, 163, 164, 22] An example of the biological origins of FBM is, for example, particles that are raft-bound have correlations in the random walk introduced through the diffusion of the raft. Similarly, FBM may arise when tracer particles diffuse in crowded environments for example with diffusion through narrow pores where the diffusion profile would become one-dimensional or single-file for large patches or complexes. FBM has been proposed to underlie the diffusion in crowded environments in experiments such as Fluorescence Correlation Spectroscopy (FCS) on lipid mixtures [127]. To contrast with CTRWs, the authors discriminated between CTRW and FBM by noting that their observations of α were constant with no time-variation. FBM would have a time-dependence on the measurement, and a subdiffusive process would only appear when correlations are present over that time-scale.

3.1.1 Statistical approaches to discriminate competing models

In the following section, I discuss the statistical properties that allow for model selection in single particle tracking. I discuss how deviations in the mean-squared displacement can be used in model selection including the models on the predicted statistical variation of the MSD. I also discuss how other statistical properties such as ergodicity of the tracks has been used in separating out differing models of subdiffusion.

3.1.1.1 Existing model selection method

As referred to in the introduction, Kusumi [93] uses a relative deviation parameter to characterise the mode of diffusion in tandem with simulations. Here, a relative deviation parameter defined as:

$$RD = \frac{MSD(n, \delta t)}{4Dn\delta t} \tag{3.5}$$

is used to characterise diffusive behaviour of *in vivo* through simulated determined pre-defined thresholds. This was not applied to subdiffusion where it is less clear how this method could be extended to discriminate subdiffusive processes. More recent methods include the cumulative distribution function (CDF) [112, 154] to discriminate between normal and anomalous diffusion. In later work, in order to address the same issues raised in reference [165], the authors develop a mean-maximal excursion method to analyse single particle tracks. This uses higher moments of the underlying probability distribution beyond the MSD, which they argue is a better discriminant of the anomalous coefficient. Various other methods include, including velocity correlation functions [166, 133], p-variation tests [163, 167], spatial-averaging algorithms [168] and first-passage observables [169, 153, 170].

In most of these cases, there is some aspect of statistical smoothing through averaging. There are two ways to combine data: through time-averaging or ensemble averaging, or both. Using the MSD as an example, the ensemble averaged mean-squared displacement (EAMSD) is given by the expectation of all traces, be they time-averaged or not and is denoted by:

$$\langle X^2(t)\rangle_{\text{ens}} = \frac{1}{N_{\text{ens}}} \sum_{\mathbf{i=1}}^{N_{\text{ens}}} X_i^2. \tag{3.6}$$

The time-averaged mean-squared displacement (TAMSD) function for a track of N consecutive image frames at a time interval δt [93] for a track in 2-dimensional space assuming a standard orthogonal xy coordinate system is given by:

$$\langle X^2(\tau)\rangle = \langle X^2(n\Delta t)\rangle = \frac{1}{N-1-n} \sum_{i=1}^{N-1-n} ([x(i\Delta t + n\Delta t) - x(i\Delta t)]^2 + [y(i\Delta t + n\Delta t) - y(i\Delta t)]^2). \tag{3.7}$$

In a thorough treatment of the statistical variation, reference [122] calculates the predicted statistical variation for a time-averaged MSD for a diffusion process. In reference [122], the assumption is of no localisation error. This chapter is developed around this assumption, although I discussed experimental errors in Chapter 2. The authors results are of practical importance in considering the dependence of statistical uncertainty upon the number of position measurements in time-averaged mean-squared displacements. I use these results in a subsequent section §3.3.1.

This statistical spread can be denoted by a standard deviation that is related to the diffusion coefficient. For a diffusion coefficient D and total track length t_n then σ at time t_i is given by Equation 3.8 [122, 171]. This statistical uncertainty is plotted in Figure 3.3.

$$\sigma(t_i) = \frac{D(t_i)}{\sqrt{t_n/t_i}} \tag{3.8}$$

3.1.1.2 Statistical properties: Ergodic and non-ergodic behaviour

In reference [172], the authors identify some of the statistical properties that can discriminate between competing models of anomalous diffusion. The researches establish the link between

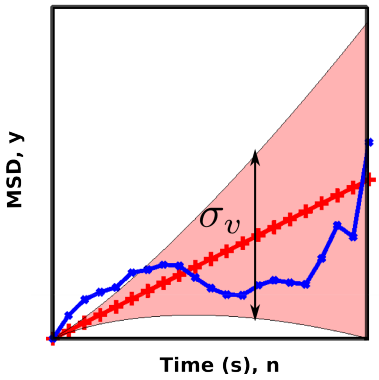


Figure 3.3: *Interpolation. The stochastic dispersion for a given model. The expected dispersion in the time-averaged MSD for a given track length N at sample point n is given by σ_v.*

non-ergodic behaviour and the underlying inhomogeneity. The standard approach in dealing with single particle tracking data is that the data are ergodic; time-averaging a long track of length T $\langle \delta X(t) \rangle_{\text{time}} = \langle \delta X(\tau) \rangle$ is the same as ensemble averaging $\overline{\langle \delta X \rangle}_{\text{ens}}$ such that for $T \ll \tau$:

$$\overline{\langle \delta X^2(t) \rangle} = \langle \delta X^2(\tau) \rangle \tag{3.9}$$

In references [172, 173, 133, 136], the authors demonstrate that there are models of anomalous diffusion that do not have this property. This has been successfully applied as a discriminatory test. This statistical artefact has been identified in observations of non-ergodic behaviour in both eukaryotic and model systems [125, 131]. Reference [125] demonstrated that both processes, ergodic and non-ergodic, may co-exist on the membrane. This suggested two different transport processes occurring for the Kv2.1 potassium channels in human embryonic kidney cells. They identify that the diffusion traces for the Kv2.1 potassium channels are non-ergodic, a property which allows them to distinguish between the subdiffusion models presented in §3.2.1. In the CTRW model, diffusion processes are anomalous and non-ergodic due to a heavy tailed waiting time. In a follow up paper, Weigel *et al.* [174] find these Kv2.1 domain sizes consistent with fluctuations in the trafficking machinery, as an example of how the diffusion profiles can be linked to the membrane architecture.

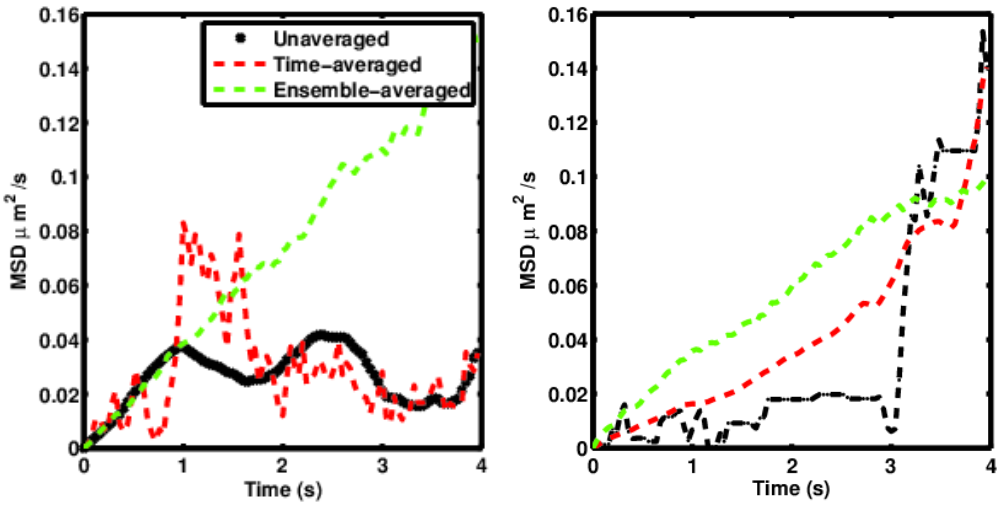


Figure 3.4: *Time-averaging of tracks in normal diffusion or the non-ergodic CTRW in the time-averaged mean-squared displacement of Equation 3.7. Left: A simulated particle with diffusion coefficient of* $D = 0.01\mu m^2/s$ *under a sampling time of* 0.04s. *Right: A CTRW model with anomalous coefficient* $\alpha = 0.8$, *using the simulation method in Reference [127]. In both cases, the ensemble is over a hundred identically simulated tracks using the un-averaged MSD.*

3.2 Theory

3.2.1 Biological Models of Diffusion

In the report here, four diffusive modes have been modelled. These are different solutions of the diffusion equation and the fractional diffusion equation. In each case, since the diffusion process is subject to boundary conditions, with possibly an advective component, they may also be solved to reflect confinement effects, and the effect of directed diffusion, respectively. In this section I present both the models of diffusion and the numerical methods in solving or simulating them.

Diffusion Equations

For a particle initially located at spatial point x, at time t, which is found at x' at the later time $t' = t + \delta t$, where δt is the sampling period, the two-dimensional diffusion-(advection) equation is given by:

$$\frac{\partial W}{\partial t} + v\nabla(W) = K_1\nabla^2 W(x' - x, t). \tag{3.10}$$

The time-fractional version, for anomalous sub-diffusion is:

$$\frac{\partial W}{\partial t} = D_t^{1-\alpha}\left[-v\nabla + K_\alpha\nabla^2\right] W(x' - x, t). \tag{3.11}$$

Here, $\mathbf{v}$ is the velocity flow vector in the case of directed diffusion, with corresponding speed v. Equation 3.11 introduces the fractional Riemann-Liouville operator ${}_0D_t^{1-\alpha}$ [120], defined in Equation A.3. The fundamental property of this function is the fractional order differential of a power. It reduces to 3.11 when $\alpha = 1$.

Propagators

A simple lattice based model is a simple way to introduce solve Brownian motion. Here, a test particle is on a 2D square lattice, with lattice constant δx, with discrete time steps of δt. Random directions are chosen. In one-dimension, the master equation is:

$$W_j(t + \delta t) = {}^1\!/_2 W_{j-1}(t) + {}^1\!/_2 W_{j+1}(t), \tag{3.12}$$

where the index j denotes the position in the underlying lattice. The prefactor ${}^1\!/_2$ denotes the probability of one specific direction being taken. In the continuum limit $\delta t \to 0$ and $\delta x \to 0$ and using the Taylor expansion:

$$W_j(t + \delta t) = W_j(t) + \delta t\frac{\partial W_j}{\partial t} + O([\delta t^2]) \tag{3.13}$$

and

$$W_{j\pm1}(t) = W(x, t) \pm \delta x\frac{\partial W}{\partial x} + \frac{(\delta x)^2}{2}\frac{\partial^2 W}{\partial x^2} + O([\delta x]^3) \tag{3.14}$$

lead to the diffusion equation:

$$\frac{\partial W}{\partial t} = D\frac{\partial^2}{\partial x^2}W(x,t). \tag{3.15}$$

The continuum limit is therefore established if the quantity:

$$D \equiv \lim_{\delta x \to 0, \delta t \to 0} \frac{(\delta x)^2}{2\delta t} \tag{3.16}$$

is finite. D here is the diffusion coefficient with dimensions of area over time: m^2/t.

The solution to this is the well known Gaussian propagator function [175]:

$$W(x,t) = \frac{1}{4\pi D t} \exp\left(-\frac{x^2}{4Dt}\right). \tag{3.17}$$

A similar approach can be taken to obtain a biased random walk - directed diffusion - with a velocity v and a time t giving:

$$W(X|D,v,t) = \frac{1}{4D\pi t} \exp(\frac{-|\mathbf{X}+\mathbf{v}t|^2}{4Dt}). \tag{3.18}$$

Anomalous diffusion has a far more complex analytical solution [176]. Here, I only implement a numerical solution. A numerical solution by solving the fractional diffusion equation on a square lattice is given by Equation 3.19[177]:

$$P(x,y,t) = \sum_{m}^{\infty}\sum_{n}^{\infty} E_\alpha(-\lambda_{nm}K_\alpha t^\alpha)\varphi_{nm}\alpha_{nm} \tag{3.19}$$

where $\lambda_{nm} = n^2\pi^2 + m^2\pi^2$ and α_{nm} are the Fourier coefficients of the initial condition as a point source $P(x_0, y_0, 0) = P_0$. E_α is the Mittag-Leffler function, which is defined as Equation A.5, with $\beta = 1$. The solution to this is depicted in Figure 3.5, showing the characteristic peaked PDF.

The final model of diffusion I use is confined diffusion. I do not use the confinement propagator for numerical reasons, discussed further in Future Work (§3.7). However, for completeness, it is given by 3.20 [178]. I do, however use the MSD relation given in the following subsequent section. Here, l

is the domain radius, $\tau = l^2/D$ and the α_{nm} is the mth zeros of the Bessel function of the first kind $J'_n(\alpha_{nm}) = 0$ of order n. Coordinates are given in cylindrical polars such that Equation 3.20 is the probability of displacement from $(\rho, \psi) \to (\rho', \psi')$ where ρ is the radius from the origin and ψ is the angle from the Cartesian y axis[179].

$$P(\mathbf{r}, \mathbf{r}', t) = \frac{1}{\pi l^2} + \frac{1}{\pi l^2} \sum_{n=-\infty}^{\infty} (n\psi - \psi') \sum_{m=1}^{\infty} \frac{\alpha_{nm}^2}{\alpha_{nm}^2 - n^2} \exp\left[-\alpha_{nm}^2 \frac{t}{\tau}\right] \frac{J_n(\alpha_{nm})(\rho/l) J_n(\alpha_{nm})(\rho/l)}{J_n(\alpha_{nm})^2} \tag{3.20}$$

MSD

I also show the expected MSDs of each of the four principal diffusion modes. I denote the expected MSDs as the expectation of the displacement X: $\langle X^2 \rangle$ at time t.

The MSDs for Brownian and directed motion are parametrised by velocity v, diffusion coefficient D. These have units of m/s and m^2/s respectively. The MSD is given by Equation 3.21:

$$\langle X^2 \rangle = 4Dt + (vt)^2. \tag{3.21}$$

Anomalous diffusion is parametrised by the fractional transport coefficient K_α and the anomalous coefficient α. The fractional transport coefficient has units of m^2/s^α, and the anomalous coefficient is unitless. The MSD for anomalous subdiffusion is given by [36] equation 3.22:

$$\langle X^2 \rangle = K \frac{t^\alpha}{\Gamma(1+\alpha)}. \tag{3.22}$$

Numerically, however, I will treat this equation with K having units of m^2/s and $\hat{K} = 1s^{1-\alpha}$ with the equivalent MSD given by:

$$\langle X^2 \rangle = K \frac{\hat{K}_\alpha t^\alpha}{\Gamma(1+\alpha)}. \tag{3.23}$$

The function $\Gamma(x)$ is known as the Gamma function, and is given in the Appendix (Equation A.4).

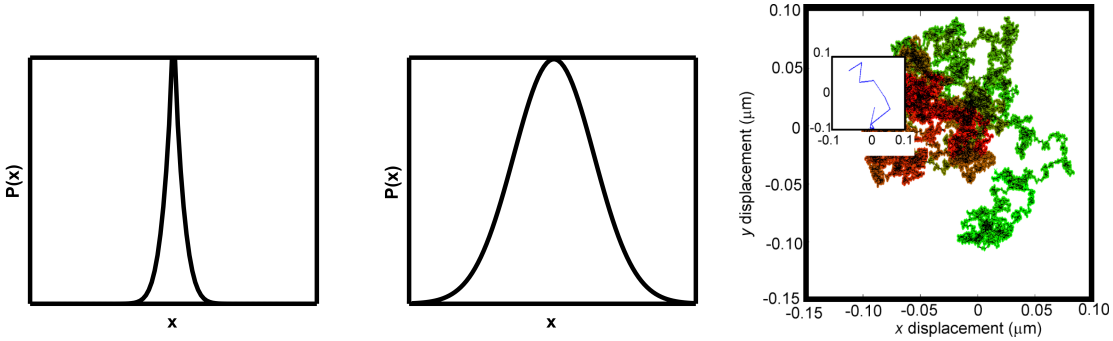


Figure 3.5: *Numerical simulations. Leftmost (a); a slice of the solution to the anomalous diffusion equation. Middle (b) ; Brownian. Rightmost (c): Simulated confined. The PDFs to these were detailed in §3.2.1 with a look up table given in Table 3.1. The numerical solution of a) is given by a rejection sampling algorithm of Equation 3.19. b) is calculated using standard libraries in* `MATLAB`*. c) The displacements in xy are of a highly sampled confined track with colouring added to indicate procession with time proceeding from red at the origin to light green. The inset shows the observed track with just $N = 10$ data points at video-rate sampling. Confinement radius $l = 0.1\mu m$.*

The final MSD used is for confined diffusion. This is solved in a circular domain with reflecting boundary conditions. Here, l is the domain radius, $\tau = l^2/D$ and the α_{nm} is the mth zeros of the Bessel function of the first kind $J'_n(\alpha_{nm}) = 0$ of order n [179]. The confined MSD is given by 3.24:

$$\langle X^2 \rangle = l^2 \left(1 - 8 \sum_{m=1}^{\infty} \exp \left[\alpha_{lm}^2 \frac{t}{\tau} \right] \frac{1}{\alpha_{lm}^2 (\alpha_{lm}^2 - 1)} \right). \tag{3.24}$$

Table 3.1: *Equations of numerical solutions to Equations 3.10 & 3.11*

Mode	**Propagator**	MSD time-relation	MSD	PDF
Brownian/Directed	Exact Standard Gaussian	Linear with time	3.21	3.18
Confined	Exact Series solution	Asymptotic with time	3.24	3.20
Anomalous	Numerical solution	sub-linear with time	3.23	3.19

Two-dimensional synthetic tracks for use in validation were generated by a stochastic random walk process, generated in MATLAB (The MathWorks, Natick, MA). This algorithm modelled the stochastic differential equation given by Equation 3.25:

$$dX = F(X,t)dt + \sqrt{2D}dW(t). \tag{3.25}$$

Here, X is particle displacement for a given spatial dimension as a function of time t, F represents drift and dW represents an zero mean additive Gaussian process (a Wiener process). Following an incremental sampling time, X changes its amount by a value δX which is normally distributed such that $\langle \delta X \rangle \sim \mathcal{N}[F\delta t, 2D]$.

I generated these steps with a small ($\ll \delta t$) time-step, where δt is the intended simulated video-rate sampling time, and repeated for a number of steps proportional to the simulated track length is. I then sample from these time-steps such that they were equivalent to 40 ms sampling time. For confined tracks, I simulated a repelling function at the boundary, such that when the particle left the confinement radius then $F(X) \propto -\mathbf{sign}((\mathbf{r}))$. I plot examples of these in Figure 3.5.

3.2.2 The Principles of Bayesian Statistical Inference

I now discuss the theoretical underpinnings of the statistical machinery that I use in this chapter. The inferential techniques I use are derived from are Bayesian in nature. These are statistical techniques underpinned by Bayes' Theorem. Bayes' Theorem codifies the strength of belief of a *proposition* in a probabilistic framework. These underpin the priors that drive Bayesian statistical methods. The following derivation of how Bayesian model selection is used comes principally from reference [180].

The proof of this emerges from the definition of conditional probabilities. The probability of two events A and B happening, $P(A \bigcap B)$, is the probability of A multiplied by the probability of B given that A has occurred:

$$\begin{aligned} P(A \bigcap B) &= P(A|B)P(B) \\ P(B \bigcap A) &= P(B|A)P(A). \end{aligned} \tag{3.26}$$

Equating the two yields:

$$P(B)P(A|B) = P(A)P(B|A) \tag{3.27}$$

Therefore leading to the eponymous Bayes' Theorem:

$$P(A|B) = \frac{P(B|A)P(A)}{P(B)}. \tag{3.28}$$

This theorem is used in the following sections to develop a model selection technique. Model selection is a complicated task because it is not possible to simply choose the model that fits the data best. More complex models will generally fit data better. However, this may lead to implausibly overparameterised models when ranking by the maximum likelihood model choice. In statistical inference, there are two principal stages. The first stage is parameter inference (§3.2.2.2). The second stage is model inference or ranking. (§3.2.2.3).

3.2.2.1 Concepts in Bayesian Statistical Inference

In Bayesian inference, a model is defined as a collection of probability distributions. These are a prior on the model and a set of conditional probabilities. A prior distribution is formed from priors over the model parameters $\mathbf{w}$ as $P(\mathbf{w}, \mathcal{M}_i)$ and the set of conditional distributions $P(\mathcal{D}|\mathbf{w}, \mathcal{M}_i)$ that the model makes on the data D. This is the likelihood. It is given by the probability of the data given a model $\mathcal{M}$ and the set of parameters $\mathbf{w}$ which define it. It is often denoted by $\mathcal{L}$. I use a bold $\mathbf{w}$ to depict that w will in general be a vector; i.e. multiple parameters. The posterior distribution is the probability distribution of a particular set of a parameters w that are used by model $\mathcal{M}_i$ given the data $\mathcal{D}$. The posterior is so named because it is calculated after (i.e. *post*) considering the data. It is referred to as the updating of a prior belief after considering the data. This is summarised in Figure 3.6. These concepts are used in the following sections.

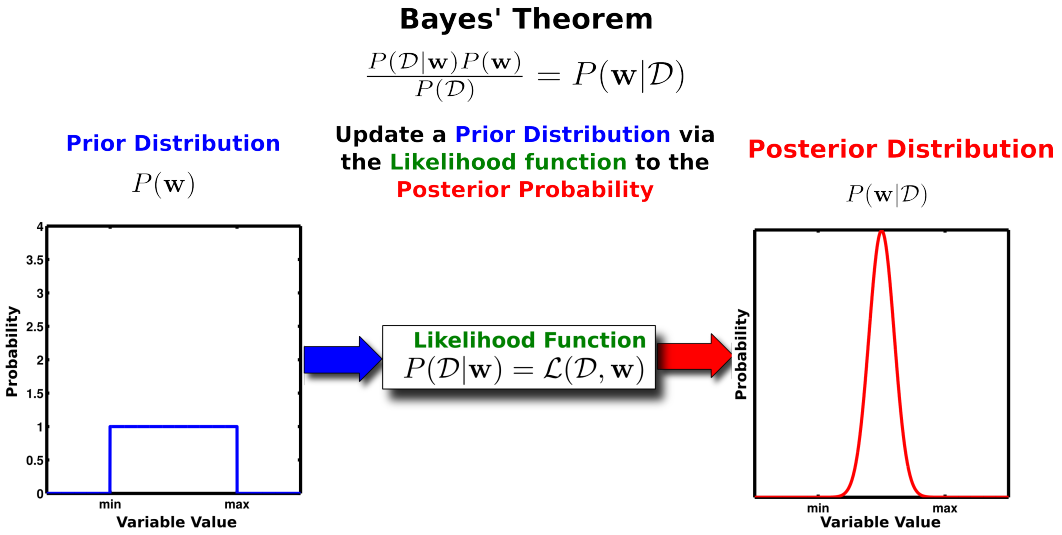


Figure 3.6: *Schematic representation of Bayesian Inference. A posterior distribution $P(\mathbf{w}|\mathcal{D})$ is defined as the product of the likelihood $P(\mathcal{D}|\mathbf{w})$ with the prior distribution $P(\mathbf{w})$, divided by the evidence $P(\mathcal{D})$. Bayesian inference updates a prior with data $\mathcal{D}$.*

3.2.2.2 Model fitting

In the first stage of statistical inference, I infer the parameters of individual models. For a model or hypothesis $\mathcal{M}$ and data $\mathcal{D}$ I have the posterior distribution of parameters $\mathbf{w}$ in Equation 3.29:

$$\overbrace{P(\mathbf{w}|\mathcal{D},\mathcal{M})}^{\text{Posterior}} = \frac{\overbrace{P(\mathcal{D}|\mathbf{w},\mathcal{M})}^{\text{Likelihood}} \overbrace{P(\mathbf{w}|\mathcal{M})}^{\text{Parameter Prior}}}{\underbrace{P(\mathcal{D}|\mathcal{M})}_{\text{Evidence}}}. \tag{3.29}$$

This produces the posterior distribution of model $\mathcal{M}_i$. Although summary parameters of the posterior (such as the mean or mode) may be used to describe the distribution, they have no fundamental status in Bayesian inference; the distribution *is* the result. This is a key difference to the frequentist framework, where a single 'true' parameter is assumed.

3.2.2.3 Model Comparison

Statistical model selection is comprised of two factors; the 'goodness of fit' or predictive value of the model and the plausibility of the model complexity. By evaluating the posterior probability of each

model, Bayesian model selection quantitatively handles model selection. The posterior distribution is given by Equation 3.30:

$$P(\mathcal{M}_i|\mathcal{D}) = \frac{\overbrace{P(\mathcal{D}|\mathcal{M}_i)}^{\text{Model Evidence}} \overbrace{P(\mathcal{M}_i)}^{\text{Model prior}}}{\sum_i P(\mathcal{D}|\mathcal{M}_i)P(\mathcal{M}_i)}. \tag{3.30}$$

The Evidence term, sometimes denoted by E is more formally known as the marginal likelihood. This is found by integrating the data over the entire parameter space and is calculated by Equation 3.31:

$$E = P(\mathcal{D}|\mathcal{M}_i) = \int P(\mathbf{w}|\mathcal{M}_i)d\mathbf{w}. \tag{3.31}$$

Given equal model prior weights, I rank models by simply ranking the model Evidence in Equation 3.30. However, in the general case, the relative model probability is given by Equation 3.32:

$$P(\mathcal{M}) = \frac{\overbrace{P(\mathcal{D}|\mathcal{M}_i)}^{\text{Model Evidence}} \overbrace{P(\mathcal{M}_i)}^{\text{Model Prior}}}{\underbrace{\sum_i P(\mathcal{M}_i)P(\mathcal{D}|\mathcal{M}_i)}_{\text{Model normalisation}}}. \tag{3.32}$$

In model fitting, an important caveat needs to be made with respect to the probabilistic outcome of model ranking. The probabilistic outcome of the model ranking approach should by no means be treated as an *absolute* probability. In other words, it can only be interpreted as the probability of the model *in the context of other models* considered, i.e. the model probabilities are *relative* only to the set of models that are tested. Models are approximations; given the scale of heterogeneity in the biological membrane a model selection approach must be open-ended. Models must be refined as the data suggest. This is exemplified by, for example, when I consider clustering; how many clusters fit the distributions of parameters and thereby the number of sub-populations (§3.3.5.2).

3.2.2.4 Bayesian inference as an 'Occam's Razor'

Consider a set of data generated by an experiment. There are two or more proposed physical models to describe the underlying process. One is a well established model. The other is an alternative, more complex model.

$$\frac{P(\mathcal{M}_1|\mathcal{D})}{P(\mathcal{M}_2|\mathcal{D})} = \frac{P(\mathcal{M}_1)P(\mathcal{D}|\mathcal{M}_1)}{P(\mathcal{M}_2)P(\mathcal{D}|\mathcal{M}_2)}. \tag{3.33}$$

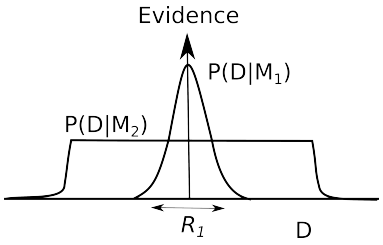


Figure 3.7: *Bayesian model comparison. The horizontal axis represents all possible data sets that models $\mathcal{M}_1$ and $\mathcal{M}_2$ are valid over. Applying these models to data $\mathcal{D}$ yields a normalised conditioned probability; $P(\mathcal{D}|\mathcal{M}_i)$, also known as the evidence. $\mathcal{M}_1$ is the simpler model of the two whereas $\mathcal{M}_2$ is a more complex model with more free parameters, but can correspondingly be applied to a wider range of data. For data that falls into the range R, I see that $\mathcal{M}_1$ has greater explanatory value and, priors being equal, this model is the more probable model.*

To see how Bayesian model selection acts as a 'Bayesian Occam Razor', I consider the model evidence:

$$P(D|\mathcal{M}_i) = \int P(D|\mathbf{w}, \mathcal{M}_i)P(\mathbf{w}|\mathcal{M}_i)d\mathbf{w} \tag{3.34}$$

If I make the assumption that the posterior distribution is well represented by a multivariate Gaussian (often true, but not always a good approximation) with a strongly peaked posterior at the most probable (peak) parameters $\mathbf{w}_{\mathrm{MP}}$ then I can approximate the posterior distribution by Laplace's method (see §A.3.2). In the 1D case, for example this is a Gaussian with a peak at $\mathbf{w}_{\mathrm{MP}}$:

$$\overbrace{P(D|\mathcal{M}_i)}^{\text{Evidence}} \approx \overbrace{P(D|\mathbf{w}_{\mathrm{MP}}, \mathcal{M}_i)}^{\text{Best fit likelihood}} \overbrace{P(\mathbf{w}_{\mathrm{MP}}, \mathcal{M}_i)\sigma_{w|D}}^{\text{Occam Factor}} \tag{3.35}$$

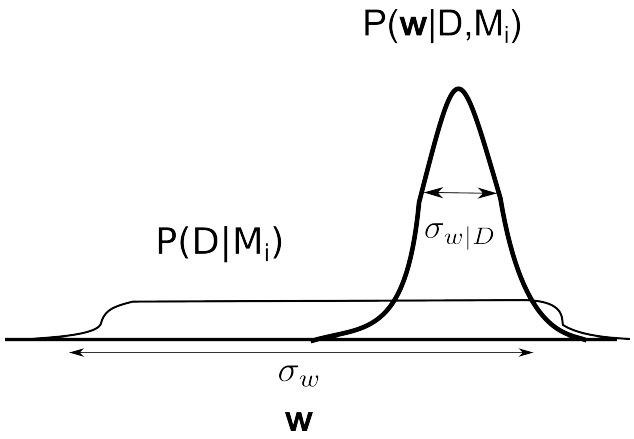


Figure 3.8: *Bayesian Occam Razor. The Occam factor $\sigma_{w|D}/\sigma_w$ has magnitude less than one. This acts as a penalty term to the model M_i.*

In this formulation, the Evidence is then comprised of two terms. The first is the best fit likelihood that the model can achieve, namely the value of the likelihood at the peak. The second term is a function of the width of this peak. The factor $\sigma_{w|D}$ is the posterior uncertainty in w, and $P(w_{\mathrm{MP}}|\mathcal{M}_i)$ is again the parameter prior. This is depicted in Figure 3.8. The Occam factor in Equation 3.35 has a magnitude less than one and acts as a penalty term for the model complexity. To see this, suppose that $P(w_{\mathrm{MP}}|\mathcal{M}_i)$ is flat, i.e. $P(w_{\mathrm{MP}}|\mathcal{M}_i) = 1/\sigma_w$, then that the Occam factor has a magnitude less than one follows from considering that $\sigma_w > \sigma_{w|D}$. In this case, $\sigma_{w|D}/\sigma_w$ is the 'Occam factor'. Bayesian model selection mechanically applies this fundamental principle.

3.3 A novel application of a Bayesian scheme to SPT in live cells.

In the following sections, I outline the development of the modelling approach to infer the data in single particle tracks. First, I outline the inference algorithm by constructing the appropriate likelihoods, priors and detail the methods to evaluate the posterior distributions. These use the MSDs, propagators and estimates of uncertainty in the earlier sections. Emphasising that parameters should be treated as distributions, I also detail methods to represent that parameters as an ensemble

through Kernel Density Estimates and Gaussian Mixture Models.

Bayesian methods have not been widely applied to SPT in the context of membrane biophysics. Researchers have used Bayesian techniques for parameter inference [181][182], but only one recent paper to my knowledge has applied this to model selection, who also use the four modes detailed here [109]. There have, however, been a few papers using Bayesian techniques for single mobility parameters [182, 181, 183].

From the previous sections §3.2.1 and §3.1.1 it is clear that statistical methodology is as important as novel experimental techniques. The requirements of an inference scheme are:

- It is capable of granular inference at the single particle level that can identify underlying dynamics. Inference does not rely on bulk ensemble measurements.
- The application must be robust to realistic *in vivo* experimental data. Many of the techniques references are applied to *in vitro* or simulated systems; often with many orders of magnitude in the time-scale. These time-scales are not obtainable in (minimally perturbing) *in vivo* experiments.
- The scheme is capable of discriminating between different propagators that may have similar moments (i.e. MSD traces) for given parameters.

Bayesian scheme for inferring diffusive behaviour

In this section, I outline the precise application of the method developed. I first formulate the likelihoods functions used in §3.3.1, then the parameter priors in §3.3.2.1, followed by the model priors in §3.3.2.2. In the final section §3.3.3, I outline how this is implemented.

3.3.1 Likelihood Functions

Likelihood functions are divided into two classes - one using the time-averaged MSD and the others using the PDF. Likelihood functions using an MSD interpolant are much more numerically tractable but the PDF approach provided greater numerical accuracy. I detail each method here.

MSD

Propagators represent a direct probability function to be used as the likelihood. I also use the propagator moments (i.e. the MSD). In order to do this, I first needed a way to represent the MSD in the form of a probability or likelihood. In this section, I outline the basis in which I can interpolate the MSD into a likelihood.

In the general case, I can define a linear interpolation model [184] of the form $y(\mathbf{x}) = \mathcal{M}(\mathbf{w}, \mathcal{D})$. It is the predicted value of a model $\mathcal{M}$ given a set of parameters w. The linear interpolation model is of the form Equation 3.36. The index n here represents the n-th point in the MSD trace and y as the inferred MSD prediction and r as the observed value:

$$r_n = y_n + \nu_n \tag{3.36}$$

The term ν is an additive noise process. Assuming that this is a zero-mean Gaussian noise with standard deviation σ_v then the likelihood of the interpolant for a given model $\mathcal{M}$ and parameters w for a datatrace of length N is given by Equation 3.37:

$$P(y|\mathbf{w}, \mathcal{M}, \beta) = \frac{\exp(-\beta E_{\mathcal{D}})}{Z_{\mathcal{D}}(\beta)} \tag{3.37}$$

where the error term $\beta = 1/\sigma_v^2$, the residuals $E_{\mathcal{D}} = \sum_n \frac{1}{2}(y(x_n) - r_n)^2$ and the normalisation factor $Z_{\mathcal{D}} = (2\pi/\beta)^{N/2}$. This is seen by writing ν as $r_n - y_n \sim \mathcal{N}[0, 1/\beta]$ where $\mathcal{N}$ is the normal distribution. The likelihood is found by assuming normal distribution of errors about the MSD as in Equation 3.36. The likelihood is given by:

$$P(D|\theta) = \prod_{i=1}^{N} \frac{1}{\sqrt{2\pi\sigma^2(t_i)}} \exp\left[-\frac{1}{2}\sum_{i=1}^{N}\left(\frac{\mathcal{D}(t_i) - \mathcal{M}(\theta, t_i)}{\sigma(t_i)}\right)^2\right] \tag{3.38}$$

where $\mathcal{D}$ is given by the time-average MSD. The origins of the noise parameter $1/\beta$ were discussed in §3.1.1.1. For a time-averaged MSD trace, this is related to the predicted spread in the MSD with

time [122]. It is given in Equation 3.39. [122, 171]:

$$\sigma(t_i) = \frac{D(t_i)}{\sqrt{t_n/t_i}} \tag{3.39}$$

PDF

The likelihood is found by evaluating the probability of each observed particle displacement. Each trajectory is comprised of an N length vector of two cartesian xy coordinates, $\mathcal{C}$, sampled uniformly over time T, as multiples of the incremental sampling time δt. The probability of each displacement over a time δt, from the nth to the $(n+1)$th coordinates, $C_n = (x_1, y_1)$ to $C_{n+1} = (x_2, y_2)$, is calculated using the propagator, $W(C_{n+1}, C_n, t)$, of each model, $\mathcal{M}$, which is parametrised by the set of parameters $\mathbf{w}$. The set of coordinates $\mathcal{C}$ are used to form the displacements, d. These are the pairwise differences of each coordinate. These form the data, $\mathcal{D}$. This is over each time window t. As there are a total of N data points, the likelihood is the product of $N-1$ evaluations of each displacement. The PDFs are given in Table 3.1. The likelihood is then given by:

$$P(D|\mathcal{M}, \mathbf{w}) = \prod_{n=1}^{N} W((C_{n+1}|C_n), \mathbf{w}, \mathcal{M}) \tag{3.40}$$

In cases where the diffusion is Markovian this can be summarised as Equation 3.41:

$$P(D|\mathcal{M}, \mathbf{w}) = \prod_{n=1}^{N} W((C_{n+1} - C_n)|\mathbf{w}, \mathcal{M}) \tag{3.41}$$

As this uses the PDFs directly, I do not need to incorporate stochastic uncertainty. Strictly however, this should incorporate uncertainty by including the experimental uncertainty, i.e. that each displacement d has a Gaussian noise term $\nu \sim \mathcal{N}[0, \sigma_{\text{exp}}]$

$$d_n = C_{n+1} - C_n + \nu_n \tag{3.42}$$

The displacement then has a standard deviation of $\sqrt{2}\sigma_{\mathbf{exp}}$. This $\sigma_{\mathbf{exp}}$ is the accuracy in locating a

centroid. (Chapter 2, §2.6). This could be incorporated by weighting each PDF by calculating it with the uncertainty. This was not implemented.

3.3.2 Prior Formulation

3.3.2.1 Parameter priors

In this section I discuss how I formulate priors about the relevant mobility parameters. These are the diffusion coefficient, confinement size, anomalous coefficient and drift velocity. My SPT data and simulations show that the diffusion coefficient tends to be distributed by a Gamma distribution. This is unsurprising, as it represents the distribution in the standard deviation of a Gaussian. A Gamma distribution can be thought of as a positive-definite Gaussian. The coefficients D_m and D_σ are calculated by best-fit of the distribution of diffusion values. The characteristic domain size, L, represents the typical domain size expected. More strictly, it is the parameter governing the prior on the distribution of domain size. Note that the uniform distribution is recovered as $L \to \infty$. Similar arguments apply to the characteristic velocity.

The transport coefficients are therefore modelled by a Gamma probability distribution (Figure 3.11). The distribution $\Gamma(k, \theta)$ is parametrised in terms of the expected diffusion value D_m and the standard deviation, σ_D. The Gamma distribution is the natural representation of the diffusion coefficient [180], a positive Gaussian-like distribution. The Gamma probability density function f for a variable x parametrised by the shape parameter k and scaling parameter θ, is:

$$f(x, k, \theta) = x^{k-1} \frac{e^{x/\theta}}{\theta^k \Gamma(k)} \tag{3.43}$$

Here, x, k and θ are > 0, and Γ is the Gamma function. The values D_m and σ_D are used to choose the parameters of the Gamma distribution, k and θ, such that the mean resides at D_m and the standard deviation is equal to σ_D. The probability density function of the prior is:

$$P(D) = \Gamma(D, \sigma_D / D_m, D_m^2 / \sigma_D) \tag{3.44}$$

For the case of anomalous sub-diffusion, I mapped the transport coefficient K_α to D by a function of the Gamma function and α using $D = K_\alpha = \Gamma(1+\alpha)$ [35]. Appropriate values of the D_m can be estimated from other experimental data, or by heuristic mobility measurements from other tracks in the same data set. In the implementation here, estimates of D_m and D_σ are used by a maximum likelihood estimate of the distribution of microscopic diffusion coefficients of the ensemble of tracks. The microscopic diffusion estimate of each track is found using the gradient of a linear fit to the first 4 data points of the time-averaged MSD [93].

$$D_m = \frac{\Delta MSD_{1-4}/\Delta t_{1-4}}{4} \tag{3.45}$$

In the case for the other coefficients such as the domain size l and the particle speed v. I regularise these parameters. A regulariser is a function that I choose to represent my prior belief about a parameter distribution. There is good reason to choose the Gamma distribution for the diffusion coefficient. However, using the confinement radius as an example, it is not clear what model should be used to represent the belief that the confinement radius should fall within certain scales. These are regularised [184] such that they have a weighted exponential decay parametrised as Equation 3.46:

$$P(w) = \frac{2e^{-\lambda^2 w^2}}{\sqrt{\pi/\lambda^2}}. \tag{3.46}$$

Here, λ is a parameter with a value chosen to ensure the bulk of the probability mass is within an appropriate range, approximated by using physically realistic assumptions on the domain size. These distributions are summarised in Table 3.2. Table 3.3 provides references for these choices. The confinement parameter prior is depicted in Figure 3.9.

3.3.2.2 Model priors

The natural choice for model priors are unbiased weights. However, with confinement, there is a difference between long and short tracks. With longer tracks, proteins may explore the entire

Coefficient	α	K, D	v	l
Range	[0.5 1]		[0,∞]	
Distribution	Uniform	Γ	Exp. Decay	
Parameters	N/A	Gamma fit	10 nm/s	100nm

Table 3.2: *Parameter prior distributions. Each coefficient is considered to vary over a given range, in which the prior of the parameter is assumed to follow the distribution given. As a uniform prior is given for the anomalous coefficient, there are no parameters for it. For the transport parameters, the parameters for the Gamma distribution are determined by a Gamma fit to the diffusion coefficients. For the drift speed and confinement radius, the parameters given are the characteristic parameters. These are the parameters that govern their regularising exponential decay functions.*

Table 3.3: *Typical mean equation parameters used representing membrane diffusion, with cited sources.*

Diffusion coefficient, D	**Anomalous transport coefficient**, K_α	**Domain radius**, l	**Anomalous exponent**, α	**Flow rate**, v	**Sampling rate**, $1/\delta t$
0.01 $\mu m^2/s$ [185, 47, 116, 48]	0.01$\mu m^2/s$ [112, 120, 35]	0.1μm [10, 115, 186, 93, 116]	0.75 [112, 120, 35]	10nm/s [48, 117]	25Hz [47]

domain exhibiting a corralled motion, but this will be limited with short tracks. I quantify this by using a corrective prior on the confinement, $P(C)$ given by:

$$P(C) = P'(C)(1 - \exp(-D_m t_N/\lambda.^2)) \tag{3.47}$$

where λ is the characteristic domain size and $P(C)$ is the probability of tracks I expect to be confined, independent of any parameters. Irrespective of the number of confinement zones, tracks that are insufficient in duration are unable to probe the surrounding confinement zone. Thus, there is a reduced expectation in observing confinement effects in short duration tracks. This is depicted in Figure 3.9.

Similar arguments extend to subdiffusive and directed drift behaviours. Consider Equation 3.38. It incorporated the expected variance based upon the number of data points through the σ defined

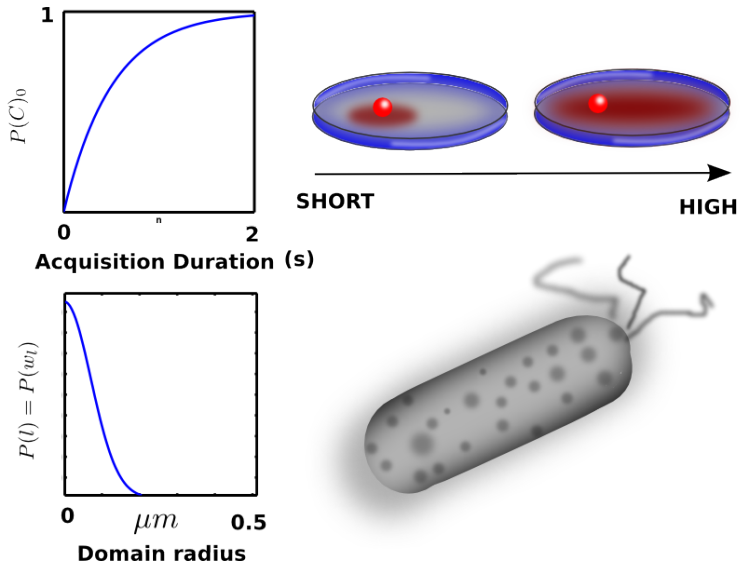


Figure 3.9: *Upper row. To avoid overfitting to short tracks that just by stochastic dispersion appear confined, a prior on $P(C)_0$ - the probability of confinement - is used (Equation 3.47). This follows given the informative prior on the confinement size (bottom row). For short duration tracks, the potential region explored by a tracer is small. For long duration tracks, and given assumptions about the domain sizes, I expect confinement models to be able to be resolved. Thus, there is an interpolation of $P(C)_0$ ranging from zero to one. Similar arguments on time-scale can be applied to other models. Lower row: Prior about the confinement radius is informed from previous experiments. The plot is of Equation 3.46 using the value in Table 3.2.*

in Equation 3.8; with the predicted statistical scatter decreasing with respect to the number of observations within a track. However, each non Brownian model has a different behaviour with respect to absolute time or time-lag, so *a priori* I expect for different experimental time-scales different models can be discriminated independent of the number of samples. In other words, for a track of a given sampling time and a given prior about the subdiffusive coefficient, I expect tracks with a longer sampling time (and the same number of acquisitions) to be capable of discriminating this behaviour relative to short tracks. For example, consider two tracks of equal number of acquisitions and different sampling times. In addition, consider that the MSD for subdiffusive motion varies as t^{α} versus t for Brownian motion. Then I only expect sub-diffusion to be capable of being seen provided that $t > t^{\langle\alpha\rangle}$, where $\langle\alpha\rangle$ is the prior expectation on α for a subdiffusive model. Using a similar regularisation $\mathcal{R}$, this generates the following model priors in Equations 3.49 and

3.48.

$$P(A) = P'(A)(1 - \exp \frac{t_n}{t_n^\alpha}) \tag{3.48}$$

$$P(D) = P'(D)(1 - \exp \frac{v^2 t_n}{D_m t}) \tag{3.49}$$

3.3.3 Inference scheme

The inference scheme is split into two forms: one using the probability distributions directly, and the other using the mean-squared displacement. All data $\mathcal{D}$ comes from the (x, y, t) traces of each track, although may be used as either the MSD or 2-D displacements. Methods exist on dealing with incomplete observations, but here I assume observations are complete. In [1] I denoted this the 'BARD' algorithm: Bayesian Analysis for Ranking Diffusion.

To implement the BARD algorithm, the following steps were taken, depicted in Figure 3.10:

1. Quantify all of the microscopic diffusion coefficients, D_m, from the single particle tracking data (shown here for simulated Brownian diffusion tracks in Figure 3.11a). Here, D_m gives a measure of the short time scale rate of diffusion and is estimated from a linear fit of the MSD data of each individual track using the first four data points. (Equation 3.45)

2. Fit a Gamma distribution to the distribution of all D_m (Figure 3.11 b) and use this fit to generate the two characteristic shape parameters of this function. Then use these shape parameters to generate the diffusion coefficient prior (see Equations 3.43 and 3.44,and Figure 3.11c, top panel).

3. Calculate the other parameter priors for K, l and v for the anomalous, confined and directed diffusion models respectively (Table 3.3).

4. To evaluate the numerator of Equation 3.29, for each separate single particle track I then calculated the likelihood (either using Equation 3.40 for the PDF method, or Equation 3.38

for the MSD method).

5. I then estimated the unnormalised posterior for each single particle track against each diffusion model, taken for the pure Brownian diffusion model as: Posterior = Likelihood(Brownian propagator) x Prior(D_m). For the anomalous diffusion model as: Posterior = Likelihood(anomalous propagator) x Prior(K_α) x Prior(α). For the confined diffusion model as: Posterior = Likelihood(confined propagator) x Prior(D_m) x Prior(l) while for the directed diffusion model as: Posterior = Likelihood(directed propagator) x Prior(D_m) x Prior(v).

   An example of the unnormalised Brownian model posterior distribution for a typical simulated track is shown in Figure 3.11c, lower panel. The posteriors for the other diffusion models are shown for the same example track in Figure 3.11d—f.

6. Normalize the parameter posterior distributions from stage 4 (Equation 3.31), calculating the evidence term. This is the final step in the parameter inference section, which bridges to the second inference stage (i.e. model selection).

7. Model selection: Calculate the model posterior. Rank the models on the basis of the size of the model posterior (a numeric probability). This final step then yields a probability estimate for a given model: $P(\mathcal{M}_i|\mathcal{D})$ For example, for the example track shown in Figure 3.11a, which was simulated using a pure Brownian diffusion propagator function, the inference ranking probabilities which were generated from the four candidate diffusion models of anomalous, Brownian, directed and confined are 33.1%, 65.6%, 1.1% and 0.2% respectively, and so in this instance Brownian diffusion is the favoured model.

8. For the top-ranked diffusion model for each single particle track I then automatically locate the centroid of the posterior, to indicate a summary statistical representative value of the transport parameter for that particular diffusion model. This is done using a Gaussian fit about the posterior peak. (c.f. §3.3.5.1)

9. Repeat this process for all single particle tracks in the data set.

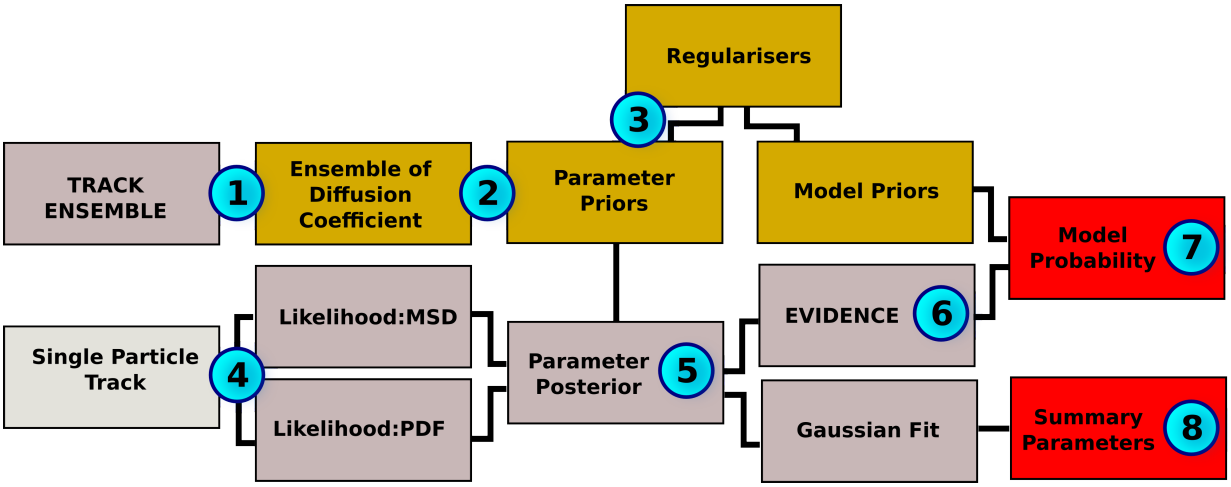


Figure 3.10: *The BARD algorithm. Each number corresponds to the enumerated list in §3.3.3*

3.3.4 Accurate model selection and parameter inference

A series of validation experiments were performed to validate BARD. These are itemised below and detailed in §3.4.

- Model ranking validation. A series of simulations at different parameter values were performed to benchmark the model selection aspect of BARD in §3.4.1.
- This was then applied to a much more realistic noisy heterogeneous data set with multiple model mixtures in §3.4.1. In this section, I also demonstrate the accurate parameter quantification.
- A series of smaller scale sensitivity tests were then performed to test the performance with respect to varying prior parameters (the hyper-parameters, also known as nuisance parameters in the BARD model). I also demonstrate the effect of the model priors here through a track length dependency test.
- To demonstrate accurate parameter inference in quantifying particular model parameters such as the diffusivity, I tested parameter inference on limited-heterogeneous simulated models. This was combined with a model selection approach that can discriminate subpopulations in §3.4.4

- In order to demonstrate that the framework presented here is extendable to more complicated cases I simulated one such case and generated synthetic tracks in these environments and determined the ranking output. Here, I simulated a change in lateral diffusion coefficient as might be experienced by a particle undergoing transitions to multiple kinetic states. This may occur in signalling systems with transitions between ligand-bound and unbound states, or a change in lateral mobility due to interactions with the underlying membrane such as local changes in viscosity [186] or interactions with the membrane cytoskeleton. §3.4.3.

3.3.5 Numerical Methods

In this section, I detail all the numerical methods used. The first is the method in which I represent parameters. The BARD algorithm does not work on the ensemble but on individual single particle tracking data. As each mobility inference produces a distribution, this produces as many distributions as there are tracks for the ensemble. Consequently, I need to combine each of these distributions into one summary distribution. To do this, I use Kernel density estimates. The second numerical method is in identifying sub-clusters in parameter clustering. The third and important numerical routine is in the calculation of the integrals in the BARD algorithm. I detail each of these below.

3.3.5.1 Parameter representation as Kernel Density Estimate

In the discussion of Laplaces method to calculate the Evidence in §3.2.2.4 a multivariate Gaussian approximation is used to represent the posterior: each parameter is represented as a Gaussian $\mathcal{N}$ with mean μ and standard deviation σ. This is a non-parametric representation of the probability distribution of the parameter in that it is not parametrised by the number or width of bin sizes as in a histogram. Instead, it assumes that the parameter has a particular distribution function. This is done for each parameter in each track in the model partitioned ensemble of the data, which is comprised of multiple tracks. The dataset is partitioned by model ranking, and would be all the confined modes in a particular dataset for example. Using the subscript k to index $\mathcal{D}$ to represent

the kth track of such a partitioning, to represent these parameters, I used a Kernel Density Estimate (KDE).

$$P(w|_{\{k\}}\mathcal{D}, \mathcal{M}_i) = \frac{\sum_k \mathcal{N}(\mu_w, \sigma_w)}{\int \sum_k P(\mathcal{M}_i|_k\mathcal{D})\mathcal{N}(\mu_w, \sigma_w)dw} \tag{3.50}$$

An addition to this, is the Weighted Kernel Density Estimate (WKDE), where the contribution of each observation is weighted by the model marginal likelihood $P(\mathcal{M}_i|_k\mathcal{D})$.

$$P(w|_{\{k\}}\mathcal{D}, \mathcal{M}_i) = \frac{\sum_k P(\mathcal{M}_i|_k\mathcal{D})\mathcal{N}(\mu_w, \sigma_w)}{\int \sum_k P(\mathcal{M}_i|_k\mathcal{D})\mathcal{N}(\mu_w, \sigma_w)dw} \tag{3.51}$$

3.3.5.2 Identifying subclusters in populations

An example of the open-ended nature of model fitting is in clustering. In section (§3.4.4) this is used to identify sub-populations which is used to simplify the Kernel Density Estimate (KDE) of Equations 3.50 and 3.51. Consider a clustering problem in which the KDE distribution is simplified as a Gaussian mixture model (GMM). The biological meaning of this is that one, or more distributions represents the difference between a single or multiple distributions of the population; i.e. sub-populations, of the parameter represented by the KDE. In general, I can cluster across all the relevant parameters. A Gaussian KDE has the same form as a GMM, given, for mean coefficients $\boldsymbol{\mu}$ and co-variance matrix $\boldsymbol{\Sigma}$ and mixing coefficient $\boldsymbol{\Pi}$ of K components, by Equation 3.52:

$$P(\mathbf{w}|K, \mathcal{D}, \mathcal{M}_i) = \sum_k^K \boldsymbol{\Pi}_k \mathcal{N}(\boldsymbol{\mu}_w, \boldsymbol{\Sigma}_\mathbf{w}) \tag{3.52}$$

Fully consistent with the model selection arguments presented earlier, are the *information criterion* metrics [187] that rank models in terms of complexity. These criteria are the Akaike (AIC) [188] and Bayes Information Criterion (BIC) [189]. With likelihood $\mathcal{L}$, k free parameters and sample size N, these are given by Equations 3.53 and 3.54 respectively.

$$AIC = 2k - 2\log(\mathcal{L}) \tag{3.53}$$

$$BIC = -2\log\mathcal{L} + k\log(n) \tag{3.54}$$

These metrics assess a model by the predictive value ($\mathcal{L}$) penalised by the degree of complexity $2k$. The metric minimum is the best estimate for the model complexity. Examples are the number of Gaussian in a mixture model. In general, BIC has a more severe penalty for complex models relative to AIC. A distribution of data can then be assigned into each cluster by calculating the PDF of each GMM element at that point, and ranking by the probability. This method only works for distributions that are realistically Gaussian distributed.

3.3.5.3 Evaluating the integrals

The evaluation of the numerical integrals that form the normalisation terms or evidence (e.g. Equation 3.31)) is achieved by a Monte Carlo integration routine [190, 180]. As the functions in the MSD are all exponential family (by construction) an analytical treatment would be possible, although not considered here. This is not necessarily the case for the PDF formulation as the PDFs for anomalous diffusion involved more complicated functions not available in standard libraries, nor easily analytically tractable. Secondly, as the routine was set-up to be open ended (adding in extra models, or doing switching tests etc.), I applied a numerical scheme throughout, rather than presuming an analytical treatment will always be appropriate. Pseudo-code is presented in A.1.
There were a set of parameters which controlled the evaluation of the numerical integrals. As the integration routine is stochastic it operated through random sampling, sampling the distribution at random points. The first set control the effective boundary on where the stochastic integration routine should explore. The second controls the accuracy; the number of samples to take. For example, the diffusion coefficient D was explored from a numerically small number, to a biologically large number. The numerical integration accuracy was determined by the degree of sampling about

the bulk of the probability mass in the distributions being integrated. Therefore, in a later version of the BARD algorithm, these were automatically adjusted to optimise the sampling routine. However, the default parameters (and for the results presented here) are given in Table 3.4.

Parameter	Numerical Bounds/Value
Range of diffusion coefficient	$[1e^{-10}\ 0.5]\ \mu\ m^2/s$
Range of domain sizes searched	$[1e^{-10}\ 1]\ \mu m$
Range of velocities	$[0\ 1]\mu\ m/s$
Number of samples in integration	400

Table 3.4: *Typical algorithm Parameters. The key parameters of the algorithm were determined by two sets of parameters. These together form the density in which the distributions were sampled in the numerical integration.*

3.4 Results

In this section, I outline the results of the testing of the BARD model. I first outline the model classification results. I then consider how the BARD model is sensitive to varying parameters by performing a sensitivity analysis of the model parameters. I then continue onto demonstrate that BARD can be used to identify switching behaviour in single particle tracking. Finally, I demons

(3.55)

trate that the parameter inferences in BARD are accurate, and can be used to identify subpopulations through a clustering of the parameter outputs.

3.4.1 Model Ranking: Classification

To determine the robustness in my method, a series of two-dimensional validation experiments were performed using simulated SPT input data using a range of mobility parameters comparable to those observed for the experimental Tat data [1]. I then analysed both the parameter estimates and

[1] Tat data is analysed in Chapter 5

model rankings outputs. Model ranking was given in terms of a classification matrix, with full two-dimensional analytical treatments throughout.

For the MSD approach I compared anomalous, Brownian and confined modes (Figure 3.12). Confined and Brownian motion can be identified correctly with greater than 50% accuracy - in the context of the other models presented - though the true identification of anomalous behaviour was poorer (30%), probably because subtle subdiffusive behaviour is not apparent for such typically short track lengths as obtained in TIRFM.

I did not apply a confinement probability distribution to the PDF approach (this required using absolute spatial positions over relative differences and marginalizing over the track start points which resulted in a weak performance combined with an impracticably large computational load, which is discussed further in §3.5). I instead compared just anomalous and Brownian modes using this method. Anomalous diffusion was correctly discriminated with an accuracy of at least 62% (Figure 3.12) that performed better than the MSD approach for corresponding diffusive modes (for example, the Brownian mode was correctly identified with an accuracy of 95% using the PDF method compared with 52% for the MSD method). However, a strict comparison cannot be made because confinement was not tested in this case, recalling the caveat made that the $P(\mathcal{M}|\mathcal{D})$ are only relative to the set of models tested.

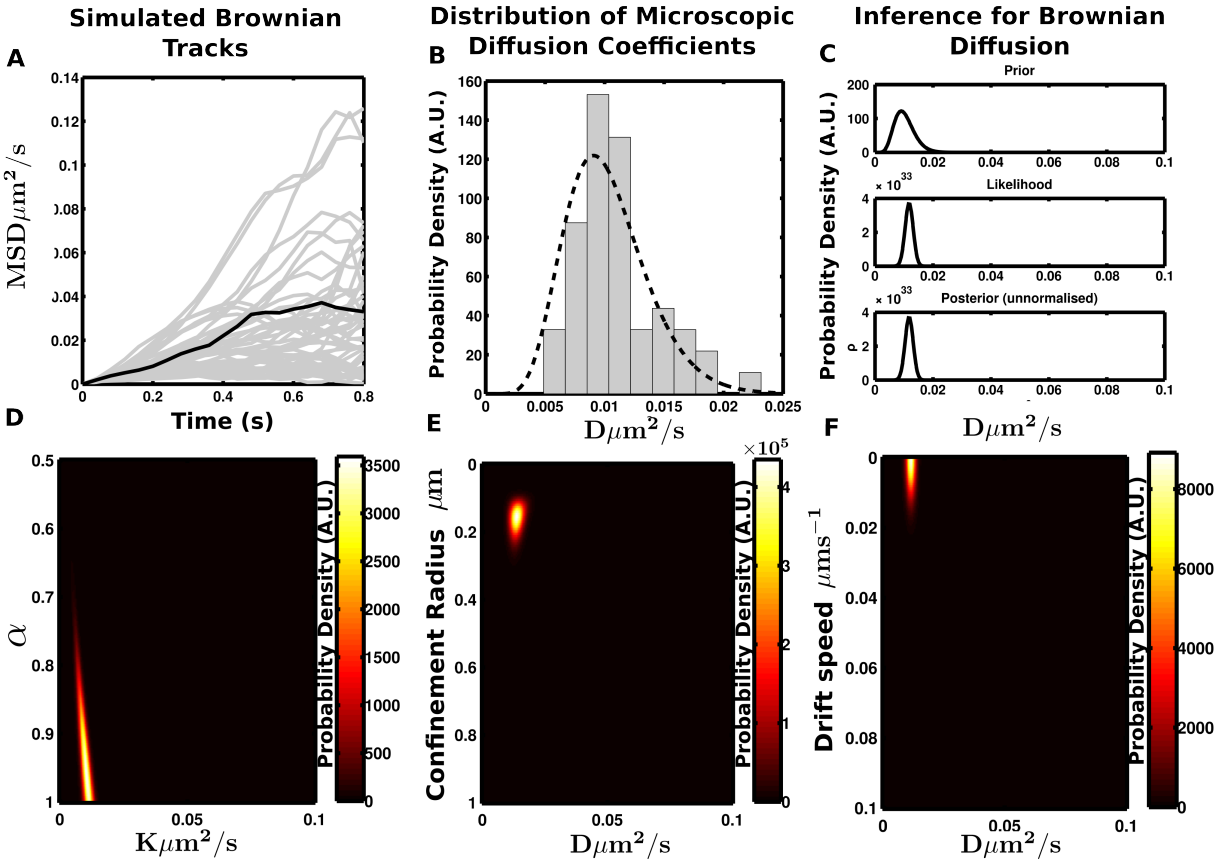


Figure 3.11: *Implementing BARD.* ***A:*** *Simulated Brownian tracks (grey) all with diffusion coefficient $D = 0.01$ μm^2/s, with one of these tracks highlighted (black) for BARD analysis.* ***B:*** *Distribution of measured microscopic diffusion coefficient Dm values from tracks in (A) with Gamma fit indicated (dashed line), that forms the prior in the top panel in (C)* ***C:*** *Constructing probability distributions used in BARD for the highlighted track of (a) tested against a Brownian diffusion model showing the unnormalised prior (upper panel), likelihood (middle panel) and posterior (lower panel). Testing against the three other diffusion model generates two-dimensional unnormalised posterior distributions for* ***D:*** *anomalous,* ***E:*** *confined and* ***F:*** *directed diffusion models. For the highlighted track shown in (a) the highest ranking probability was measured at 65% for the Brownian mode, thus correctly identified with a probability which was more than twice as much as the next ranked mode of anomalous diffusion.*

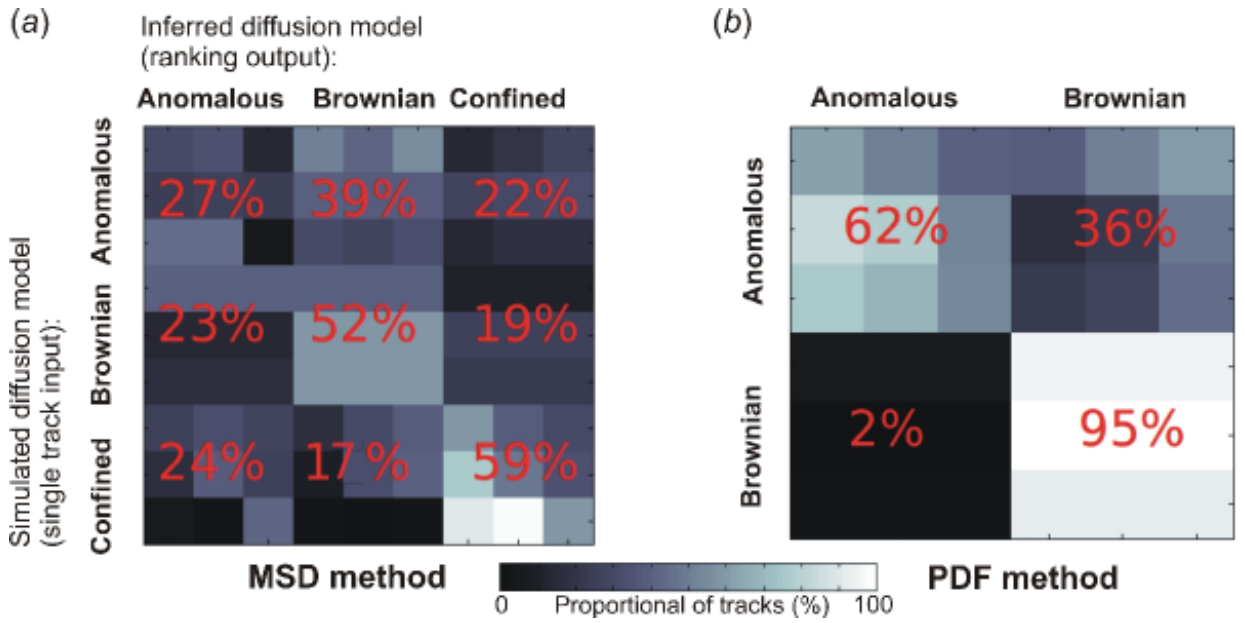


Figure 3.12: *Characterizing the error in the BARD analysis using classification matrices for (a) the MSD method, and (b) the PDF method. Each 'pixel' in the matrix represents a combination of a type of simulated track against an inferred highest ranked diffusion model from the BARD analysis, with gray scale indicating the individual inference ranking percentage. Each diffusion mode here was simulated with three different tracks, and therefore each matrix is composed of individual 3x3 sub-matrices, with the percentage in red indicating the mean average inference ranking relative percentage within that sub-matrix. Thus, the diagonal of (a) and (b) constitutes the true-positive classification values. There are a range of values presented in each 9 element square. For A, the three rows for anomalous sources represent D=0.005, 0.01, 0.5* $\mu m^2/s$ *(rows 1, 2, 3). This is repeated down the rows, with rows 4, 5, 6 and 7, 8, 9 corresponding to* $D = 0.005, 0.01, 0.5$ $\mu m^2/s$*, respectively. The columns of A represent different degrees of anomalous subdiffusion (0.7, 0.8, 0.9), respectively. Likewise, the columns of 'Confined' represent different domain sizes, (50,100,200* nm *). The percentage overlay gives the average of each 3x3 block. Rows sum to one hundred to complete the set of tested models, with the remaining percentages being the percentage classified as 'Directed' modes (12, 6 and 0% for simulated anomalous, Brownian and confined modes respectively). Similar tests were not included for directed modes.*

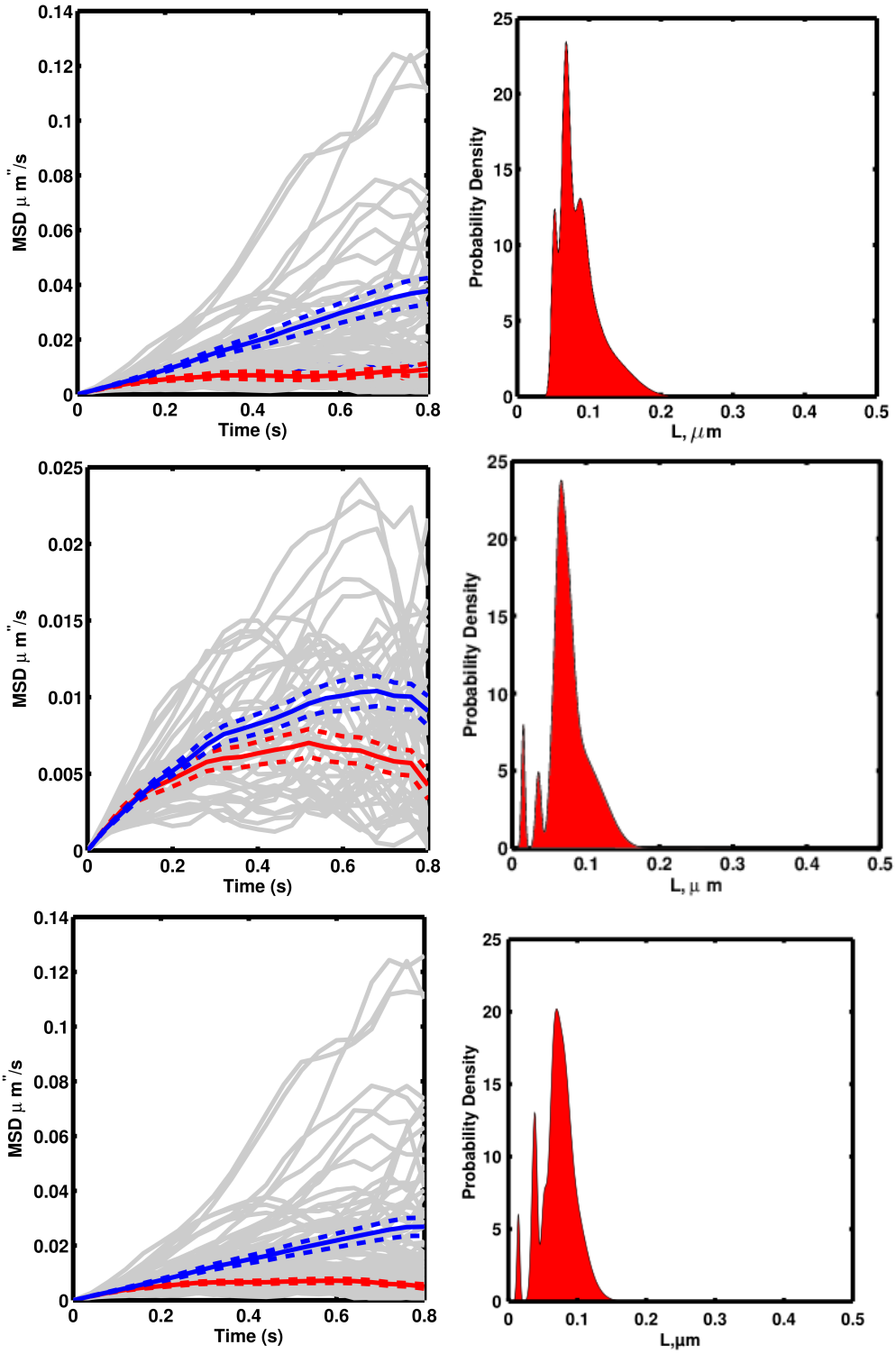


Figure 3.13: *Applying BARD to simulated data of increasing complexity. In the upper row, freely diffusing Brownian unconfined tracks are simulated. The middle row has purely confined tracks ($L = 0.1\mu m$. The latter row has both sets. The blue MSD traces indicate track averages of mobile (i.e. Brownian) tracks. The red traces indicate track averages of confined tracks. From top to bottom, the mobile/immobile rankings were* 41/9,30/20 *and* 35/65 *(of which* 25 *were correctly classified as confined and the remaining* 10 *miscategorised). The second column are the kernel density estimates of the inferred confinement size.*

3.4.2 Sensitivity Analysis

A sensitivity analysis tests the robustness of a model subject to varying parameters. I consider the sensitivity of BARD subject to parameter variation and a changing experimental timescale, as the inference output was unsurprisingly found to be a function of track length and confinement domain size. These issues are discussed in the following sections.

3.4.2.1 Prior parameter sensitivity

In order to test the sensitivity of the inference approach and to demonstrate that the priors are not dominating, a sensitivity analysis was performed on the effect of the priors. Classifications were performed with varying characteristic prior parameters. In Table 3.5 the results of the sensitivity analysis for confinement model inference are shown. Two test datasets are used, one with free diffusion and the other with confined diffusion. The change in model sensitivity is shown by using an appropriate prior over the confinement size. Although the uninformative prior has the greatest sensitivity to identify confinement, this decreases sensitivity when identifying free diffusion. When calculating sensitivity by accounting for both test data sets a finite λ (see Equation 3.46) has the most even sensitivity between for both models. Consequently, a non-flat prior is preferred, and the regularised Gaussian decay is used.

Table 3.5: Sensitivity Analysis for parameter priors

Confined: R=100 D=0.01, N = 50

Mode	**Characteristic Prior Parameter**			
	Flat	0.2	0.1	0.05
Anomalous	20	22	26	32
Brownian	14	26	24	14
Confined	62	40	44	40
Directed	4	12	6	14

Brownian: D=0.01 N=50

Mode	**Characteristic Prior Parameter**			
	Flat	0.2	0.1	0.05
Anomalous	10	26	12	16
Brownian	32	42	46	54
Confined	42	22	28	12
Directed	16	10	14	18
True-positive %	47 (31+16)	41 (20+21)	45 (22+23)	47 (20+27)

Table 3.5: *The upper table represents tests on a set of confined tracks with varying the parameters of the prior distributions. Numbers indicate percentage identification of the respective mode (A=Anomalous, B = Brownian, C=Confined, D= Directed) For example, for a parameter* $(1/\lambda)$ *of 0.05, 32% of the tracks are identified as anomalous. Numbers are highlighted in green to indicate the most ideal results (upper table, high C percentages, lower table, high B percentages). Red highlights indicate poor results: (upper table: high B per percentages, lower table, high C percentages). The last row indicates the sensitivity accounting for both datasets. The numbers in brackets indicate the summation over the number of true positive classifications. In other words, 45% represents 22 correct C identifications out of 50 plus 23 correct B identifications out of 50.*

3.4.2.2 Time-scale sensitivity

This test uses a specific study to characterise the cases of non-zero directed velocities. I used a typical directed motion velocity of 10 nm/s parameter prior comparable to [117] and simulated over a range of comparable conditions (to the referenced paper) to determine when this behaviour could be correctly identified. Related to their study, I included a lower sampling rate but comparable number of track data points. I characterised fully how this varies with different values of diffusion coefficient, drift velocity v and sampling time using a dimensionless parameter $\xi_v = v^2\delta t/D$ (Figure 3.15). In a similar manner for confinement, I characterised these changes in inference probability using the dimensionless parameter $\xi_L = ND\delta t/L^2$, where δt is the sampling time and N is the number of data points in a track. Intuitively I expect fast diffusion particles in a small domain over a long time period to be readily identified compared to the slow particles in a large domain. Figure 3.15 shows how the discrimination ability varies as a function of $\epsilon_l = ND\delta t/L^2$. The intercept of around 20% is the approximate bias as reported in §3.4.1. Figure 3.14 also depicts how the model output changes with track length.

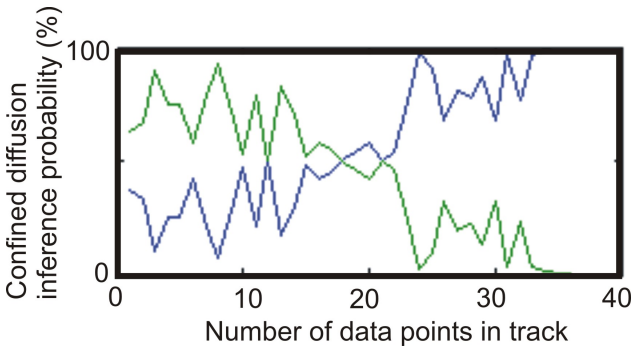


Figure 3.14: *Variation of ranking probability with number of track data points. A single track was simulated using a confinement radius $l = 0.1\mu m$ and microscopic diffusion coefficient of $D = 0.01\mu m^2 s^{-1}$. Model ranking inference was then applied against two possible diffusion models of confined (blue) and Brownian (green) diffusion, with the vertical axis here indicating the inference ranking probability for confined diffusion.*

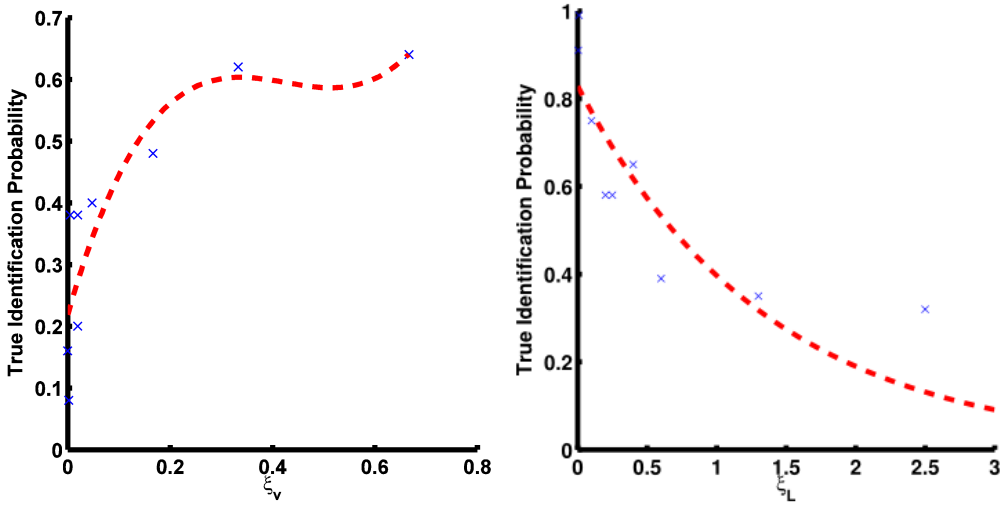


Figure 3.15: *Directed diffusion validation. Tracks were simulated over a variety of non-dimensional parameters ξ. ξv is a measure of degree of directed to random drift and is given by $\xi_v = (vt)^2/((vt)^2 + 4Dt))$. Y-intercept and control simulations (where there is no directed motion) gives an estimate of the systematic error at around 20%. The diffusion coefficients simulated were $D = 1 \times 10^{-5}, 10^{-4}$ and 10^{-3} $\mu m^2 s^{-1}$ with corresponding velocities of v of 1,10 and 20* nm/s *(see Table 3.3). In addition, three controls were performed at the listed diffusion coefficients at zero velocity. . A similar test was performed for the confinement with $\xi_L = ND\delta t/L^2$. This is displayed in the right figure.*

3.4.3 Multistate kinetics: Identifying dynamics

In order to simulate mode switching, whereby single particles crossed from one environment to another, tracks were simulated with a change in lateral diffusion coefficient of the diffusing particle. Examples are changes in lipid environment or other examples of switching behaviour [33]. These are depicted in Figure 3.16. To do this, I introduce a new model with Brownian diffusion before with a switching event in which the diffusion coefficient changes. This model used two Brownian propagators with two independent diffusion coefficients. In this simple generalisation, it is assumed that the time scale of the reaction step was much less than the sampling period. Here, particles were assumed to make the switch at the half way point of their full simulated trajectory. At this point, particles were assumed to switch to a higher diffusion coefficient (from D = 0.01 $\mu m^2/s$ to either D = 0.05$\mu m^2/s$) or D = 0.10 $\mu m^2/s$), assuming true Brownian diffusion in each case and a video-rate sampling time interval of for us 40 ms so that the number of data points in each half of a

trajectory is N = 10. Figure 3.17 illustrates the typical simulated individual and time-averaged MSD outputs with model ranking predictions. This relatively simple switching model can correctly predict switching behaviour characterised by two separate diffusion coefficients over a simple Brownian diffusion mode which assumes just one effective diffusion coefficient. The mean emergent probability of the switching model is 65-85%, depending upon the size of the switch in D.

3.4.4 Multistate kinetics: Identifying sub-populations

There have been reported cases of multiple sub-populations of single modes of membrane complexes in complexes such as the Tat system [191]. In order to determine whether sub-populations can be identified an additional classification needs to be made. Unlike in discriminating whether a single track is mode-switching, this is a classification on an ensemble.

This demonstrates how model selection can facilitate the identification of such a distinction. I also use this section to demonstrate that parameter inference is accurate. To do this, I apply the GMM clustering (Equation 3.52) to three levels of detail, dependent upon whether $P(B)$, the Brownian probability is used or not. The number of components in the clustering is determined by AIC/BIC metrics (Equations 3.53,3.54, respectively). The following gives the level of detail:

- Full detail; of the Brownian tracks identified, $P(B), D_\mu$ and D_σ are parameter variables forming a 3D parameter set for clustering.
- Mid detail; of the Brownian tracks identified, D_μ and D_σ form the parameter space for clustering.
- Low detail; model evidence $P(B)$ ignored and all tracks from the ensemble, not just the ones identified Brownian.

The results are summarised in Figure 3.19.

A second test is comparing multiple modes, rather than sub-populations (i.e. a mixture of Brownian and confined, rather than two sub-populations of Brownian motion). The results are presented in Table 3.7.

Model	Component	Mixing	D $\mu m^2/s$	D_σ $\mu m^2/s$	P(B)
Full	1	0.5	0.017	0.004	0.7
	2	0.5	0.009	0.002	0.7
Mid	1	0.46	0.009	0.002	N/A
	2	0.54	0.017	0.003	N/A
Low	1	0.28	0.007	0.002	N/A
	2	0.11	0.015	0.004	N/A
	3	0.46	0.009	0.001	N/A
	4	0.15	0.021	0.004	N/A
Control	1	1	0.008	0.002	0.7

Table 3.6: *Gaussian parameter fits of Figure 3.19. The ensemble is a 50/50 mix ($N = 100$) of two Brownian populations of $D = 0.01$ and $D = 0.02$ $\mu m^2/s$ of track length between 5 and 20. Accuracy is seen to decrease with model resolution. The Full model using all of the parameters D, D_σ and $P(B)$ identifies correctly the 50/50 mix of D =0.01 and 0.02 $\mu m^2/s$ diffusion rates with appropriate clustering. The control is the correct identification of D =0.01 $\mu m^2/s$. These are depicted in Figure 3.19. The N/As are where the information is not used for the model detail.*

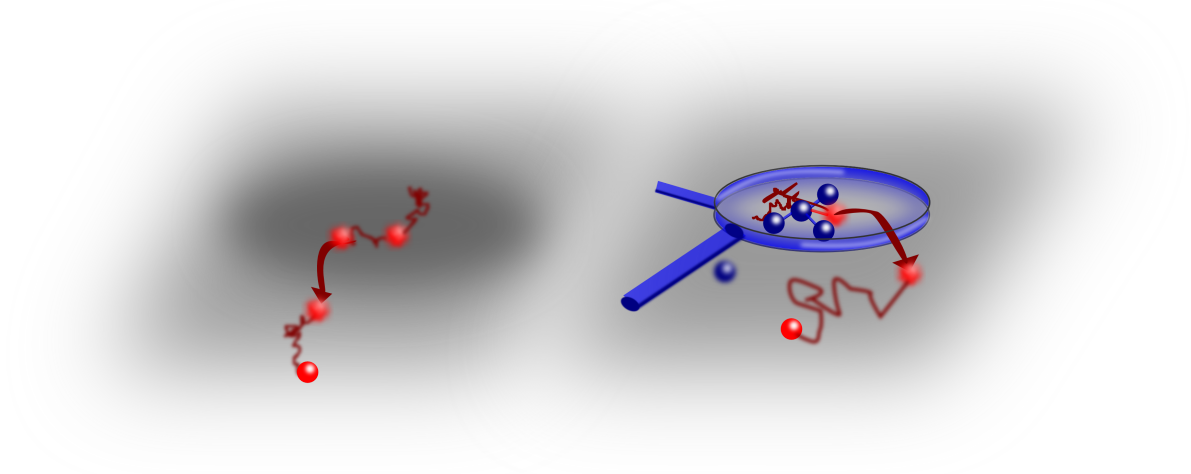


Figure 3.16: *Schematic of mode switching. Left: A particle goes from one lipid environment to another, modulating the diffusion coefficient. Right: A particle goes from a confining microdomain to freely diffusing. The underlay in both represents the appearance of lipid microdomains.*

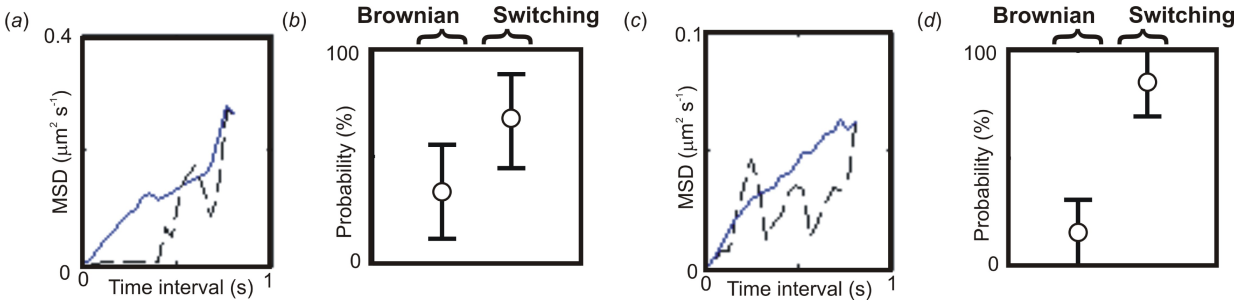


Figure 3.17: *Inferring a sudden change in diffusion coefficient. (a) MSD relation for a single track simulated assuming Brownian diffusion (black) and the mean average of 20 such tracks (blue) for which the diffusion coefficient D switches from 0.01 to 0.10* $\mu m^2/s$. *(b) Associated ranking inference probabilities for a single D Brownian (B) and two D Switching (S) model. (c) MSD relation for a single track (black) and average of several tracks (blue) for which D switches from 0.01 to 0.05* $\mu m^2/s$. *(d) Associated ranking inference predictions*

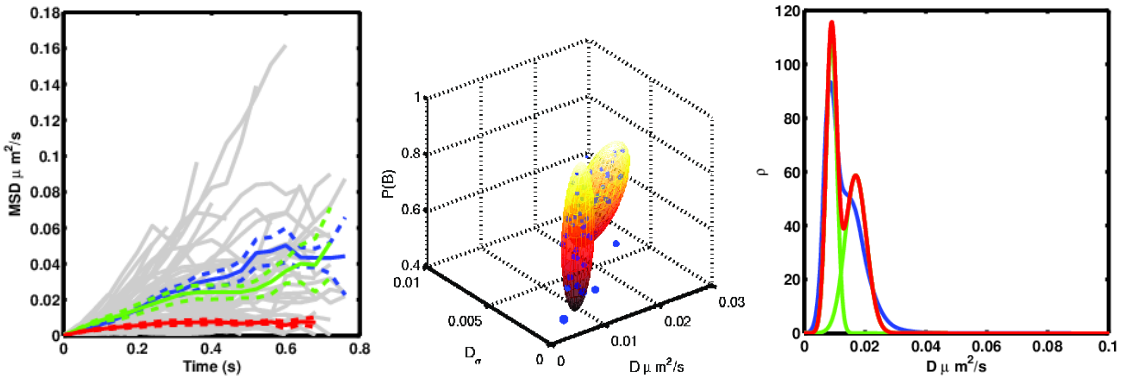


Figure 3.18: *a) The MSDs of the mixed Brownian distribution, simulated with a 50/50 mix of D =0.01 and 0.02* $\mu m^2/s$ *respectively, and then shortened to a randomly chosen uniformly distributed length of [5,20] Key: Red: Confined (36 identified confined), Blue: Brownian (58), Green: Anomalous (6), Directed (0). b) The GMM of fit of the 3D parameter space* $(D_\mu, D_\sigma, P(B))$ *in the (x,y,z) axes respectively. The ellipsoidal boundaries of the Gaussians are drawn at* 2σ*; representing 87% of the probability mass. The blue points are the data, with a size to portray depth as an inverse function of distance away from the origin. c) The KDE estimate with the two fitted Gaussians (blue: KDE, green: individual Gaussian fit, red: GMM fit). Means of the GMM parameters are summarised in Table 3.6*

Model	Component	Mixing	D µm^2/s	D_σ µm^2/s	L µm	L_σ µm	P(M)
Brownian	1	1	0.010	0.001	N/A	N/A	0.81
Confined	1	0.34	0.012	0.003	N/A	N/A	0.97
	2	0.66	0.011	0.002	N/A	N/A	0.98
	1	1	N/A	N/A	0.049	0.005	0.98

Table 3.7: *Multimode parameter clustering. A combined set of confined ($N = 25, D = 0.01\mu m^2/s, L = 0.05$µm and Brownian $D = 0.01\mu m^2/s$) P(M) is the probability of the respective mode.*

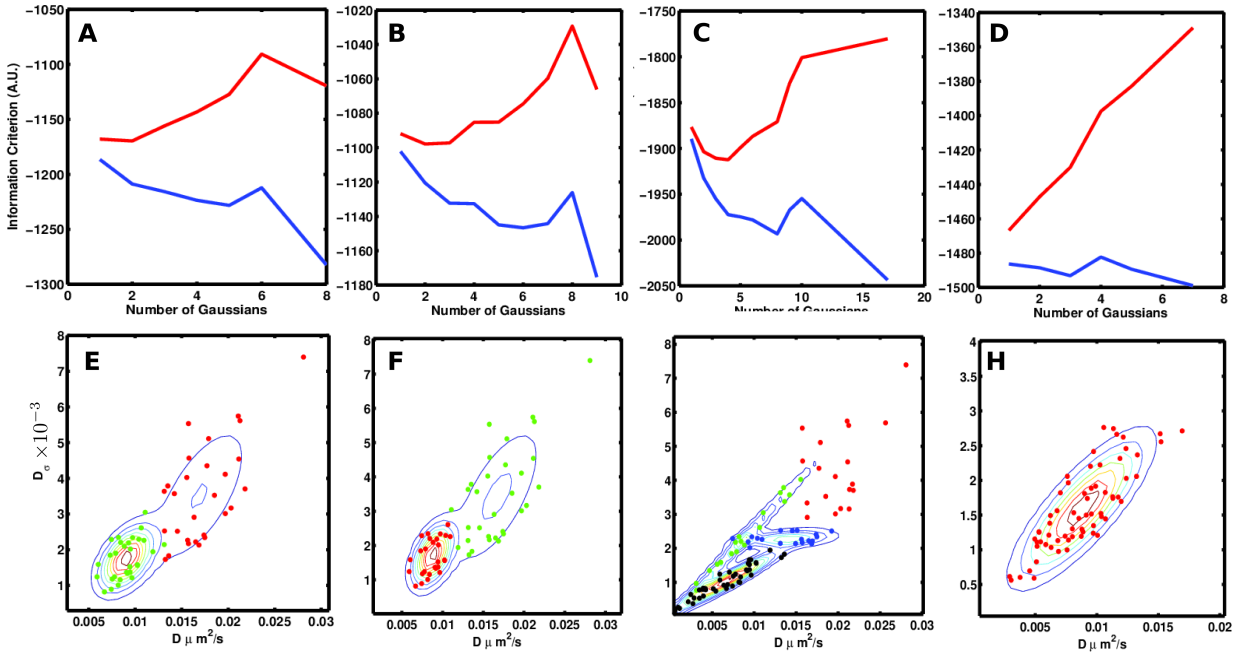


Figure 3.19: *GMM clustering. The upper row represent the AIC (blue), BIC (red) metrics, varying with the number of Gaussian Mixture components. Using the models described as full and mid detail, both of which account for $P(B)$, the minimum BIC is at with two Gaussians ((A) and (B) respectively). This minimum shifts to four when $P(B)$ isn't accounted for, shown in (C) with four Gaussians (Note that four Gaussians are plotted, one has a high variance and therefore not well identified on the contour map). The bottom row are the Gaussian clusters identified. The fourth pair (D,H) are the control, with only one population of freely diffusion protein ($N = 100$,$D = 0.01\mu m^2/s$). The minimum number of Gaussian clusters identified by BIC here is 1. Note that the Information metrics are not comparable, to different models or to each other. For example, AIC cannot be compared to BIC or the BIC in A compared to the BIC in B). In all cases here AIC is a poor metric for discrimination.*

3.5 Discussion

In this study, I describe an analytical method to discriminate different modes of diffusion, applicable for data obtained from single particle tracking of fluorescent labelled proteins in the cell membrane. I report our approach based on both modelling and stochastic simulation of multiple biologically-relevant diffusive modes experienced by membrane proteins in different underlying micro-environments. Priors are formulated from both simulation and experimental work. I demonstrate how the use of the interpolation or propagator functions can permit discrimination between Brownian, directed, confined and anomalous diffusion, even for relatively sparse data tracks. When comparing two diffusive modes in a pair-wise fashion our results indicate that model ranking predicts the correct diffusive mode for a single video-rate sampled track as short as 0.4 s in duration. Furthermore, the model can be extended to permit discrimination for a diffusion model involving sudden switching of the diffusion coefficient during a particles trajectory, and for subpopulations within a dataset.

Two approaches were used, one using the MSD approach and the other using the PDF approach. In each case, a prior formulation was used to describe the expected distribution of the parameters. Although neither approach could effectively discriminate between anomalous and confined modes of motion, which from the MSD curves have qualitatively similar shapes for noisy short tracks, I find that the PDF and MSD approach in tandem have different resolving power. The MSD approach effectively identifies confinement from simple Brownian motion, and the PDF approach effectively identifies anomalous diffusion from Brownian diffusion. In addition, the PDF approach has a strong resolving power in that it can identify dynamics within a single track, as observed in the simulations of switching. Unfortunately, due to the weak resolving power of anomalous diffusion, and the lack of inferring confinement using the PDF (within this framework), there was no ability to separate between anomalous and confined motions. These have similar subdiffusive effects but have different biological environments. Indeed, at high degrees of anomalous subdiffusive behaviour long range percolation is shut off. However this is a separate phenomenon to that of a protein being confined

due to lipid partitioning or cytoskeletal corralling.

Beyond model ranking, two further biologically feasible systems were modelled for discrimination to complete the toolset. The first is identifying dynamics; protein switching behaviour, where proteins switch from a slow to fast moving model. This biologically could occur with hopping between compartments of differing lipid distributions. Moreover, this switching behaviour was designed to show the adaptability of this framework and portrayed bimodal behaviour when a model was split into two. This can naturally be extended into multi-model processes such as moving from free diffusion to confined diffusion, rather than two configurations of the same free diffusion.

The second approach was in identifying sub-populations. This required an extension of the analytical tools, as the priors had been constructed without any sensitivity to that models may have multiple sub-populations. Correspondingly, I introduce a clustering approach in order to discriminate multiple sub-populations within particular modes. I used this to demonstrate that the algorithm was capturing the simulated mobility parameters as I find the Gaussian Mixture Model can find the centroid about the distribution of parameters, centred on the true value. In addition, I can estimate the number of sub-populations through a BIC measure.

In each case, BARD was validated through the use of synthetic data. Ideally, these should also be deployed on control data from a simple control system, such as a simple single or multicomponent vesicle, under temperature controlled conditions. Ideal probes in such a control system can include long-lifetime fluorescent probes. Single particle tracking data of such probes in single component vesicles, and mixed multicomponent vesicles, compared with phase separated multicomponent vesicles, would be informative.

3.6 Conclusion

The *in vivo* video-rate particle trajectories contain approximately 10-30 times fewer data points than those used in previous studies utilizing tracking of gold particles [10],[93][116][48], organic dye labelling of clusters containing hundreds of molecules [123] or quantum-dot tracking ([126]). The

trajectories are of comparable duration to those obtained previously using single molecule fluorescence microscopy either in artificial lipid layers or in vivo [47][112][124]. The authors implemented a variety of different methodologies to analyse single particle trajectories involving either regression fitting of the MSD versus time interval relation, application of a relative deviation parameter or constructed probability distributions representative of the modes of interest.

These propagator and interpolation functions model the likelihood of an observed track. This study also includes how the distribution of the parameters which formulate these models can be used to aid in discrimination of the diffusion processes. In fluorescence microscopy, with typically such short tracks observed, it is generally infeasible to analyse such trajectories without some form of population averaging. Exceptions are made of course to the occasional long track which is observed, or tracks which appear representative, but a majority of the body of data captured is noisy, and unrepresentative if multiple modes of behaviour are under investigation.

This study aimed at being able to discriminate, without population averaging, such tracks. Once individual particle trajectories are categorised into different modes of diffusive behaviour, models can be built allowing greater physiological interpretation of the protein mobility characteristics in functional, living cells, and an understanding of their underlying membrane microstructure in a biologically-relevant context.

Since the inference scheme is probabilistic there will inevitably be some trajectories which are falsely categorized with the wrong behaviour, most often into simple Brownian motion, as shown in the classification matrices. I included details on how model ranking varies with respect to the number of data points to demonstrate that there will often be a crossover between mis-categorisation and the correct identification. If this crossover is unreachable in the experimental framework it will at least inform the experimentalist on the typical minimum duration of track which needs to be detected to permit reliable discrimination. This, possibly directing them to change the characteristics of the optical setup and/or the related biological and physico-chemical conditions, such as the type of fluorophore used and whether the application of anti-bleaching reagents is required.

Separating such different mobility characteristics into different categories will allow insight into

several important biological questions: how proteins partition dynamically in the cell membrane, how signalling events are linked to membrane architecture, how motor proteins shuttle in or near to cell membranes, and the extent to which interacting proteins rely upon random collisions or are part of putative confined solid-state reaction zones. Such tools might also be further extended to larger length scale investigations such as rheological or cell migration studies at the level of cellular populations.

The main criticism of this work may be whether such a deployment is necessary over simpler methods. I would argue yes. As indicated, Bayesian methods have only just started to be applied to single particle tracking data despite a prevalence in other fields such as signal processing, finance, bioinformatics and other areas of applied machine learning applied to stochastic processes. However, most of the methods have been on long well-sampled tracks. With the advent of non-perturbing *in vivo* experimental methods where the data is typically shorter and noisier, applying the techniques of Bayesian inference offers succinct advantages. As a multitude of microscopic experiments rely on tracking experiments, a proposal for model selection and parameter inference in such a framework will offer distinct advantages. It is open ended, algorithmically rather than analytically driven, and operates in a more intuitive framework to my mind.

3.7 Future Work

There are three key ways in which this work could be improved in decreasing order of impact. The first, which will not be discussed in detail is to repackage the code and rewrite the algorithms used into a programming language such as `C/C++`. Although this wouldn't change the workings of the model one issue I found was the speed of the PDF inference was slow; the computational bottleneck in evaluating the numerical integrals involved at a high sampling rate. This is undoubtedly due to the poor code design and did not take advantage of e.g. parallelisation techniques or GPU (Graphics processing unit) work. This is why the confinement PDF was not applied as it was very slow to evaluate in the code framework I have developed. Improving this, however, neatly leads onto the

second model extension that would appropriately utilise a more efficient code base, and is related to the unmentioned hidden stage in statistical inference as set out by [184].

The model developed in §3.3 had parameters that parametrised the priors. These were the λ that set the shape of the exponential decay regulariser i.e. how strong a belief that confinement should fit for a certain time. A sensitivity analysis was performed in order to evaluate the effect of these parameters in §3.4.2. The *shapes* of these prior distributions were parametrised but the functions themselves were fixed - i.e. there was no distribution about these hyper parameters (or a change in the regularising function). Referencing these parameters as λ then in an consistent framework, these can be updated in a manner of the form Equation 3.56.

$$P(\lambda|\mathcal{D},\mathcal{M},\mathcal{R}) = \frac{(\mathcal{D}|\lambda,\mathcal{M},\mathcal{R})P(\lambda)}{P(\mathcal{D}|\mathcal{R},\mathcal{M})} \tag{3.56}$$

The choice of initial priors of λ can be Gaussian or Gamma distributions with a mean/mode at the default values as listed in Table 3.3. At present, these λ are (judiciously) chosen to identify confinement with the length-scales typically associated with *E. coli*. Allowing these hyper parameters to update (and therefore the priors they parametrise) in a quantitative manner would both reduce the need to fix these parameters *a priori*, but also to be able to mechanically apply BARD to different data sets in a consistent framework. Reference [184] details the caveat on how this assumption can be made given that this prior hyper parameters is updated through a posterior on $\mathcal{D}$.

The next step would be to calculate the posterior of w, which is marginalised over the λ. This marginalisation integrates over all possible values of these hyper parameters (also known as nuisance parameters) marginalising them. The end result would produce an evidence term that was independent of any particular λ, in a similar manner that the evidence terms here are independent of any particular value of parameters w.

The third improvement, would be to use more realistic distributions as appropriate. For example, the noise term that predicts the dispersion about the MSD was fixed for all models; when actually I would expect this dispersion to change between differing modes. Similarly, as GMM distributions

was used to cluster parameters, but as all of these were positive-definite and we've already stated these as gamma distributions, a gamma mixture model may be more appropriate.

On top of these model improvements, the BARD model can be deployed to investigate different models of subdiffusion detailed in the introduction. It is likely that only a PDF model could be used to achieve this, due to the similar MSD profiles of anomalous diffusion. However, as indicated, the PDF method is slow. Subsequent chapters use the MSD method entirely because of this. However, the PDF method offers advantages in that it uses the full information from the propagators, rather than moments of the distribution. This bypasses issues with statistical averaging and uncertainty about the moments. However, the MSD method was sufficient for me to continue using it in the next chapters, although I downplay the discussion of anomalous diffusion in them, and focus on confinement.

Outside of improving BARD itself, one other useful avenue of research to pursue would be to validate BARD through the use of a simple control system. This would be a single or multicomponent membrane, where the behaviour is relatively more understood than that of *in vivo* systems, but more realistic than that of simulation. A model membrane system would have the advantage that the mobility measurements inferred by BARD would also be measurable directly in a model membrane system [16]. Preparation of such vesicles is not technically demanding to achieve (relative to *in vivo* systems). In addition to this, it would be useful to test the performance of BARD on long duration tracks (beyond the typical scope of *in vivo* SPT experiments). This can either be through simulation or experimentation, and a vesicle based control system may offer this.

3.8 Chapter Summary

- Reviewed present models of diffusion of integrated membrane complexes.
- Reviewed present methods in discriminating diffusive behaviour
- Outlined the principles and methods in Bayesian inference and model selection used in BARD
- Developed the BARD model; a Bayesian approach to ranking diffusive behaviour
- Validated the BARD model:
  - Over a wide parameter regime
  - Applied to realistic noisy heterogeneous data
  - Through a sensitivity analysis of algorithm parameters and data-length
  - on simulated switching between two different diffusion rates
  - on identifying subpopulations of free diffusion. This also demonstrated accurate parameter inference.
- Discussed the limitations of BARD and potential future developments.

Chapter 4

Characterising *Escherichia Coli* Biological Membrane Heterogeneity through a non-native transmembrane helix and fluorescent lipid probes

Abstract

The processes which drive the partitioning of proteins into the plasma membrane is one of the key questions in membrane biophysics. The basis for understanding membrane structure was built around the classic Singer-Nicolson model. In this model, proteins are embedded within a fluid lipid bilayer and able to diffuse laterally within a sea of lipid. However, emerging experimental data are supporting a more complicated membrane environment where the underlying membrane heterogeneity requires models beyond the Singer-Nicolson model. Such heterogeneity can emerge from a variety of elements within the membrane environment including the lipid microphase separation of the membrane, cytoskeletal interactions and membrane crowding. Here, I report lipid

and protein diffusion in the plasma membrane of live cells of the bacterium *Escherichia coli* using Total Internal Reflection Fluorescence Microscopy. In these experiments, lipid and protein mobility within the membrane were probed by visualising an artificial fluorescent lipid and a simple model membrane protein consisting of either single or multimers of a simple non-native membrane-spanning transmembrane alpha-helix with a Green Fluorescent Protein (GFP) tag on the cytoplasmic side. In addition to the size variation of the helix probe, I also effectively perturb the membrane by growing *Escherichia-coli* at different growth temperatures. This modulation in growth temperature is reported to alter the lipid composition of the membrane and thereby alter the critical phase transition temperature of the membrane. Usually, this phase behaviour is reported by fluorescent lipid probes. In these experiments, I investigate how proteins deviate from simple Brownian motion as suggested by the Singer-Nicolson model and partition into the putative underlying microphase separated mobile membrane domains or 'patches'. I find these protein probes partition into domains of size $\approx$ 100 nm that are either mobile or pinned, with size characteristics that support the origins of microphase separation as emerging from the underlying phase behaviour.

4.1 Introduction

As reported in Chapter 1, I discussed the putative origins of membrane heterogeneity. This heterogeneity however still needs to be tightly regulated. *E. coli* membranes, for example, are adapted to the growth conditions of the bacterium. This is in order to maintain membrane fluidity about the expected temperature range. This is known as homeoviscous adaptation. This adaptation means that the biological growth temperatures are reported to alter the lipid composition of the plasma membrane. In two such examples with *E. coli* the authors in [59, 192] showed that the lipid composition of the membrane was dependent upon the growth temperature. This was achieved by comparing different growth temperatures to the experimentally determined phase transition temperature of the membrane. The transition temperatures were typically around 10^oC below the growth temperature [193, 43] (Figure 4.1). Model membrane experiments have also suggested that

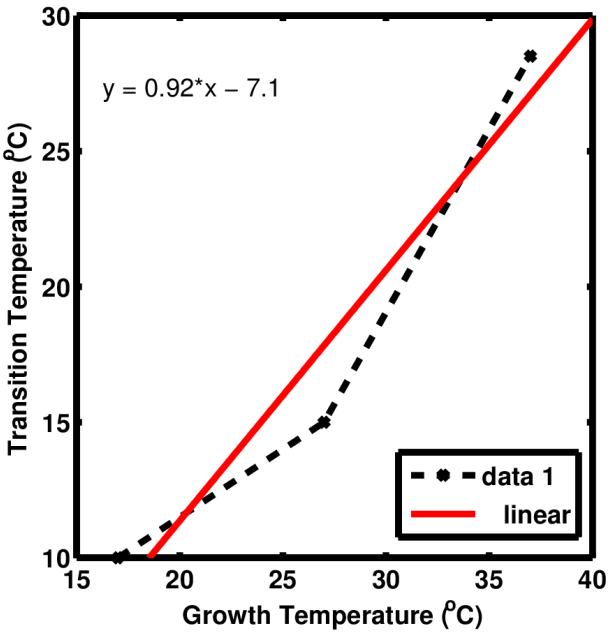


Figure 4.1: *Variation of the transition temperature with the growth temperature in E. coli. Data taken from reference [192]. The growth temperatures used in reference [192] are at 17,27 and 38 °C, similar to the growth temperatures used in this report of 15,25,39 and 37 °C. The red line is a linear fit with the equation in-picture where x is the growth temperature and y is the transition temperature.*

the plasma membrane may be 'tuned' to reside near these critical points [50]. Live cells are typically known to exhibit phase behaviour over biological temperature regimes [194]. The origin of this phase transition is well understood from such model membrane experiments and *in silico* models. In *in vivo* experiments on *E. coli*, it has been observed that this transition temperature regulation is by the relative composition of lipids. It is the balance of those constituting a bilayer and those forming non-lamella structures [59, 43, 195]. These adjustments keep the membrane plasma in a window [43, 196] between a gel crystalline phase, and a non-lamellar phase. These represent how lipid molecules pack. In a gel phase, lipids are tightly packed, and relatively rigid. In a non-lamella phase, the bilayer breaks down. This property of a modulation in the critical temperature due to a change in the growth temperature is a property I exploit in this chapter.

Work on model membranes have suggested that membranes are adjusted to reside near such critical

points [197, 55]. This is intriguing, because it may relate to observed membrane heterogeneity, such as the microphase separation observed *in vivo*. However, assuming that the underlying lipid compositions govern the formation of biological membrane domains, it is not clear how sub-micrometre domains are prevented from ripening into larger domains. Neither is it clear how sub-micrometer domains are stabilised when entropically disfavoured. The exterior temperature relative to the plasma membrane lipid phase transition temperature determines the scenario. At temperatures above the phase transition temperature, domains are disfavoured. At temperatures below the phase transition temperature, macroscopic sized domains are favoured. One hypothesis is that the domains are transient [61, 50]. However the lifetime of such domains are likely to be much less than the lifetime of domains observed *in vivo*, which again implies some form of stabilisation is occurring. The key motivation for research into this area is that these microphase separated domains or membrane 'patches' may act as protein sorting centres, corralling proteins into 'reaction centres' [48, 36]. Therefore, investigations into the relation between protein partitioning into membrane patches and the origins of the underlying composition is of substantial importance.

In the introductory Chapter 1, I reported a novel helix membrane protein as being an ideal protein based membrane probe; helix1021-GFP. In this Chapter, I use these probes to investigate how such ideal probes partition into the membrane. The helix probe is a simple non-native trans-membrane with a cytoplasmic GFP attached by a short linker. The helix has been shown to partition nearly exclusively into the plasma membrane of *E. coli* rather than the cytosol. As it is non-native, it is not subject to specific *in vivo* control. This, therefore, allows the protein to diffuse through the plasma membrane and partition within putative membrane domains under entirely passive processes. Our lab has four different sizes of these helix proteins, existing as different multimers built from different repetitions of the transmembrane helix section motif. This allows me to explore the size dependence of protein diffusion in the plasma membrane. Two experiments using this helix protein are performed using TIR microscopy. In the first experiment, four different sizes of helix proteins were used. The sizes are controlled by the number of transmembrane elements as depicted in Figure 4.2. These will be referred to as the 'x1','x2', 'x4' and 'x6' helix proteins, corresponding to the

number of transmembrane elements. In the second case, the helix protein molecular weight was fixed, solely using helix-x1, but the growth temperature of *E. coli* was varied thereby modulating the critical temperature. An additional final experiment was performed using the fluorescent lipid analogue BODIPY. This lipid tag allows me to visualise how the underlying lipid behaves. As also reported in Chapter 1 and in the working paper [3], the lab of Conrad Mullineux reported that the phase behaviour of *E. coli* membrane can be investigated using the BODIPY probe.

The different sizes of the helix protein provide an ideal test model for comparing the difference in diffusion rates for proteins. There have already been investigations into the size dependence of protein diffusion in the membrane [198][199][18]. However, these were often using either large tracer tags such as gold particles, or were of proteins that were native to the system. The most widely accepted model to date is the Saffman-Delbrück [9] model of diffusion, although recently this has been improved on [200] by accounting for larger membrane inclusions. It is however the use of the helix probe under varying membrane growth conditions that is the key result of this report. In these experiments, I considered the findings from model membrane experiments that considered how membranes were 'tuned' to reside near critical points. The authors noted discontinuities about the transition points [50]. My intention was to investigate this *in vivo*, using the toolkit developed in Chapter 3. Accurate identification of confinement [50] and anomalous diffusion [68] was key to this. Reference [50] identifies properties such as the line tension which reduce to zero as the transition temperature is approaches from a negative temperature difference. Consequently, I expect observed confinement sizes of any lipid domains to increase in negative temperature difference, and decrease in a growing positive temperature difference. Other experiments have suggested that there may be discontinuities about the transition temperature [60], so I use growth temperatures that have transition temperatures on both sides of the imaging temperature.

4.2 Materials and Methods

Full details of the helix protein are given in §1.5.2 in Chapter 1. In summary, a model helix protein (helix1020-GFP) was constructed by a gene coding from a membrane based protein in *Syncechocystis* with no known native function and no identified homologue in *E.coli*. The ends of the predicted transmembrane helix lack any of the two-residue motifs that are important for specific interactions with phospholipid head groups. Helix-1021-GFP is non-genomic but is expressed in *E. coli* from an arabinose-inducible pBAD24 vector. The arabinose-inducible promoter PBAD is subject to all-or-none induction, in which intermediate concentrations of arabinose give rise to subpopulations of cells that are fully induced and uninduced [201]. It is known to localise in the cell membrane through SDS-PAGE fractionation experiments [3]. It was also seen in my data by a halo appearing in epi-fluorescence as seen in Figure 4.2. With the uniform excitation in epi-fluorescence, the entire membrane is excited causing stronger emission along the periphery of the cell. The estimated size of these proteins were estimated by a western blot by collaborators [3], where a GFP-helix protein of the size 28-29 kDa was identified. Subtracting the size of free GFP (26.9 kDa) [83, 79, 202] provides an estimate of the x1-helix molecular weight at around 1-2 kDa. Although the model membrane protein carries a relatively large GFP tag on the cytoplasmic side, its diffusion is expected to be mainly controlled by the environment of the transmembrane domain, since the viscosity of the cell membrane is significantly greater than that of the cytoplasm.

In order to vary the phase transition temperature the following protocol was used. For the Helix1021GFP 'x1' strain, cells were grown in Luria-Bertani (LB) medium [203] aerobically by shaking overnight at 37^{o}C, and supplemented with 50 µg/ml ampicillin for correct antibiotic-resistant colony selection. Cells were diluted by 1:100 from the saturated cultured into M63 minimal media for sub-culturing, and were grown to mid-exponential phase at varying growth temperatures. L-arabinose was added to the culture at a final concentration of 2 mM. Cells were injected into a 5-10 µL flow-cell with poly-L-lysine-coated glass coverslips as the lower surface, allowed to settle for 10 min, washed with excess M63 and incubated with a 0.1% suspension of 202 nm diameter

latex microspheres (Invitrogen Ltd., Paisley, UK) for 2 min to mark the coverslip surface, and washed with excess M63 buffer. Imaging protocol is as in 2.3.3, with flow cell preparation as in 2.3.3. Deviations from the growth protocol were in the incubation times. Cells grown at 37^{o}C and 30^{o}C were grown for 5 hours each. Cells grown at 25^{o}C were grown for 6 hours. Cells grown at 15^{o}C were typically grown for approximately 24 hours. Similarly, the different helix multimers had some different required incubation time. All were grown at 37^{o}C, with the 'x2' and 'x4' grown for 5 hours each. but the slower growing 'x6' strain was incubated for approximately 8 hours in order to reach the same optical density.

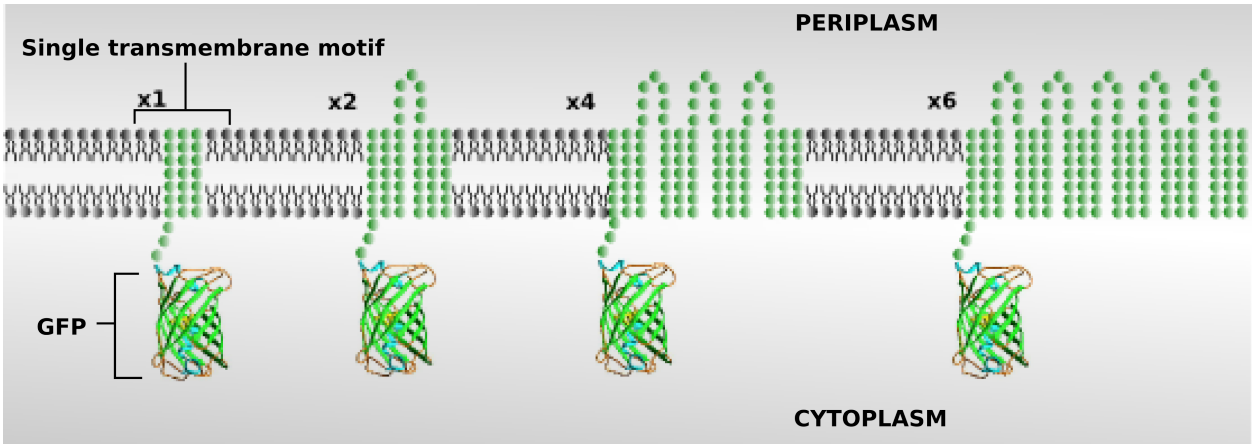
Cells grown in L-B after heated shaking were left in a temperature controlled cooled environment ($\approx 5^o$C). However, for cultures in the incubation growth phase prior to imaging (in minimal media with arabinose induction), these cultures were prepared for imaging immediately at the end of incubation. Uncultured flow-cells were prepared before this phase ended, but there was typically a lag time before these cells are imaged. This lag time consisted of incubating cell culture in the flow-cell in a humidity chamber (20 minutes), washing (2 minutes), and, where applicable, an additional round of incubation (5 minutes) and washing (2 minutes) of latex beads. Occassionaly, slides prepared were not suitable for imaging (no cells, cells damaged, excessive fluorescence to name typical problems), so the process was restarted with a new flow-cell (and a backup flow-cell) from the incubated stock cell culture. Cell culture is stored in a fridge during this period, but destroyed after each daily imaging period and not used in later experiments. The typical lag-time across all strains between incubation and imaging is between 20-50 minutes.

For comparison with the behaviour of the model protein, an artificial fluorescent lipid, BODIPY FL-C_{12}, consisting of a green fluorophore linked to a 12-carbon fatty acyl tail. This was used to probe membrane fluidity in a cyanobacterium [204]. They have been shown to localise into the membrane by observing a halo when viewing in confocal imaging [3], consistent with localisation in the membrane. Further tests indicated that BODIPY localised to the inner cytoplasmic membrane. Two different cultures were prepared at high (1µm)and low concentrations (0.2 µm)of BODIPY,

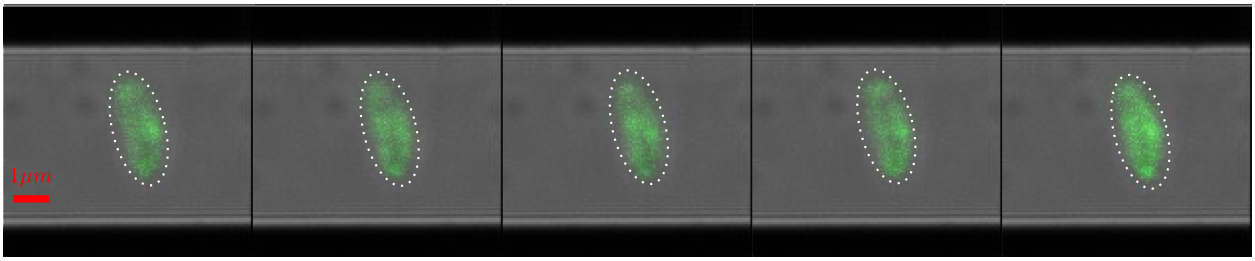
in M63 minimal media. A cell culture was incubated with an appropriate volume of 10mM stock solution of BODIPY (Invitrogen), the cells were washed down repeatedly with L-B, centrifuged and then all resuspended in M63 after another washing phase. All cultures were grown to mid-exponential phase ($\mathrm{OD}_{600}nm = 0.3 - 0.4$).

The experimental setup was that as reported in Chapter 2. Illumination was with a 473 nm laser with fluorescence emission expected between 500 and 527nm and imaged at 25 Hz with either a 512x512 52.8nm (iXon DV860-BV, Andor Technolog) or 128x128 35.6nm/(iXon DU897-BV, Andor Technology) pixel, cooled, back-thinned electron-multiplying charge coupled device camera in frame transfer mode. Images were sampled for around 10 s in both epifluorescence and total internal fluorescence excitation modes. Acquisition data were processed by image analysis algorithms to identify spots and their trajectories as detailed in Chapter 2.

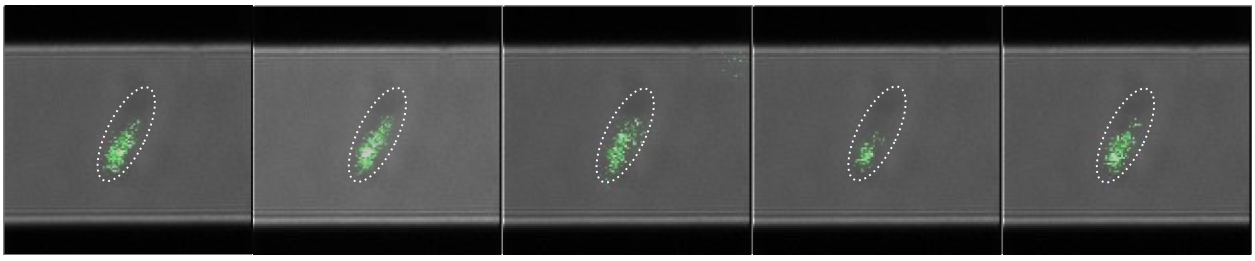
Where appropriate, the growth temperature is converted into the critical temperature by interpolating the data in Figure 4.1. This was a simple linear fit to the prior published data, with which other transition temperatures at other growth temperatures was interpolated. Ideally, these experiments would be repeated under the imaging and growth conditions performed here, however this simple correction is sufficient to investigate putative trends.



(a)



(b)



(c)

Figure 4.2: *Helix protein.* ***A)*** *Each multimer of the helix protein has a GFP attached to it on the cytoplasmic side. The helix protein has four different molecular weights by repeated single transmembrane motifs. Helix protein imaging sequences.* ***B)*** *Epi-fluorescence imaging. The presence of a halo appearing indicates membrane localisastion.* ***C)*** *TIR images for TIR illumination of the helix-x1 protein. These images also show the higher contrast images possible with TIR.*

4.2.1 Analysis

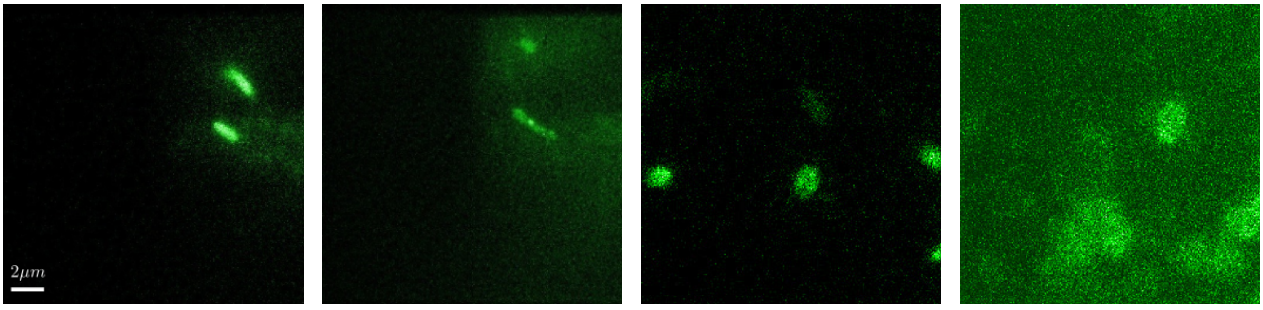
The BARD algorithm (Chapter 3, [1]) was applied to both the helix and BODIPY datasets. For each dataset I compare the model ranking, estimated stoichiometry and the inferred diffusion and confinement values. These parameters are those defined in Chapter 3. These are the weighted kernel density estimate (Equation 3.51), the Brownian diffusion coefficient (Equation 3.21), the confined diffusion coefficient and the confinement radius (Equation 3.24), and the respective model beliefs $P(B)$ and $P(C)$ as defined in Equation 3.32. Although the arabinose concentration was fixed in the growth protocol, there were different growth conditions for each dataset. This was in order to obtain a mid-logarithm growth phase culture. Therefore, instead of comparing the absolute stoichiometric values between datasets I introduce a stoichiometric ratio. This is used to compare the different stoichiometry levels in inferred-Brownian and inferred-confined tracks. It is defined by a ratio $R[0,1]$ and is determined by the ratio of the mean Brownian stoichiometry S_B and the mean confined stoichiometry S_C for each dataset. It serves as a measure of propensity of partitioning into immobile or mobile environments respectively. It is given in Equation 4.1:

$$R_{BC} = \frac{S_B}{S_B + S_C}. \tag{4.1}$$

with an error term given by quadrature error propagation of the standard error σ_{S_B} and σ_{S_C} given by Equation 4.2

$$\sigma_R^2 = R^2 \left(\frac{\sigma_{S_B}^2}{S_B^2} + \frac{\sigma_{S_B}^2 + \sigma_{S_C}^2}{(S_B + S_C)^2} \right). \tag{4.2}$$

Other errors were detailed in Chapter 2 and Chapter 3. Stoichiometry error estimates are propagated forward from the estimated errors in the TIR calibration. Parameter uncertainties are the standard deviation of posterior distributions. Where the algorithm doesn't converge, S.E.M estimates are used. This occurred approximately 1-2% of the time. Experimental resolution is calculated for the average SNR and centroid localisation uncertainty as given in Chapter 2, Figure 2.16.



(a) *(b)* *(c)* *(d)*

Figure 4.3: *a) Helix1021-GFP at high promoter concentration (10mM arabinose) b) Helix1021-GFP at low promoter concentration (1mM arabinose). At this level of expression contrast is sufficient to resolve individual spots. c) and d) BODIPY incubation under two different concentration levels. . At low concentrations, putative spots are found that are identified by the tracking algorithm. At high concentrations (d), spots are much less discernible as both cellular fluorescence and background noise increases. Spots are resolvable at low concentrations (c).*

4.3 Results

In this section, I outline the results of the three different experiments. These are the SPT experiments on two types of helix protein probe experiment, and the second is the fluorescent lipid protein probe experiment. First, I discuss the characteristics of the probe itself [3] in comparison to the behaviour of the fluorescent lipid and find in both cases that they partition into mobile membrane patches. Second, I investigate the stoichiometry of the patches with respect to assorted mobility parameters. In the subsequent sections I discuss how the average mobility data vary across data sets, considering how the different model beliefs, mean diffusion coefficients, mean confinement sizes and stoichiometry vary. These are with respect to the size variation of the helix protein at different multimer states and then followed by the variation of partitioning under different growth temperatures. I summarise the mobility analysis in Table 5.1.

4.3.1 Lipid and protein mobility in the plasma membrane of *E. coli*

To investigate the partitioning and mobility of membrane probes I compared the diffusion and mobility of BODIPY and helix1021-GFP using video-rate TIRF microscopy. When expression of

the helix1021-GFP is strongly induced (10mM arabinose) a uniform distribution of fluorescence was found (Figure 4.3 a). However, when using weaker induction, GFP flourescence was found to be concentrated in distinct mobile foci in the membrane (Figure 4.3 b). In a similar manner, the concentration of BODIPY was varied between high (Figure 4.3 c) and low (Figure 4.3 d). The fluorescence lipid analogue also appeared to have a spotty appearance, although these data were noisier. In both cases there was no measurable bias to specific regions of the membrane around the cell. This is relevant because curvature is known to mediate the localisation of lipid and protein in bacterial membrane [69]. The lack of the formation of superclusters - spots of extremely highly concentrated fluorescence - suggests that an aggregation effect is not occurring in the low concentration data in each case.

In the next step, I quantified the mobility data of both the BODIPY and the helix-x1 datasets. The following properties of the datasets were found. Starting from the mean squared deviation (Figure 4.4 a)), I quantified the model belief of each track in the dataset (the $P(B), P(C)$ etc. detailed in Chapter 3), into a set of diffusive models. These were anomalous, Brownian, confined and directed models. I also found the weighted kernel density estimates (WKDE) of each model parameter, such as the diffusion coefficient (Figure 4.4 b). Then, the variation of appropriate model parameters with respect to others; such as the variation of the diffusion coefficient versus the inferred confinement size, or the diffusion coefficient versus the stoichiometry (Figure 4.4 c). The equivalent BODIPY data are presented in Figure 4.5. However, as no stoichiometry calibration was performed on the BODIPY data, instead of comparing the stoichiometry I plot the variation in the estimated intensity of each spot (Figure 4.5 b). In a similar manner, I compute the WKDE of each parameter such as the confinement size (Figure 4.5 c).

The mean Brownian diffusion coefficient of BODIPY was 0.009 $\pm$ 0.005 $\mu m^2/s$ (one s.d.). Of those confined, the inferred domain was of diameter 60 nm (Figure 4.5 c). This is within the estimated centroid localisation accuracy ($\approx$ 70 nm) for the typical SNR of the BODIPY dataset so I cannot separate whether these are confined or immobile. The mean diffusion rate of the helix-x1 data were around 0.03 $\pm$ 0.007 $\mu m^2/s$(one s.d.).

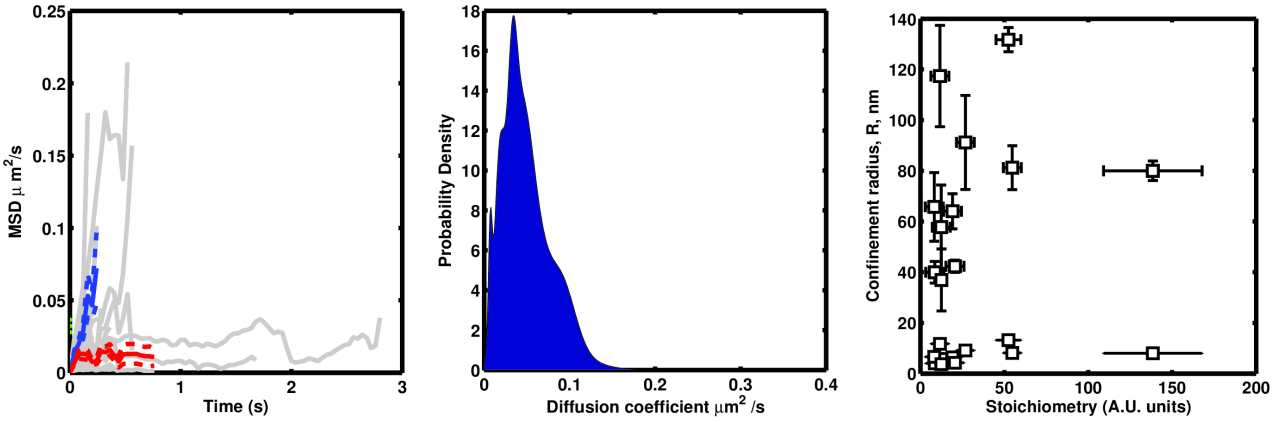


Figure 4.4: *TIR data of a single 'x1' TIR dataset. a) time-averaged MSD traces. The gray traces represent individual tracks. Coloured traces represent averaged tracks of different diffusion modes plus and minus one standard error. Average tracks are not plotted unless there are at least three tracks at time t. The key is blue (Brownian) and red (confined). b) The weighted kernel density estimates of the Brownian diffusion coefficient for all tracks c) Inferred stoichiometry vs. confinement radius for confined tracks.*

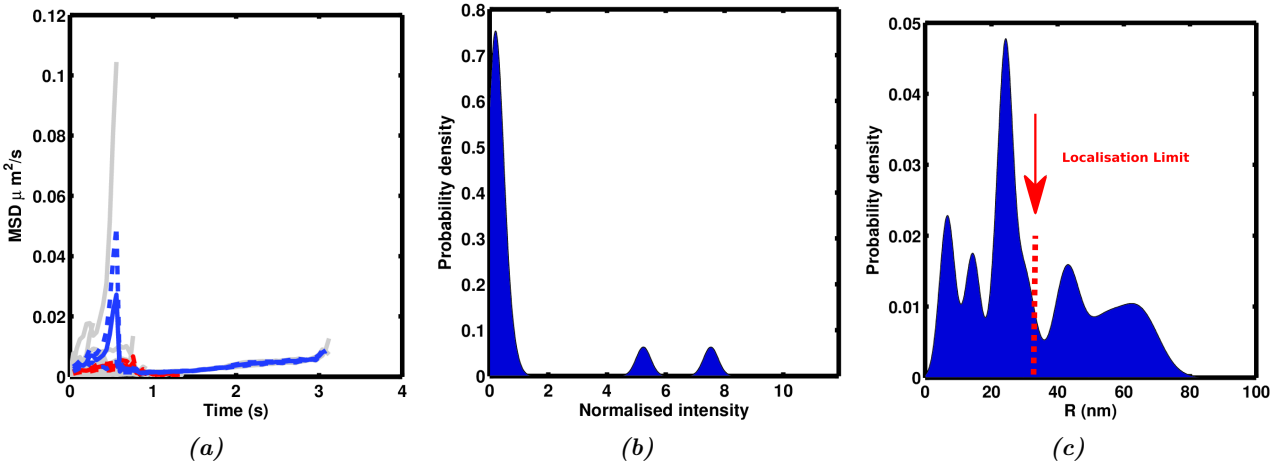


Figure 4.5: *BODIPY analysis.* ***a)*** *Averaged tracks (Key: Blue: Brownian, Red: Confined).* ***b)*** *Normalised Intensity. As a stoichiometry assay was not done for BODIPY, the estimated initial intensities are normalised by their mean ($N = 17$) and plotted in as a Kernel Density Estimate with the error distribution given as one S.E.M. c) The WKDE of the confinement radius. The typical averageinitial localisation error is marked (dashed red line), but it should be noted that this error increases as fluorophores photobleach.*

4.3.2 Spot stoichiometry has no relation to other mobility parameters

To determine the effect of the stoichiometry on the various model parameters, I looked at a particular dataset. Using one of the largest datasets, the helix-x1 grown at 25^o, I compared the relationship of the spot stoichiometry with the confinement probability, the model diffusion coefficient and the confinement radius (Figure 4.6). In the case here, the stoichiometry has no predictive power for either the confinement probability, the model diffusion coefficient or the confinement radius[1]. Under a patch model, this is expected. The reasoning for this is as follows. Recalling that the estimated percentage area occupancy of helix protein in a patch ($100 < 1\%$), then it would require substantially greater variation in the stoichiometry in order to affect the occupation percentage. Secondly, as the molecules appear not to aggregate (due to the lack of superclusters with strong induction), the molecules are probably in a loose pool in the patch. Therefore, diffusion rates of the tracked spots are unlikely to be strongly affected by the stoichiometry, as the observed PSF is an aggregation of multiple single GFP.

4.3.3 Overview of size and growth temperature dependence

To investigate the dependence on size, the dependence of the mobility parameters with respect to the helix size (the number of transmembrane helicies) was investigated. This was performed in TIR. Cells expressing the x1, x2, x4 and x6 helix proteins respectively were all grown at 37^o. In Figure 4.8 the BARD-inferred TIR data is displayed for each helix strain. Here, I see that there is no correspondence between the helix size and the inferred probability, as both the x1 and the x6 model beliefs are equal with uncertainty (Figure 4.8 A). The trend in the diffusion coefficient appears to be increasing with respect to helix size, but with only a small difference between the x1 and x6 (Figure 4.8 B). However, there was no statistical difference between the distribution of Brownian diffusion coefficients of all tracks between the two datasets (Student's t-test, 5%). Similarly, there was no statistical difference between the confinement sizes of x1 and x6 (Figure 4.8 C). Stoichiometry ratios

[1]However, as will be seen in the next chapter for different data, single particle tracking is sufficiently accurate to see the relation between stoichiometry and diffusion. The difference in those data is that the fluorescent proteins are aggregated, and not in a diffuse pool as estimated here.

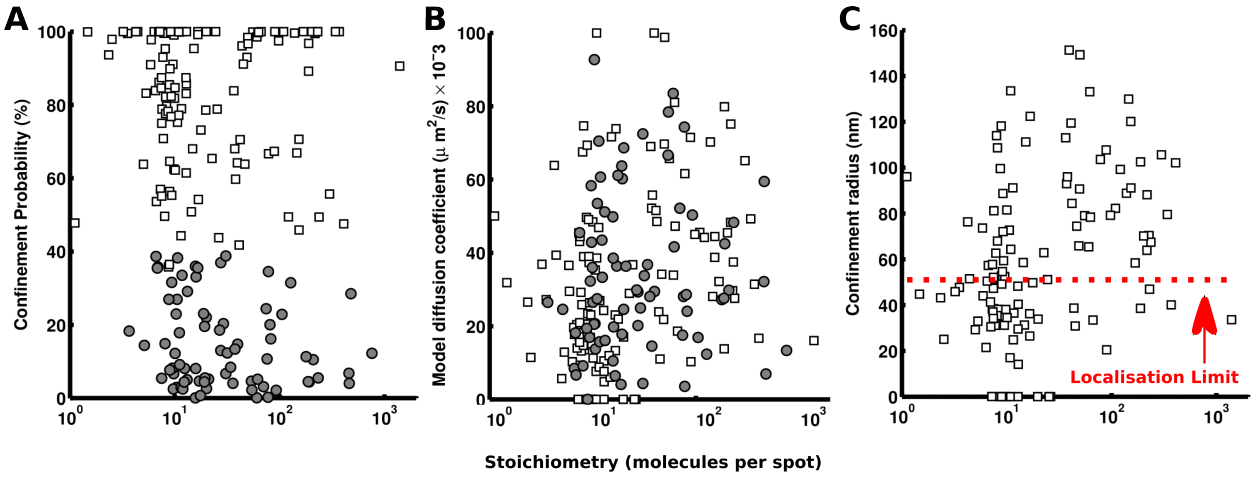


Figure 4.6: *Stoichiometry per spot versus measured parameters. Key: Brownian (grey circles), Confined (White squared).* ***A)*** *Stoichiometry versus the confinement probability.* ***B)****Stoichiometry versus the model diffusion coefficient.* ***C)*** *Stoichiometry versus the confinement radius. In each case, there is no clear association with the stoichiometry. The typical averageinitial localisation error is marked (dashed red line), but it should be noted that this error increases as fluorophores photobleach.*

Table 4.1: *Helix protein mobility analysis, indicating proportion of tracks in each dataset being identified as either anomalous, Brownian, confined or directed of the analysed TIR datasets.*

Dataset	Proportion of tracks inferred in each diffusion model (%)				
	Anomalous	Brownian	Confined	Directed	Number of tracks
15 ^{o}	0	69	30	0	13
25 ^{o}	11	34	55	0	235
30 ^{o}	13	42	45	0	167
37 ^{o} / x1	5	45	50	0	22
x2	30	50	20	0	10
x4	20	22	57	1	137
x6	42	45	51	0	96
BODIPY	30	24	47	0	17

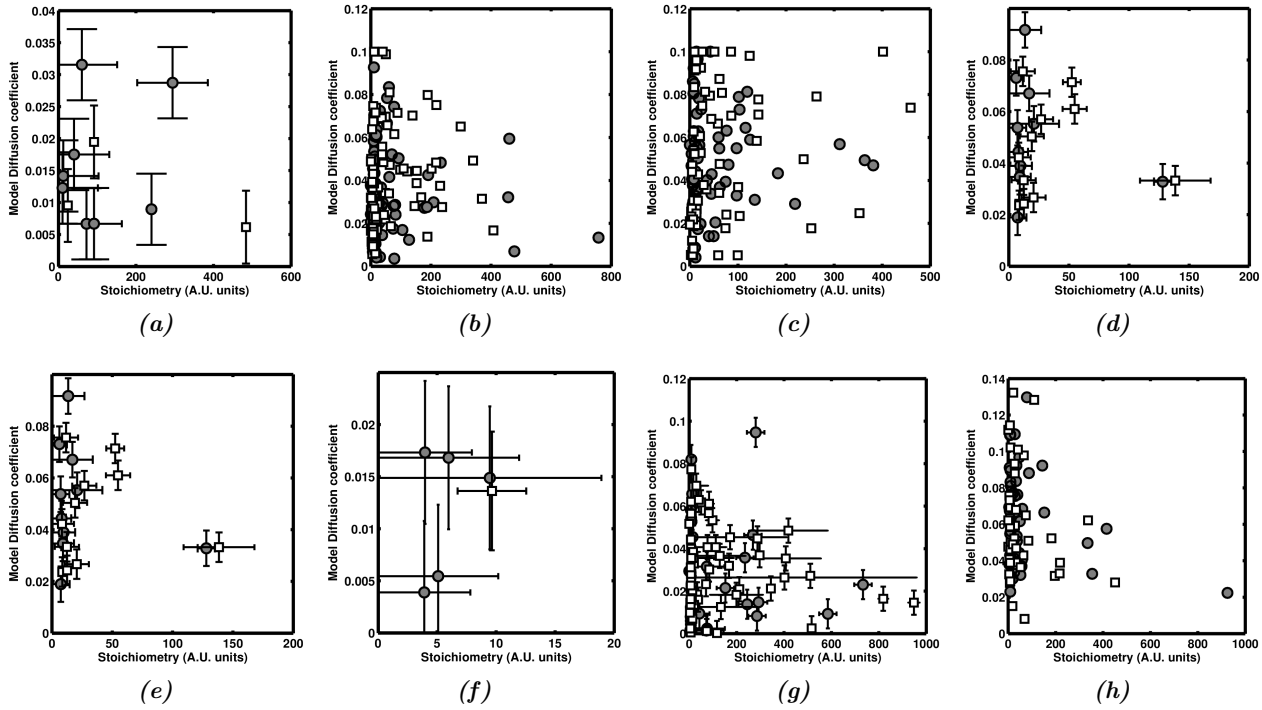


Figure 4.7: *Comparison of the stoichiometry versus the model diffusion coefficient for all TIR data analysed. a)-d) are 15,25,30 and 37°C datasets, and e)-h) are the x1,x2,x4 and x6 datasets. No clear trends or clustering is seen.*

were equal for the x1, x2 and x4 datasets, except the x6 was greater (Figure 4.8 D).

To investigate the dependence on the critical temperature, the dependence of the diffusion coefficient to the *E. coli* growth temperature was investigated. This was performed in TIR. Cells were grown at 15, 25, 30 and 37 ^{o}. In Figure 4.8 the TIR data is displayed for each helix strain. The temperature difference in these Figures are the ambient temperature minus the interpolated critical temperature. I see that there is an increase in mobility with the model belief of confinement $P(C)$ going from 50% at -5 ^{0} temperature difference down to 32% at 15 ^{0} (Figure 4.8 E). The diffusion coefficient has a downward trend, with a peak when imaging just above the transition temperature (Figure 4.8 F). The mean confinement size has a downward trend going 72 nm at a negative temperature difference (-5 ^{o}) to 45 nm at a positive temperature difference (+ 15 ^{o}). Although the -5 ^{o} and the +15 ^{o} datapoints do not statistically separate (due to smaller datasets), the 2 and 7 ^{o} are statistically significant (two-tailed Student's t-test, 5%, Figure 4.8). The stoichiometric ratio was a linear relationship, going from a greater partitioning into confined domains at low temperature difference, to a greater partitioning into mobile domains at high temperature difference.

To estimate the sizes of the mobile patches I consider the point-spread function (PSF) (Figure 4.9). Viewing the PSF, mobile domains (Brownian model) have similar but increased PSFs relative to confined domains. The increased PSF of mobile domains to immobile domains can be attributed in part to the integration error of mobile particles [205, 206, 207]. This is the dynamic localisation uncertainty. The expected ratio between the FWHM (Full Width Half Maximum) of the PSF of mobile and immobile particles was discussed in §2.6.1. It is related by the integration time δt, diffusion coefficient D and single PSF standard deviation s and is given Equation 4.3:

$$R = \sqrt{1 + \frac{D\delta t}{s_0^2}} \tag{4.3}$$

For typical values of D =0.05μm^2/s,s_0=200nm and δt=0.04s this gives a ratio of the PSF width between mobile and immobile domains of around 5%. This is about the difference seen in the PSF plot. This suggests that the mobile and immobile domain sizes have similar distributions in size

(Figure 4.9) after accounting for the dynamic integration error.

I can also estimate the size of the patches by using the PSF. By considering the size of the point spread function of isolated GFP (250-350 nm) (Figure 4.9) C) and considering the size of the point spread function of the observed *in vivo* spots (350-400 nm) ((Figure 4.9 C), I can estimate the size of the patches as being around 100-150 nm diameter. These are in agreement with the observed confinement radii (Figure 4.8 G). As an aside, I can also estimate the size of an isolated GFP PSF by considering the variation of the inferred confinement radius of a single dataset (25 ^{o}) with respect to the FWHM. The intercept estimates the FWHM of a single isolated immobile GFP. The value obtained was 326 $\pm$ 72 nm, in agreement with that observed in isolated GFP (Figure 4.9 C). By considering the typical stoichiometries (Figure 4.6), the inferred confinement sizes of both mobile and immobile patches, and the lack of aggregation and correspondence to the size of lipid domains (Figure 4.3) I consider that the helix proteins are partitioning into domains of diameter 50-150 nm, with average stoichiometry of around 150 $\pm$ 100 (S.E.M.). In the patches observed in these data, the typical diffusion rate of these domains varies from 1-100 $\times 10^{-3}$ $\mu m^2/s$. This is similar to that observed of similarly sized domains, but only in certain conditions. Model membrane raft domains of these sizes 10-100 nm are observed in such GUVs, although these are with cholesterol ([16].

4.3.4 Domain mobility is heterogeneous

For a patch model, I now consider the mobility of the patches as a function of the domain size. The variation of the domain size to the diffusion rate of the putative domain is difficult to determine. The spots are in two forms, mobile and immobile. Mobile spot-patches offer measurements of unconfined mobility but no clear confinement size. Immobile patches offer measurements of confinement sizes but no measurement of the mobility. I attempted to estimate this by correcting for the blurring of the PSF by the mobility at the single-track level (Equation 4.3, converting the PSF to an estimate of the domain size (Figure 4.9) and then comparing to the inferred Brownian diffusion coefficient. This method produces spurious negatively sized domains due to the conversion of the FWHM to the domain size which I discard. This does not effect the trend. The mobility has no clear relation

which would be expected for isolated diffusing domains [16] from the Saffman-Delbrück Equation as defined in Chapter 1:

$$D_T = \frac{k_B T}{4\pi\mu h}\left(\log\frac{\mu h}{\mu' a} - \gamma\right) \tag{4.4}$$

This conversion is done by Equation 4.5. For a spot standard deviation σ, converted into a FWHM by $2\sqrt{2\log 2}$, and converted by the linear fit in Figure 4.9 B parametrised by intercept s_0 and conversion gradient m in $s_0 + Rm$:

$$R_{\text{cor}} \approx \frac{2\sqrt{2\log 2}\sigma - s_0}{\sqrt{1 + \frac{D\delta t}{s_0^2}m}}. \tag{4.5}$$

Within the interpretation of a patch model, there appears to be a population of mobile and immobile patches. These appear of comparable size because when considering the averages, the mobile domains have a FWHM that falls within the correction term implied by the FWHM blurring with respect to the immobile domains. In general, it is not clear what is making these patches immobile, as only the confinement can be inferred. Either the patches are anchored, or other obstacles prevent the diffusion of the patches themselves.

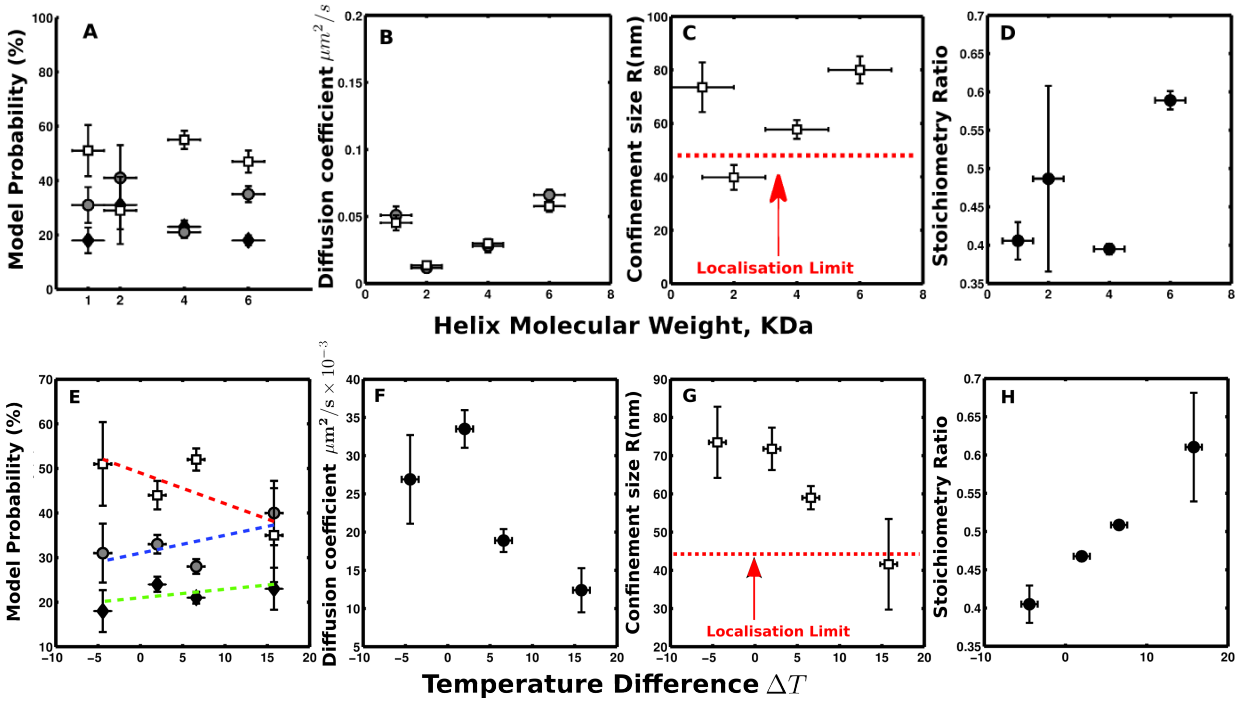


Figure 4.8: *Helix mobility measurements for molecular weight (upper) and growth (critical) temperature dependence (lower). Key: Brownian (grey circles), Confined (White squared), Anomalous (black diamond), all tracks (black circles).* ***A:*** *Mean model probability ranking estimate of BARD with respect to the helix molecular weight.* ***B:****. The variation in the model diffusion coefficient (D_C) and (D_B) for confined and Brownian tracks respectively.* ***C:*** *Confinement radius with respect to helix molecular weight.* ***D:*** *The stoichiometry propensity comparing Brownian and confined modes (Equation 4.1)*
E: *Mean model probability ranking estimate of BARD with respect to the temperature difference. Linear trend fit demonstrates an increase in mobile modes (anomalous and Brownian motion) with respect to increased temperature difference, with a respective decrease in mean confinement probability with respect to increasing temperature difference.* ***F:****. The variation in the Brownian diffusion coefficient for all tracks.* ***G:*** *Confinement radius with respect to the temperature dependence. The general trend is an increasing confinement radius with respect to decreasing temperature.* ***H:*** *The stoichiometry ratio between Brownian and confined modes with respect to the temperature difference.*

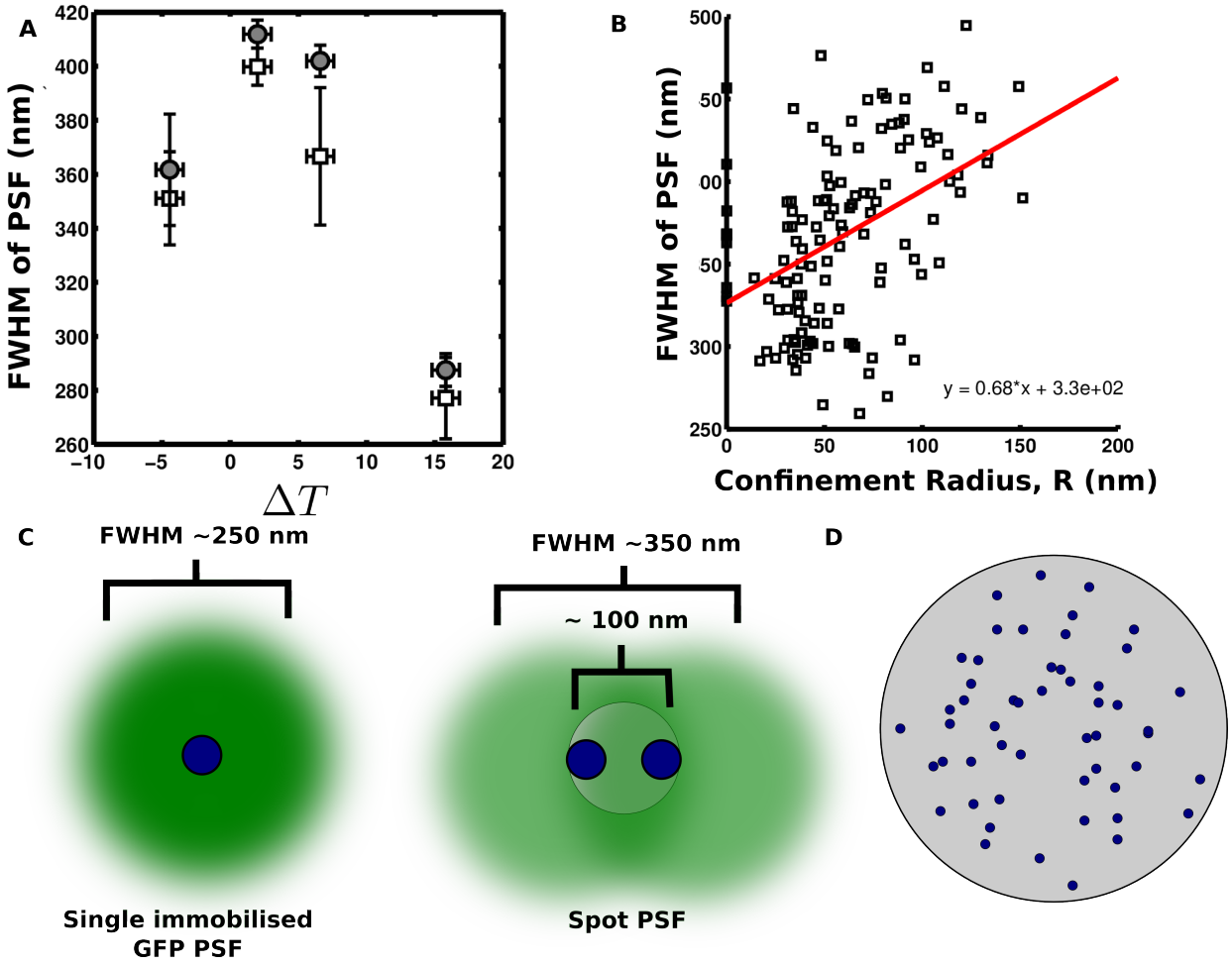


Figure 4.9: *Helix partitioning model.* ***A:*** *The FWHM of the PSF for only Brownian and confined modes. In each case, I see that the FWHM for brownian motion is higher than the respective confined spot size FWHM.* ***B:*** *The variation of the FWHM of the PSF with respect to the inferred confinement radius.* ***D:*** *The PSF for a single immobilised GFP and a combined PSF.* ***D:*** *The helix protein partitions into microphase separated lipid domains of around 100* nm. *They exist in two forms; mobile and immobile. The size of these domains are related to critical phase transition temperature of the system.*

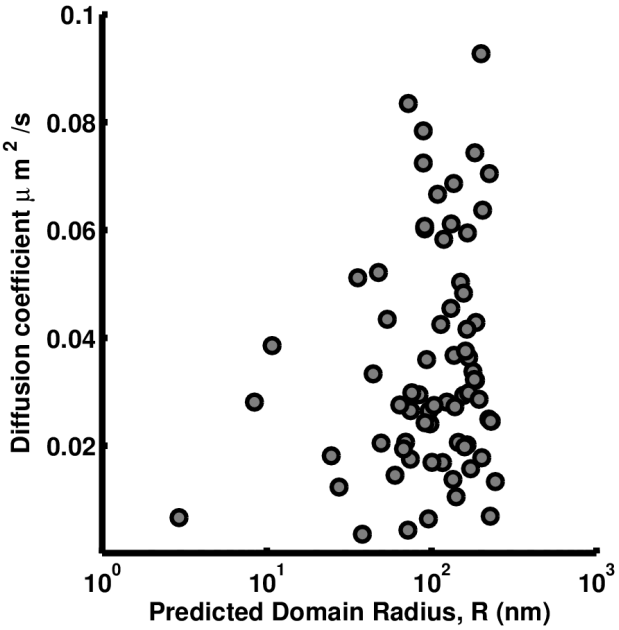


Figure 4.10: *The relation of the extrapolated domain size to the Brownian diffusion spots. The Saffman-Delbrück Equation predicts log-sensitivity between the domain radius and the diffusion coefficient.*

4.4 Discussion

In this report, I investigate the diffusion of protein and lipid *in vivo*. This is in contrast to model membrane systems that cannot recreate the full native biological context. I used two forms of fluorescent probes. The first was a protein based membrane spanning α-helix with a GFP reporter domain predicted to be exposed on the cytoplasmic side of the membrane. The protein localises to the inner cytoplasmic membrane, and the GFP tag allows for the use of TIR to perform single particle tracking at high-contrast video-rate imaging. The second probe was a lipid based probe. This was the BODIPY FL-C_{12}, a fluorescent lipid analogue with a 12-carbon fatty acid tail. This preferentially localises to the plasma membrane so that I can compare the diffusion of both protein in the same membrane. Although earlier experiments (Chapter 1) show that BODIPY followed the expected temperature behaviour, in this report, I show that BODIPY can be seen to be 'spotty' (with observable points of relatively high intensity) at low concentrations. This indicates a putative heterogeneous distribution of the lipid at low concentrations. Given the appearance of spots, I establish that the appearance of these spots is not just due to the emergence of a heterogeneous profile due to the low concentration, but are an actual heterogeneous distribution of the lipid.

I also reported the use of an ideal membrane helix probe. Two experiments were performed. One was studying the diffusion of the helix protein at different multimer levels; with different number of repetitions of the transmembrane helix motif. The second, was investigating the behaviour of partitioning of the helix protein into the membrane in a pertubed membrane environment. This perturbation was introduced by altering the putative transition temperature of the membrane. This property was not controlled directly, but through altering the growth temperature of the bacterium. This is in order to investigate the behaviour of the partitioning of the model helix protein at different lipid compositions while maintaining a fully native system. This allowed me to investigate partitioning at mobility at approximately constant temperature whilst using a nominally different membrane composition. This kept the energetics of the interactions the same (through similar Boltzmann rates), rather than keeping a fixed growth temperature and altering the imaging

temperature.

The helix protein appears to partition into membrane 'patches'. The reasoning for this is as follows. Under weak induction, the helix protein is present in reduced concentration in the membrane. At higher concentrations these distinct spots of fluorescence are less visible (Figure 4.3. This behaviour suggests that the formation of fluorescent spots is not due to the concentration dependence aggregation observed with over-expressed membrane proteins [208]. Instead the protein segregates into domains between 50-100 nm radius with 150 $\pm$ 100 helix1021-GFP partitioned within (Figures 4.4). The stoichiometry of the fluorescence spots and the domain sizes did not appear to correlate. At higher concentrations, it is likely that domains are not visible due to the drop in contrast as more spots become visible, reducing the average space between spots to less than the optical resolution. For the helix1021 grown at 37^{o}C, the area density of the helix protein into the domain patches is less than 1%.

The next experiment that supported a patch model was the lack of inverse dependence with respect to protein size (weight). In fact, the trend appeared to relate a larger protein molecular weight to diffusion rate. This is surprising, because single particle tracking support a reduced diffusion rate at higher stoichiometry. On inspection, however, there was no statistical difference between the mobility rates of the x1 and the x6 helices, which would offer the biggest difference in mobility.

The lack of dependence on size appears to be that these helix proteins are not at the single particle level. The observable point spread function of the helix protein at large stoichiometry shows that the helix protein are associated at separation distances less than the optical resolution. I have already argued that this is not an aggregation effect because of the lack of super-clusters at high concentration. That there is little size dependence suggests that the spots of the helix protein are not at the single particle level where a size dependence is known. I propose that the helix protein partitions as a pool into a domain patch and that the observable PSF is the collective PSF of multiple point spread functions of individual helix-GFP co-diffusing with the domain diffusion. Further, there is a reasonable case to make that the x2 data, which was erroneous in each mobility measurement, should not be counted, thereby removing the counter-intuitive trends seen. The

reasoning for this is because of the erroneous data, that the stoichiometry was far lower than in other experiments (Figure 4.7), and that the confinement lengths were below the resolution (Figure 4.8 G).

The growth temperature experiments revealed some interesting behaviour of the helix protein. Under the assumption that the helix protein is partitioning into microphase separated domains, the data offered some support to these domains emerging from the phase behaviour of the membrane. Considered in terms of a temperature difference between the imaging temperature and the inferred critical temperature, I effectively imaged the helix1021-GFP protein in four different membrane with different critical phase transition temperatures. The working paper [3] does visualise the transition by a step-change in the mobility, but these were not performed in this report.

With decreasing temperature offset, there was a trend to increase confined behaviour. This was supported by both the trend in increased confinement size at decreasing temperature offset and the increased probability at negative temperature differences (Figure 4.8 E). This was measured in two ways, the first as the inferred radius of confinement (Figure 4.8 G) as taken from the BARD algorithm. The second, was in the size of the PSF (Figure 4.9), which mostly correlated with the confinement size. The stoichiometry ratio was surprisingly linear, going from a high stoichiometry ratio to a low stoichiometry ratio at decreasing temperature difference. What this measures is less clear, but could be an increase in lifetime of the mobile domains at positive temperature differences. In addition, there was a discontinuity in the trends seen in the diffusion coefficients as a function of temperature difference, peaking just above the transition point, although more data points are needed at negative temperature differences. Cast in terms of domains formed from the phase transition behaviour, each of these trends agree qualitatively with predictions. At low differences, the proportion of tracks that are confined and size of confinement increases as domains are favoured. At high temperature difference, the proportion of tracks and size of confinement decreases. Domains appear to have both mobile and immobile characteristics and mobile domains appear to be of approximately the same size as the confined domains after correction for the integration error.

4.5 Conclusion

The primary motivation for these experiments came from several papers [50, 209, 210] that looked at model membranes systems around transition points. The authors show that lipid vesicles, fluctuations appear of the order 50 nm. These are the domains sizes that are seen in *in vivo* in E.coli. The presently favoured model is domains or compositional fluctuations being drive by phase separation, it is unclear how they are prevented from ripening into larger domains. Protein partitioning into such domains may play a part but also other cellular architecture such as the cytoskeleton. These results indicate that lateral segregation of the membrane can occur for simple model protein with no specific *in vivo* interactions. This partitioning appears to be into domains that are related to the lipid composition driven by the phase behaviour. That the helix has no native control with any interactions general rather than specific suggests that this partitioning is passive. These data didn't show any clear relation between mobility coefficients (diffusion rate, confinement size) or model probability. As the area occupation of all helix protein in a single patch is less than one percent, I believe that this is explained through a patch model, provided that occupancy of the patches is low (Figure 4.6). It is less clear why the predicted domain radius does not strongly correlate with the diffusion coefficient (Figure 4.10), and I have no strong argument to explain this, in the framework of the patch model presented. It is possible in both cases that there is a selection bias of tracked spots that skews the distribution of mobility coefficients, as brighter spots are better tracked. This is in contrast to published demonstrations of domain size and mobility measurements, where the domains are able to be directly tracked, whereas in this case, both the domain size and the domain mobility are inferred only from the aggregate point spread function of the populating helix probes. These factors may influence the observed measurements of stoichiometry correlations and the domain size/mobility measurements presented here.

Moreover, should the patch model be the correct interpretation of these data, the precise factors that cause and stabilise segregation of these helix proteins into the membrane domains are the subject for future study, but I believe that this work is relevant in considering how proteins partition

into submicrometer membrane domains that emerge from the underlying phase behaviour *in vivo* systems.

4.6 Future Work

There are a few obvious avenues in order to continue work in this report. The first is to identify the critical temperature of the membrane using the BODIPY fluorescent analogue at each of the growth temperatures used here, rather than using the interpolated transition temperatures. The second is to perform these experiments with temperature control to see how the domain characteristics change with respect to different imaging temperatures. In this report, I was unable to consider the rate of change of the system when the system was imaged at temperatures away from the growth temperatures. In this case, there may be biological factors that rapidly remodel the membrane according to the new environment. I believe however that this rate was not so rapid to remove the effect of the growth temperature given the trends seen in the helix protein measurements.

Other aspects of imaging could also be improved. For the questions being discussed here, the sampling time were chosen on the basis of other experiments [47] using similar fluorophores. The reasoning behind this was that, for the helix proteins investigated herein, observations of nanoscopic confinement was the biological question being addressed. It had already been noted in the experiments of [47], and therefore the photon budget considerations (Chapter 2 were comparable in application here. Mobility, and confinement effects were being investigated, and so an identical video rate sampling frequency of 25 Hz (40ms sampling time), was used here. For these helix data, there is room to optimise with respect to the photon budget. However, in this case, multiple different sets of experiments were being performed, with both different growth temperatures and different multimer strains. As comparable analysis required comparable imaging conditions, and so identical sampling times, consequently imaging conditions across all strains would need to be optimised over, and as image acquisition had proceeded with video rate imaging, with only imaging power varying, the end result was optimising with respect to the illumination power, and not the sampling time.

A prudent future experiment then, would be both to optimise the photon budget considerations but also to explore whether different dynamics of the helix protein change when imaged at different sampling times and imaging durations. Should a change in behaviour be observed over a wider lag-time range, then this would preclude further experimentation across all experiments.

The full array of tools developed in Chapter 3 were also not deployed on these data. I developed a switching model to determine mode switching in single particle tracks that in future work could be applied to these data. This could provide extra data on the transitions of the domains between being mobile and immobile. I also did not consider whether there were multiple sub-populations in the dataset. There didn't appear to be any obvious clustering however considering Figure 4.7.

4.7 Chapter Summary

- Briefly outlined the characteristics of phase behaviour in the membrane and protein partitioning
- Outlined the properties of ideal membrane probes. Namely a non-native helix probe and a fluorescent lipid analogue.
- Detailed the experimental set-up and experimental conditions for seven different helix protein experiments and one fluorescent lipid experiment
  - Use of a fluorescent lipid analogue as a helix probe at two different concentrations. These suggested BODIPY had a 'patchy' spatial profile.
  - Use of a helix protein probe at two different concentrations. At low concentrations spots were visible, but not at single molecule level.
  - Size dependence of the helix protein probe using different multimeric units. Counter-intuitive diffusion-size profile further suggested that imaging was not at single-molecule level.
  - Growth temperature experiments. The membrane was natively altered to a different critical temperature. The localisation profile of the helix protein was investigated in four different growth conditions.
- Discussed a model of helix partitioning into membrane patches that have mobile and immobile profiles. Partitioning is loose and not tight so that the helix protein are in a pool in the domain. Profile of domains as inferred from the helix protein under different conditions suggested that the domains related to the critical temperature and thereby reflect the phase behaviour of the membrane.

4. CHARACTERISING *ESCHERICHIA COLI* BIOLOGICAL MEMBRANE HETEROGENEITY THROUGH A NON-NATIVE TRANSMEMBRANE HELIX AND FLUORESCENT LIPID PROBES

Chapter 5

Characterising *Escherichia Coli* Biological Membrane Heterogeneity through native protein-FP fusion hybrids.

5.1 Abstract

In this Chapter, I apply the BARD algorithm to two *in vivo* datasets. These are the twin-arginine translocase (Tat) system, and the oxidative phosphorylation system (OXPHOS) system, both of *E. coli*. This is the shortest chapter, as I collected neither dataset, but merely serves to present BARD being applied to other *in vivo* data. When applying the algorithm to the Tat data, I recover the ring model reported in the original reference, however in the report here, I show that the BARD approach converges on the data and identifies this with reduced uncertainty. For the OXPHOS system, I report the mobility analysis of the eight different strains. I also consider the aggregate diffusion rates and the confinement radii observed.

5.2 Introduction

In this chapter, two datasets are investigated, both crucial to the native functioning of *E.coli*. The first, the twin-arginine translocase system, is responsible for the transport of folded proteins across the cytoplasmic membrane. This translocation is challenging as it involves the translocation of folded proteins; typically bigger and more variable in size than the equivalent transport pathway (the Sec system) for unfolded peptides. It is a useful model protein as it represents a heterogeneous, oligomeric membrane protein system. In *E.coli*, the essential components of the Tat system are the integral membrane proteins TatA, TatB and TatC. TatB and TatC form a large membrane receptor complex that recognises an N-terminal signal peptide present on the substrate. Low resolution structures of purified TatA show doughnut shaped particles with an internal cavity large enough to contain the typical substrates for transport in the Tat system. It was suggested in reference [47] that the TatA system forms a ring-like structure based upon the variation of the stoichiometry with the diffusion rate. These data were obtained with TIRFM-SPT. In this chapter, I re-analyse these data with the same analysis except using the output of BARD [1]. I recover the proposed ring-structure proposed in [47] with a greater accuracy.

The second dataset analysed was the OXPHOS system. I will speak more on these as I had a greater role in obtaining these data, although the dataset actually used herein was generated by Oliver Harriman, Heiko Erhardt and Tchern Lenn. Isabel Llorente-Garcia takes credit for all of the analysis aside from the diffusion analysis presented here. The OXPHOS system is the basis of the electron transport respiratory chain (ETC). Oxidation of electron donors by membrane-bound enzymes is coupled by a series of stepwise redox reactions, resulting in the generation of the p.m.f. (protonmotive force). This powers the F_1F_0-ATPase machine, generating the universal cellular fuel of ATP. It largely consists of five enzyme complexes, Complex I (NADH dehydrogenase), Complex II (succinate dehydrogenatse), Complex III (cytochrome bc_1, Complex IV (cytochrome c oxidase) and Complex V (the F_1F_0-ATPase). In addition, there are mobile electron carriers, uniquinol and cytochrome c, which functionally link complexes I-IV, making up the ETC. This in turn is linked to

Complex V by the p.m.f. that is generated through the coupling of proton translocation with the electron transfer reactions in the ETC.

5.3 Materials and Methods

5.3.1 Bacterial cell strain and preparation

One was cell strain AyBC, as studied previously [47], using identical cell preparation conditions. The cell strain contained a construct specifying a C-terminal enhanced YFP tag (Clontech Laboratories Inc., Mountain View, CA) to the native E. coli protein TatA on the cytoplasmic side of the membrane. Imaging was with a home-built inverted epifluorescence microscope with excitation at 532 nm, intensity $\approx$ 260 W/cm^2 with a separate path allowing light to be focused to a width of $\approx$ 1 µm with intensity $\approx$ 60 kW/cm^{2}for 0.5 s FRAP bleaches. The focal plane was set at the middle of the cell approximately 0.5µm from the coverslip with emission imaged at 25 Hz by a 128$\times$ 128 pixel (50nm per pixel) camera, cooled, back-thinned electron-multiplying CCD camera (iXon DV860-BI, Andor Technology).

OXPHOS imaging was imaged at near-TIRF/shallow-angle epi-fluorescence imaging resulting in a highly opaque illumination field. The field was uniform over the cell but had reduced back-scattering creating high-contrast fluorescence imaging. In the working paper [4] we are looking at the model of the OXPHOS system in *E. coli*. Colloborators created strains with the five key OXPHOS protein complexes with genomically expressed fluorescent fusion protein tags. This was with both single and dual labelled strains so that multi-colour imaging was possible, allowing for co-localisation analysis. There are three models for OXPHOS molecular organisation. One is a random diffusion model, in which OXPHOS enzymes are interspersed in the membrane and interact via random collisions. The second is a solid-state model in which electron flow betweein OXPHOS complexes is mediated through super-complexes in functionally and structurally isolated parts of the membrane. The third model is essentially a mixture of these two models. Earlier work [48, 211, 156] suggested that OXPHOS complexes were localised to specialised membrane patches called 'respirazones'. This

was evidenced by TIR recordings of diffusing spots of complexes at stoichiometries of between 10 and 100 molecules in patches of diameter 100-200nm. This suggested a combination of a 'solid-state' model of the OXPHOS system, and a diffusive interaction model.

5.4 Results

5.4.1 Application to experimental Tat data.

Applying the scheme to the Tat data, I found that there is evidence that a sub-population of TatA protein complexes that instead of being simply 'immobile' as described previously [47] are in fact 'confined. A significant population may be immobilised anchored to the membrane but there is a substantial population that appears confined to domain lengths larger than the estimated experimental particle localisation error. Neither a sufficient number of anomalous or directed modes were detected using the MSD approach (to within the bias error of the classification matrix (Chapter 3, Figure 3.12), and so these could not be conclusively discriminated from a simple Brownian mode) but there was a significant number of confined tracks observed, with domain size of 60 $\pm$ 40 nm. I estimate 186 out of the 422 tracks observed (44%) appeared putatively confined or immobilised while the remaining 56% could be categorised as non-confined. This included simple diffusion along with unbounded anomalous ($n = 34$) and directed behaviour ($n = 0$), however in the latter two cases, the numbers fell within the predictions for mis-categorisation of the classification matrix so I attribute all unconfined motion to simple Brownian motion collectively. Further, I compare the protein size to three different parameters; the probability of confinement (Figure 5.2 A), the Brownian diffusion coefficient (Figure 5.2 B), and the putative confinement domain size (Figure 5.2 C).

There were two models proposed in [47] for the assembly of the TatA complexes. These were a disc model and a ring model. In [47], it was proposed that the TatA complexes formed a ring model. This was due to the relationship between the diffusion coefficient and the number of TatA-YFP molecules. In Figure 5.2, a log-log fit is plotted to the data of the stoichiometry versus the Brownian

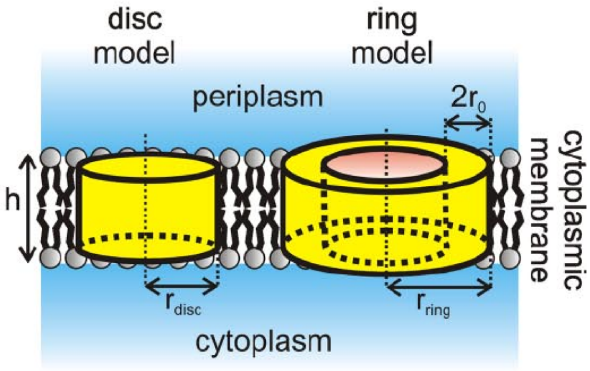


Figure 5.1: *The Tat system was suggested to exist in two forms; either a ring system or a disk system. Figure adapted from [47].*

diffusion rate. To distinguish between the ring structure and the disc structure, I compare the variation with stoichiometry. Detailed in [47], the authors identify the two different scaling relations between the diffusion coefficient and stoichiometry. Correspondingly, the gradient of a log-log plot can distinguish between the ring model and the disc model. For the log-log plot of the log stoichiometry $\log(S)$ versus the log diffusion coefficient $log(D)$, a gradient of -1 suggests a ring model, and a gradient of -0.5 suggests a disc model. Using a weighted-least square fit with known covariance the gradient I obtain is -1.00 ± 0.05 (1 s.d.). In this case, the weighting is the inverse of the posterior standard deviation about the Brownian diffusion coefficient; $1/\sigma_{D_B}$. In my fit, I use each single particle coefficient, rather than the histogram used in [47]. I believe that this offers a good test for BARD. By using all data and not discarding the uncertainty about each datum, accurate inferences can be made in parameter model fitting scenarios such as this. By comparison, the approach used in [47] used a histogram approach and yielded -1.2 ± 0.4.

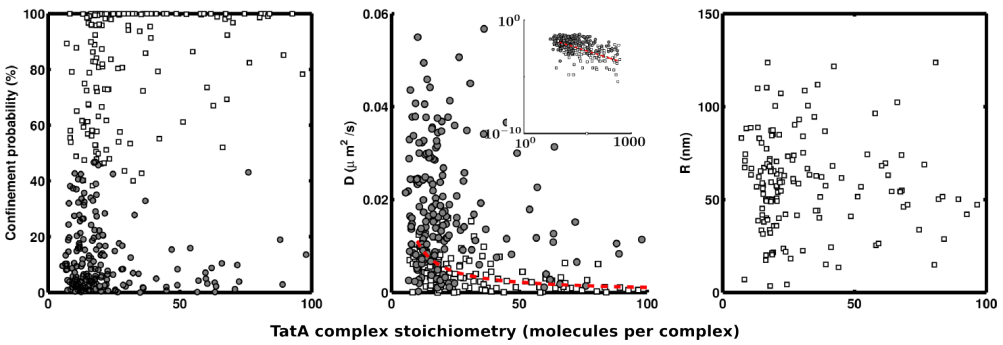


Figure 5.2: *Variation in (a) the probability that the top ranked diffusion mode will be confined, (b) the inferred Brownian diffusion coefficient and (c) the confinement radius R versus estimated molecular stoichiometry for the TatA-YFP complexes, predicted confined (white squares) and mobile (grey circles) tracks indicated.*

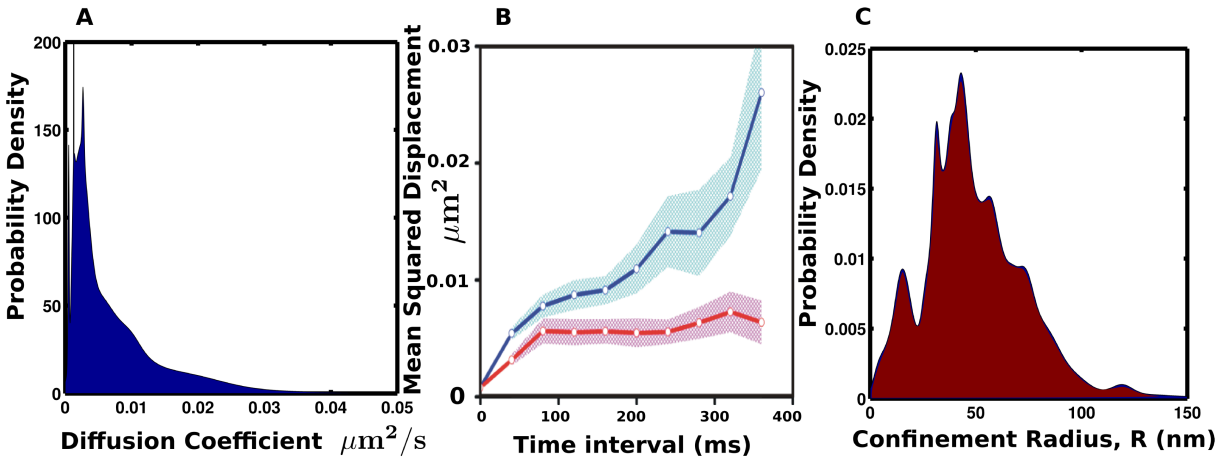


Figure 5.3: *Spot mobility analysis. A) Kernel Density Distribution of Brownian diffusion coefficients across all cell strains. B) Examples of the mean-squared displacement (Key: Blue (Brownian) Red (Confined)) of one strain (NuoF-GFP). C) KDE of confinement radius across all cell strains.*

5.4.2 Application to experimental OXPHOS data

To compare the different models of the OXPHOS system, I used the BARD analysis developed in Chapter 3. I find that approximately 57 ± 15 % have unconfined mobility in the cell membrane with the remaining fraction (43%) appearing as confined. Of those confined, they are localised into domains of radius between 50 ± 20 nm, consistent with earlier estimates based on the FWHM [48]. The degree of confinement of these complexes varies from 14-66%. By this variation, this suggests a mixed model. There was no significant dependence within experimental error for either the diffusion coefficient or the confinement radii between cell strains. This suggests that they localise into similar patches.

5.5 Conclusion

In this Chapter, I applied the BARD algorithm of Chapter 3 to two *in vivo* datasets. When applied to the Tat data, I recover the results of the original reference [47]. By considering the mobility as a function of stoichiometry, I re-extract the disc model of the Tat system to a greater degree of

Table 5.1: *Helix protein mobility analysis, indicating proportion of tracks in each dataset being identified as either anomalous, Brownian, confined or directed of the analysed TIR datasets.*

Dataset	**Proportion inferred in each diffusion model** (%)				
	Anomalous	Brownian	Confined	Directed	Number of tracks
(**NuoF**-GFP:SdhC-mCherry)	22.2	30.6	47.2	0	36
(**NuoF**-GFP:CydB-mCherry)	30.8	23.5	45.7	0	94
(NuoF-GFP:**SdhC**-mCherry)	5.6	23.5	45.7	0	18
(**AtpB**-GFP:CydB-mCherry)	29.1	29.1	41.8	0	134
(NuoF-GFP:**CydB**-mCherry)	46.1	15.4	38.5	0	34
(AtpB-GFP:**CydB**-mCherry)	46.1	15.4	38.5	0	26
(**CyoA**-mCherry)	57.1	28.6	14.3	0	7

accuracy. This is achieved through applying a full treatment of the posterior uncertainty about each data-point. In the second dataset, I infer the mobility of a complex *in vivo* dataset. This dataset is comprised of the mobility inferences of multiple complexes involved in the OXPHOS system, which is being used in the working paper [4]. I aggregate the diffusion coefficients and confinement radii and suggest how this relates to the solid-state or freely diffusing model. The OXPHOS complexes appear to partition into patches that have no statistical difference, although different strains have different propensities of being either confined or mobile. These mobility data suggest a mixed model; proteins partition into domains of similar sizes and diffusion rates, but they have different propensity in partitioning into mobile or immobile domains. It is the subject of [4] that considers co-localisation, which is analysis that was not performed by me.

5.6 Summary

- Re-analysed the Tat data using BARD with a weighted least-squares fit with a known variance (that is from the posterior distribution of the parameter). This analyses was in agreement with the previous analysis, although reached the same conclusion with reduced uncertainty.

- Applied BARD to the OXPHOS data. This analysis showed that there exists a range in mobility behaviour including a different propensity of being identified either mobile or immobile.

5. CHARACTERISING *ESCHERICHIA COLI* BIOLOGICAL MEMBRANE HETEROGENEITY THROUGH NATIVE PROTEIN-FP FUSION HYBRIDS.

Chapter 6

Conclusions

The processes on the membrane are critical to the healthy functioning of a cell. The technological developments in experimental biological physics over the past decade have allowed us to explore the biophysical processes on the membrane at the single molecule level. These experiments allow the *in vivo* environment of integrated membrane protein to be explored at the scale of the individual molecule. These experimental techniques are beginning to address the most fundamental questions of membrane systems biology. New experimental methods are only part of the toolset. In fields that require the measurement of tiny signals in environments dominated by noise, our understanding of integrating the data obtained from *in vivo* single molecule experimentation is of substantial importance in pushing the field forward.

The work presented in this thesis has covered a wide range of topics related to the diffusive behaviour of integrated membrane complexes. There were two principle contributions. The first was the development of an algorithmic model to infer mobilities of single particle tracks of noisy *in vivo* data. The second was experimental. These novel experiments investigated the relationship between protein membrane partitioning and the underlying membrane heterogeneity. I now outline each Chapter.

Chapter 1 was a literature review. In this chapter, I wrote an exposition of the present state of the research of the themes covered in this thesis. I provided a context for the research of this thesis and detailed the array of experimental methodologies in *in vivo* single particle tracking. I discussed the

present and historical understanding of ideas behind membrane heterogeneity.

Chapter 2 was the first experimental chapter. The first part was a review section focussing the discussion on Total Internal Reflection Fluorescence Microscopy. This is the basis of all experimental data presented in Chapters 4 and 5. I follow up with an outline of all the experimental, imaging and growth protocols that I used. I then detailed all the experimental calibrations for the TIR data in Chapter 4. This involved the microscopic calibrations, ranging from the excitation field calibrations in TIR, the stoichiometric calibrations of isolated and immobile GFP and the experimental error propagation.

Chapter 3 is the statistical inference chapter. This chapter started with a fairly focused review of the diffusion models used in single particle tracking. This Chapter developed the BARD algorithm; a Bayesian based ranking system that is used in the subsequent chapters for inferring the diffusive mode in single particle tracks. There were other methodological developments in this chapter, covering the identification of sub-populations in such data, and switching dynamics, where a particle track is seen to switch between different diffusive modes.

The algorithm developed in Chapter 3 was then applied to a novel set of experiments in Chapter 4. These experiments explored the mobility of protein and lipid based probes in the membrane of *E. coli*. Both were found to appear spotty in TIR images. These spots represent a co-localisation of the helix protein into distinct patches. These patches appear to be domains of radii similar to that observed in GUVs. By varying the growth temperature which is known to change the lipid composition and thus the phase transition temperature, my suggestions is that these domains emerge from the underlying phase behaviour of the lipid. Prokaryotic systems are historically less studied relative to their eukaryotic counterparts

In Chapter 5 I also apply the BARD algorithm to two other *in vivo* datasets. These were the twin arginine translocase system and the oxidative phosphorylation systems, both of *E. coli.*. In the first case, I find on reapplying the BARD algorithm, that similar inferences between stoichiometry and diffusive behaviour can be resolved at greater accuracy. For the OXPHOS system, I find that the mobility data supports the OXPHOS complexes also as partitioning into similarly sized domains as

the helix protein of Chapter 4.

6.1 Future Work and Outlook

In each chapter, I included a future work section. For the thesis as a whole, there are two distinct directions to go. The first is building upon the BARD algorithm in Chapter 3. There would be reasonable utility in doing this as such algorithms are necessary; the development of a robust toolkit for using in single particle tracking is in demand from the biophysical community, evidenced by the number of publications in this area. However, the purpose of these tools is to be applied to experimental data such as in Chapters 4 and 5. While Chapter 5 was a simple showcase of BARD, used to infer the mobility of a specific set of membrane proteins, it is the helix data from Chapter 4 that could offer the greatest insights into the dynamics of membrane integrated proteins.

Consequently, from the developments in this thesis, the next steps would be in continuing these experiments, rather than continuing in a methodological direction in developing BARD. Specific experiments to suggest would be using the BODIPY probe over different growth temperature experiments, and performing them with temperature control. With both datasets, the data would be ideal for modelling.

In addition to this, further experimentation on optimising the photon budget via changing the sampling rate, and as a means to explore whether the behaviour of the helix protein changed when imaged over a wider time-lag, would be of interest. Further analytical treatment can also be pursued here, such as accounting for the changing static error during the course of imaging, as the localisation error increases as fluorophores begin to photobleach, and, or better estimates for stoichiometry by accounting for out-of-frame (and out of focus) excitation. There are two factors to consider here. The first is excitation of fluorophores prior to being captured by the tracking algorithm. The second is the correction required for non-uniform excitation such as that in TIR, where the excitation profile changes across the cell.

One additional future avenue of research would also be the inclusion of testing on model control

membrane systems, such as a simple single or multicomponent vesicle. These are not technically challenging, and offers a useful bridge between BARD validation on simulation to that of the deployment to *in vivo* data. A model membrane system has the additional advantage in that the mobility measurements would be able to be experimentally tested also, as measurements such as domain sizes and mobility have been recorded in other publications.

6.1.1 Outlook

By first developing a statistical toolset in Chapter 3, I was able to approach the thematic question of the field set out at the start of the thesis. These were on the interplay between cellular membrane architecture and the dynamics of diffusing membrane complexes. By considering model membrane experiments, I designed experiments that investigated the behaviour of model proteins selectively partitioning into membrane domains *in vivo*. I then applied the same statistical toolset to single molecule studies of natively expressed protein. It is my hope that the methods I have developed will be able to contribute to future endeavours in the field of single particle tracking and that my experimental observations of protein partitioning are useful for future studies in the field.

Appendix A

A.1 Numerical Integration routine pseudocode

Integration is performed through a Monte Carlo integration routine [180, 190]. A Monte Carlo integration approach was chosen because of the complexity of the models. Although the parameter space is fairly small (2-3 features at most), and analytical solutions could feasibly be developed for all the models. More complex models in future iterations of the BARD algorithm would potentially be unsolvable at the analytical level, thereby requiring a numeric approach to calculate integrals. The integration routine is derived from a publicly available library for (`MATLAB`,mathworks.com, http://www.mathworks.co.uk/matlabcentral/fileexchange/12447-mcint) and works through a random darts method. The numerical integral is calculated by sampling at random points in the distribution.

A.2 Estimating Stoichiometry

In order to estimate the stoichiometry of a single track I fit the data trace to the function given by Equation A.2. However, as both the noise ν and the photobleaching decay rate $(1/\tau)$ are dependent upon the experimental conditions rather than specific to each track, we can use the same τ and ν for all tracks. This makes two assumptions. First, that the photobleaching rate is constant for all fluorophores. This is reasonable given that all the fluorophores will be under the same conditions. The second assumption is that the background noise level is the same. The difference in the noise

level was quantified in §2.6. However, the assumption that ν is a constant here also assumes that the background noise between different cells is also approximately equal. The heterogeneity in illumination in §2.6 did not include live cells that would have their own background noise.

Therefore, in order to fit all the $I(0)_i$, where $I(0)_i$ is the estimated initial intensity count at time $t = 0$ for the ith track, I use a least-squares approach that finds fitting functions through minimising an objective function. This is for observed intensity values I_{actual} and fitting value I_{est} at absolute time $T = n\delta$. The integer variable n is such that it runs over each observed intensity data-point at times $n\delta t$. The objective function is given by the sum of squared residuals for each track in the dataset (Equation A.1).

$$\sum_{i}\sum_{n}^{N}(I_{\text{est}}(n\delta t) - I_{\text{actual}}(n\delta t))^2. \tag{A.1}$$

The modelled fit value for each track $I_{\mathbf{est}}$ is then given by Equation A.2:

$$I_{\mathbf{est}}(t) = I_0 \exp\left(-\frac{t}{\tau}\right) + \nu. \tag{A.2}$$

Appendix B

A.3 Mathematical Appendix

A.3.1 Functions and Operators used in Diffusion Theory

The Riemann-Liouville Operator, $D_t^{1-\alpha}$ is defined as:

$$D_t^{1-\alpha} W(x,t) = \frac{1}{\Gamma(\alpha)} \frac{\partial}{\partial t} \int_a^x \frac{f(t)}{(x-t)^\alpha} dt \tag{A.3}$$

Γ (z) is the Gamma-function defined as:

$$\Gamma(z) = \int_0^\infty t^{z-1} e^{-t} dt \tag{A.4}$$

The Mittag-Leffler function is defined as:

$$E_{\alpha,\beta}(z) = \sum_{k=0}^{\infty} \frac{z^k}{\Gamma(\alpha + k\beta)} \tag{A.5}$$

A.3.2 Laplace's Method

For many problems the posterior $P(\mathbf{w}|D, \mathcal{M}_i) \propto P(D|\mathbf{w}, \mathcal{M}_i)P(\mathbf{w}|\mathcal{M}_i)$ is strongly peaked at the most probabaly parameters $w_{\mathbf{mp}}$. In the simple one-dimensional case, the evidence term can be approximated by the height of the peak of the integrand $P(\mathcal{D}|\mathbf{w})\mathcal{M}_i)P(\mathbf{w}|\mathcal{M}_i)$ multiplied by its width, $\sigma_{w|\mathcal{D}}$. This is know as the Laplace approximation. By considering the posterior $P(w|\mathcal{D}|\mathcal{H}_i$

as a strong peaked Gaussian at the value w_p, with height $P(w_p)$ and FWHM width σ then from standard Gaussian integration the integral over all space in 1D is given approximately by $\sim P(w_p)\sigma$, i.e.:

$$P(D|\mathcal{H}_i) \approx P(\mathcal{D}|\mathbf{w}_{WP}, \mathcal{H}_i) \times P(\mathbf{w}_{WP}|\mathcal{H}_i)\sigma_{w|D} \tag{A.6}$$

References

[1] A. Robson, K. Burrage and M. C. Leake, 'Inferring diffusion in single live cells at the single-molecule level.', *Philosophical transactions of the Royal Society of London. Series B, Biological sciences*, vol. 368, no. 1611, p. 20 120 029, 2013.

[2] I. M. Dobbie, A. Robson, N. Delalez and M. C. Leake, 'Visualizing single molecular complexes in vivo using advanced fluorescence microscopy.', *Journal of visualized experiments : JoVE*, no. 31, p. 1508, 2009.

[3] A. Nenninger, G. Mastroianni, A. J. Robson, Y. T. Lenn, Q. Xue, M. C. Leake and C. W. Mullineaux, 'Independent mobility of proteins and lipids in the plasma membrane of Escherichia coli', *In preparation*, 2012.

[4] I. Llorente-Garcia, T. Lenn, H. Erhardt, O. L. Harriman, L. Liu, A. Al-Mahmood, A. Robson, S.-W. Chiu, S. Matthews, C. Bray, T. Friedrich, C. W. Mullineax and M. C. Leake, 'Molecular architecture and dynamics of functional oxidative phosphorylation machinery observed by in vivo single-molecule imaging', *In preparation*, 2013.

[5] A. Robson, A. Nenninger, C. W. Mullineax and M. Leake, 'Passive partitioning of a non-native transmembrane helix protein into transition-temperature sensitive membrane domains of Escherichia-coli', *In preparation*, 2013.

[6] A. Robson, M. Tyndall, P. Maini and M. C. Leake, 'Developing Statistical Diagnostic Tools For Discriminating Between Different Diffusive Modes Of Fluorescently Tagged Protein

Complexes In Living Cells For Short Duration Trajectories', *Biophysical Journal*, vol. 96, no. 3, 33a, 2009.

[7] J. A. Op den Kamp, 'Lipid asymmetry in membranes.', en, *Annual review of biochemistry*, vol. 48, pp. 47–71, 1979.

[8] S. Singer and G. Nicolson, 'The fluid mosaic model of the structure of cell membranes.', *Science (New York, N.Y.)*, vol. 175, no. 4023, pp. 720–731, 1972.

[9] P. G. Saffman and M Delbrück, 'Brownian motion in biological membranes', *Proceedings of the National Academy of Sciences*, vol. 72, no. 8, pp. 3111–3113, 1975.

[10] A. Kusumi, C. Nakada, K. Ritchie, K. Murase, K. Suzuki, H. Murakoshi, R. S. Kasai, J. Kondo and T. Fujiwara, 'Paradigm shift of the plasma membrane concept from the two-dimensional continuum fluuid to the partitioned fluid: high-speed single-molecule tracking of membrane molecules', *Annual Review of Biophysics and Biomolecular Structure*, vol. 34, no. 1, pp. 351–378, 2005.

[11] D. M. Engelman, 'Membranes are more mosaic than fluid', *Nature*, vol. 438, no. 7068, pp. 578–580, 2005.

[12] K. Jacobson, O. G. Mouritsen and R. G. W. Anderson, 'Lipid rafts: at a crossroad between cell biology and physics.', *Nature cell biology*, vol. 9, no. 1, pp. 7–14, 2007.

[13] G Vereb, J Szöllosi, J Matkó, P Nagy, T Farkas, L Vigh, L Mátyus, T. Waldmann and S Damjanovich, 'Dynamic, yet structured: The cell membrane three decades after the Singer-Nicolson model.', *Proceedings of the National Academy of Sciences of the United States of America*, vol. 100, no. 14, pp. 8053–8058, 2003.

[14] B. D. Hughes, B. A. Pailthorpe and L. R. White, 'The translational and rotational drag on a cylinder moving in a membrane', English, *Journal of Fluid Mechanics*, vol. 110, no. -1, p. 349, 1981.

[15] E. P. Petrov and P. Schwille, 'Translational diffusion in lipid membranes beyond the Saffman-Delbruck approximation.', *Biophysical journal*, vol. 94, no. 5, pp. L41–3, 2008.

[16] P. Cicuta, S. L. Keller and S. L. Veatch, 'Diffusion of Liquid Domains in Lipid Bilayer Membranes', *The Journal of Physical Chemistry B*, vol. 111, no. 13, pp. 3328–3331, 2007.

[17] Y Gambin, R Lopez-Esparza, M Reffay, E Sierecki, N. Gov, M Genest, R. Hodges and W Urbach, 'Lateral mobility of proteins in liquid membranes revisited.', *Proceedings of the National Academy of Sciences of the United States of America*, vol. 103, no. 7, pp. 2098–2102, 2006.

[18] K. Seki, S. Ramachandran and S. Komura, 'Diffusion coefficient of an inclusion in a liquid membrane supported by a solvent of arbitrary thickness', *Physical Review E*, vol. 84, 2011.

[19] S. Ramadurai, A. Holt, V. Krasnikov, G. van den Bogaart, J. A. Killian and B. Poolman, 'Lateral Diffusion of Membrane Proteins', *J. Am. Chem. Soc.*, vol. 131, no. 35, pp. 12 650–12 656, 2009.

[20] G Guigas and M Weiss, 'Sampling the cell with anomalous diffusion - the discovery of slowness.', *Biophysical journal*, vol. 94, no. 1, pp. 90–94, 2008.

[21] F. Harb, J. Sarkis, N. Ferte and B. Tinland, 'Beyond Saffman-Delbruck approximation: a new regime for 2D diffusion of α-hemolysin complexes in supported lipid bilayer.', *The European physical journal. E, Soft matter*, vol. 35, no. 11, p. 118, 2012.

[22] M Saxton, 'A Biological Interpretation of Transient Anomalous Subdiffusion. I. Qualitative Model', *Biophysical Journal*, vol. 92, no. 4, pp. 1178–1191, 2007.

[23] N. Destainville, A. Saulière and L. Salomé, 'Comment to the article by Michael J. Saxton: A biological interpretation of transient anomalous subdiffusion. I. qualitative model.', *Biophysical journal*, vol. 95, no. 7, 3117–9; author reply 31202–, 2008.

[24] M. J. Saxton, 'Response to Comment by Destainville et al.', *Biophysical Journal*, vol. 95, no. 7, pp. 3120–3122, 2008.

[25] E. L. Elson, E. Fried, J. E. Dolbow and G. M. Genin, 'Phase separation in biological membranes: integration of theory and experiment.', *Annual review of biophysics*, vol. 39, pp. 207–26, 2010.

[26] L. B. Oddershede, 'Force probing of individual molecules inside the living cell is now a reality.', *Nature chemical biology*, vol. 8, no. 11, pp. 879–86, 2012.

[27] J. Silvius and I. R. Nabi, 'Fluorescence-quenching and resonance energy transfer studies of lipid microdomains in model and biological membranes (Review)', *Molecular Membrane Biology*, vol. 23, no. 1, pp. 5–16, 8211.

[28] J Hwang, L. A. Gheber, L Margolis and M Edidin, 'Domains in cell plasma membranes investigated by near-field scanning optical microscopy.', *Biophysical journal*, vol. 74, no. 5, pp. 2184–2190, 1998.

[29] A. Kusumi, Y. M. Shirai, I. Koyama-Honda, K. G. N. Suzuki and T. K. Fujiwara, 'Hierarchical organization of the plasma membrane: investigations by single-molecule tracking vs. fluorescence correlation spectroscopy.', *FEBS letters*, vol. 584, no. 9, pp. 1814–23, 2010.

[30] C. Eggeling, C. Ringemann, R. Medda, G. Schwarzmann, K. Sandhoff, S. Polyakova, V. N. Belov, B. Hein, C. von Middendorff, A. Schönle and S. W. Hell, 'Direct observation of the nanoscale dynamics of membrane lipids in a living cell.', *Nature*, vol. 457, no. 7233, pp. 1159–62, 2009.

[31] M. J. Skaug, R. Faller and M. L. Longo, 'Correlating anomalous diffusion with lipid bilayer membrane structure using single molecule tracking and atomic force microscopy.', *The Journal of chemical physics*, vol. 134, no. 21, p. 215 101, 2011.

[32] I. Casuso, P. Sens, F. Rico and S. Scheuring, 'Experimental evidence for membrane-mediated protein-protein interaction.', *Biophysical journal*, vol. 99, no. 7, pp. L47–9, 2010.

[33] C. Das, K. H. Sheikh, P. D. Olmsted and S. D. Connell, 'Nano-scale mechanical probing of supported lipid bilayers with atomic force microscopy', *Physical Review E - Statistical, Nonlinear and Soft Matter Physics*, vol. 82, no. 4 Pt 1, p. 6, 2010.

[34] D. Lingwood and K. Simons, 'Lipid rafts as a membrane-organizing principle.', *Science (New York, N.Y.)*, vol. 327, no. 5961, pp. 46–50, 2010.

[35] D. V. Nicolau, J. F. Hancock and K. Burrage, 'Sources of Anomalous Diffusion on Cell Membranes: A Monte Carlo Study', *Biophys. J.*, vol. 92, no. 6, pp. 1975–1987, 2007.

[36] D. V. Nicolau, K. Burrage, R. G. Parton and J. F. Hancock, 'Identifying optimal lipid raft characteristics required to promote nanoscale protein-protein interactions on the plasma membrane.', *Molecular and cellular biology*, vol. 26, no. 1, pp. 313–323, 2006.

[37] T. S. van Zanten, J. Gómez, C. Manzo, A. Cambi, J. Buceta, R. Reigada and M. F. Garcia-Parajo, 'Direct mapping of nanoscale compositional connectivity on intact cell membranes.', en, *Proceedings of the National Academy of Sciences of the United States of America*, vol. 107, no. 35, pp. 15 437–42, 2010.

[38] Y. Lavi, M. a. Edidin and L. a. Gheber, 'Dynamic patches of membrane proteins.', *Biophysical journal*, vol. 93, no. 6, pp. L35–7, 2007.

[39] T. Harder, P. Scheiffele, P. Verkade and K. Simons, 'Lipid Domain Structure of the Plasma Membrane Revealed by Patching of Membrane Components', *The Journal of Cell Biology*, vol. 141, no. 4, pp. 929–942, 1998.

[40] I. Levental, M. Grzybek and K. Simons, 'Raft domains of variable properties and compositions in plasma membrane vesicles', *Proceedings of the National Academy of Sciences*, vol. 108, no. 28, pp. 11 411–11 416, 2011.

[41] K. Simons and J. L. Sampaio, 'Membrane organization and lipid rafts.', en, *Cold Spring Harbor perspectives in biology*, vol. 3, no. 10, a004697, 2011.

[42] E. Mileykovskaya and W. Dowhan, 'Cardiolipin membrane domains in prokaryotes and eukaryotes', *Biochimica et Biophysica Acta (BBA) - Biomembranes*, vol. 1788, no. 10, pp. 2084–2091, 2009.

[43] S. Morein, A.-S. Andersson, L. Rilfors and G. Lindblom, 'Wild-type Escherichia coli Cells Regulate the Membrane Lipid Composition in a Window between Gel and Non-lamellar Structures', *Journal of Biological Chemistry*, vol. 271, no. 12, pp. 6801–6809, 1996.

[44] E Mileykovskaya and W Dowhan, 'Visualization of phospholipid domains in Escherichia coli by using the cardiolipin-specific fluorescent dye 10-N-nonyl acridine orange.', *Journal of bacteriology*, vol. 182, no. 4, pp. 1172–5, 2000.

[45] D. López and R. Kolter, 'Functional microdomains in bacterial membranes', *Genes & Development*, vol. 24, no. 17, pp. 1893–1902, 2010.

[46] L. D. Renner and D. B. Weibel, 'Cardiolipin microdomains localize to negatively curved regions of Escherichia coli membranes', *PNAS*, vol. 2011, 2011.

[47] M. C. Leake, N. P. Greene, R. M. Godun, T. Granjon, G. Buchanan, S. Chen, R. M. Berry, T. Palmer and B. C. Berks, 'Variable stoichiometry of the TatA component of the twin-arginine protein transport system observed by in vivo single-molecule imaging.', *Proceedings of the National Academy of Sciences of the United States of America*, vol. 105, no. 40, pp. 15 376–81, 2008.

[48] T. Lenn, M. C. Leake and C. W. Mullineaux, 'Are Escherichia coli OXPHOS complexes concentrated in specialized zones within the plasma membrane?', *Biochemical Society Transactions*, vol. 36, no. 5, pp. 1032–1036, 2008.

[49] R. Mukhopadhyay, K. C. Huang and N. S. Wingreen, 'Lipid localization in bacterial cells through curvature-mediated microphase separation.', *Biophysical journal*, vol. 95, no. 3, pp. 1034–49, 2008.

[50] S. L. Veatch, P. Cicuta, P. Sengupta, A. Honerkamp-Smith, D. Holowka and B. Baird, 'Critical Fluctuations in Plasma Membrane Vesicles', *ACS Chemical Biology*, vol. 3, no. 5, pp. 287–293, 2008.

[51] D. Lingwood, H.-J. Kaiser, I. Levental and K. Simons, 'Lipid rafts as functional heterogeneity in cell membranes.', *Biochemical Society transactions*, vol. 37, no. Pt 5, pp. 955–60, 2009.

[52] B. B. Machta, S. Papanikolaou, J. P. Sethna and S. L. Veatch, 'Minimal model of plasma membrane heterogeneity requires coupling cortical actin to criticality.', *Biophysical journal*, vol. 100, no. 7, pp. 1668–77, 2011.

[53] R. Reigada and J. Buceta, 'Phase separation in three-component lipid membranes : From Monte Carlo simulations to Ginzburg-Landau equations', pp. 1–10, 2008.

[54] S. L. Veatch, O. Soubias, S. L. Keller and K. Gawrisch, 'Critical fluctuations in domain-forming lipid mixtures.', *Proceedings of the National Academy of Sciences of the United States of America*, vol. 104, no. 45, pp. 17 650–17 655, 2007.

[55] S. L. Veatch and S. L. Keller, 'Seeing spots: complex phase behavior in simple membranes.', *Biochimica et biophysica acta*, vol. 1746, no. 3, pp. 172–85, 2005.

[56] S. A. Johnson, B. M. Stinson, M. S. Go, L. M. Carmona, J. I. Reminick, X Fang and T Baumgart, 'Temperature-dependent phase behavior and protein partitioning in giant plasma membrane vesicles.', *Biochimica et biophysica acta*, vol. 1798, no. 7, pp. 1427–35, 2010.

[57] H. Heerklotz, 'Interactions of surfactants with lipid membranes', *Quarterly Reviews of Biophysics*, vol. 4, pp. 205–264, 2008.

[58] L. V. Schäfer, D. H. de Jong, A. Holt, A. J. Rzepiela, A. H. de Vries, B. Poolman, J. A. Killian and S. J. Marrink, 'Lipid packing drives the segregation of transmembrane helices into disordered lipid domains in model membranes', *Proceedings of the National Academy of Sciences*, vol. 108, no. 4, pp. 1343–1348, 2011.

[59] M Sinensky, 'Homeoviscous adaptation–a homeostatic process that regulates the viscosity of membrane lipids in Escherichia coli.', *Proceedings of the National Academy of Sciences of the United States of America*, vol. 71, no. 2, pp. 522–5, 1974.

[60] A. Jin, M Edidin, R Nossal and N. Gershfeld, 'A singular state of membrane lipids at cell growth temperatures.', *Biochemistry*, vol. 38, no. 40, pp. 13 275–13 278, 1999.

[61] V. Frolov, Y. Chizmadzhev, F. Cohen and J. Zimmerberg, 'Entropic Traps in the Kinetics of Phase Separation in Multicomponent Membranes Stabilize Nanodomains', *Biophys J*, vol. 91, no. 1, pp. 189–205, 2006.

[62] E. J. Deeds, O. Ashenberg, J. Gerardin and E. I. Shakhnovich, 'Robust proteinprotein interactions in crowded cellular environments', *Proceedings of the National Academy of Sciences*, vol. 104, no. 38, pp. 14 952–14 957, 2007.

[63] D. Hall and M. Hoshino, 'Effects of macromolecular crowding on intracellular diffusion from a single particle perspective', *Biophysical Reviews*, vol. 2, no. 1, pp. 39–5353–, 2010.

[64] H. C. Berg, *Random Walks in Biology*, Revised. Princeton University Press, 1993.

[65] M. J. Saxton and K. Jacobson, 'SINGLE-PARTICLE TRACKING:Applications to Membrane Dynamics', *Annual Review of Biophysics and Biomolecular Structure*, vol. 26, no. 1, pp. 373–399, 1997.

[66] G. Peskir, 'On the diffusion coefficient: The Einstein relation and beyond', *Stochastic Models*, vol. 19, no. 3, pp. 383–405, 2010.

[67] A. P. Liu and D. a. Fletcher, 'Actin polymerization serves as a membrane domain switch in model lipid bilayers.', *Biophysical journal*, vol. 91, no. 11, pp. 4064–70, 2006.

[68] J. Ehrig, E. P. Petrov and P. Schwille, 'Near-critical fluctuations and cytoskeleton-assisted phase separation lead to subdiffusion in cell membranes.', *Biophysical journal*, vol. 100, no. 1, pp. 80–89, 2011.

[69] K. C. Huang, R. Mukhopadhyay and N. S. Wingreen, 'A curvature-mediated mechanism for localization of lipids to bacterial poles.', *PLoS computational biology*, vol. 2, no. 11, e151, 2006.

[70] B. Sorre, A. Callan-Jones, J.-B. Manneville, P. Nassoy, J.-F. Joanny, J. Prost, B. Goud and P. Bassereau, 'Curvature-driven lipid sorting needs proximity to a demixing point and is aided by proteins.', *Proceedings of the National Academy of Sciences of the United States of America*, vol. 106, no. 14, pp. 5622–6, 2009.

[71] A. Roux, G. Koster, M. Lenz, B. Sorre, J.-B. Manneville, P. Nassoy and P. Bassereau, 'Membrane curvature controls dynamin polymerization.', *Proceedings of the National Academy of Sciences of the United States of America*, vol. 107, no. 9, pp. 4141–6, 2010.

[72] M. M. Kamal, D. Mills, M. Grzybek and J. Howard, 'Measurement of the membrane curvature preference of phospholipids reveals only weak coupling between lipid shape and leaflet curvature.', *Proceedings of the National Academy of Sciences of the United States of America*, vol. 106, no. 52, pp. 22 245–50, 2009.

[73] F Mayer, 'Cytoskeletons in prokaryotes', *Cell Biology International*, vol. 27, no. 5, pp. 429–438, 2003.

[74] J. Errington, 'Dynamic proteins and a cytoskeleton in bacteria.', *Nature Cell Biology*, vol. 5, no. 3, pp. 175–178, 2003.

[75] M. A. de Pedro, C. G. Grunfelder and H. Schwarz, 'Restricted Mobility of Cell Surface Proteins in the Polar Regions of Escherichia coli', *Journal of Bacteriology*, vol. 186, no. 9, pp. 2594–2602, 2004.

[76] T. J. Silhavy, D. Kahne and S. Walker, 'The bacterial cell envelope.', *Cold Spring Harbor perspectives in biology*, vol. 2, no. 5, a000414, 2010.

[77] J. Huang, 'Exploration of molecular interactions in cholesterol superlattices: effect of multibody interactions.', *Biophysical journal*, vol. 83, no. 2, pp. 1014–25, 2002.

[78] C Hunte, 'Specific protein-lipid interactions in membrane proteins.', *Biochemical Society transactions*, vol. 33, no. Pt 5, pp. 938–942, 2005.

[79] B. Cormack, R. Valdivia and S Falkow, 'FACS-optimized mutants of the green fluorescent protein (GFP).', *Gene*, vol. 173, no. 1 Spec No, pp. 33–38, 1996.

[80] L. M. Guzman, D Belin, M. J. Carson and J Beckwith, 'Tight regulation, modulation, and high-level expression by vectors containing the arabinose PBAD promoter.', *Journal of Bacteriology*, vol. 177, no. 14, pp. 4121–4130, 1995.

[81] P. Natale, T. Brüser and A. J. Driessen, 'Sec- and Tat-mediated protein secretion across the bacterial cytoplasmic membraneDistinct translocases and mechanisms', *Biochimica et Biophysica Acta (BBA) - Biomembranes*, vol. 1778, no. 9, pp. 1735–1756, 2008.

[82] J. D. Thomas, R. A. Daniel, J. Errington and C. Robinson, 'Export of active green fluorescent protein to the periplasm by the twin-arginine translocase (Tat) pathway in Escherichia coli', *Molecular Microbiology*, vol. 39, no. 1, pp. 47–53, 2001.

[83] C. W. Mullineaux, A. Nenninger, N. Ray and C. Robinson, 'Diffusion of Green Fluorescent Protein in Three Cell Environments in Escherichia Coli', *Journal of Bacteriology*, vol. 188, no. 10, pp. 3442–3448, 2006.

[84] H. Murakoshi, R. Iino, T. Kobayashi, T. Fujiwara, C. Ohshima, A. Yoshimura and A. Kusumi, 'Single-molecule imaging analysis of Ras activation in living cells.', *Proceedings of the National Academy of Sciences of the United States of America*, vol. 101, no. 19, pp. 7317–22, 2004.

[85] J Korlach, P Schwille, W. W. Webb and G. W. Feigenson, 'Characterization of lipid bilayer phases by confocal microscopy and fluorescence correlation spectroscopy.', *Proceedings of the National Academy of Sciences of the United States of America*, vol. 96, no. 15, pp. 8461–6, 1999.

[86] M. Brameshuber, J. Weghuber, V. Ruprecht, I. Gombos, I. Horváth, L. Vigh, P. Eckerstorfer, E. Kiss, H. Stockinger and G. J. Schütz, 'Imaging of mobile long-lived nanoplatforms in the

live cell plasma membrane.', *The Journal of biological chemistry*, vol. 285, no. 53, pp. 41 765–41 771, 2010.

[87] M Edidin, 'Lipid microdomains in cell surface membranes.', *Current opinion in structural biology*, vol. 7, no. 4, pp. 528–32, 1997.

[88] C. a. Day and A. K. Kenworthy, 'Tracking microdomain dynamics in cell membranes.', *Biochimica et biophysica acta*, vol. 1788, no. 1, pp. 245–53, 2009.

[89] G. W. Feigenson, 'Phase behavior of lipid mixtures.', *Nature chemical biology*, vol. 2, no. 11, pp. 560–3, 2006.

[90] R. Alford, H. M. Simpson, J. Duberman, G. C. Hill, M. Ogawa, C. Regino, H. Kobayashi and P. L. Choyke, 'Toxicity of organic fluorophores used in molecular imaging: literature review.', *Molecular imaging*, vol. 8, no. 6, pp. 341–54, 2009.

[91] M. C. Leake, J. H. Chandler, G. H. Wadhams, F. Bai, R. M. Berry and J. P. Armitage, 'Stoichiometry and turnover in single, functioning membrane protein complexes', *Nature*, vol. 443, no. 7109, pp. 355–358, 2006.

[92] R. M. Dickson, A. B. Cubitt, R. Y. Tsien and W. E. Moerner, 'On/off blinking and switching behaviour of single molecules of green fluorescent protein', *Nature*, vol. 388, no. 6640, pp. 355–358, 1997.

[93] A Kusumi, Y Sako and M Yamamoto, 'Confined lateral diffusion of membrane receptors as studied by single particle tracking (nanovid microscopy). Effects of calcium-induced differentiation in cultured epithelial cells.', *Biophys. J.*, vol. 65, no. 5, pp. 2021–2040, 1993.

[94] J. W. Lichtman and J.-A. A. Conchello, 'Fluorescence microscopy.', *Nature methods*, vol. 2, no. 12, pp. 910–919, 2005.

[95] D Axelrod, N. Thompson and T. Burghardt, 'Total internal inflection fluorescent microscopy.', *Journal of microscopy*, vol. 129, no. Pt 1, pp. 19–28, 1983.

[96] D. Toomre, 'Cellular Imaging Using Total Internal Reflection Fluorescence Microscopy: Theory and Instrumentation', *Cold Spring Harbor Protocols*, vol. 2012, no. 4, 2012.

[97] D Axelrod, 'Total internal reflection fluorescence microscopy in cell biology.', *Traffic (Copenhagen, Denmark)*, vol. 2, no. 11, pp. 764–74, 2001.

[98] J. B. Pawley, '¡italic¿Handbook of Biological Confocal Microscopy, Second Edition¡/italic¿', *Optical Engineering*, vol. 35, no. 9, p. 2765, 1996.

[99] A. M. Takalkar, A. L. Klibanov, J. J. Rychak, J. R. Lindner and K. Ley, 'Binding and detachment dynamics of microbubbles targeted to P-selectin under controlled shear flow.', *Journal of controlled release*, vol. 96, no. 3, pp. 473–482, 2004.

[100] T Jø ssang, J Feder and E Rosenqvist, 'Photon correlation spectroscopy of human IgG.', *Journal of protein chemistry*, vol. 7, no. 2, pp. 165–171, 1988.

[101] S. H. Chung and R. A. Kennedy, 'Forward-backward non-linear filtering technique for extracting small biological signals from noise.', *Journal of neuroscience methods*, vol. 40, no. 1, pp. 71–86, 1991.

[102] M. F. Garcia-Parajo, G. M. J. Segers-Nolten, J.-A. Veerman, J. Greve and N. F. van Hulst, 'Real-time light-driven dynamics of the fluorescence emission in single green fluorescent protein molecules', *Proceedings of the National Academy of Sciences*, vol. 97, no. 13, pp. 7237–7242, 2000.

[103] T Wilson and J. W. Hastings, 'Bioluminescence.', *Annual review of cell and developmental biology*, vol. 14, pp. 197–230, 1998.

[104] U Kubitscheck, O Kückmann, T Kues and R Peters, 'Imaging and tracking of single GFP molecules in solution.', *Biophysical journal*, vol. 78, no. 4, pp. 2170–9, 2000.

[105] T. Savin and P. S. Doyle, 'Static and dynamic errors in particle tracking microrheology.', *Biophysical journal*, vol. 88, no. 1, pp. 623–638, 2005.

[106] R. E. Thompson, D. R. Larson and W. W. Webb, 'Precise nanometer localization analysis for individual fluorescent probes.', *Biophysical journal*, vol. 82, no. 5, pp. 2775–83, 2002.

[107] X. Michalet, 'Mean square displacement analysis of single-particle trajectories with localization error: Brownian motion in an isotropic medium', *Physical Review E*, vol. 82, no. 4, 2010.

[108] P. R. Bevington, *Data reduction and error analysis for the physical sciences*, D Bruflodt, Ed. McGraw-Hill, 1969, vol. 336, p. 336. arXiv:0706.0168v1.

[109] N. Monnier, S.-M. M. Guo, M. Mori, J. He, P. Lénárt and M. Bathe, 'Bayesian Approach to MSD-Based Analysis of Particle Motion in Live Cells.', *Biophysical journal*, vol. 103, no. 3, pp. 616–626, 2012.

[110] R Peters and R. J. Cherry, 'Lateral and rotational diffusion of bacteriorhodopsin in lipid bilayers: experimental test of the Saffman-Delbrück equations', *Proceedings of the National Academy of Sciences*, vol. 79, no. 14, pp. 4317–4321, 1982.

[111] A. Naji, A. J. Levine and P. A. Pincus, 'Corrections to the Saffman-Delbruck Mobility for Membrane Bound Proteins', *Biophys. J.*, vol. 93, no. 11, pp. L49–51, 2007.

[112] G. J. Schütz, H Schindler and T Schmidt, 'Single-molecule microscopy on model membranes reveals anomalous diffusion.', *Biophysical journal*, vol. 73, no. 2, pp. 1073–80, 1997.

[113] L. S. Barak and W. W. Webb, 'Diffusion of low density lipoprotein-receptor complex on human fibroblasts.', *The Journal of cell biology*, vol. 95, no. 3, pp. 846–852, 1982.

[114] M. P. Sheetz, S Turney, H Qian and E. L. Elson, 'Nanometre-level analysis demonstrates that lipid flow does not drive membrane glycoprotein movements.', *Nature*, vol. 340, no. 6231, pp. 284–288, 1989.

[115] S. Wieser, M. Moertelmaier, E. Fuertbauer, H. Stockinger and G. J. Schütz, '(Un)Confined Diffusion of CD59 in the Plasma Membrane Determined by High-Resolution Single Molecule Microscopy', *Biophys J*, vol. 92, no. 10, pp. 3719–3728, 2007.

[116] F. Daumas, N. Destainville, C. Millot, A. Lopez, D. Dean and L. Salomé, 'Confined diffusion without fences of a g-protein-coupled receptor as revealed by single particle tracking.', *Biophysical journal*, vol. 84, no. 1, pp. 356–366, 2003.

[117] S. Y. Kim, Z. Gitai, A. Kinkhabwala, L. Shapiro and W. E. Moerner, 'Single molecules of the bacterial actin MreB undergo directed treadmilling motion in Caulobactercrescentus', *Proceedings of the National Academy of Sciences*, vol. 103, no. 29, pp. 10 929–10 934, 2006.

[118] J. P. Bouchaud and A. Georges, 'Anomalous diffusion in disordered media: Statistical mechanisms, models and physical applications', *Phys. Rep.*, vol. 195, no. 4-5, pp. 127–293, 1990.

[119] M. J. Saxton, 'Single-particle tracking: models of directed transport.', *Biophysical journal*, vol. 67, no. 5, pp. 2110–9, 1994.

[120] R. Metzler and J. Klafter, 'Subdiffusive transport close to thermal equilibrium: From the Langevin equation to fractional diffusion', *Physical Review E*, vol. 61, no. 6, 2000.

[121] J. Lippincott-Schwartz and G. H. Patterson, 'Development and Use of Fluorescent Protein Markers in Living Cells', *Science*, vol. 300, no. 5616, pp. 87–91, 2003.

[122] H Qian, M. Sheetz and E. Elson, 'Single particle tracking. Analysis of diffusion and flow in two-dimensional systems.', *Biophysical journal*, vol. 60, no. 4, pp. 910–921, 1991.

[123] A. Bruckbauer, P. D. Dunne, P. James, E. Howes, D. Zhou, R. Jones and D. Klenerman, 'Selective Diffusion Barriers Separate Membrane Compartments', *Biophys J*, vol. 99, no. 1, pp. L1–L3, 2010.

[124] M. J. Schaaf, W. J. Koopmans, T. Meckel, J. van Noort, E. E. Snaar-Jagalska, T. S. Schmidt and H. P. Spaink, 'Single-molecule microscopy reveals membrane microdomain organization of cells in a living vertebrate.', *Biophysical journal*, vol. 97, no. 4, pp. 1206–1214, 2009.

[125] A. V. Weigel, B. Simon, M. M. Tamkun and D. Krapf, 'Ergodic and nonergodic processes coexist in the plasma membrane as observed by single-molecule tracking.', *Proceedings of the National Academy of Sciences of the United States of America*, vol. 108, no. 16, pp. 6438–43, 2011.

[126] F. Pinaud, X. Michalet, G. Iyer, E. Margeat, H.-P. P. Moore and S. Weiss, 'Dynamic partitioning of a glycosyl-phosphatidylinositol-anchored protein in glycosphingolipid-rich microdomains imaged by single-quantum dot tracking.', *Traffic (Copenhagen, Denmark)*, vol. 10, no. 6, pp. 691–712, 2009.

[127] J. Szymanski and M. Weiss, 'Elucidating the origin of anomalous diffusion in crowded fluids.', *Physical review letters*, vol. 103, no. 3, 2009.

[128] M. R. Horton, F. Höfling, J. O. Rädler and T. Franosch, 'Development of anomalous diffusion among crowding proteins', *Soft Matter*, vol. 6, no. 12, p. 2648, 2010.

[129] M. Magdziarz, A. Weron and K. Burnecki, 'Fractional Brownian Motion Versus the Continuous-Time Random Walk: A Simple Test for Subdiffusive Dynamics', *Physical Review Letters*, vol. 103, no. 18, pp. 1–4, 2009.

[130] M. Hellmann, J. Klafter, D. W. Heermann and M. Weiss, 'Challenges in determining anomalous diffusion in crowded fluids.', *Journal of physics. Condensed matter : an Institute of Physics journal*, vol. 23, no. 23, p. 234 113, 2011.

[131] J. H. Jeon, V. Tejedor, S. Burov, E. Barkai, C. S. Unkel, K. B. Sø{}rensen, L. Oddershede and R. Metzler, 'In Vivo Anomalous Diffusion and Weak Ergodicity Breaking of Lipid Granules', *Physical Review Letters*, vol. 106, 2011.

[132] a. Fuliski, 'Anomalous diffusion and weak nonergodicity', *Physical Review E*, vol. 83, no. 6, pp. 1–5, 2011.

[133] S. Burov, J.-H. Jeon, R. Metzler and E. Barkai, 'Single particle tracking in systems showing anomalous diffusion: the role of weak ergodicity breaking.', *Physical chemistry chemical physics : PCCP*, vol. 13, no. 5, pp. 1800–12, 2011.

[134] I. Goychuk, 'Viscoelastic subdiffusion: From anomalous to normal', *Physical Review E*, vol. 80, no. 4, pp. 1–11, 2009.

[135] S. Coscoy, E. Huguet and F. Amblard, 'Statistical analysis of sets of random walks: how to resolve their generating mechanism.', *Bulletin of mathematical biology*, vol. 69, no. 8, pp. 2467–92, 2007.

[136] A Rebenshtok and E Barkai, 'Distribution of time-averaged observables for weak ergodicity breaking.', *Physical review letters*, vol. 99, no. 21, 2007.

[137] D. Meder, M. J. Moreno, P. Verkade, W. L. C. Vaz and K. Simons, 'Phase coexistence and connectivity in the apical membrane of polarized epithelial cells.', *Proceedings of the National Academy of Sciences of the United States of America*, vol. 103, no. 2, pp. 329–34, 2006.

[138] K. Murase, T. Fujiwara, Y. Umemura, K. Suzuki, R. Iino, H. Yamashita, M. Saito, H. Murakoshi, K. Ritchie and A. Kusumi, 'Ultrafine Membrane Compartments for Molecular Diffusion as Revealed by Single Molecule Techniques', *Biophys. J.*, vol. 86, no. 6, pp. 4075–4093, 2004.

[139] S. Semrau and T. Schmidt, 'Membrane heterogeneity from lipid domains to curvature effects', *Soft Matter*, vol. 5, no. 17, p. 3174, 2009.

[140] M. Edidin, 'Shrinking patches and slippery rafts: scales of domains in the plasma membrane', *Trends in Cell Biology*, vol. 11, no. 12, pp. 492–496, 2001.

[141] D. S. Banks and C. Fradin, 'Anomalous Diffusion of Proteins Due to Molecular Crowding', *Biophysical Journal*, vol. 89, no. 5, pp. 2960–2971, 2005.

[142] W. Pan, L. Filobelo, N. D. Q. Pham, O. Galkin, V. V. Uzunova and P. G. Vekilov, 'Viscoelasticity in Homogeneous Protein Solutions', *Physical Review Letters*, vol. 102, no. 5, 2009.

[143] M. Weiss, M. Elsner, F. Kartberg and T. Nilsson, 'Anomalous Subdiffusion Is a Measure for Cytoplasmic Crowding in Living Cells', *Biophys J*, vol. 87, no. 5, pp. 3518–3524, 2004.

[144] G Guigas, C Kalla and M Weiss, 'The degree of macromolecular crowding in the cytoplasm and nucleoplasm of mammalian cells is conserved.', *FEBS letters*, vol. 581, no. 26, pp. 5094–5098, 2007.

[145] I. Golding and E. C. Cox, 'Physical Nature of Bacterial Cytoplasm', *Physical Review Letters*, vol. 96, no. 9, 2006.

[146] J. M. Haugh, 'Analysis of reaction-diffusion systems with anomalous subdiffusion.', *Biophysical journal*, vol. 97, no. 2, pp. 435–42, 2009.

[147] J. A. Dix and A. Verkman, 'Crowding Effects on Diffusion in Solutions and Cells', *Annual Review of Biophysics*, vol. 37, no. 1, pp. 247–263, 2008.

[148] M. Hellmann, D. W. Heermann and M. Weiss, 'Anomalous reaction kinetics and domain formation on crowded membranes', *EPL (Europhysics Letters)*, vol. 94, no. 1, p. 18 002, 2011.

[149] J. S. Kim and A. Yethiraj, 'Crowding effects on association reactions at membranes.', *Biophysical journal*, vol. 98, no. 6, pp. 951–8, 2010.

[150] M. J. Saxton, 'A biological interpretation of transient anomalous subdiffusion. II. Reaction kinetics.', *Biophysical journal*, vol. 94, no. 3, pp. 760–71, 2008.

[151] S. R. McGuffee and A. H. Elcock, 'Diffusion, Crowding & Protein Stability in a Dynamic Molecular Model of the Bacterial Cytoplasm', *PLoS Computational Biology*, vol. 6, no. 3, 2010.

[152] S. Havlin and D. Ben-Avraham, 'Diffusion in disordered media', *Advances in Physics*, vol. 51, no. 1, pp. 187–292, 2002.

[153] S. Condamin, O. Benichou, V. Tejedor, R. Voituriez and J. Klafter, 'First-passage times in complex scale-invariant media', *Nature*, vol. 450, no. 7166, pp. 77–80, 2007.

[154] M. Deverall, E. Gindl, E.-K. Sinner, H. Besir, J. Ruehe, M. Saxton and C. Naumann, 'Membrane Lateral Mobility Obstructed by Polymer-Tethered Lipids Studied at the Single Molecule Level', *Biophysical Journal*, vol. 88, no. 3, pp. 1875–1886, 2005.

[155] J. T. Mika and B. Poolman, 'Macromolecule diffusion and confinement in prokaryotic cells', *Current Opinion in Biotechnology*, vol. 22, no. 1, pp. 117–126, 2011.

[156] T. Lenn, M. C. Leake and C. W. Mullineaux, 'Clustering and dynamics of cytochrome bd-I complexes in the Escherichia coli plasma membrane in vivo.', *Molecular microbiology*, vol. 70, no. 6, pp. 1397–407, 2008.

[157] S. Havlin, J. E. Kiefer and G. H. Weiss, 'Anomalous diffusion on a random comblike structure', *Physical Review A*, vol. 36, no. 3, 1987.

[158] T Zavada, N Südland, R Kimmich and T. F. Nonnenmacher, 'Propagator representation of anomalous diffusion: the orientational structure factor formalism in NMR.', *Physical review. E, Statistical physics, plasmas, fluids, and related interdisciplinary topics*, vol. 60, no. 2 Pt A, pp. 1292–8, 1999.

[159] D. Fulger, E. Scalas and G. Germano, 'Monte Carlo simulation of uncoupled continuous-time random walks yielding a stochastic solution of the space-time fractional diffusion equation', *Physical Review E*, vol. 77, no. 2, pp. 1–7, 2008.

[160] E. W. Montroll and G. H. Weiss, 'Random Walks on Lattices. II', *Journal of Mathematical Physics*, vol. 6, no. 2, pp. 167–181, 1965.

[161] M. Platani, I. Goldberg, A. I. Lamond and J. R. Swedlow, 'Cajal Body dynamics and association with chromatin are ATP-dependent', *Nat Cell Biol*, vol. 4, no. 7, pp. 502–508, 2002.

[162] H. Search, C. Journals, A. Contact, M. Iopscience and I. P. Address, 'Path integral representation for fractional Brownian motion', *Time*, vol. 4305, 1995.

[163] M. Magdziarz and J. Klafter, 'Detecting origins of subdiffusion: P-variation test for confined systems', *Physical Review E*, vol. 82, no. 1, pp. 1–7, 2010.

[164] J. Wu and K. M. Berland, 'Propagators and time-dependent diffusion coefficients for anomalous diffusion.', *Biophysical journal*, vol. 95, no. 4, pp. 2049–2052, 2008.

[165] V. Tejedor, O. Bénichou, R. Voituriez, R. Jungmann, F. Simmel, C. Selhuber-Unkel, L. B. Oddershede and R. Metzler, 'Quantitative Analysis of Single Particle Trajectories: Mean Maximal Excursion Method', *Biophys J*, vol. 98, no. 7, pp. 1364–1372, 2010.

[166] S. C. Weber, A. J. Spakowitz and J. a. Theriot, 'Bacterial Chromosomal Loci Move Subdiffusively through a Viscoelastic Cytoplasm', *Physical Review Letters*, vol. 104, no. 23, pp. 1–4, 2010.

[167] S. Wieser, M. Axmann and G. J. Schütz, 'Versatile analysis of single-molecule tracking data by comprehensive testing against Monte Carlo simulations.', *Biophysical journal*, vol. 95, no. 12, pp. 5988–6001, 2008.

[168] S. Jin and A. S. Verkman, 'Single Particle Tracking of Complex Diffusion in Membranes: Simulation and Detection of Barrier, Raft, and Interaction Phenomena', *The Journal of Physical Chemistry B*, vol. 111, no. 14, pp. 3625–3632, 2007.

[169] S. Condamin, O. Bénichou and M. Moreau, 'First-Passage Times for Random Walks in Bounded Domains', *Physical Review Letters*, vol. 95, no. 26, pp. 1–4, 2005.

[170] S. Condamin, V. Tejedor, R. Voituriez, O. Benichou and J. Klafter, 'Probing microscopic origins of confined subdiffusion by first-passage observables', *Proceedings of the National Academy of Sciences*, vol. 105, no. 15, pp. 5675–5680, 2008.

[171] P. Dieterich, R. Klages, R. Preuss and A. Schwab, 'Anomalous dynamics of cell migration', *Proceedings of the National Academy of Sciences*, vol. 105, no. 2, pp. 459–463, 2008.

[172] A. Lubelski, I. M. Sokolov and J. Klafter, 'Nonergodicity Mimics Inhomogeneity in Single Particle Tracking', *Physical Review Letters*, vol. 100, no. 25, 2008.

[173] Y. Meroz, I. M. Sokolov and J. Klafter, 'Subdiffusion of mixed origins: When ergodicity and nonergodicity coexist', *Physical Review E*, vol. 81, no. 1, pp. 1–4, 2010.

[174] A. V. Weigel, P. D. Fox, E. J. Akin, K. H. Ecklund, M. M. Tamkun and D. Krapf, 'Size of Cell-Surface Kv2.1 Domains is Governed by Growth Fluctuations', *Biophys J*, vol. 103, no. 8, pp. 1727–1734, 2012.

[175] A Einstein, 'On the movement of small particles suspended in a stationary liquid demanded by the molecular-kinetic theory of heat', *Annalen der Physik (Leipzig)*, vol. 17, pp. 549–560, 1905.

[176] R. Metzler and J. Klafter, 'The random walk's guide to anomalous diffusion: a fractional dynamics approach', *Physics Reports*, vol. 339, no. 1, pp. 1–77, 2000.

[177] Q. Yang, I. Turner, F. Liu and M. Ilić, 'Novel Numerical Methods for Solving the Time-Space Fractional Diffusion Equation in Two Dimensions', en, *SIAM Journal on Scientific Computing*, vol. 33, no. 3, pp. 1159–1180, 2011.

[178] T Bickel, 'A note on confined diffusion', *Physica A: Statistical Mechanics and its Applications*, vol. 377, no. 1, pp. 24–32, 2007.

[179] P. J. Bickel, B. Li, A. B. Tsybakov, S. a. Geer, B. Yu, T. Valdés, C. Rivero, J. Fan and A. Vaart, 'Regularization in statistics', *Test*, vol. 15, no. 2, pp. 271–344, 2006.

[180] D. J. C. MacKay, *Information theory, inference and learning algorithms*, First Edit. Cambridge University Press, 2007.

[181] S. Türkcan, A. Alexandrou and J.-B. Masson, 'A Bayesian Inference Scheme to Extract Diffusivity and Potential Fields from Confined Single-Molecule Trajectories', *Biophys J*, vol. 102, no. 10, pp. 2288–2298, 2012.

[182] G. Voisinne, A. Alexandrou and J.-B. Masson, 'Quantifying biomolecule diffusivity using an optimal Bayesian method.', *Biophysical journal*, vol. 98, no. 4, pp. 596–605, 2010.

[183] J. Masson, D Casanova, S Türkcan, G Voisinne, M. Popoff, M Vergassola and A Alexandrou, 'Inferring maps of forces inside cell membrane microdomains.', *Physical review letters*, vol. 102, no. 4, 2009.

[184] D. J. MacKay, 'Bayesian Interpolation', *Neural Computation*, vol. 4, pp. 415–447, 1991.

[185] M. Vrljic, S. Y. Nishimura, S. Brasselet, W. Moerner and H. M. McConnell, 'Translational diffusion of individual class II MHC membrane proteins in cells.', *Biophysical journal*, vol. 83, no. 5, pp. 2681–2692, 2002.

[186] L. J. Pike, 'The challenge of lipid rafts', *Journal of Lipid Research*, vol. 50, no. Supplement, S323–S328, 2009.

[187] C. M. Bishop, *Pattern recognition and machine learning*, 1st ed. 20. Springer, 2006.

[188] H. Akaike, 'A new look at the statistical model identification', *IEEE Transactions on Automatic Control*, vol. 19, no. 6, pp. 716–723, 1974.

[189] G. Schwarz, 'Estimating the Dimension of a Model', *The Annals of Statistics*, vol. 6, no. 2, pp. 461–464, 1978.

[190] R. E. Caflisch, 'Monte Carlo and quasi-Monte Carlo methods', *Acta Numerica*, vol. 7, no. -1, pp. 1–49, 1998.

[191] S. M. J. L. van den Wildenberg, Y. J. M. Bollen and E. J. G. Peterman, 'How to quantify protein diffusion in the bacterial membrane.', *Biopolymers*, vol. 95, no. 5, pp. 312–21, 2011.

[192] H Nakayama, T Mitsui, M Nishihara and M Kito, 'Relation between growth temperature of E. coli and phase transition temperatures of its cytoplasmic and outer membranes.', *Biochimica et biophysica acta*, vol. 601, no. 1, pp. 1–10, 1980.

[193] A. G. Rietveld, J. A. Killian, W Dowhan and B de Kruijff, 'Polymorphic regulation of membrane phospholipid composition in Escherichia coli.', *The Journal of biological chemistry*, vol. 268, no. 17, pp. 12 427–33, 1993.

[194] C. Klose, C. S. Ejsing, A. J. García-Sáez, H.-J. Kaiser, J. L. Sampaio, M. A. Surma, A. Shevchenko, P. Schwille and K. Simons, 'Yeast lipids can phase-separate into micrometer-scale membrane domains.', *The Journal of biological chemistry*, vol. 285, no. 39, pp. 30 224–32, 2010.

[195] G. Lindblom, G. Orädd, L. Rilfors and S. Morein, 'Regulation of Lipid Composition in Acholeplasma laidlawii and Escherichia coli Membranes: NMR Studies of Lipid Lateral Diffusion at Different Growth Temperatures', *Biochemistry*, vol. 41, no. 38, pp. 11 512–11 515, 2002.

[196] M. C. Mansilla, L. E. Cybulski, D. Albanesi and D. de Mendoza, 'Control of membrane lipid fluidity by molecular thermosensors.', *Journal of bacteriology*, vol. 186, no. 20, pp. 6681–8, 2004.

[197] H. M. McConnell, 'Understanding Membranes', *ACS Chemical Biology*, vol. 3, no. 5, pp. 265–267, 2008.

[198] P. Lague, M. J. Zuckermann and B. Roux, 'Lipid-Mediated Interactions between Intrinsic Membrane Proteins: Dependence on Protein Size and Lipid Composition', *Biophys. J.*, vol. 81, no. 1, pp. 276–284, 2001.

[199] E. Reister and U. Seifert, 'Lateral diffusion of a protein on a fluctuating membrane', *EPL (Europhysics Letters)*, vol. 71, no. 5, pp. 859–865, 2005.

[200] G. Guigas and M. Weiss, 'Size-dependent diffusion of membrane inclusions.', *Biophysical journal*, vol. 91, no. 7, pp. 2393–8, 2006.

[201] A. Khlebnikov, O. Risa, T. Skaug, T. A. Carrier and J. D. Keasling, 'Regulatable Arabinose-Inducible Gene Expression System with Consistent Control in All Cells of a Culture', *Journal of Bacteriology*, vol. 182, no. 24, pp. 7029–7034, 2000.

[202] G. C. Franke, S Dobinsky, D Mack, C.-J. Wang, I Sobottka, M Christner, J. K.-M. Knobloch, M. A. Horstkotte, M Aepfelbacher and H Rohde, 'Expression and functional characterization of gfpmut3.1 and its unstable variants in Staphylococcus epidermidis.', *Journal of microbiological methods*, vol. 71, no. 2, pp. 123–32, 2007.

[203] J. Sambrook and D. W. Russell, *Molecular Cloning: A Laboratory Manual*, Third. Cold Spring Harbor Laboratory Press, 2001.

[204] M. Sarcina, N. Murata, M. J. Tobin and C. W. Mullineaux, 'Lipid diffusion in the thylakoid membranes of the cyanobacterium Synechococcus sp.: effect of fatty acid desaturation', *FEBS Letters*, vol. 553, no. 3, pp. 295–298, 2003.

[205] R. J. Ober, S. Ram and E. S. Ward, 'Localization accuracy in single-molecule microscopy.', *Biophysical journal*, vol. 86, no. 2, pp. 1185–200, 2004.

[206] X. Michalet, 'Mean square displacement analysis of single-particle trajectories with localization error: Brownian motion in an isotropic medium.', *Physical review. E, Statistical, nonlinear, and soft matter physics*, vol. 82, no. 4 Pt 1, 2010.

[207] X. Michalet and A. J. Berglund, 'Optimal diffusion coefficient estimation in single-particle tracking.', *Physical review. E, Statistical, nonlinear, and soft matter physics*, vol. 85, no. 6 Pt 1, p. 061 916, 2012.

[208] N. Ray, A. Nenninger, C. W. Mullineaux and C. Robinson, 'Location and mobility of twin arginine translocase subunits in the Escherichia coli plasma membrane.', *The Journal of biological chemistry*, vol. 280, no. 18, pp. 17 961–8, 2005.

[209] A. R. Honerkamp-Smith, P. Cicuta, M. D. Collins, S. L. Veatch, M. den Nijs, M. Schick and S. L. Keller, 'Line Tensions, Correlation Lengths, and Critical Exponents in Lipid Membranes Near Critical Points', vol. 95, no. 1, pp. 236–246, 2008.

[210] A. R. Honerkamp-Smith, S. L. Veatch and S. L. Keller, 'An introduction to critical points for biophysicists; observations of compositional heterogeneity in lipid membranes.', *Biochimica et biophysica acta*, vol. 1788, no. 1, pp. 53–63, 2009.

[211] Y. T. Lenn, 'Complexes in the Escherichia coli plasma', *Queen Mary, University of London, Ph.D Thesis*, 2010.